

# Microwave Observations of Uranus

Thesis by  
Mark David Hofstadter

In Partial Fulfillment of the Requirements  
for the Degree of  
Doctor of Philosophy

California Institute of Technology  
Pasadena, California

1992

(Defended 1 October 1991)

© 1992

Mark D. Hofstadter

All Rights Reserved

*For my Father*



## Acknowledgments

*"Don't look back."*  
— Boston

This is an important part of the thesis because, while my name is the only one that appears on the title page, the many people who helped, inspired, and supported me in this task deserve second author credit. This section is also very special for me because, unlike the couple hundred pages to follow, I can write it in the first person and use the word "spleen" if the mood strikes me.

First of all, I want to acknowledge my family for the love and support that has let me pursue what interests me. I am very fortunate and proud to have them beside me. I also want to recognize my thesis advisor, Dewey Muhleman, who suggested this project my first year here. I have very much enjoyed the opportunity to work with him, and expect to continue to do so in the future. He is an excellent teacher, and I encourage anyone who can accept bluntness as honesty to get to know him.

I would also like to express my appreciation to the faculty here at Caltech. Without exception, they were willing to discuss my work and, like my mom, they somehow always managed to be right. The professional and support staff here are particularly professional and supportive. Fortunately, they also know when not to be professional. While most of my interactions have been with the Planetary People, the above comments apply to the other options as well. Professors Bob Sharp and Lee Silver deserve special mention in this category. If I had run into them earlier, today I might be a field geologist.

And now for that most important group, my friends. This is a very broad category that runs from people I've known since grade school to graduate students I recently met.

The insanity, intelligence, and companionship they have provided have been invaluable to me. You guys have made the journey worthwhile.

Finally, I'm left with all these little bits I feel it is important to mention. One is 154 South Mudd. We've mellowed an awful lot in the last couple years (does that have anything to do with Bill graduating, me writing a thesis, and Bruce getting married?), but the noises, smells, and contraptions that have lumbered out our door (and sometimes through the walls) have tried the patience of all those around us. I hope they have been a source of amusement as well. Another special mention goes to Mike, who cheerfully fought against the rapid decay of my aging terminal as I desperately tried to finish this thesis. Bruce and Kathy... 'nuff said. Bruce and Bruce... I'll seriously consider your advice (on different topics) to be less cautious. State Beach... it and its inhabitants were often the light at the end of the tunnel.

One more important thing that I'd like to acknowledge is a sense of fun and adventure. There's a special feeling about sunrise on a remote, snow-dusted plateau, and stepping out into the cold to see 27 gleaming white antennas pointed at a little piece of the sky that you've chosen. Observing runs, enthusiastic researchers and technicians, DPS volleyball games, and people who thought that what I was doing sounded neat, even if they didn't understand it all, have kept the excitement alive.

## Abstract

This thesis explores the atmosphere of Uranus using microwave observations at wavelengths from 1 to 20 cm, with primary emphasis on high resolution VLA data at wavelengths of 2 and 6 cm. While radio maps of Uranus have been published previously, this is the first detailed analysis and interpretation of such observations. Atmospheric structures are mapped to depths greater than has been seen on any giant planet. Several features of the data are immediately clear. First, there are strong horizontal and vertical gradients in the atmospheric properties that control the radio brightness. Polar regions are much brighter than lower latitudes, and the deep troposphere (pressures greater than a few tens of bars) appears much dimmer than would be expected based on the upper troposphere. (Both these results had been postulated in previous works, but older observations lacked the resolution to confirm them.) A second important feature of the data is that the intrinsic latitudinal brightness variations determined in this work at 2 cm and 6 cm are highly correlated with each other and with Voyager infrared measurements, suggesting a common cause. Because these data sets probe different altitudes between 50 and 0.1 bar, the cause must be acting over this altitude range of about 250 km. Another immediate result, independent of atmospheric modeling, is that the radio brightness features have not changed significantly in the 8 years between 1981 and 1989.

Since radio brightness is a function of temperature and composition, the observations can be used to map these properties as a function of latitude and height. Arguments are presented that indicate compositional gradients are the dominant factor controlling the brightness variations, and these compositional changes are used as a tracer to infer the

general circulation and some of the chemical processes of the atmosphere. The most likely interpretation of the data is that the Southern Hemisphere is dominated by a single meridional circulation cell, with an upwelling centered near  $-25^\circ$  latitude that brings absorber rich air parcels from 50 bars up to the 0.1 bar region. As parcels rise, the absorber mixing ratio drops by a factor of about 100 between 25 and 10 bars, and then a further factor of 2 at higher altitudes. These depletions are probably due to condensation. The absorber depleted parcels then move poleward and descend, dominating the atmospheric composition over the pole down to 50 bars, but not deeper. This circulation is consistent with the zonal winds and upper atmospheric temperatures observed by Voyager in the context of a simple, linear, dynamical model. The model suggests that the forcing driving these motions occurs within the upper few hundred bars of the atmosphere. The species most likely to be responsible for microwave absorption in the atmosphere is  $\text{NH}_3$ , and at depth it appears to have a molar mixing ratio within an order of magnitude of  $1.4 \times 10^{-4}$ , the solar value. The formation of an  $\text{NH}_4\text{SH}$  cloud above 30 bars can account for the primary depletion of  $\text{NH}_3$ , while  $\text{NH}_3$  ice condensation at 5 bars accounts for the rest. Most of the results discussed here, however, are independent of what the absorbing species actually is.

Superimposed on the large scale brightness pattern are smaller brightness oscillations, less than about  $15^\circ$  wide in latitude. These long lasting features are reminiscent of the zones and belts of Jupiter, and could be the result of variations in either cloud altitudes or the depth of penetration of subsiding air parcels. A more extensive analysis is needed, however, to understand these small scale structures. The final point addressed in this work is the seasonal variability of the atmosphere. While no variations exist in the current high resolution data set, which covers about 10 years of the mid-summer season, it is expected that detectable changes will occur over 20 to 40 year time scales (each season on Uranus lasts 21 years). The magnitude of the variations, however, cannot be determined from the available data.

# Contents

<b>Acknowledgments</b>	<b>v</b>
<b>Abstract</b>	<b>vii</b>
<b>Table of Contents</b>	<b>ix</b>
<b>List of Figures</b>	<b>xiii</b>
<b>List of Tables</b>	<b>xv</b>
<b>1 Introduction</b>	<b>1</b>
<b>2 The Model Atmosphere</b>	<b>5</b>
2.1 Basic Principles .....	5
2.2 Model Details .....	7
2.2.1 The Thin Layer Approximation .....	7
2.2.2 Composition .....	10
2.2.3 Temperature .....	13
2.2.4 Saturation and Clouds .....	21
2.2.5 Absorption .....	31
NH <sub>3</sub> Absorption .....	32

H <sub>2</sub> O Vapor Absorption .....	36
Liquid H <sub>2</sub> O Absorption .....	37
H <sub>2</sub> Absorption .....	38
Unmodeled Absorbers .....	42
2.3 Modeling Disk Averaged Data .....	44
2.3.1 Disk Averaged Data .....	45
2.3.2 Model Fitting .....	47
2.3.3 The Reference Model .....	58
2.3.4 Summary of Unresolved Observations .....	66
<b>3 High Resolution Observations</b> .....	<b>67</b>
3.1 The VLA .....	67
3.1.1 Physical Location and Layout .....	67
3.1.2 Theory of Operation .....	68
3.1.3 Mapping .....	71
3.1.4 Observing Procedures .....	74
3.2 The Data .....	76
3.2.1 Summary of Observations .....	76
3.2.2 Intrinsic Brightness Structures .....	83
<b>4 Data Analysis</b> .....	<b>93</b>
4.1 Generating Observed Features .....	93
4.1.1 Absorber Gradients .....	93
4.1.2 Explaining the Absorber Gradients .....	108
4.1.3 Temperature Gradients .....	118
4.2 Dynamical Modeling .....	125
4.2.1 Overview .....	125

4.2.2 The Model .....	128
Governing Equations .....	128
Boundary Conditions .....	134
4.2.3 Results .....	137
4.3 Time Variability .....	149
<b>5 Summary</b>	<b>155</b>
<b>Appendix</b>	<b>159</b>
<b>References</b>	<b>163</b>



## List of Figures

2.1	Atmospheric temperature profile .....	14
2.2	Model vapor pressures and cloud densities .....	30
2.3	Disk averaged data and initial models .....	48
2.4	Spectra of models with extra absorber at depth .....	50
2.5	Spectra of isothermal models .....	52
2.6	Spectra of models with water absorption .....	53
2.7	Effects of $\text{NH}_3\text{-H}_2\text{S}$ chemistry on the spectrum .....	56
2.8	Weighting functions .....	59
2.9	Effects of the uncertainty in the $\text{NH}_3$ line shape .....	62
2.10	Spectrum using alternate $\text{H}_2$ and $\text{H}_2\text{O}$ line shapes .....	63
2.11	Effects of the uncertainty in the temperature profile .....	65
3.1a	Map of Uranus at 6 cm from 1981 data .....	79
3.1b	Map of Uranus at 6 cm from 1989 data .....	80
3.1c	Map of Uranus at 2 cm from 1985 data .....	81
3.2a	Difference map, 1989 6 cm data minus the reference model .....	85
3.2b	Difference map, 1985 2 cm data minus the reference model .....	86
3.3	Intrinsic radio brightness and IRIS temperatures .....	87
4.1	Zonally averaged 2 cm brightness .....	95
4.2	Difference plot of 2 cm data and initial models .....	96

4.3	Difference plot of 2 and 6 cm data with model .....	98
4.4	Fitting bi-modal model to 2 and 6 cm data .....	100
4.5	Effect of adding an absorber depleted Northern Hemisphere .....	101
4.6	Setting limits on the absorber altitude .....	103
4.7	More limits on the absorber altitude .....	104
4.8	Setting limits on the transition latitude .....	106
4.9	More limits on the transition latitude .....	107
4.10	Schematic diagram of absorber distribution and circulation pattern .....	109
4.11	Spectrum of high resolution models .....	111
4.12	Atmospheric composition of nominal model .....	114
4.13	Deviations of nominal model from the data .....	115
4.14	Schematic of nominal model absorber distribution and circulation pattern ..	117
4.15	Intrinsic brightness and IRIS temperatures .....	119
4.16	Fitting polar regions with the nominal temperature profile .....	121
4.17	Polar and low-latitude temperature profiles .....	123
4.18	Observed zonal winds .....	126
4.19	Pole to pole IRIS temperature scan .....	127
4.20	Atmospheric stability versus height .....	133
4.21	The frictional damping time, $\tau_f$ .....	135
4.22	Contour plot of model stream function .....	138
4.23	Contour plot of model temperatures .....	139
4.24	<b>Model zonal winds</b> .....	141
4.25	Vertical profile of model zonal winds .....	142
4.26	Meridional profile of model temperatures .....	144
4.27	Vertical profile of model vertical winds .....	145
4.28	Decoupling cloud top zonal winds from the deep atmosphere .....	147
4.29	The time variability of Uranus' spectrum and model fits .....	150

## List of Tables

2.1	Model atmosphere composition .....	11
2.2	Polynomial coefficients from Poynter and Kakar .....	35
3.1	High resolution observations .....	77



## Chapter 1

### Introduction

*"It's been such a long time, I think I should be going."*  
— Boston

It is difficult to conjure up an inspiring description for a planet that, at first glance, resembles a cue ball. To the naked eye, Uranus appears to be a faint star; in fact, it was recorded as such on star charts as long ago as 1690. Not until 1781, when William Herschel pointed his telescope at it, was Uranus "discovered" as a planet. While Herschel could clearly see the disk of the planet, no features were observed on it. Even cameras on the Voyager spacecraft found Uranus to be rather bland. Uranus' visible appearance, however, is misleading. This thesis describes the first detailed analysis of high resolution radio images of Uranus. It will be seen that there are strong variations across the disk of the planet, and that these variations can be traced deeper into the atmosphere than has been seen on any other Jovian planet. It is the goal of this work to explain the observed features in terms of the composition, dynamics, and chemistry of the atmosphere.

A major motivation for this work was the fact that Uranus was a new and relatively unknown world that had just become "knowable". Ground based instruments have only recently become capable of resolving Uranus, and the Voyager spacecraft made its flyby in January 1986. Furthermore, there were intriguing hints that Uranus was quite different from the other Jupiter-like planets. Most obvious was the fact that Uranus has an obliquity of  $98^\circ$ —which creates an unusual solar insolation pattern and unique viewing geometries. Uranus also has no detectable internal heat source, while all the other giant planets have

significant ones. Finally, early radio observations showed Uranus to be different in composition from Jupiter and Saturn (Gulkis *et al.* 1978), to be changing with time (Klein and Turegano 1978), and at some wavelengths to have latitudinal variations in brightness (Briggs and Andrew 1980).

The next chapter begins by describing the radiative transfer model used in this work to analyze radio observations of Uranus. Included are a general discussion of what passive radio instruments “see,” definitions of important terms, and a discussion of the relevant physical properties of Uranus. This part (Sections 2.1 and 2.2) is intended to be a reference for use in constructing such models, and therefore contains some detail and derivations not normally provided. The second half of the chapter, Section 2.3, is a summary and analysis of low resolution observations made prior to the current work. This is included in the model description chapter for two reasons. First, comparing the model to previous results is part of the testing procedure. Second, by analyzing the low resolution data with the model, the reader will get a feel for how various model parameters can be constrained by observations. This knowledge will be an aid in interpreting the high resolution data presented in Chapter 3. The last section of this chapter contains a concise summary of the disk-averaged results.

Chapter 3 describes the instrument and procedures used to make the high resolution maps that are the heart of this research. The data maps themselves are then presented. (As was the case in Chapter 2, some parts of this discussion are tutorial in nature. Sections that the casual or advanced reader may want to skip are pointed out at the start of the chapter.) The data presented consist of 2 cm observations made in 1985, and 6 cm observations made in 1981 and 1989. A straightforward analysis of these data yields three important results: the deep atmosphere appears less bright than one would expect based on the upper atmosphere; the South Pole is brighter than low latitudes over a wide altitude range; and there have been no significant changes in the brightness pattern between 1981 and 1989.

These results are analyzed in detail in Chapter 4. In the first section, several possible interpretations of the data are presented. The favored one involves compositional gradients maintained by a meridional circulation pattern. The second section uses a simple dynamical model to explore the plausibility of the suggested circulation. The chapter concludes with a discussion of the seasonal variability of the atmosphere as constrained by radio observations.

The concluding chapter, Chapter 5, contains a summary and a discussion of possible future work. Early stages of this research have been described in Hofstadter and Muhleman (1987, 1989) and Hofstadter *et al.* (1990). Reference will be made to these works at appropriate places in the text.



## Chapter 2

# The Model Atmosphere

*"Ain't nothing like it, a shiny machine."  
— Van Halen*

Sections 2.1 and 2.2 of this chapter are a description of the model atmosphere used to analyze the observed radio brightness of Uranus. Section 2.3 contains a fairly detailed application of this model to unresolved observations of Uranus. The intent is to allow the reader to develop some intuition for how various atmospheric parameters might effect the radio observations. The figure captions and Sub-Section 2.3.4 provide a quick overview of this discussion.

## 2.1 Basic Principles

All objects naturally emit electromagnetic radiation. The emission, called thermal radiation, can be thought of as resulting from the thermal vibrations of molecules in the object. The molecules carry some charge and these accelerating charges radiate energy. (The word "charge" is used liberally and can include currents and spin.) The amount of energy radiated depends on how much energy is in the vibrations—which is determined by the temperature, and how easily these vibrations interact with electromagnetic radiation—which is related to the absorption coefficient. Thus, hotter things and molecules with large electric dipoles tend to radiate more energy than those that are cooler or lacking strong dipole moments. A demonstration of this effect can be had by heating a piece of metal to the point that it begins to emit detectable visible radiation (*i.e.*, you see it glow). Radio

waves are just a lower energy form of this radiation. The goal of this discussion is to make plausible the idea that the amount of radio energy emitted by an object (be it solid, liquid, or gas) depends on the object's temperature and absorption coefficient, and nothing else. Furthermore, in the absence of scattering, the absorption coefficient (a measure of how well an object couples to a radiation field) is a function of the composition only, so radio observations of a planet can tell us about its temperature and composition. Once it is known how these properties vary with latitude and altitude, it is possible to infer things about the circulation and cloud structure as well.

A useful concept used throughout this work is that of brightness temperature, which is a standard measure of the energy radiated by an object. It is the kinetic temperature a blackbody (a perfect absorber) would need to have for it to radiate the same amount as the object in question. (If an object is a good absorber, its brightness temperature will be close to its actual kinetic temperature.) Thus brightness will usually be referred to in units of Kelvin, with "hotter" objects being brighter than "cold" ones.

The overall technique for analyzing actual observations is as follows. An initial atmospheric composition and vertical temperature profile is assumed. Since some constituents condense, the saturation vapor pressure of each species is compared to the assumed abundance at all altitudes. If the saturated abundance is smaller, it becomes the new vapor abundance at that level, the excess being assumed to have condensed out and formed a cloud. The absorption coefficient at each altitude is then calculated from knowledge of the composition (vapor and cloud), and is combined with the temperature profile to calculate the radiative properties of the atmosphere. These model emissions are then compared to observations, and the temperature and composition adjusted until model and observations match. The next section presents the details of this modeling procedure.

## 2.2 Model Details

### 2.2.1 The Thin Layer Approximation

The brightness temperature as a function of position on the observed disk of the planet is calculated using the radiative transfer equation in the Rayleigh-Jeans limit, with no scattering (Chandrasekhar 1960). To apply this equation, the atmosphere of the planet is approximated by many thin, horizontal layers. Each layer has a constant temperature, pressure, and composition (and therefore a constant absorption coefficient). Radiative effects of the interface between layers (such as reflection) are neglected because the actual atmospheric properties vary continuously and will not have these boundary effects. Refraction, however, is included.

Looking at one of these atmospheric layers from above, there are two components to the observed radiation; one represents the flux from all the deeper layers that is transmitted through the top layer, and the other representing the energy radiated from the top layer itself. The first (transmitted) component is just

$$B_T = B_{\text{in}} e^{-k_\nu h/\mu},$$

where  $B_{\text{in}}$  is the brightness entering the layer from below ( $\text{erg cm}^{-2} \text{ s}^{-1} \text{ Hz}^{-1} \text{ strad}^{-1}$ ),  $k_\nu$  is the absorption coefficient of the layer ( $\text{cm}^{-1}$ ),  $h$  is the thickness of the layer, and  $\mu$  is the cosine of the observing angle (the angle between vertical and the observing line of sight). Note that  $h/\mu$  is just the path length through the layer. To calculate the emitted term, consider each infinitesimal volume along the line of sight. The emitted intensity from such a volume at a height  $z$  in the layer (the layer running from  $z = 0$  to  $z = h$ ) is its thermal emission attenuated by the fraction of the layer between it and the observer:

$$dB_E(z) = k_\nu \left[ \frac{2k_B T}{\lambda^2} \right] e^{k_\nu(h-z)/\mu} dz/\mu,$$

where the exponential term is the attenuation coefficient due to the part of the layer between the test volume and the layer top, the bracketed term is the blackbody thermal

emission from the Planck Law in the long wavelength limit (the Rayleigh-Jeans approximation, which is appropriate for radio waves), the leading factor of  $k_\nu$  accounts for the emissivity of the volume, and  $dz/\mu$  is the path length through the test volume. In the blackbody brightness term,  $k_B$  is Boltzmann's constant,  $T$  is the kinetic temperature of the layer, and  $\lambda$  is the free space observing wavelength. (There is a subtle point that's been swept under the rug here. The wavelength to be used is the free space value, where the refractive index,  $n$ , is 1. In a planet's atmosphere, where  $n \neq 1$ , a factor of  $n^2$  should appear in the blackbody term. There is, however, a defocusing effect due to refraction that also goes as  $n^2$ , and the two factors cancel, so the correct result is found by just assuming  $n = 1$  everywhere.) Integrating  $dB_E$  from  $z = 0$  to  $h$ , we get the total brightness emitted by the layer

$$B_E = B_B(1 - e^{-k_\nu h/\mu}),$$

where  $B_B$  is the blackbody brightness,  $\frac{2k_B T}{\lambda^2}$ .

Thus, the observed brightness out of the top of any atmospheric layer is

$$T_{\text{out}} = T_{\text{in}} e^{-k_\nu h/\mu} + T(1 - e^{-k_\nu h/\mu}), \quad (2.1)$$

where brightness is expressed as a temperature (note that  $T$  is still the kinetic temperature of the emitting layer). In Equation 2.1, the first term on the right represents the brightness from below that is transmitted through the layer, and the second term represents the emission from the layer itself. When calculating  $\mu$ , the planet is assumed to be an ellipsoid of revolution, with equatorial and polar radii 25,559.0 and 24,973.0 km, respectively (Lindal *et al.* 1987). For a pole-on geometry, corresponding to 1985 observations, the brightness for an elliptical and spherical planet deviate appreciably (about 5 K) only when within  $\sim 10^\circ$  latitude of the equator.

To calculate the brightness of the atmosphere with Eq. 2.1, start with a layer at 500 bar (about 500 km below the 1-bar level). This is deep enough that  $T_{\text{in}}$  is unimportant because none of it will be seen from the top of the atmosphere.  $T_{\text{out}}$  can be calculated

for this layer using the temperature and absorption profiles discussed later. This  $T_{\text{out}}$  becomes  $T_{\text{in}}$  for the next layer up in the atmosphere. This process is repeated until  $T_{\text{out}}$  from the 100 mbar level (about 60 km above 1 bar) is found, which for our purpose is well above any significant atmosphere and represents the observed brightness from Earth. The thickness of layers to use is determined empirically by running test cases and finding the fewest number of layers required to give brightnesses within 0.1 K of the results when the number of layers gets arbitrarily large. The pressure increments used between layers are 10 bar for pressures greater than 100 bar, 0.2 bar between 100 and 10 bar, and 0.1 bar at pressures less than 10 bar. This yields a model with about 600 layers. (While in principle one can minimize the number of calculations needed by stepping through the atmosphere from the top down and using the calculated opacity to determine when layers are too deep to affect observations, the bottom up approach is necessary for a general treatment of  $\text{NH}_4\text{SH}$  condensation [Section 2.2.3] and for cold-trapping [Section 2.2.5].)

In this analysis scattering has been neglected. This is desirable because it makes things easier. Fortunately, this assumption is also justifiable. Since we are dealing with relatively long wavelengths ( $\sim 1$  to 20 cm), most regions of the atmosphere are unlikely to have suspended particles large enough to be effective scatterers. Even if scatterers are large, there need to be enough of them to have a significant effect on macroscopic scales. Thus, while Carlson *et al.* (1988) suggest the methane cloud near 1 bar has a mean particle radius near 0.5 cm, the fractional volume occupied by ice is  $< 5 \times 10^{-5}$ , which is small enough to ignore. The one place scattering may be significant is in the liquid water cloud, at pressures  $\geq 100$  bar, where even though suspended particles are small (according to Carlson *et al.*), a steady rain of up to centimeter size water drops may exist. We can still safely ignore scattering, however, because not only are these scattering regions likely to be too deep to effect most of the data discussed here, but also uncertainties in the absorptive properties of the water cloud are large enough to mask any scattering effects that might be seen in the data. Thus, the inclusion of scattering would

not alter the results of this work.

### 2.2.2 Composition

In order to calculate the temperature and absorption profiles of the atmosphere, we need to know its composition. While the main results of this thesis are based on relative variations within the atmosphere, it is still desirable to be as accurate as possible in determining absolute abundances. The starting point for such a discussion is usually a “solar” composition, which attempts to match the abundances in the solar nebula, and presumably the sun as well (Cameron 1982). Of course, details of the evolution of the solar nebula and the planetary formation process itself drive planetary compositions away from solar (the terrestrial planets being a prime example). Nonetheless, the notion that the giant planet’s atmospheres are composed primarily of  $H_2$  and He, with smaller amounts of oxygen and carbon (presumably in the form of  $H_2O$  and  $CH_4$  due to the reducing environment) as well as the idea that the farther reaches of the solar system will be enriched relative to solar in the “ices” such as  $H_2O$ ,  $CH_4$ , and  $NH_3$ , is well established in observations and theory.

The model atmosphere used in this work is composed of  $H_2$ , He,  $CH_4$ ,  $H_2O$ ,  $NH_3$ , and  $H_2S$  vapor, and various clouds, which are discussed in section 2.2.4. The abundances, expressed as a molar (number) mixing ratio relative to the total atmosphere, are listed in Table 2.1. (Also appearing are heat capacities, which will be used in the next section.)

Based on Voyager infrared and radio science observations, the He to  $H_2$  molar ratio is set to 15/85 (which means the part of the atmosphere not accounted for by other species will be filled with He and  $H_2$  in this ratio), and the  $CH_4$  ratio is 2.3% (Lindal *et al.* 1987). Microwave observations are used to constrain the water abundance, which is discussed in part 3 of this chapter. It appears the water abundance needs to be greater than or equal to a roughly solar abundance of  $1.0 \times 10^{-3}$ . This is in agreement with studies of the bulk density and gravitational moments of Uranus (Podolak *et al.* 1990).

**Table 2.1**  
Model Atmosphere Composition

Species	Molar Mixing Ratio	Heat Capacity $c_p/R$
H <sub>2</sub>	.829	2.5 to 3.5*
He	.146	2.5
CH <sub>4</sub>	.023	4.3
H <sub>2</sub> O	$\geq 1 \times 10^{-3}$	4.0
NH <sub>3</sub>	$1.4 \times 10^{-4}$ *	4.5
H <sub>2</sub> S	$1.39 \times 10^{-4}$ *	4.0

\*Variable, see text

For the nominal model, the lower limit of  $1.0 \times 10^{-3}$  is used. The NH<sub>3</sub> abundance is also fit using observations (Chapter 4), and appears to vary dramatically with latitude and altitude due to various dynamical and chemical processes. The nominal model has a solar NH<sub>3</sub> abundance of  $1.4 \times 10^{-4}$  above the liquid water cloud (it will be shown later that any value within an order of magnitude of this can be made to fit the data), though dynamics and condensation drive this to as low as  $\sim 10^{-7}$  in some regions, while deeper than the water cloud it is likely that the bulk atmosphere is enriched above a solar abundance. Hydrogen sulfide, H<sub>2</sub>S, is used in the model only because it reacts with NH<sub>3</sub> to form NH<sub>4</sub>SH clouds, and thereby effects the opacity by removal of NH<sub>3</sub>. The model H<sub>2</sub>S abundance is therefore controlled by the efficiency of the NH<sub>4</sub>SH cloud formation process as well as the opacity structure of the data. This is discussed further in Section 2.2.4 and Chapter 4, but assuming a 100% efficiency for condensation of NH<sub>4</sub>SH from a saturated vapor mixture, and assuming the NH<sub>3</sub> abundance of Table 2.1, the H<sub>2</sub>S molar mixing ratio is near  $1.39 \times 10^{-4}$ .

The species included account for what are generally accepted as the major mass constituents of the atmosphere (H<sub>2</sub>, He, CH<sub>4</sub>, and H<sub>2</sub>O), as well as the main microwave absorbers (NH<sub>3</sub> vapor, H<sub>2</sub>O vapor and liquid, and at millimeter wavelengths, H<sub>2</sub>). Of course, being generally considered correct is no proof of correctness. Based on cosmic

abundances, however, and the fact that all available data is satisfied reasonably well by a primarily  $\text{H}_2$ , He,  $\text{CH}_4$ , and  $\text{H}_2\text{O}$  mixture, it is fairly certain that there are no unknown major mass constituents in the parts of the atmosphere probed by radio waves. There is some uncertainty, however, in identifying all the microwave absorbers because trace species may be strongly absorbing. This problem is discussed more fully in section 2.2.5, but two important points are first, the main results of this work are based solely on relative variations of the absorber abundance and are therefore independent of what the absorbing species are, and second, when exact mixing ratios or cloud densities for  $\text{NH}_3$  or  $\text{H}_2\text{O}$  are quoted they are to be considered correct only under the assumption of no unmodeled absorbers. Having presented this warning, it should be noted that both ground based radio observations and Voyager occultation results indicate that on Jupiter, Saturn, and Neptune,  $\text{NH}_3$  is the only major opacity source in the upper atmosphere (Grossman 1990, Lindal *et al.* 1990, de Pater *et al.* 1991). This is particularly significant in the case of Neptune because its microwave spectrum is very similar to that of Uranus. This, combined with the ability of the model to fit all available data on Uranus, suggests it is unnecessary to introduce unmodeled absorbers, such as the  $\text{H}_2\text{S}$  suggested by de Pater *et al.* (1991).

A final important factor in the composition of the atmosphere is the hydrogen *ortho-para* ratio. These two forms of hydrogen are distinguished by the quantum mechanical property "spin". Ortho-hydrogen is an  $\text{H}_2$  molecule in which the nuclear spins of each atom are aligned. Para-hydrogen, which has a slightly lower energy, has the two spins anti-parallel. In equilibrium, the *ortho* to *para* abundance ratio is determined by the kinetic temperature. Because the heat capacities of *ortho* and *para* hydrogen are very different at temperatures below about 300 K (see Wallace 1980, Fig. 1), the *ortho-para* ratio is important for calculating the temperature lapse rate. In reviewing the literature (Trafton 1967, Wallace 1980, Orton *et al.* 1986) one finds the favored assumption is to use Trafton's "frozen" ratio (which Wallace calls intermediate hydrogen). Trafton's work

assumes that at any level in the atmosphere, the *ortho-para* ratio is in equilibrium with the ambient temperature, but that the time scale to come to equilibrium is much longer than the convective time scale. Thus, the *ortho-para* ratio is frozen during convection of air parcels, but is assumed to re-equilibrate with its surroundings after moving. For this reason, “frozen equilibrium hydrogen” is the common term for this type of mixture. Observations indicate frozen equilibrium is a reasonable approximation for the actual atmosphere. Based on Voyager infrared observations (Hanel *et al.* 1986) and radio science data (Lindal *et al.* 1987) tropospheric lapse rates at pressures greater than about 0.6 bar fall between the equilibrium and frozen equilibrium values. As discussed in the next section, the differences between these lapse rates are unimportant for the purposes of this paper. The microwave absorptive properties of frozen equilibrium H<sub>2</sub> are identical to those of equilibrium H<sub>2</sub>.

### 2.2.3 Temperature

When fitting radio observations, the two free parameters are temperature and composition. These parameters are not independent, however, because the abundance of the absorbing species is temperature dependent, as are some of the absorptive properties. The approach used here is to make assumptions about the true temperature profile of Uranus, and then allow for variations from this reference profile. It will turn out that variations in temperature are relatively unimportant, and the reference profile described here will be used in the nominal Uranus model.

The temperature profile used is shown in Figure 2.1. It consists of the Voyager radio occultation “nominal profile” of Lindal *et al.* (1987) from 100 mbar down to 2.3 bar, which is the deepest level probed by the radio link, and then an extrapolation along a pseudo-adiabat (Gill 1982) to higher pressures. In inverting the radio science data, Lindal *et al.* assume an atmosphere composed of He, H<sub>2</sub>, and CH<sub>4</sub>. Our model atmosphere differs from theirs on two points, neither of which is significant. First, we include H<sub>2</sub>O, NH<sub>3</sub>,

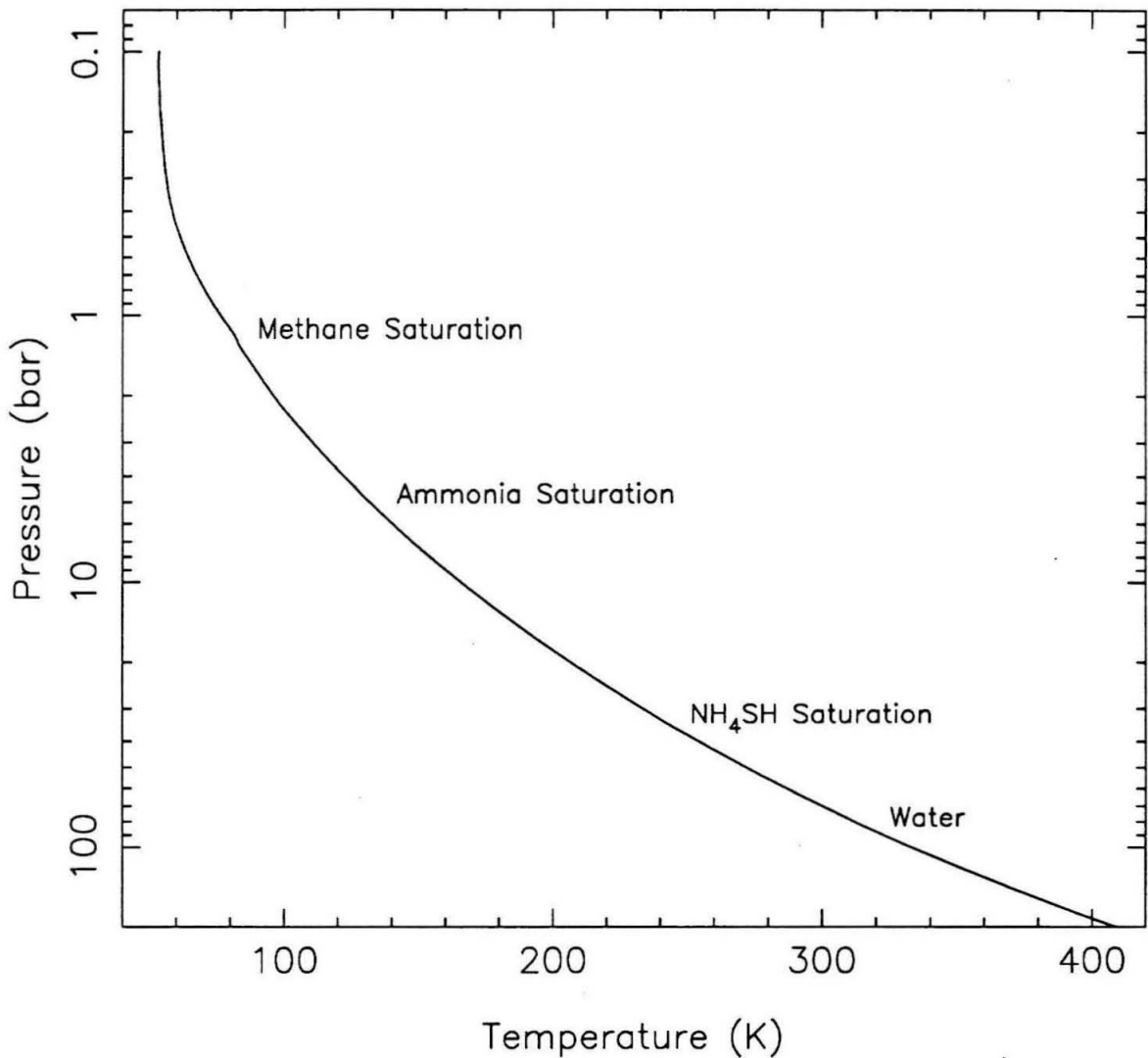


**Figure 2.1:** The temperature profile used in the model atmosphere. The points above 2.3 bars are taken from the Voyager radio occultation experiment. Below this, temperatures are extrapolated along a pseudo-adiabat to higher pressures. The altitude of the methane ( $\text{CH}_4$ ), ammonia ( $\text{NH}_3$ ), ammonium hydrosulfide ( $\text{NH}_4\text{SH}$ ), and water ( $\text{H}_2\text{O}$ ) cloud bases for the mixing ratios listed in Table 2.1 are shown. The vertical distance between the 0.1 and 100 bar levels is about 350 km.

and  $\text{H}_2\text{S}$  in our atmosphere. The amounts of these gases above 2.3 bars are so small that their inclusion does not alter the temperature profile. The second point on which our model differs is that we allow  $\text{CH}_4$  to be saturated above the methane cloud, while Lindal *et al.* find that it appears to be sub-saturated at these levels. Our inclusion of extra  $\text{CH}_4$  above the cloud deck has a negligible effect on the calculated brightness temperatures, even at millimeter wavelengths. There are also two main uncertainties associated with the nominal occultation profile that need to be addressed. The first is the uncertainty in the  $\text{CH}_4$  abundance, and the second is the uncertainty in how representative of the entire planet the occultation experiment is, given that it only probed latitudes between  $-2^\circ$  and  $-7^\circ$ . Lindal *et al.* indicate that temperature profiles that deviate from the nominal model by up to 8 K are plausible, the variations being controlled by the relative humidity of  $\text{CH}_4$  above its cloud deck. In Section 2.2.3 it will be shown that deviations of this magnitude are not important for the results to be presented; they would not change the inferred circulation pattern, and the adjustments to the derived molar mixing ratios of  $\text{H}_2\text{O}$ ,  $\text{NH}_3$ , and  $\text{H}_2\text{S}$  would be smaller than those due to uncertainties in the line shape functions and cloud properties. The question of whether the radio occultation profile is representative of the entire planet also turns out to be unimportant. The Voyager IRIS instrument indicates temperatures near 1 bar vary by no more than 2 K (Hanel *et al.* 1986), and variations of this magnitude in the starting point for the adiabatic extrapolation used here are too small to be significant. (The possibility of much larger latitudinal temperature variations existing deeper in the atmosphere is discussed in section 4.2.)

To estimate the temperature structure at pressures greater than those probed by Voyager, the occultation results are extrapolated to deeper levels. On the major planets other than Uranus, a convective adiabat seems the logical choice because they all have strong internal heat sources. (There may be some room for argument on this point because the distribution of internal heat observed at the cloud tops is not uniform [Ingersoll 1976], suggesting some regions might be heated from below less than others.) On Uranus,

which has a very small internal heat source (Pearl *et al.* 1987, 1990), it can be argued that convection is less vigorous. In fact, one possible interpretation of long wavelength radio observations is that the Uranian atmosphere becomes isothermal at pressures greater than about 40 bar. This possibility is discussed in section 2.3. Higher in the atmosphere, however, there is clear evidence for adiabatic lapse rates. First of all, as discussed briefly under composition, Voyager infrared and radio science data indicate an adiabatic lapse rate between 0.6 and 2.3 bar. (Radiative rather than convective processes dominate above this range, and the instruments did not probe deeper than 2.3 bar.) There are two reasons to suspect that the adiabatic lapse rates extend below 2.3 bar. The first is that there appears to be an internal redistribution of energy. As on the other giant planets, Voyager observations show thermal emission to be nearly constant with latitude (Hanel *et al.* 1986) in spite of the fact that the solar insolation is not uniform. This indicates convective motions are transporting heat in at least some areas. The second reason to believe in adiabatic lapse rates, or at least a non-isothermal atmosphere, is that ground-based radio observations at wavelengths from 1 to 6 cm show Uranus' brightness to increase with increasing wavelength (Gulkis *et al.* 1978 and Section 2.3 of this work), which requires temperature to increase with depth.

Given, then, that an adiabatic lapse rate will be used to extrapolate the Voyager radio science temperature profile to deeper levels (at least as an initial guess), there remains a question of how to account for condensible species. Because of latent heat effects and the presence of suspended particles, cloud formation can significantly affect the atmospheric temperature profile. The extrapolation used here is along a pseudo-adiabat (Gill 1982). This adiabat follows rising air parcels, and assumes any species whose vapor abundance is above its saturation mixing ratio will condense until the vapor is at its saturated value. The condensed material falls out of the parcel and does not convect. (A true wet adiabat would be one in which the condensate remains entrained within convecting air parcels.) The validity of the above assumptions is difficult to assess. Supersaturated

vapor abundances are possible where condensation may be inhibited due to, for example, a lack of nucleation sites (de Pater *et al.* 1989). Alternatively, some species may be sub-saturated above their cloud deck, as has been suggested for CH<sub>4</sub> (Lindal *et al.* 1987). Furthermore, entrainment of some condensate in convecting parcels is possible.

Fortunately, the effect of condensation on the current analysis turns out to be small, and whether a wet-adiabat, pseudo-adiabat, or even a dry-adiabat (one in which no condensation occurs) is used, the temperature profile would not be significantly different. The reason for this is that the amount of condensate in the regions of interest to us is small. This can be seen in Figure 2.1 by inspecting the shape of the temperature profile near each condensation level. Clearly, CH<sub>4</sub> saturation affects the profile near 1.2 bar, but this occurs above the starting point of the extrapolation, so it is not a factor. The abundances of NH<sub>3</sub>, H<sub>2</sub>S, and NH<sub>4</sub>SH are all small enough that they have negligible thermal effects. While the H<sub>2</sub>O abundance is significant at depth, the temperature at altitudes above about 80 bars is low enough that water's saturated vapor pressure is quite small (mixing ratios < 10<sup>-3</sup>).

To summarize, a pseudo-adiabat is used to extrapolate to higher pressures, but the final results are not very sensitive to details of the chosen adiabat. Possible variations from the assumed temperature profile are discussed in the context of data fitting in Section 4.2. Turning now to some details of how the pseudo-adiabatic lapse rate is calculated, we start with the First Law of Thermodynamics applied to a rising air parcel that consists of both condensible and non-condensable species:

$$dq = c_v dT + PdV + Ldm. \quad (2.2)$$

This says the energy added to the parcel,  $dq$ , (erg g<sup>-1</sup>) equals the change in total energy of the parcel. The first term on the right is the energy change of the parcel due to kinetic temperature changes, the second term is the energy associated with expansion, and the last term is the latent heat released from a condensible species (for now, assume only one species condenses).  $c_v$  is the specific heat of the parcel at constant volume (erg g<sup>-1</sup> K<sup>-1</sup>),

$dT$  is the change in temperature,  $P$  is the pressure of the parcel, and  $V$  is the specific volume, which is the reciprocal of the density,  $V = 1/\rho$ .  $L$  is the latent heat of the condensible species (erg  $g^{-1}$ ), and  $m$  is the saturation mass mixing ratio,  $m = \rho_s/\rho$ , where the subscript 's' refers to the saturated condensible, and non-subscripted values refer to the total vapor content of the parcel. The subscript 'a' is used to refer to the non-condensable portion of the parcel. (Note that it is more common to see  $m$  defined as  $m = \rho_s/\rho_a$ , but this definition requires an additional factor of  $\frac{1}{1-m}$  on the last term of Equation 2.2.)  $c_v$  is taken to be constant, which is valid for small displacements or when  $m \ll 1$ , the latter constraint being true over most of the region of interest to us.

Using the ideal gas law

$$P = \frac{R}{\mu} \rho T$$

(where  $R$  is the universal gas constant and  $\mu$  is the molecular weight of the parcel), and assuming hydrostatic equilibrium so that

$$dP = -\rho g dz$$

( $z$  is height above a reference level), and using the relation between specific heats at constant volume and constant pressure,

$$c_p - c_v = R/\mu,$$

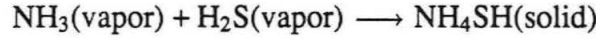
Equation 2.2 can be written as

$$c_p \frac{dT}{dz} + g + L \frac{dm}{dz} = 0, \quad (2.3)$$

where  $dq$  has been set to zero for an adiabatic process. Assuming both the condensible vapor and the total atmosphere can be treated as ideal gases,  $m$  can be written as  $m = (P_s \mu_s)/(P \mu)$ . Differentiating this and assuming hydrostatic equilibrium yields

$$\frac{dm}{dz} = \frac{\mu_s}{\mu} \frac{1}{P} \frac{dP_s}{dT} \frac{dT}{dz} + \frac{\mu_s}{\mu} \frac{P_s}{P^2} \rho g.$$

This equation also applies to the condensation reaction



if  $P_s$  is taken to be the sum of the  $\text{NH}_3$  and  $\text{H}_2\text{S}$  partial pressures, and  $\mu_s$  is taken to be the sum of their molecular weights. Note that the formation of  $\text{NH}_4\text{SH}$  uses the same number of  $\text{NH}_3$  and  $\text{H}_2\text{S}$  molecules, so that in the  $\text{NH}_4\text{SH}$  cloud the change in the partial pressure of  $\text{NH}_3$  is equal to the change in the  $\text{H}_2\text{S}$  pressure (this will be of use later). Substituting the expression for  $\frac{dm}{dz}$  into Equation 2.3 and solving for  $\frac{dT}{dz}$ , we get

$$\frac{dT}{dz} = -\frac{g}{c_p} \left\{ \left( 1 + \frac{LP_s\mu_s}{PRT} \right) / \left( 1 + \frac{L\mu_s}{c_p P \mu} \frac{dP_s}{dT} \right) \right\}.$$

The final step in this derivation is to use the Clausius-Clapeyron Equation to express the latent heat,  $L$ , of all condensible species other than  $\text{NH}_4\text{SH}$  as

$$L = \frac{dP_s}{dT} \frac{T}{\rho_s},$$

where the assumption is made that the density of the condensate in the vapor phase is much less than the density of the condensed phase. For  $\text{NH}_4\text{SH}$ , the latent heat (or more correctly, the heat of formation) is taken from Atreya (1986) to be constant at

$$L_{\text{NH}_4\text{SH}} = 1.826 \times 10^{10} \text{ erg g}^{-1}.$$

Substituting the expressions for  $L$  in, and allowing for multiple condensing species

$$\frac{dT}{dz} = -\frac{g}{c_p} \left\{ \frac{1 + \frac{T}{P} \sum_i \frac{dP_i}{dT} + \frac{L_{\text{NH}_4\text{SH}} \mu_{\text{NH}_4\text{SH}}}{PRT} (P_{\text{NH}_3} + P_{\text{H}_2\text{S}})}{1 + \frac{RT^2}{c_p P \mu} \sum_i \frac{1}{P_i} \left( \frac{dP_i}{dT} \right)^2 + \frac{L_{\text{NH}_4\text{SH}} \mu_{\text{NH}_4\text{SH}}}{c_p P \mu} \frac{dP_{\text{NH}_4\text{SH}}}{dT}} \right\}, \quad (2.4)$$

where the sums are over the  $i$  species (other than  $\text{NH}_4\text{SH}$ ) that are condensing at the altitude in question, and the terms involving  $L_{\text{NH}_4\text{SH}}$  appear only at altitudes where  $\text{NH}_4\text{SH}$  is forming. Expressions for the saturation vapor pressure of the condensibles as

a function of temperature, used in calculating  $dP_i/dT$ , are presented in the next section. The molecular weight of the atmospheric parcel is calculated using the abundances of Table 2.1, corrected for any species that have condensed. In a similar fashion, the heat capacity of the atmosphere is calculated from the heat capacities of Table 2.1 combined with each species mass mixing ratio. In Table 2.1, the heat capacities, with the exception of  $H_2$ , are taken from Atreya (1986), and are expressed as the heat capacity divided by the universal gas constant,  $R = 8.314 \times 10^{-7}$  erg mol<sup>-1</sup> K<sup>-1</sup>. The heat capacity of  $H_2$  is a function of temperature and the *ortho-para* ratio. The calculations of Trafton (1967) for frozen equilibrium  $H_2$  are used in the nominal model, and  $c_p/R$  varies from 2.5 at temperatures below about 40 K, up to 3.5 for temperatures above 300 K. For comparison, if heat capacities appropriate for equilibrium  $H_2$  are used (taken from Farkas 1935), temperatures would be slightly lower than those of Fig. 2.1 (lower by 9 K at 50 bar, and 11 K at 100 bar).

In principle, one would like to apply Equation 2.4 to the deepest point of the radio occultation profile (2.3 bar) and work downward. In practice, however, it is more flexible to guess at a temperature and pressure deep in the atmosphere where no species are saturated, and shoot upward towards the radio science data points. The initial temperature assumed for the deep atmosphere is then iteratively modified until it gives results that match the known high altitude profile. This “shooting from below” is used because, as we shall see in the next section, conditions above the  $NH_4SH$  cloud depend on the  $NH_3$  to  $H_2S$  ratio at the cloud base, so if one wants to allow for either of these species to condense deeper than  $NH_4SH$ , the adiabat must start deep and work upward. (It turns out that for the mixing ratios found on the outer planets,  $NH_4SH$  is the deeper condensate, so working from below is not required.)

This is an appropriate time to discuss calculations of  $g$ , the gravitational acceleration, which enters the model via the equation of hydrostatic equilibrium. The true gravitational acceleration can vary with latitude and depth. Variations of  $g$  with depth, however, are

negligible for our purposes, so the value of  $g$  calculated at the 1 bar level is used at all altitudes. The largest contribution to variations of  $g$  with latitude is the variable distance of the 1 bar pressure level from the center of the planet. Taking the mass of Uranus from Tyler *et al.* (1986), treating the gravitational field as that of a point mass at the center of the planet, and using the geoid determined by Lindal *et al.* (1987),  $g$  is about 5% weaker at the equator than at the pole. This variation in  $g$  changes the disk averaged brightness from that of a spherical planet by less than 0.5 K at 2 and 6 cm, and changes any one pixel in a brightness map by less than  $\sim 1$  K. Variations of this magnitude are well within the noise of the data, so it is not necessary to calculate the next largest corrections to the gravitational field, which are due to the non-spherical shape of the field (the  $J_2$  gravitational moment) and centrifugal forces due to planetary rotation and zonal winds. Both of these corrections are on the order of 2% of  $g$ , or less than half of the oblateness correction just described.

#### 2.2.4 Saturation and Clouds

In the model atmosphere,  $\text{CH}_4$ ,  $\text{NH}_3$ ,  $\text{H}_2\text{S}$ ,  $\text{H}_2\text{O}$ , and  $\text{NH}_4\text{SH}$  are allowed to condense, which changes the mixing ratio of the species in question, and creates a cloud of suspended particles. This happens whenever the molar mixing ratio of a condensible yields a partial pressure greater than the local saturation vapor pressure or, in the case of  $\text{NH}_4\text{SH}$ , when the product of the partial pressures of  $\text{NH}_3$  and  $\text{H}_2\text{S}$  is greater than the  $\text{NH}_4\text{SH}$  equilibrium constant. In the first part of this section, the equations and assumptions used in estimating saturated abundances and the cloud structure are presented. This is followed by a discussion of the likelihood and the effect of errors in these assumptions. The effect of the incorporation of various species into an aqueous solution in the water cloud is also discussed, and the section ends with a description of the cloud structure for the nominal model.

Saturation vapor pressures for  $\text{H}_2\text{O}$ ,  $\text{CH}_4$ , and  $\text{NH}_3$  are taken from Goodman (1969)

and Wallace (1980), as quoted in de Pater and Massie (1985), the saturation pressure of H<sub>2</sub>S from Atreya (1986), and the NH<sub>4</sub>SH equilibrium constant from Lewis (1969). For pressures in mbar and temperatures in Kelvin, the equations are:

For H<sub>2</sub>O:

$$\begin{aligned} P_{\text{H}_2\text{O}} &= (4.383 \times 10^{10})e^{-6194.0/T} && \text{for } T \leq 273.0 \\ &= (1.555 \times 10^9)e^{-5273.0/T} && \text{for } T > 273.0. \end{aligned} \quad (2.5)$$

For CH<sub>4</sub>:

$$\begin{aligned} P_{\text{CH}_4} &= (4.598 \times 10^7)e^{-1168.1/T} && \text{for } T \leq 90.7 \\ &= (1.032 \times 10^7)e^{-1032.5/T} && \text{for } T > 90.7. \end{aligned} \quad (2.6)$$

For NH<sub>3</sub>:

$$P_{\text{NH}_3} = (1.342 \times 10^{10})e^{-3753.6/T}. \quad (2.7)$$

For H<sub>2</sub>S:

$$\begin{aligned} P_{\text{H}_2\text{S}} &= (13.3329) \times 10^{(-1329.0/T+9.28588-.0051263T)} && \text{for } T \leq 187.6 \\ &= (13.3329) \times 10^{(-1145.0/T+7.94746-.00322T)} && \text{for } T > 187.6, \end{aligned} \quad (2.8)$$

and for NH<sub>4</sub>SH, the equilibrium relation is:

$$P_{\text{NH}_3}P_{\text{H}_2\text{S}} = (1.0 \times 10^6)e^{34.151-10834.0/T}. \quad (2.9)$$

(In Lewis 1969, Eq. 25, there is a typographical error, and the partial pressures appear as a ratio instead of a product.)

Equation 2.9 is made more useful by noting that the number of NH<sub>3</sub> molecules consumed in the formation of NH<sub>4</sub>SH is the same as the number of H<sub>2</sub>S molecules consumed, so the change in partial pressures of the two gases (assuming both are ideal) are the same. Thus, as pointed out in Briggs and Sackett (1989), if  $P_x^o$  refers to the partial pressure of species  $x$  at the base of the NH<sub>4</sub>SH cloud, then at any altitude where the partial pressure of species  $x$  is  $P_x$ ,

$$P_{\text{NH}_3}^o - P_{\text{NH}_3} = P_{\text{H}_2\text{S}}^o - P_{\text{H}_2\text{S}}.$$

This holds as long as  $\text{NH}_4\text{SH}$  condensation is the only sink for  $\text{NH}_3$  or  $\text{H}_2\text{S}$  vapor between the cloud base and the altitude in question. We shall find this is a valid assumption because the  $\text{NH}_3$  or  $\text{H}_2\text{S}$  clouds form at altitudes well above any significant  $\text{NH}_4\text{SH}$  condensation. Using this relation with Equation 2.9 to solve for the partial pressures yields

$$P_{\text{NH}_3} = \frac{1}{2} \left\{ P_{\text{NH}_3}^{\circ} - P_{\text{H}_2\text{S}}^{\circ} + \sqrt{(P_{\text{NH}_3}^{\circ} - P_{\text{H}_2\text{S}}^{\circ})^2 + (4 \times 10^6)e^{(34.151 - 10834.0/T)}} \right\} \quad (2.10)$$

and

$$P_{\text{H}_2\text{S}} = \frac{1}{2} \left\{ P_{\text{H}_2\text{S}}^{\circ} - P_{\text{NH}_3}^{\circ} + \sqrt{(P_{\text{NH}_3}^{\circ} - P_{\text{H}_2\text{S}}^{\circ})^2 + (4 \times 10^6)e^{(34.151 - 10834.0/T)}} \right\}. \quad (2.11)$$

At any level in the atmosphere, the actual molar mixing ratio of any condensible species is taken to be the minimum of:

- 1) The molar mixing ratio given in Table 2.1.
- 2) The saturation pressure given by equations 2.5 through 2.11, divided by the total atmospheric pressure.
- 3) The minimum molar mixing ratio encountered below the current level.

The first value is just the assumed bulk composition of the atmosphere. The second condition is the assumption that all species will be in equilibrium with their surroundings and there will be no super-saturated abundances. The final value is a “cold-trapping” constraint; the mixing ratio of a species is assumed not to increase with height because any air parcel is assumed to have moved through all levels below it.

The cloud density at any level is calculated using the method of Weidenschilling and Lewis (1973). This scheme assumes that as an air parcel rises, the mass of condensible necessary to keep the vapor in equilibrium with its surroundings condenses out and forms a cloud. Any condensate that forms stays at the altitude of its condensation. To convert this to a mathematical expression, one starts with the fact that, in hydrostatic equilibrium, the mass per unit area in the atmosphere above a pressure level (called the column mass) is

$$M = P/g.$$

Consider a level in the atmosphere where the mass mixing ratio of a condensible species is  $\sigma_1$ . In the absence of any condensation at or above this level, the column mass of this species is

$$m_1 = \sigma_1 M_1,$$

where  $m_1$  is the condensible column mass above level 1, and  $M_1$  is the total atmospheric column mass above this level. If a slightly higher level in the atmosphere is now considered, the mass mixing ratio has changed due to condensation between the levels. Neglecting condensation above this second level,

$$m_2 = \sigma_2 M_2.$$

If levels 1 and 2 are close together,  $M_1 \simeq M_2$ , and the difference between  $m_1$  and  $m_2$  is due only to condensation. The total mass removed from a column due to condensation between levels 1 and 2 is therefore

$$D_A = \sigma_1 M_1 - \sigma_2 M_2. \quad (2.12)$$

Note that this expression takes into account cold-trapping: the mass of condensate is related to the total column mass, not just the mass between levels 1 and 2.

Since the total atmospheric pressure does not change significantly between levels 1 and 2,  $M_1$  and  $M_2$  can be replaced by the average column mass,  $\bar{P}/g$ . Using this, and dividing Equation 2.12 by the layer thickness,  $h$ , to yield the average density of condensates in the region (*i.e.*, the cloud density),  $D$ , one finds

$$D = (\sigma_1 - \sigma_2) \frac{\bar{P}}{gh}.$$

To get this in terms of the molar mixing ratio,  $\chi$ , use

$$\sigma = \frac{\mu_c}{\mu} \chi,$$

where  $\mu_c$  is the molecular weight of the condensible and  $\mu$  is that of the total atmosphere.

The final expression is

$$D = \frac{1}{100} \frac{\mu_c}{\mu} \frac{(\chi_1 - \chi_2)}{gh} \frac{(P_1 + P_2)}{2}, \quad (2.13)$$

where pressures are in mbar,  $h$  is in km, and all other units are cgs (the factor of 1/100 converts mbar/km to cgs units). This cloud model is consistent with the assumptions made when calculating the pseudo-adiabatic lapse rate: vapor pressures are in equilibrium and condensed aerosols do not convect.

Are these assumptions, along with the “cold-trapping” mentioned earlier, valid? It was already pointed out in Section 2.2.3 that they are reasonable assumptions to use in determining the temperature profile. Another aspect, however, is how the microwave absorption at any altitude is affected, because absorption is directly proportional to the abundance of condensibles such as  $\text{NH}_3$ . Here too it can be argued that the model assumptions are reasonable. Addressing the issue of whether condensibles are saturated above their cloud decks, it should first be noted that there is little reason to suspect super-saturated conditions. We will be concerned with the atmosphere deeper than 2 bars, and unlike the stratosphere, collisions are frequent enough and nucleation sites are likely to be prevalent enough that condensation occurs rapidly. Furthermore, vigorous vertical motions are not expected because of the relatively low energy inputs into the atmosphere that were mentioned previously. These two points suggest super-saturated abundances are unlikely. As far as sub-saturated abundances are concerned, there are two plausible ways they could be generated. One is if the Uranian atmosphere is not well mixed and the condensible species, which are the densest components of the atmosphere, preferentially settle to deeper layers, or are trapped in thin convecting layers (Gierasch and Conrath 1987). (This can explain why the lapse rate appears to follow a frozen equilibrium adiabat.) The radio data, however, indicate that there are broad altitude ranges deeper than 5 bars where the absorber mixing ratio is relatively constant. For example, disk averaged radio observations indicate that this is the case in the 5 to 30 bar region of the atmosphere (de Pater *et al.* 1989 and Section 2.3 of this thesis), while high resolution data confirm that, though the mixing ratio is varying latitudinally, it is constant with altitude in this region (Hofstadter *et al.* 1990 and Chapter 4 of this work). Thus, if layering exists,

it does not appear to be strong enough to show up in the radio data.

The second mechanism to create sub-saturated abundances, which also explains the latitudinal variability just referred to, involves the circulation of the atmosphere. Consider a circulation cell that consists of a region of updraft connected to a region of subsidence. The rising parcels are well described by the pseudo-adiabat and saturated vapor profiles assumed here. Parcels rise and cool, and condensation removes just enough vapor to keep things in equilibrium. The regions of subsidence, however, are a different story. Here, as air parcels sink and heat up, there is no source to replenish condensibles that have been removed from the parcels, so the condensible's vapor is sub-saturated. This effect is seen on the Earth in both large and small scale motions. On the largest scales there is the Hadley cell (Wallace and Hobbs 1977) which consists of an upwelling over the tropics and subsidence at  $\pm 30^\circ$  latitude. These regions of subsidence are relatively dry, and account for some of the Earth's great deserts being located at these latitudes. Such large-scale motions will be invoked in Chapter 4 to explain the high resolution observations, and the model will be modified accordingly. At this point, however, there is no basis to assume them. Small scale motions can create a similar effect. Regions of net upward energy transport can consist of relatively small rising "towers" of air surrounded by slow subsidence, making the areal average of condensible abundances sub-saturated. There is currently no way of knowing these small scale patterns in the deep atmosphere of Uranus, and it is quite possible that, over 1000 km horizontal scales, condensibles may not be saturated above their cloud bases. The two main reasons to keep the saturation assumption, however, are first, there is no clearly better alternative, and second, the results are not particularly sensitive to it. Of the cloud layers involving absorbers ( $\text{NH}_3$ ,  $\text{NH}_4\text{SH}$ , and  $\text{H}_2\text{O}$ ) this work is primarily sensitive only to the region above the  $\text{NH}_4\text{SH}$  cloud, and an error in Equation 2.9 (which controls the absorber abundance there) will only alter the  $\text{H}_2\text{S}/\text{NH}_3$  ratio in the final model. This will be discussed more fully in Chapter 4, but if  $\text{NH}_3$  is sub-saturated above the  $\text{NH}_4\text{SH}$  cloud, the present model will

over-estimate the  $\text{H}_2\text{S}/\text{NH}_3$  ratio because it will interpret the low  $\text{NH}_3$  abundance as being due to removal by  $\text{H}_2\text{S}$ . Similarly, if  $\text{NH}_3$  is supersaturated in this region, the model will under-estimate the  $\text{H}_2\text{S}/\text{NH}_3$  ratio.

If the cold-trapping assumption is in error, it will also only effect the  $\text{H}_2\text{S}/\text{NH}_3$  ratio of the final model. This is because the cold-trapping constraint only acts on the stratosphere, where temperatures increase with height, and on the region above the  $\text{NH}_4\text{SH}$  cloud, where the saturation *pressure* is roughly constant with height (which means as the total atmospheric pressure decreases with altitude, the saturation *mixing ratio* increases). The stratosphere is totally transparent to centimeter and longer radio wavelengths, so it can be ignored. Above the  $\text{NH}_4\text{SH}$  cloud some degree of cold-trapping must occur because, as pointed out earlier, observations indicate a roughly constant absorber mixing ratio with altitude. If there is a small increase in the  $\text{NH}_3$  mixing ratio with altitude, however, the model will interpret it as a slightly higher  $\text{NH}_3$  ratio in the region as a whole, and lower the  $\text{H}_2\text{S}/\text{NH}_3$  ratio accordingly.

The third assumption to discuss is that of cloud densities. The only cloud of importance to us in this regard is liquid  $\text{H}_2\text{O}$  (as explained in Section 2.2.5, none of the other clouds are expected to interact strongly with radio waves). The accuracy of the cloud model is uncertain, and cloud layers can be highly variable (as is the case on the Earth). In the data analysis, cloud densities are therefore allowed to vary by as much as an order of magnitude from the standard model of Weidenschilling and Lewis (1973). Weidenschilling and Lewis point out, however, that cloud densities on Earth are generally lower than predicted by this method, and it probably is appropriate to consider these calculations an upper limit to the actual density. Another source of error to mention here is possible errors in the saturation relations, Equations 2.5 through 2.11. For current purposes, it is sufficient for these equations to be only approximate because the results are based primarily on relative variations across the disk of the planet rather than absolute abundances. It is unlikely that the expressions will be far enough off to alter

our conclusions.

An important point to bring up here is that in the initial model there is no attempt to account for the solubility of  $\text{NH}_3$ ,  $\text{H}_2\text{S}$ , or any other species in the liquid water cloud. These aqueous solution clouds have been most recently discussed in a review paper by Fegley *et al.* (1991). Solution effects have the potential to influence radio emissions by altering the temperature lapse rate, removing absorbers from the vapor phase, and by depressing the freezing point of water. The temperature effects are negligible because the abundances involved are small, so this effect will not be discussed further. The other two processes are not incorporated into the initial model because their effects cannot be accurately modeled. As pointed out by Fegley *et al.*, the calculations are difficult, and some of the laboratory data used seem to be in error. Furthermore, even if the physics is well understood, the calculations can be extremely sensitive to atmospheric conditions near the critical point of water ( $\sim 2300$  bar and 650 K), where very little is known about Uranus. Thus, one finds in the literature estimates that anywhere from a negligible amount to 68% of the  $\text{NH}_3$  can be removed from the vapor phase (Carlson *et al.* 1987, de Pater *et al.* 1989), and the freezing point of water may be depressed anywhere from a few to 100 K (see Weidenschilling and Lewis 1973, Figure 1).

Because these effects cannot be accurately calculated at this time, the approach used here is to leave them out of the basic model, but include a parameterization of them during the data analysis to estimate their impact on the observations. Since most of the incorporation of  $\text{NH}_3$  into solution occurs at the water cloud base, where cloud densities are highest, and since the observations do not probe deep enough to see this region (for solar or greater water abundances), the analysis does not change if the model includes this mechanism for  $\text{NH}_3$  depletion. In Chapter 4, however, it will be discussed how solution effects at depth can explain the  $\text{H}_2\text{S}/\text{NH}_3$  ratio observed at altitude. (Basically,  $\text{NH}_3$  is more soluble than  $\text{H}_2\text{S}$ , so one expects the  $\text{H}_2\text{S}/\text{NH}_3$  ratio to be higher at altitude than it is in the interior.) Depressing the freezing point of water can be a significant effect

of aqueous solutions because, while water ice is essentially transparent to radio waves, liquid water is not. For the cloud densities calculated according to Weidenschilling and Lewis (1973), the amount of condensate at temperatures less than 273 K is small enough that it is unimportant whether it is liquid or not. In Chapter 4, however, it is found that if cloud densities are ten times the expected value, and if water remains liquid at temperatures down to 200 K, this solution can be a significant opacity source.

The model vapor and cloud structure for significant species is shown in Figure 2.2, which assumes the temperature profile of Figure 2.1 and the composition of Table 2.1. Starting at depth, below all cloud levels, mixing ratios are constant with altitude. The first species to condense is  $\text{H}_2\text{O}$  (dot-dashed curve) at a pressure of 82.9 bar and 314.8 K. This cloud base level is calculated for a roughly solar mixing ratio of  $1 \times 10^{-3}$ . If the abundance is greater (which is likely), saturation occurs deeper. Above this point, the  $\text{H}_2\text{O}$  vapor mixing ratio is seen to fall off rapidly with altitude due to the decreasing temperature. The dotted curve of the figure shows the density of the water cloud in  $\text{g cm}^{-3}$ . The kink in the density profile at 50 bar is due to the transition from liquid to ice condensation at 273 K. Continuing up the atmosphere,  $\text{NH}_4\text{SH}$  is the next species to begin to condense, at 33.7 bar and 241.4 K. Formation of this cloud depletes both  $\text{NH}_3$  (solid curve) and  $\text{H}_2\text{S}$  (dashed line), and as we rise further, the reaction continues until one of these species is almost entirely removed. For the nominal model,  $\text{NH}_3$  is the species to survive at altitude, and has a mixing ratio near  $1 \times 10^{-6}$  above the  $\text{NH}_4\text{SH}$  formation region. Pure  $\text{NH}_3$  begins to condense at 5.0 bar and 132.3 K. The mixing ratio of  $\text{NH}_3$  is constant between the  $\text{NH}_4\text{SH}$  and  $\text{NH}_3$  clouds because of cold-trapping (the partial pressure of  $\text{NH}_3$  given by Equation 2.10 asymptotically approaches a constant value in this region, which would result in an increasing mixing ratio with altitude as total atmospheric pressure decreases). The last condensible species of the model,  $\text{CH}_4$ , condenses at 1.2 bar and 82 K.

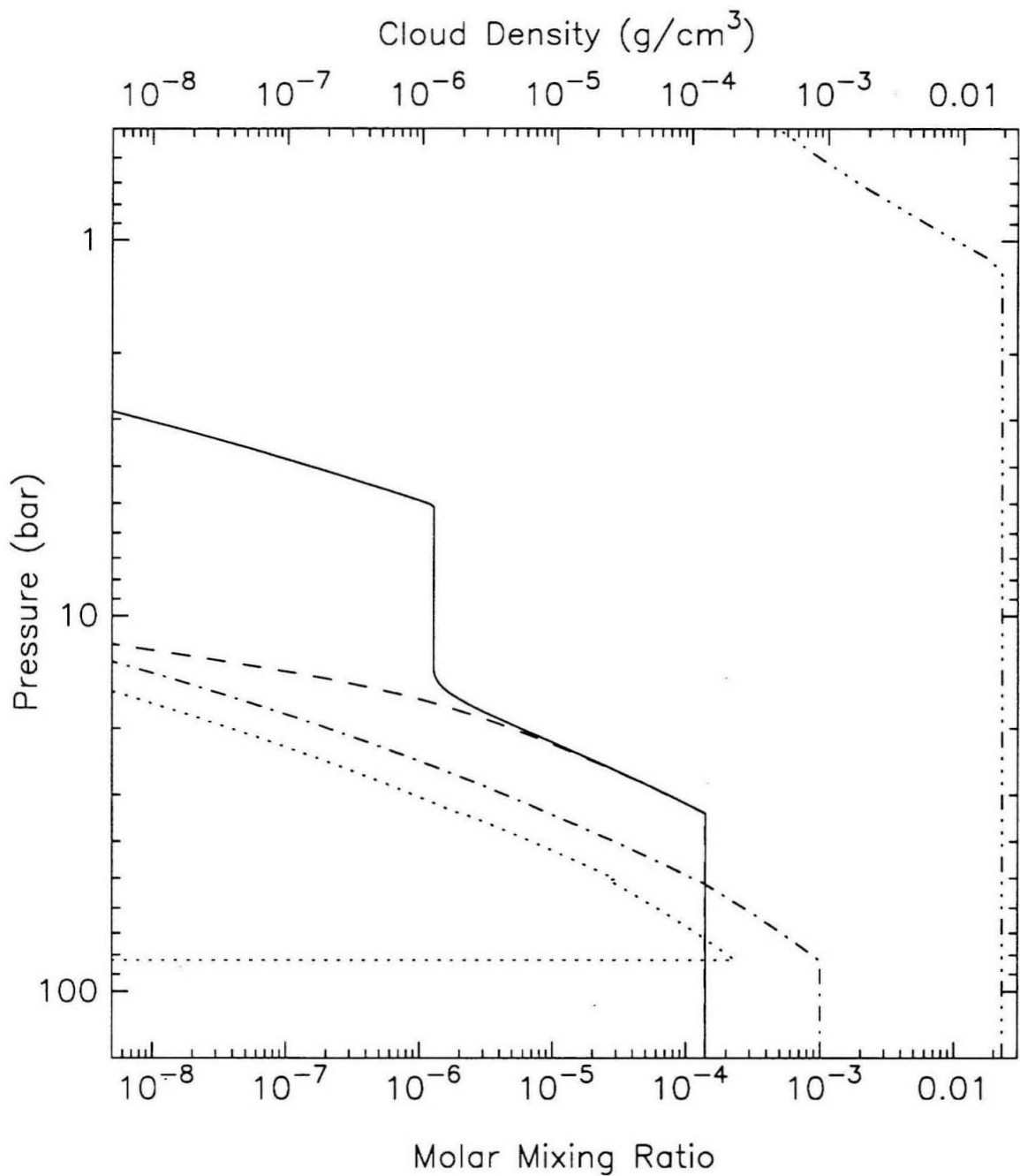


**Figure 2.2:** Atmospheric vapor pressures and cloud densities. Molar mixing ratios for all condensible species are shown as a function of height, as is the water cloud density, in  $\text{g cm}^{-3}$ . (The other cloud particles do not effect the observations, so their densities are not shown.) The solid curve is the  $\text{NH}_3$  mixing ratio, the dashed is the  $\text{H}_2\text{S}$  ratio, and the dot-dashed is the  $\text{H}_2\text{O}$  ratio. The dotted curve is the  $\text{H}_2\text{O}$  cloud density. The  $\text{CH}_4$  mixing ratio is indicated by the dash-triple-dotted curve. See text for details.

### 2.2.5 Absorption

The absorbers in the model atmosphere are  $\text{NH}_3$ ,  $\text{H}_2\text{O}$ , and  $\text{H}_2$  gas, and liquid water drops. The absorption coefficient of the atmosphere at any altitude is the sum of the absorption coefficients of each of these components. This section describes how absorption is calculated for each of these species, and then discusses why absorption and scattering by other atmospheric components can be neglected. The reader should pay careful attention to the units used in this section because, in an effort to be consistent with the literature, different units are used with the different absorbing species. (For example,  $\text{NH}_3$  absorption is described with pressure measured in atmospheres, while elsewhere, pressure is in mbar.)

Before delving into the details, it may be worthwhile to consider in a general sense just why and how molecules absorb radiation. Quantum mechanics requires molecules to be in discrete energy levels. Electromagnetic radiation, such as radio waves, is one way for a molecule to lose or gain energy and thereby to move between allowed states. Because of this, molecules are particularly good at absorbing and emitting radiation of a wavelength that corresponds to the energy difference between two states, and one might expect there to be only precise frequencies at which a molecule absorbs. In the real world, however, each transition causes absorption at a range of frequencies, primarily because the motions of the molecules and collisions between them slightly alter the energy needed to trigger a transition. These line broadening processes are called Doppler broadening and collisional or pressure broadening, respectively. The energies associated with microwave radiation usually match the rotational energies of molecules. In some cases, ammonia being one, vibrational-type motions can couple to radio wavelengths. Because microwave absorption is often tied to the relatively large scale motion of atoms and molecules, one finds that gases, which allow the greatest freedom of motion, generally will be better absorbers than a liquid, and ices will be still poorer absorbers.

## NH<sub>3</sub> Absorption

Longward of a few millimeters in wavelength, NH<sub>3</sub> becomes the dominant absorber in the Uranian atmosphere (as well as all the other Jovian planets). The absorption is due to the pressure broadened inversion band, which has line centers from about 0.7 to 1.7 cm. The NH<sub>3</sub> molecule resembles a 3-sided pyramid, with the three hydrogen atoms at the corners of the base and the nitrogen at the peak. The nitrogen atom vibrates, moving towards and away from the base, and can even punch through the base (which is a potential barrier), inverting the pyramid. (This is different from a simple rotation of the entire molecule.) It is these inversions which result in absorption lines in the microwave region. In this work, a semi-empirical expression following the work of Wrixon and Welch (1970) and Wrixon *et al.* (1971), as modified by Berge and Gulkis (1976), is used to express the absorption coefficient as a sum over all inversion lines. Each line is distinguished by its  $J$  and  $K$  quantum numbers, and the absorption coefficient,  $k_{\text{NH}_3}(\nu)$ , is in  $\text{cm}^{-1}$ :

$$k_{\text{NH}_3}(\nu) = \sum_{J=1}^{\infty} \sum_{K=1}^J 1.23 \frac{P_{\text{NH}_3}}{T^{3.5}} \frac{S(K)(2J+1)K^2}{J(J+1)} \times \exp \left\{ -\frac{4.8}{T} [(2.98)J(J+1) - (1.09)K^2] \right\} F(\nu, J, K), \quad (2.14)$$

where  $P_{\text{NH}_3}$  is the partial pressure of NH<sub>3</sub> in atmospheres,  $T$  is the temperature of the gas in Kelvin,  $S(K) = 3$  for  $K$  a multiple of 3 and  $S(K) = 1.5$  otherwise, and  $F(\nu, J, K)$  is a shape function (units of MHz), which determines the shape of the absorption line as a function of observing frequency and ambient conditions. (In Equation 2 of Wrixon *et al.* 1971, there appears a factor of  $1 \times 10^{-6}$  which should be removed if the shape function is measured in MHz.)

The shape factor,  $F$ , is a difficult quantity to calculate theoretically or determine experimentally (see Wrixon *et al.* 1971, Berge and Gulkis 1976, Spilker 1990). Most of the complications arise in determining the temperature dependence and the effect of collisions with other molecules. Following Wrixon and Welch (1970), this work uses

the Van Vleck-Weisskopf (VW) shape at total atmospheric pressures less than 5 bar, or when within 1 mm in wavelength of the inversion band line centers:

$$F(\nu, J, K) = \nu^2 \Delta\nu \left[ \frac{1}{(\nu - \nu_0)^2 + \Delta\nu^2} + \frac{1}{(\nu + \nu_0)^2 + \Delta\nu^2} \right],$$

where  $\nu$  is the observing frequency,  $\Delta\nu$  is the line width (determined below), and  $\nu_0$  is the line center frequency of the  $(J, K)$  transition (all frequencies in MHz). The line width is also from Wrixon and Welch,

$$\Delta\nu = \left( \frac{10^6}{T} \right) \left\{ 6.23 \left[ \frac{K^2}{J(J+1)} \right]^{\frac{1}{2}} P_{\text{NH}_3} + \left[ \frac{K^2}{J(J+1)} \right]^{\frac{1}{3}} (0.755 P_{\text{H}_2} + 0.231 P_{\text{He}}) \right\},$$

where  $\Delta\nu$  is in MHz, partial pressures are in atmospheres, and it is assumed that collisions occur only among  $\text{H}_2$ ,  $\text{He}$ , and  $\text{NH}_3$ . (Given the overall uncertainty in the line width, the effect of collisions with  $\text{CH}_4$  can be ignored.)

At higher pressures where, among other things, multiple collisions become important, the VW line shape is no longer appropriate. At total pressures greater than 5 bar, or when more than 1 mm away from line centers, a Ben Reuven (BR) line shape is used, taken from Wrixon and Welch (1970), with the correction factor of Berge and Gulkis (1976). This line shape will be referred to as the modified BR shape, and is given by

$$F(\nu, J, K) = 2\nu^2 C \left[ \frac{(\gamma - \zeta)\nu^2 + (\gamma + \zeta)(\nu_0^2 + \gamma^2 - \zeta^2)}{(\nu^2 - \nu_0^2 - \gamma^2 + \zeta^2)^2 + 4\nu^2\gamma^2} \right],$$

where  $\gamma$  is a line width parameter, given in MHz by

$$\gamma = 76 \times \left[ 229 \left( \frac{300}{T} \right) P_{\text{NH}_3} + \left( \frac{300}{T} \right)^{0.8} (22.8 P_{\text{H}_2} + 5.3 P_{\text{He}}) \right],$$

where again it is assumed that  $\text{H}_2$ ,  $\text{He}$ , and  $\text{NH}_3$  are the only colliding molecules, and all partial pressures are in atmospheres. The coupling parameter,  $\zeta$ , is given in MHz by

$$\zeta = 76 \times \left\{ \left[ 229 \left( \frac{300}{T} \right) - 79 \left( \frac{300}{T} \right)^{1.26} \right] P_{\text{NH}_3} + \left[ 22.8 \left( \frac{300}{T} \right)^{0.8} - 11.4 \left( \frac{300}{T} \right)^{1.11} \right] P_{\text{H}_2} + \left[ 5.3 \left( \frac{300}{T} \right)^{0.8} - 2.7 \left( \frac{300}{T} \right)^{0.91} \right] P_{\text{He}} \right\}.$$

The remaining factor,  $C$ , is the high pressure correction term from Berge and Gulikis (1976),

$$C = 1.0075 + \left( 0.0308 + 0.0552 \frac{P_{\text{H}_2}}{T} \right) \frac{P_{\text{H}_2}}{T}.$$

This factor brings the BR line-shape into conformity with the experimental data of Morris and Parsons (1970), but has an appreciable effect only at pressures greater than about 50 bar. It changes calculated brightness temperatures at wavelengths shorter than 20 cm by less than 0.3 K.

On Uranus, where the  $\text{NH}_3$  mixing ratio is very low above 5 bars due to the cold temperatures, the above combination of line shapes is almost identical to using a modified BR line shape exclusively. Recently, Spilker (1990) has done extensive laboratory work on  $\text{NH}_3$  absorption in simulated Jovian atmospheres, and has developed a new formalism for describing the shape function that is much more accurate than either the modified BR or VVW line shapes at temperatures greater than 210 K and pressures less than 8 bar. At frequencies of interest to us here, the modified BR shape appears to be correct to within a few tens of percent in this temperature and pressure regime. There still remains a great deal of uncertainty in the true line shape under Uranian conditions, however, which are cooler and higher pressure than conditions created in the laboratory. Because of this, the current work will continue to use the modified BR line shape at high pressures, but will allow for errors of up to 60% in the calculation. The sensitivity of the model and the results to the line shape will be discussed further in Section 2.3. It will be seen that the uncertainties in the absorption coefficient result in 60% uncertainties in the absolute  $\text{NH}_3$  abundances derived, but that the relative variations in abundance across the disk of Uranus are unaffected.

The summation in Equation 2.14 is actually carried out only for transitions involving the 16 most populous energy levels ( $J = 1$  to 16), resulting in 136 lines being accounted for. The line center frequencies are taken from Poynter and Kakar (1975), most of which were determined experimentally. For the 17 lines not observed, a 15-term exponential fit

from Poynter and Kakar is used:

$$\begin{aligned} \nu_o(J, K) = a_1 \exp[ & a_2 \Upsilon + a_3 \Omega + a_4 \Upsilon^2 + a_5 \Omega \Upsilon + \\ & + a_6 \Omega^2 + a_7 \Upsilon^3 + a_8 \Omega \Upsilon^2 + a_9 \Omega^2 \Upsilon + a_{10} \Omega^3 + \\ & + a_{11} \Upsilon^4 + a_{12} \Omega \Upsilon^3 + a_{13} \Omega^2 \Upsilon^2 + a_{14} \Omega^3 \Upsilon + a_{15} \Omega^4] \end{aligned} \quad (2.15)$$

$$\Upsilon \equiv K^2 \quad \Omega \equiv J(J+1),$$

where  $J$  and  $K$  are the quantum numbers of ammonia's energy state, and the coefficients are given in Table 2.2. If  $K = 3$ , the line center frequency is shifted from that given by Equation 2.15 due to a rotation-vibration interaction. The magnitude of the shift is given by Townes and Schawlow (1975), Equation 12-21, as

$$\delta = (3.07 \times 10^{-4}) \times J(J+1) \times [J(J+1) - 2] \times [J(J+1) - 6],$$

where  $\delta$  is in MHz and the leading coefficient has been renormalized to match the observed shift of the  $J = 14$ ,  $K = 3$  line in the data of Poynter and Kakar. If  $K$  is a higher multiple of 3, a similar but much smaller shift occurs. The only line for which there is not an observed frequency that this would apply to is the  $J = 16$ ,  $K = 6$  line, but the magnitude of the shift is less than 1 MHz, so it is ignored.

**Table 2.2**

Poynter and Kakar, Fifteen-Term Exponential Fit\*

$a_1 = 23785.910$	
$a_2 = 8.89160 \times 10^{-3}$	$a_9 = 6.86470 \times 10^{-9}$
$a_3 = -6.37110 \times 10^{-3}$	$a_{10} = -1.90500 \times 10^{-9}$
$a_4 = 6.65068 \times 10^{-7}$	$a_{11} = 4.77460 \times 10^{-12}$
$a_5 = -2.02306 \times 10^{-6}$	$a_{12} = -1.53420 \times 10^{-11}$
$a_6 = 9.65690 \times 10^{-7}$	$a_{13} = 1.74630 \times 10^{-11}$
$a_7 = 3.08580 \times 10^{-9}$	$a_{14} = -8.07600 \times 10^{-12}$
$a_8 = -7.99760 \times 10^{-9}$	$a_{15} = 1.16870 \times 10^{-12}$

\* $a_1$  is in MHz, all others dimensionless.

Ammonia's rotational absorption band, which has line centers below 0.5 mm, is not included in the model. These lines have no effect on absorption at centimeter wavelengths, and even at wavelengths near 1 mm they should only decrease calculated brightnesses by a few degrees (de Pater and Massie 1985).

### H<sub>2</sub>O Vapor Absorption

At wavelengths longer than about 2 cm, observations begin to probe deep enough (pressures greater than 40 bar) that water becomes an important absorber. The absorption is due to rotational transitions, which have one line at 1.2 cm, and then many lines at wavelengths shorter than a few millimeters. These lines are modeled using the review paper of Waters (1976). Waters presents an expression that uses a Van Vleck-Weisskopf line profile, with an empirical correction term. The absorption is treated as if it is due to only two lines. One line corresponds to the 1.2 cm line, while the second line represents all the shorter wavelength lines, which appear as a single line due to pressure broadening. The absorption coefficient is given in  $\text{cm}^{-1}$  by

$$k_{\text{H}_2\text{O}}(\nu) = \rho \nu^2 \Delta \nu_1 T^{-1.5} \left\{ 2.77 \times 10^{-2} + \frac{(7.18 \times 10^6) e^{-644/T}}{T} \frac{1}{(494.40190 - \nu^2)^2 + 4\nu^2 \Delta \nu_1^2} \right\},$$

where

$$\Delta \nu_1 = 2.96 \left( \frac{P}{1013} \right) \left( \frac{300}{T} \right)^{0.626} \left( 1 + (1.8 \times 10^4) \frac{\rho T}{P} \right).$$

In these expressions,  $\rho$  is the density of water vapor in  $\text{g cm}^{-3}$ , the observing frequency,  $\nu$ , and line width parameter,  $\Delta \nu_1$ , are in GHz (not MHz), and  $P$  is the total atmospheric pressure in mbar (not atmospheres). This expression fits laboratory data to better than 5% at wavelengths longer than 0.3 cm and total atmospheric pressures  $\leq 1$  bar (Waters 1976). Even though this expression will be used at much greater pressures, it is probably accurate enough for current purposes. In Section 2.3 it is shown that alternative expressions for the absorption coefficient do not appreciably change calculated brightness temperatures.

### Liquid H<sub>2</sub>O Absorption

Liquid water drops, suspended as a cloud, can be an important absorber deep in the atmosphere. Van de Hulst (1981) gives the absorption cross section for a single, spherical drop of radius,  $r$ , and complex index of refraction,  $m$ . Under the assumption that the particle radius is much smaller than the observing wavelength, the cross section is

$$C_{\text{abs}} = -\frac{6\pi}{\lambda} v \Im \left\{ \frac{m^2 - 1}{m^2 + 2} \right\}, \quad (2.16)$$

where  $v$  is the volume of the sphere,  $\lambda$  is the radiation wavelength, and  $\Im\{\}$  is the imaginary part of the bracketed expression. If it is assumed that each drop in the liquid water cloud acts as an independent absorber, the absorption coefficient due to such a cloud is given by Equation 2.16 with  $v$  replaced by  $V$ , the fractional volume occupied by the absorbing spheres. As is appropriate, this absorption coefficient has units of  $1/\lambda$ .

To calculate  $m$ , the Debye formula is used,

$$m^2 = \frac{\epsilon_0 - \epsilon_\infty}{1 + i \frac{\Delta\lambda}{\lambda}} + \epsilon_\infty,$$

with parameters taken from Kerr (1951) for water at a temperature of 273 K:  $\epsilon_0 = 88.0$ ,  $\epsilon_\infty = 5.5$ , and  $\Delta\lambda = 3.59$  cm. This temperature is chosen because it turns out that most of the liquid water absorption in the models occurs near the 273 K, 50 bar level. Deeper in the atmosphere, as temperature increases,  $m$  gets smaller. Near 310 K,  $m^2$  has dropped by about a factor of 4. Variations of this order (as well as uncertainties in the absorptive properties of a super-cooled liquid) can be ignored because the uncertainty in  $V$ , the abundance of condensed particles, is much greater. The assumption of small, noninteracting, spherical drops is valid for even the densest fogs on the Earth, which have densities near  $1 \times 10^{-6}$  g cm<sup>-3</sup> (Van de Hulst 1981). In Figure 2.2 it can be seen that calculated cloud densities on Uranus may be higher, which may invalidate some of these assumptions. It is believed, however, that the overall features of this expression are

accurate enough to allow trends in the data due to spatial variations in the total absorber abundance to be recognized.

## H<sub>2</sub> Absorption

Symmetric molecules, such as H<sub>2</sub>, generally have very weak dipole moments, and are not good absorbers. When H<sub>2</sub> molecules collide with other atoms, however, a dipole can be induced. The rotational-translational energy levels of this dipole do interact with microwave radiation. At millimeter wavelengths, this is a major opacity source. At the centimeter and longer wavelengths we will be primarily concerned with, H<sub>2</sub> absorption is relatively small. (Removing all H<sub>2</sub> absorption from the model atmosphere increases the 2 cm brightness by 2.8 K, or 1.5%.) The works of Dore *et al.* (1983) and Bachet *et al.* (1983) are used to model absorption caused by H<sub>2</sub>-H<sub>2</sub> collisions, the work of Cohen *et al.* (1982) to model H<sub>2</sub>-He collisions, and a model suggested by Orton *et al.* (1983) to account for H<sub>2</sub>-CH<sub>4</sub> collisions. The total H<sub>2</sub> absorption is the sum of the three terms.

For H<sub>2</sub>-H<sub>2</sub> collisions, the absorption coefficient, in cm<sup>-1</sup>, is

$$k_{\text{H}_2}(\nu) = F_1 \frac{\nu}{c} (1 - e^{-h\nu/(kT)}) \left[ \frac{P_{\text{H}_2}}{1000} \frac{273.15}{T} \right]^2, \quad (2.17)$$

where  $P_{\text{H}_2}$  is in mbar (the square bracketed term is the density of H<sub>2</sub> in amagat, one amagat being the number density of an ideal gas at STP,  $2.68 \times 10^{19}$  molecules cm<sup>-3</sup>).  $\nu$  is the observing frequency in Hz,  $c$  is the speed of light in cm/s,  $k$  is Boltzmann's constant, and  $F_1$  is a combination of intensity and shape functions, with units of cm<sup>6</sup>,

$$F_1 = \frac{4\pi^3 n_o^2}{3\hbar} I \left\{ S(\nu) \sum_{J=0}^4 \rho_J \frac{J(J+1)(2J+1)}{(2J-1)(2J+3)} + \sum_{J=0}^4 \rho_J (2J+1) \left[ \frac{3(J+1)(J+2)}{2(2J+1)(2J+3)} \right] S(\nu - \nu_{J,J+2}) \right\}. \quad (2.18)$$

In this equation,  $I$  is an empirical intensity function in erg cm<sup>6</sup>,

$$I = 281 \left( \frac{T}{273.15} \right)^{0.235} k(1.0 \times 10^{-48}),$$

where the last two factors convert the  $\text{K } \text{\AA}^6$  used by Dore *et al.* to  $\text{erg cm}^6$ . Returning to Equation 2.18,  $n_o$  is Loschmidt's number,  $\hbar$  is Planck's constant over  $2\pi$ , and  $\rho_J$  is the Boltzmann factor, which for equilibrium  $\text{H}_2$  (see Section 2.2.2 for a discussion of the *ortho-para* ratio) is

$$\rho_J = \frac{g_J e^{-h\nu_J/(kT)}}{\sum_{J'} g_{J'} (2J' + 1) e^{-h\nu_{J'}/(kT)}}.$$

In this expression,  $g_J$  is a statistical factor due to nuclear spin,  $g_J = 1$  for  $J$  even,  $g_J = 3$  for  $J$  odd, and the frequency, in Hz, associated with the rotational quantum state  $J$  is

$$\nu_J = c [59.3392(J^2 + J) - 0.04599(J^2 + J)^2 + 0.000052(J^2 + J)^3] \quad (2.19)$$

(Bachet *et al.* 1983), where  $c$  is the speed of light in cm/s.

The remaining undefined terms in Equation 2.18 are the spectral function,  $S(\nu)$ , which is related to the shape function, and  $\nu_{J,J+2}$ , which is the frequency associated with the rotational transition between the  $J$  and  $J+2$  levels. To calculate it, Equation 2.19 is used, and

$$\nu_{J,J+2} = \nu_{J+2} - \nu_J.$$

The spectral function, in units of seconds, is

$$S(\nu) = \frac{\tau_1}{\pi} \frac{z K_1(z)}{1 + (2\pi\nu\tau_1)^2} e^{(\tau_2/\tau_1 + 2\pi\nu\tau_0)}. \quad (2.20)$$

In this equation,

$$\begin{aligned} \tau_0 &= \frac{\hbar}{2kT} \\ \tau_1 &= 4.68 \times 10^{-14} \left( \frac{273.15}{T} \right)^{0.605} \\ \tau_2 &= 2.23 \times 10^{-14} \left( \frac{273.15}{T} \right)^{0.607}, \end{aligned}$$

where each  $\tau$  is in seconds. The function  $z$  is defined as

$$z = z(\nu) = \frac{1}{\tau_1} \sqrt{(1 + (2\pi\nu\tau_1)^2) (\tau_2^2 + \tau_0^2)},$$

and  $K_1(z)$  is a modified Bessel function of the second kind. The approximation

$$z K_1(z) = e^{-z} \sqrt{1 + (1.6191)z}$$

is used, which is correct to within 1.5%. Note that in Dore *et al.* (1983) Equation 9, which corresponds to the above expression, the 'z' under the square root is misprinted as a '2'.

For H<sub>2</sub>-He collisions, the work of Cohen *et al.* (1982) is used. The general form of the calculations is the same as for H<sub>2</sub>-H<sub>2</sub>, with changes to the empirically derived expressions for  $I$  and the  $\tau$ 's, and an additional term because the colliding molecules are not identical. The expressions, using many previously defined terms, are:

$$k_{\text{He}}(\nu) = F_2 \frac{\nu}{c} (1 - e^{-h\nu/(kT)}) \left[ \frac{1}{1000} \frac{273.15}{T} \right]^2 P_{\text{H}_2} P_{\text{He}},$$

where

$$F_2 = \frac{8\pi^3 n_o^2}{3\hbar} \left\{ I_i S_i(\nu) + I_q \left( S_q(\nu) \sum_{J=0}^4 \rho_J \frac{J(J+1)(2J+1)}{(2J-1)(2J+3)} \right. \right. \\ \left. \left. + \sum_{J=0}^4 \rho_J (2J+1) \frac{3(J+1)(J+2)}{2(2J+1)(2J+3)} S_q(\nu - \nu_{J,J+2}) \right) \right\}$$

and the intensity factors are

$$I_i = 33.53 \left( \frac{T}{77.4} \right) k(1.0 \times 10^{-48})$$

$$I_q = 12.06 \left( \frac{T}{77.4} \right)^{0.57} k(1.0 \times 10^{-48}),$$

which have units of erg cm<sup>6</sup>. The subscript  $i$  refers to an isotropic component, and  $q$  to an anisotropic component. Finally, the shape function,  $S$ , is the same as in Equation 2.20, but with different parameters for the isotropic and anisotropic cases:

$$\tau_{1i} = 3.43 \times 10^{-14} \sqrt{\frac{T}{77.4}}$$

$$\tau_{2i} = 6.56 \times 10^{-14} \sqrt{\frac{T}{77.4}}$$

$$\tau_{1q} = 8.94 \times 10^{-14} \left( \frac{77.4}{T} \right)^{0.6}$$

$$\tau_{2q} = 3.02 \times 10^{-14} \left( \frac{77.4}{T} \right)^{0.3}$$

(all in seconds).

The absorption induced by H<sub>2</sub>-CH<sub>4</sub> collisions is calculated using a model suggested by Orton *et al.* (1983) which uses expressions identical to those for H<sub>2</sub>-He collisions, with the following substitutions:

$$I_i = 648 \left( \frac{T}{195} \right)^{0.14} k(1.0 \times 10^{-48})$$

$$I_q = 223 \left( \frac{T}{195} \right)^{-0.3} k(1.0 \times 10^{-48})$$

$$\tau_{1i} = 2.16 \times 10^{-14} \sqrt{\frac{195}{T}}$$

$$\tau_{2i} = 3.00 \times 10^{-14} \sqrt{\frac{195}{T}}$$

$$\tau_{1q} = 9.55 \times 10^{-14} \sqrt{\frac{195}{T}}$$

$$\tau_{2q} = 4.40 \times 10^{-14} \sqrt{\frac{195}{T}},$$

and, of course, the partial pressure of CH<sub>4</sub> should be used instead of He. Note that in the appendix of Orton *et al.* (1983), the exponential factors for  $\tau_{1q}$  and  $\tau_{2q}$  from Cohen *et al.* (1982) for H<sub>2</sub>-He collisions are misquoted.

All of the above expressions for H<sub>2</sub> absorption are based on experimental work at submillimeter wavelengths. Since we will be discussing observations at centimeter wavelengths, there is some uncertainty due to the extrapolation to longer wavelengths. In Section 2.3 the above expressions will be compared to similar calculations for normal, rather than equilibrium, H<sub>2</sub>, as well as with a completely different formulation of H<sub>2</sub>

absorption. It will be found that the observations are insensitive to details of the  $H_2$  absorption coefficient.

### Unmodeled Absorbers

The previous pages have described the absorbers used in the model atmosphere. This section discusses why other sources of opacity are neglected, and the effect of unknown absorbers on the final results. (Section 2.2.1 already discussed why scattering is neglected.) There are some species that are expected to be present in the atmosphere, but that have been ignored because their effects are believed to be small. Starting high in the atmosphere, there are hazes in the stratosphere (probably hydrocarbon photochemical products, Pollack *et al.* 1987) and free electrons in the ionosphere. Abundances are so small at these altitudes, however, that they are not expected to influence centimeter wavelength observations. (This is also the reason why all gases above 100 mbar are neglected, as mentioned in Section 2.2.1.) This assumption is confirmed by the Voyager radio occultation experiment, which found no measurable extinction at wavelengths of 3.6 and 13 cm (Lindal *et al.* 1987)—which is in the heart of the wavelength range of interest to us, roughly 2 to 18 cm.

Deeper in the atmosphere, absorption by He and  $CH_4$  gas is neglected. Both these species have essentially no permanent dipole moment, and even during collisions, He is not expected to interact with microwaves.  $CH_4$  has a larger collision induced dipole moment, and its absorption has been measured in the laboratory and addressed theoretically (see Fox 1974 and references therein). At centimeter wavelengths, however,  $CH_4$  absorption is many orders of magnitude weaker than  $NH_3$  and  $H_2O$  absorption, and even weaker than  $H_2$  absorption (Berge and Gulkis 1976). Thus, while  $CH_4$  may contribute to the millimeter opacity of the Uranian atmosphere, it can be ignored for the current study.

Absorption in the  $CH_4$  cloud is neglected because this cloud consists of ice, and ice is generally a very poor microwave absorber. Furthermore, as already mentioned, the

Voyager occultation experiment probed the region of the methane cloud and found no evidence of absorption. The “ice is a poor absorber” argument is also used to discount absorption in the  $\text{NH}_3$  and  $\text{NH}_4\text{SH}$  clouds. Even if the ice is absorbing, since these clouds only form in the presence of strongly absorbing  $\text{NH}_3$  vapor, it can be expected to be insignificant compared to the vapor absorption. The absorptive properties of water ice have been measured (Mishima *et al.* 1983) and it too is not a significant opacity source. Using the cloud model described in Section 2.2.4, the total path length of condensed water at temperatures less than 273 K is less than 40 cm, which is undetectable.

The last constituent of the model atmosphere whose absorption is neglected is  $\text{H}_2\text{S}$ . While the nominal model has no  $\text{H}_2\text{S}$  cloud because it is all removed in the  $\text{NH}_4\text{SH}$  cloud, if  $\text{H}_2\text{S}$  does condense in the upper atmosphere, it will be ice and is not expected to contribute significantly to atmospheric opacity.  $\text{H}_2\text{S}$  gas, on the other hand, has rotational absorption lines at wavelengths less than 2 mm. These are normally ignored when calculating absorption in giant planet atmospheres because at millimeter wavelengths, one does not see deep enough into the atmosphere for there to be appreciable amounts of  $\text{H}_2\text{S}$ , and at longer wavelengths,  $\text{NH}_3$  absorption totally dominates. De Pater *et al.* (1991) have pointed out, however, that if all the  $\text{NH}_3$  is removed from the upper atmosphere, and if  $\text{H}_2\text{S}$  has a large pressure broadening coefficient, it might be an important opacity source. This does not seem likely, however, because there is no reason to expect  $\text{NH}_3$  to be completely removed from the upper atmosphere and, as will be found shortly, the radio data require an absorber to be present that is similar to  $\text{NH}_3$ . The one argument used by de Pater *et al.* to postulate the lack of  $\text{NH}_3$  is that the planetary formation model of Pollack and Bodenheimer (1989) calls for the sulphur to nitrogen ratio to be greater than 1, which can (depending on cloud properties) consume all the  $\text{NH}_3$  in the formation of the  $\text{NH}_4\text{SH}$  cloud. Since, however, Neptune is also predicted to have a sulphur to nitrogen ratio greater than 1 by this model, and the Voyager radio occultation experiment determined  $\text{NH}_3$  and not  $\text{H}_2\text{S}$  is present in Neptune’s upper atmosphere (Tyler *et al.* 1989,

Lindal *et al.* 1990), it appears the one available observational test of the theory does not support the assumptions. (As an aside, both Jupiter and Saturn are also determined to have  $\text{NH}_3$  opacity in their upper atmospheres, Lindal *et al.* 1981, 1985. Unfortunately, the Voyager occultation experiment at Uranus did not probe deep enough for  $\text{NH}_3$  to be detectable.) Another reason to suspect the presence of  $\text{NH}_3$  is that the ground-based data on Uranus discussed in Sections 2.3 and Chapter 4 require an absorber to be present in the upper atmosphere that is similar to  $\text{NH}_3$ . It therefore seems reasonable to assume that  $\text{NH}_3$  is indeed present, and that  $\text{H}_2\text{S}$  absorption can be ignored.

Having explained why  $\text{H}_2\text{S}$  is not believed to be the observed opacity source in the upper atmosphere of Uranus, the fact remains that this cannot, as of yet, be proven. Thus, while the data is used here to derive  $\text{NH}_3$  abundances,  $\text{NH}_3$  absorption in the model can be thought of as only a parameterization of the actual absorption, and the main results of this work will be based on the absorber distribution independent of what the absorbing species is. The possibility of unknown species being present in the atmosphere that are significant sources of extinction (extinction including both absorption and scattering) can be addressed in a similar fashion as  $\text{H}_2\text{S}$  absorption. Whether they are present or not, the opacity distribution seen in the data (Chapters 3 and 4) is real, and significant results can be found from it regarding the circulation of the atmosphere. The calculated  $\text{NH}_3$ ,  $\text{H}_2\text{O}$ , and cloud abundances in the model are to be believed only to the extent that one discounts the presence of unknown absorbers. The fact that all available data on the deep atmosphere of Uranus can be explained using known, cosmochemically abundant absorbing species, however, is circumstantial evidence that the major opacity sources have been identified.

### 2.3 Modeling Disk Averaged Data

In this section the model atmosphere is compared to unresolved radio observations of Uranus. Most previous work has involved these disk averaged data, so the discussion

will allow the model to be tested against published work, and provides a framework for reviewing the literature. (Primary references are Gulkis *et al.* 1978, Gulkis and de Pater 1984, de Pater and Massie 1985, and de Pater *et al.* 1989.) This opportunity will also be used to explore the model sensitivity to various parameters. Finally, a reference model will be chosen for comparison to the high resolution data of the next chapter. Given the strong latitudinal brightness variations that exist on Uranus, are disk averaged results meaningful? If the temperature profile does not vary significantly with latitude (which is believed to be a reasonable assumption, see Hanel *et al.* 1986, Flasar *et al.* 1987, and Friedson and Ingersoll 1987), the absorber abundance as a function of depth inferred from unresolved observations is an accurate measure of the areal averaged abundance on the Earthward facing hemisphere. It is questionable, however, if the chemical and dynamical processes operating in the atmosphere can be deduced from these data because these processes may not average by area. For this reason, a determination of the gross structure of the atmosphere is all that will be attempted here, and a detailed analysis is left for the high resolution data of the next chapter. The limitations of unresolved observations should be kept in mind in the following discussion, and when reviewing the literature.

### 2.3.1 Disk Averaged Data

Most of the disk averaged brightness measurements used here are taken from the compilation of Gulkis and de Pater (1984). Their compilation consists of 51 measurements made at wavelengths between 0.1 and 20.5 cm, spanning the years from 1965 (the first published radio observation of Uranus) to 1983. All brightness temperatures listed are renormalized to a common assumed radius for Uranus of 25,392 km (the size of the planet is used to convert the flux measured at the telescope to a brightness per unit area). To this compilation are added the observations reported in de Pater and Gulkis (1988) at 1.3, 2, 6, and 20 cm (note that some of these measurements supersede preliminary

values reported in Gulkis and de Pater 1984), Muhleman and Berge (1989) at 0.266 cm, Berge *et al.* (1988) at 2 cm, Jaffe *et al.* (1984) at 2 and 6 cm, Hofstadter *et al.* (1990) at 6 cm, and McKinnon (1981) at 6 and 21 cm. These additional observations have not been renormalized to a common radius because the correction would be less than the quoted error bars, and for current purposes high accuracy is not needed. The error bars on the Hofstadter *et al.* 6 cm measurement have been increased from 5 to 9 K to allow for a 3% calibration uncertainty.

The observations are shown in Figure 2.3, along with a representative sampling of quoted error bars. The data are divided into three groups. Crosses indicate older, pre-1973 data, and the open circles are 1973 and newer observations. The filled circles are disk averaged brightnesses from high resolution data that will be analyzed in detail in the next chapters. These three points correspond to the 2 cm observations of Berge *et al.* (1988), the 1981 6 cm observations reported in Jaffe *et al.* (1984), and the 6 cm observations of Hofstadter *et al.* (1990). These data are near the average value of all measurements at the same wavelengths, and the two 6 cm measurements are almost identical even though they were made 8 years apart. This confirms the accuracy and calibration of these observations. The division of the data set around the year 1973 is based on the apparent position of Uranus' South Pole. (In this thesis, the IAU definitions of north and south are used. The IAU Southern Hemisphere corresponds to the northern dynamical hemisphere.) Because of Uranus' 98° obliquity, Earth-based observers get drastically different views of the planet over its 84 year orbit. In 1965, the South Pole appeared on the Western limb of the planet (corresponding to mid-Spring for that hemisphere). By solstice in 1985, the South Pole had moved to near the disk center as seen from the Earth. Since then, the pole has continued moving eastward. Observations made before 1973 have the pole nearer the limb than the disk center, corresponding to Spring in the Southern Hemisphere. Newer observations have the pole closer to the sub-Earth point, and correspond to summer.

Looking at the data, it is clear that the older observations tend to be cooler than more recent ones. This was first realized by Klein and Turegano (1978), and discussed further in Briggs and Andrew (1980), Gulkis *et al.* (1983), Jaffe *et al.* (1984), Gulkis and de Pater (1984), and Hofstadter and Muhleman (1989). This trend could be due to true secular variations in the atmosphere's structure, or due to a static structure being observed from different angles as Uranus orbits the sun, or a combination of the two. Because the high resolution observations shed some light on this question, a discussion of time variability is deferred to Chapter 4, Section 3. For now, the older observations will be ignored, and our attention and model fitting will be focused on the newer data.

### 2.3.2 Model Fitting

This section discusses various ways to fit the model to the newer observations between 1 and 20 cm. (Millimeter data and model calculations are included in the figures, but some effects have been ignored that could be important at these wavelengths, such as the rotational absorption band of  $\text{NH}_3$ . See Orton *et al.* 1986 for a more detailed analysis of millimeter and sub-millimeter data.) The model starting point is the temperature profile of Figure 2.1 and the abundances of Table 2.1, except for  $\text{NH}_3$ ,  $\text{H}_2\text{O}$ , and  $\text{H}_2\text{S}$ , which will be adjusted to fit the data.

The initial models do not have any  $\text{H}_2\text{O}$  or  $\text{H}_2\text{S}$  in the atmosphere, and use  $\text{NH}_3$  as the only significant opacity source. (Using a single absorber provides some insights into the opacity distribution of the atmosphere.) Figure 2.3 shows model results for various  $\text{NH}_3$  abundances. The solid curve is for a solar molar mixing ratio of  $1.4 \times 10^{-4}$ . It is clearly much too cold to fit the observations. Gulkis *et al.* (1978) were the first to point this out, and suggested that  $\text{NH}_3$  is depleted from a solar abundance in the upper atmosphere. Decreasing the absorber abundance allows radio waves to emerge from deeper, hotter levels of the atmosphere, and can improve the fit at some wavelengths. This is shown by the dashed curve, with a 1/10 solar  $\text{NH}_3$  abundance, and the dot-dashed

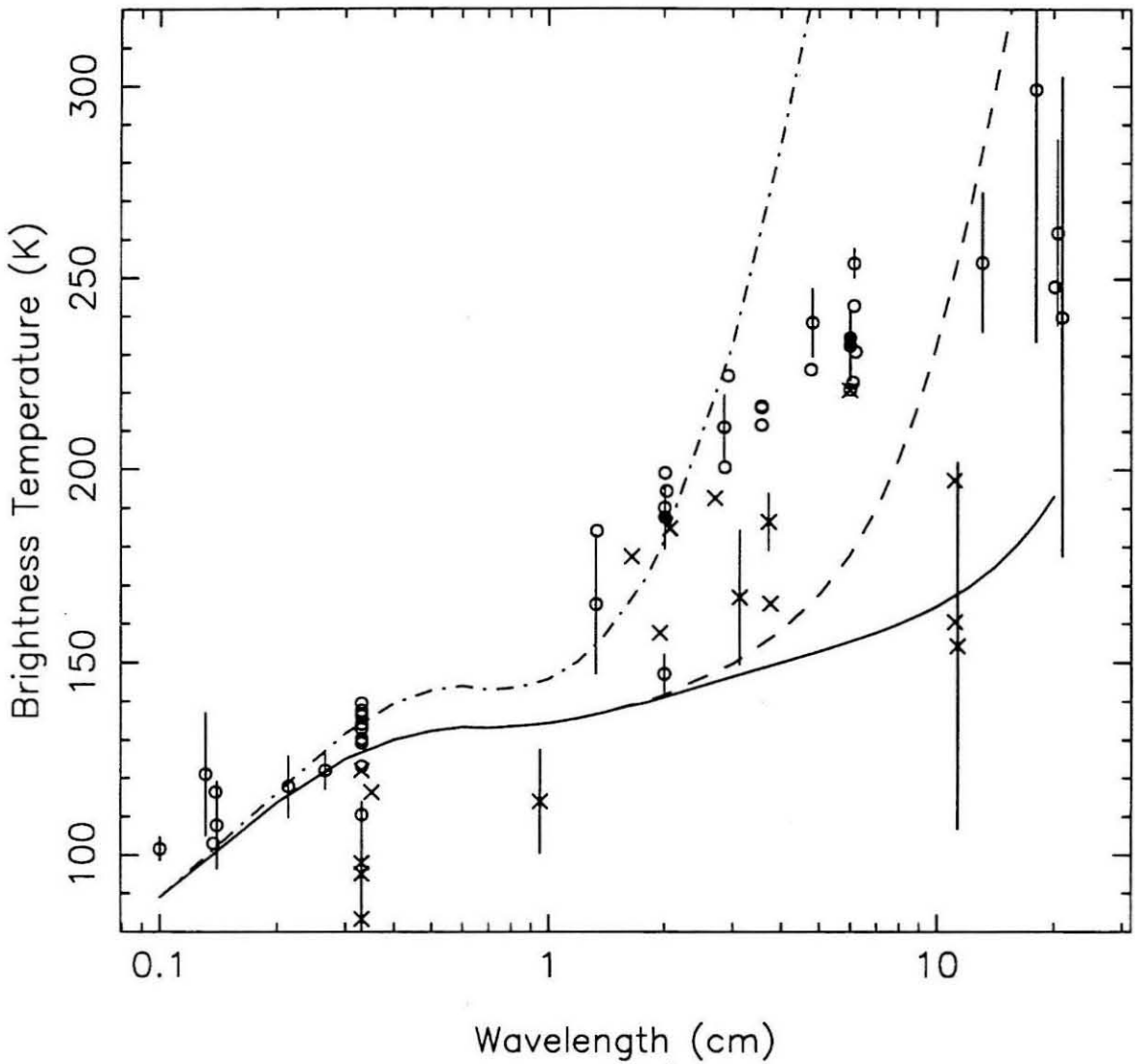


**Figure 2.3:** Disk averaged data points and initial model fitting. The data points are taken from various sources listed in the text, and are divided into three categories. Crosses indicate observations made before 1973, while circles indicate 1973 and newer data. The three filled circles are from high-resolution data sets that will be studied more thoroughly in later chapters. A sampling of error bars is shown. The solid curve is for a model with a solar  $\text{NH}_3$  mixing ratio of  $1.4 \times 10^{-4}$ , and no  $\text{H}_2\text{O}$  or  $\text{H}_2\text{S}$ . The dashed curve is similar, but the  $\text{NH}_3$  ratio is reduced by a factor of 10. The dot-dashed curve has the  $\text{NH}_3$  abundance reduced further, to  $1.0 \times 10^{-6}$ .

curve, with a molar ratio of  $1.0 \times 10^{-6}$ . The latter curve is fairly close to the data at short centimeter wavelengths, but beyond 3 cm diverges significantly. Clearly the shape of Uranus' spectrum differs from the model, the model curves rising much too sharply at the longer wavelengths.

De Pater and Massie (1985) point out that the longer wavelength model temperatures can be flattened out by increasing absorption at depth, by a nearly isothermal atmosphere at depth, or by the presence of a solid or ocean surface near the 250 K temperature level (about 40 bars). The latter possibility seems ruled out by gravitational data (see, for example, Podolak and Reynolds 1987), and will not be considered further. Figure 2.4 shows the results of pursuing the deep absorber hypothesis with models that use a high  $\text{NH}_3$  mixing ratio below a chosen altitude. For reference, the dot-dashed curve in Figure 2.4 is the same as in Figure 2.3, corresponding to an  $\text{NH}_3$  ratio of  $1.0 \times 10^{-6}$  and no extra absorber at depth. The solid curve is the same, except it increases the  $\text{NH}_3$  molar mixing ratio to  $1.4 \times 10^{-3}$  below the 50 bar, 270 K level. It does a much better job of recreating the spectrum between 1 and 20 cm. If the strongly absorbing layer is placed deeper than about 60 bars ( $\sim 290$  K), the longer wavelength observations cannot be fit because atmospheric levels are probed that are too warm. This is shown by the dashed curve, which transitions to an  $\text{NH}_3$  ratio of 0.15 below 70 bars (the  $\text{NH}_3$  abundance is increased as the transition level is made deeper in an attempt to improve the fit). Similarly, there is a limit to how high in the atmosphere the transition level can be brought. Placing it at lower pressures requires the deep layer to have a smaller  $\text{NH}_3$  abundance to fit the short centimeter data, but can make the long wavelength data too warm. This is shown by the dotted curve, which transitions to a mixing ratio of  $1.0 \times 10^{-5}$  at pressures greater than 20 bar. The conclusion to draw from Figure 2.4 is that if the temperature profile is adiabatic, the average absorber mixing ratio at pressures greater than about 30 bars is at least 100 times, the average mixing ratio at lower pressures.

What if the atmospheric temperature profile is not adiabatic everywhere? De Pater

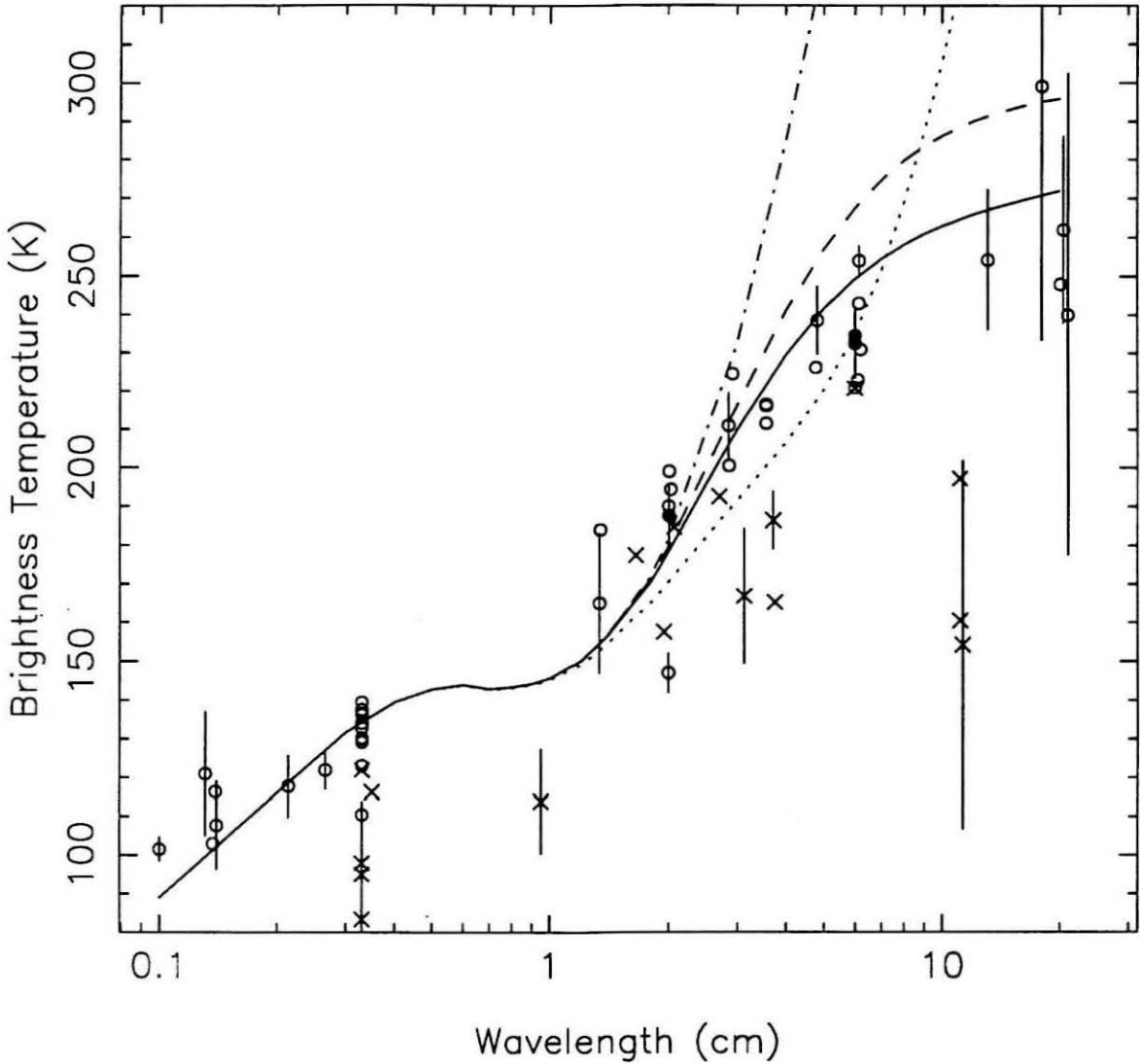


**Figure 2.4:** Adding extra absorption at depth. The dot-dashed curve is from Figure 2.3, and has an  $\text{NH}_3$  molar mixing ratio of  $1.0 \times 10^{-6}$ . The solid curve demonstrates how adding additional absorbers at depth, in this case an  $\text{NH}_3$  ratio of  $1.4 \times 10^{-3}$  at pressures greater than 50 bar (temperatures greater than 270 K), can improve the model fit. The dashed curve increases the  $\text{NH}_3$  ratio to 0.15 below the 70 bar, 300 K level, and indicates the data cannot be fit if the deep absorbing layer is placed at deeper, hotter levels. Similarly, raising the deep layer in altitude degrades the fit, as shown by the dotted curve which transitions to an  $\text{NH}_3$  ratio of  $1.0 \times 10^{-5}$  deeper than the 20 bar, 210 K level.

*et al.* (1989) point out that the increasing brightness temperature between 1 and 6 cm implies temperature does increase with depth at least up to a temperature of about 240 K, but that models with an isothermal atmosphere deeper than this can fit the observations. This is shown in Figure 2.5. The solid curve has an  $\text{NH}_3$  molar mixing ratio of  $6.0 \times 10^{-7}$  and uses the temperature profile of Figure 2.1 down to a temperature of 255 K, which occurs at about 40 bars. Deeper than 40 bars, the temperature is held constant at 255 K. The effect of an isothermal region is very similar to that of a strongly absorbing layer, and similar constraints exist if the data is to be fit. Bringing the isothermal region to higher, cooler altitudes, requires decreasing the absorber abundance to fit observations, while pushing it to deeper, hotter regions calls for an increased absorber abundance. The lowest temperature at which the model atmosphere can become isothermal and still fit the data is about 230 K, which occurs near the 30 bar level (dashed curve). The highest isothermal temperature allowed is about 290 K starting at 60 bar (dot-dashed curve).

The radio data at wavelengths less than 20 cm cannot distinguish between the deep isothermal and deep absorbing models (Figures 2.4 and 2.5), but they clearly indicate that a change in atmospheric properties occurs somewhere between about 30 and 60 bars. It is highly likely that there is a deep absorbing layer of some extent due to the presence of water: based on a solar composition, water is expected to be one of the most abundant species after  $\text{H}_2$  and He (Cameron 1982), and the “ices” are expected to be enriched in the outer solar system. More realistic models that include the presence of water shall now be explored.

Figure 2.6 demonstrates the effect of adding water as an absorber. The dotted curve is a model with an  $\text{NH}_3$  molar mixing ratio of  $8.0 \times 10^{-7}$ , and a near solar  $\text{H}_2\text{O}$  ratio of  $1.0 \times 10^{-3}$ . Absorption by water vapor, but not the water cloud, is included. It provides a marginal fit to the data, being too warm at the longer wavelengths. Increasing the water abundance does not improve the fit significantly because at solar and greater abundances, water saturates relatively deep (see Figure 2.1), and it is the saturation vapor pressure

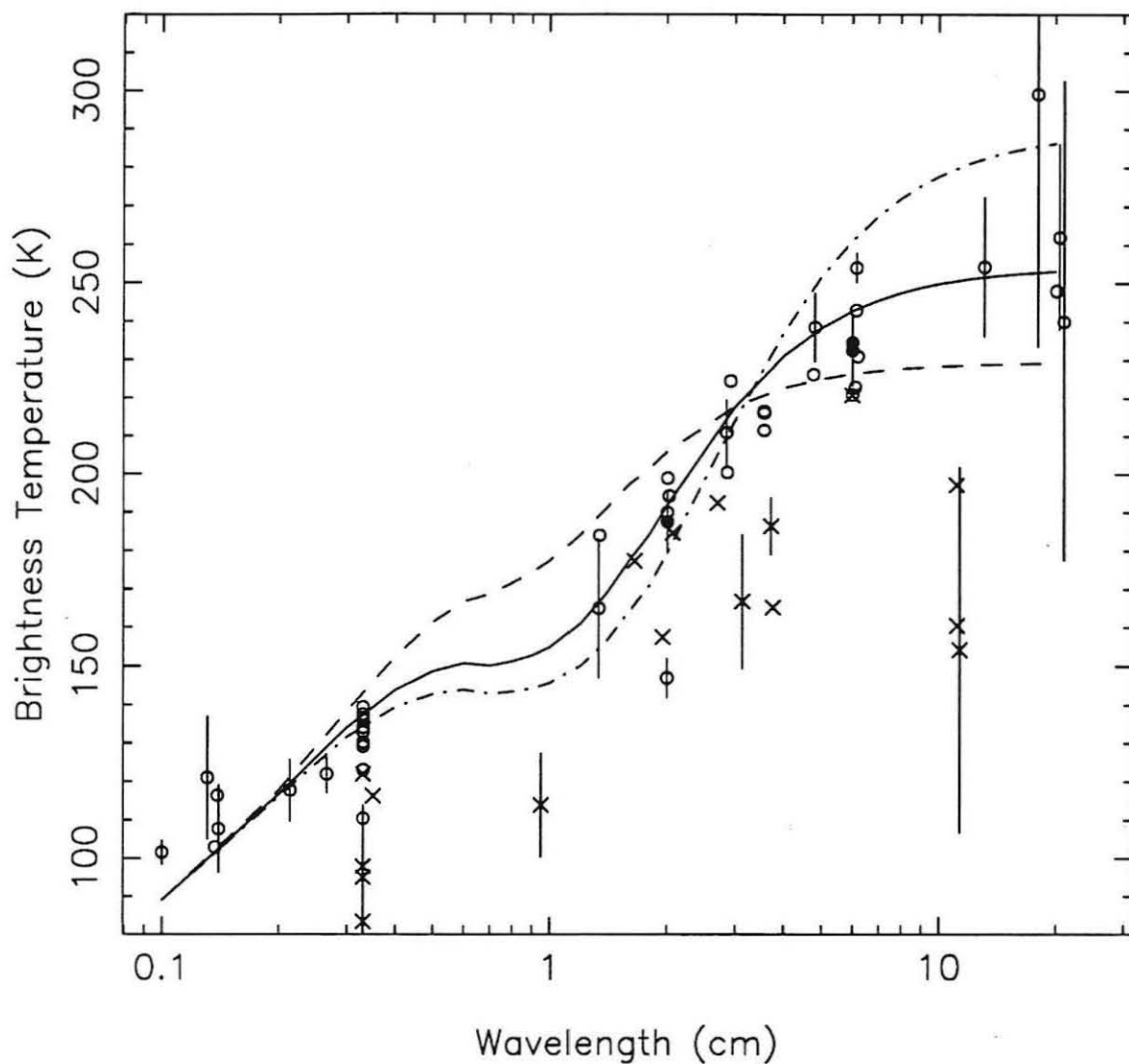


**Figure 2.5:** Isothermal atmospheres. These three curves indicate the range of temperatures at which the model atmosphere can become isothermal in order to fit the data. The solid curve has an NH<sub>3</sub> molar mixing ratio of  $6.0 \times 10^{-7}$ , and is isothermal at 255 K at pressures greater than about 40 bar. The dashed curve has an NH<sub>3</sub> ratio of  $2.0 \times 10^{-7}$  and becomes isothermal at 230 K and 30 bar. The dot-dashed curve has an NH<sub>3</sub> abundance of  $1.0 \times 10^{-6}$  and becomes isothermal starting at 290 K and 60 bar.

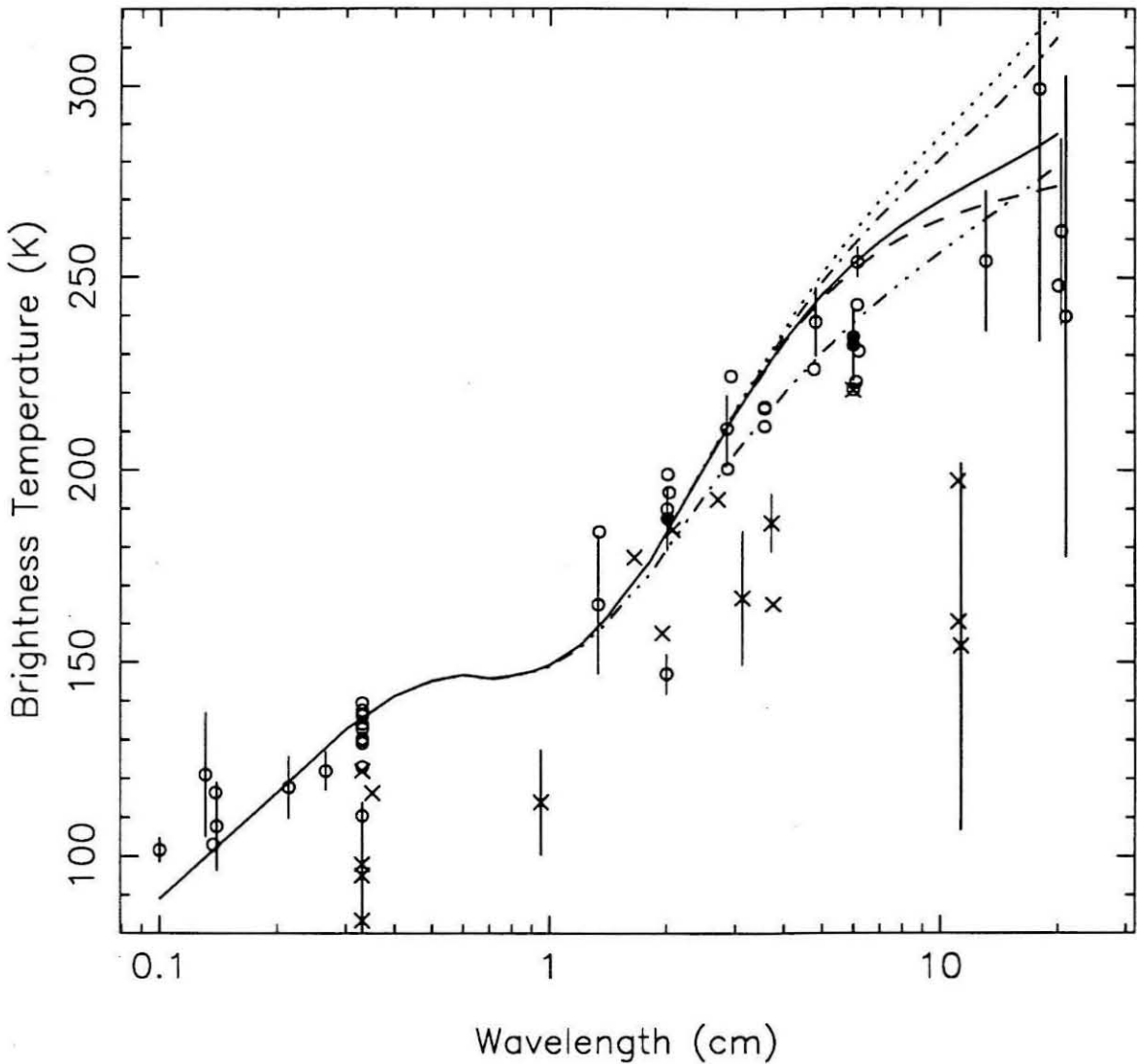


**Figure 2.6:** The effects of adding water absorption. The dotted curve has an  $\text{NH}_3$  molar ratio of  $8.0 \times 10^{-7}$  and an  $\text{H}_2\text{O}$  ratio of  $1.0 \times 10^{-3}$ . This curve does not include absorption due to the water cloud. The solid curve adds cloud effects, and assumes the water cloud is liquid at temperatures greater than 273 K. The dashed curve is similar, except it has increased the water cloud density by a factor of 10 from that calculated by the method of Weidenschilling and Lewis, while the dot-dashed curve decreases the cloud density by a factor of 10. The dash-triple-dotted curve is the same as the solid curve ( $\text{NH}_3$  ratio  $8.0 \times 10^{-7}$ ,  $\text{H}_2\text{O}$  ratio  $1.0 \times 10^{-3}$ , cloud effects included), but now the water cloud is assumed to be liquid down to a temperature of 200 K, as will happen if other species are placed in solution in the cloud.

which is controlling the abundance in the region we are most sensitive to. (When the water abundance is increased, there are two mechanisms at work to decrease calculated brightnesses. One is the extra opacity which screens the deeper, hotter regions from observations. The second is the latent heat released by condensation: the extra water means a wet adiabat is followed deeper into the atmosphere, slowing the temperature increase with depth.) Decreasing the water ratio from  $10^{-3}$  makes brightness temperatures increase rapidly longward of 6 cm (indicating we are seeing below the cloud base), and clearly does not fit the data.

Accounting for absorption by the liquid water cloud provides an extra opacity source. The solid curve of Figure 2.6 is the same as the dotted, except now the water cloud is assumed to be liquid at temperatures greater than 273 K, and its opacity is included. As before, increasing the water mixing ratio will not improve the data fit, while decreasing it degrades it. The remaining curves of Figure 2.6 demonstrate some of the uncertainties of the nominal cloud model. The dashed curve has the same vapor abundances as the solid curve, but cloud densities are assumed to be ten times that calculated by the method of Weidenschilling and Lewis (1973). Alternatively, the dot-dashed curve shows the effect of clouds only 1/10 as dense as the nominal model. Finally, the dash-triple-dotted curve shows the effect of using the nominal cloud abundances, but allowing water to remain liquid down to 200 K due to solution effects (Section 2.2.4). The conclusion to be drawn from this analysis of water absorption is that a solar or greater water abundance, combined with a relatively low  $\text{NH}_3$  abundance high in the atmosphere, can provide a reasonable fit to the data, especially if solution effects depress the freezing point of water—which seems quite likely.

While the absorber abundance and identity in the atmosphere deeper than 30 bars may be uncertain, it is clear that higher in the atmosphere, ammonia is strongly depleted. Given that the planet as a whole is expected to have a near solar or greater  $\text{NH}_3$  abundance (see Fegley *et al.* 1991 for a discussion), there have been two main arguments presented

to explain this depletion. Gulkis *et al.* (1978) suggested that if the  $\text{H}_2\text{S}/\text{NH}_3$  abundance ratio is nearly one (a solar ratio is about 1/5, while type CI-chondritic meteorites have a ratio of 12), the formation of an  $\text{NH}_4\text{SH}$  cloud could create the observed depletion. Atreya and Romani (1984) proposed instead that trapping of  $\text{NH}_3$  in the liquid water cloud could explain the depletion. Most recently the idea that both mechanisms are operating seems favored (Carlson *et al.* 1987, de Pater *et al.* 1989, 1991, Fegley *et al.* 1991).

Models that include  $\text{H}_2\text{S}$  and the formation of  $\text{NH}_4\text{SH}$  will now be considered. The formation of aqueous solutions is not modeled. This is because most of the placement of  $\text{NH}_3$  (and other species) into solution occurs well below the 30 bar level (de Pater *et al.* 1989, Fegley *et al.* 1991), and it was already discussed how uncertainties in the water cloud absorption prevent a detailed determination of atmospheric properties at these levels. Furthermore, the assumptions required to model solution effects (such as the planet-wide abundance of trace species, temperature profiles to depths of hundreds or even thousands of bars, and cloud properties to the same depths), make the results of such modeling rather speculative. The approach used here, therefore, is to use the data to infer  $\text{NH}_3$  and  $\text{H}_2\text{S}$  abundances in the upper few tens of bars of the troposphere, and to realize that these observed abundances may be controlled by processes operating deeper in the atmosphere, and that they do not necessarily reflect the bulk composition of the planet.

Figure 2.7 shows the effects of  $\text{NH}_4\text{SH}$  formation. All curves use a solar  $\text{H}_2\text{O}$  mixing ratio of  $1.0 \times 10^{-3}$  and include liquid water cloud absorption at temperatures greater than 273 K. The dashed curve is for a model with roughly solar abundances of  $\text{NH}_3$  and  $\text{H}_2\text{S}$ :  $1.4 \times 10^{-4}$  and  $3.1 \times 10^{-5}$ , respectively. This  $\text{H}_2\text{S}$  abundance does not remove enough  $\text{NH}_3$  from the atmosphere to fit the data. The dot-dashed curve has equal  $\text{NH}_3$  and  $\text{H}_2\text{S}$  mixing ratios of  $1.4 \times 10^{-4}$ , while the dotted curve has half as much  $\text{NH}_3$  as  $\text{H}_2\text{S}$ , the mixing ratios being  $1.4 \times 10^{-4}$  and  $2.8 \times 10^{-4}$ , respectively. These last two curves

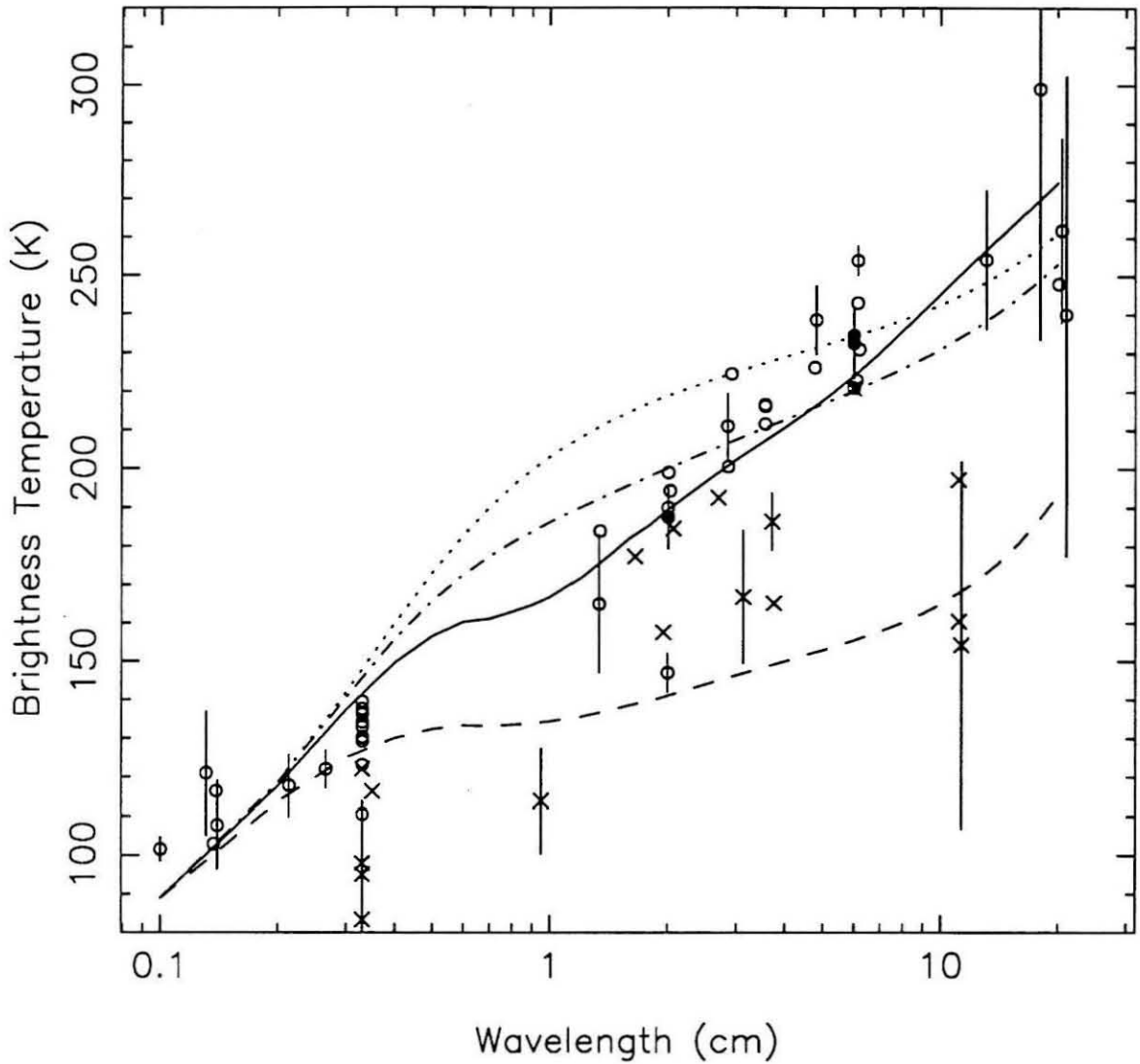


**Figure 2.7:**  $\text{NH}_3$ - $\text{H}_2\text{S}$  chemistry. All curves are models with an  $\text{H}_2\text{O}$  molar mixing ratio of  $1.0 \times 10^{-3}$  and include absorption by the liquid water cloud at temperatures greater than 273 K. The dashed curve has roughly solar  $\text{NH}_3$  and  $\text{H}_2\text{S}$  ratios of  $1.4 \times 10^{-4}$  and  $3.1 \times 10^{-5}$ , respectively. The dot-dashed curve has both the  $\text{NH}_3$  and  $\text{H}_2\text{S}$  molar ratios set to  $1.4 \times 10^{-4}$ , while the dotted curve has the  $\text{H}_2\text{S}$  ratio increased to  $2.8 \times 10^{-4}$ . The solid curve has an  $\text{NH}_3$  ratio of  $2.0 \times 10^{-5}$  and an  $\text{H}_2\text{S}$  ratio of  $1.99 \times 10^{-5}$ .

remove essentially all the  $\text{NH}_3$  from the upper atmosphere, which is too much (model brightnesses near 1 cm are too high). The solid curve, which provides a fair fit to the data, has an  $\text{NH}_3$  mixing ratio of  $2.0 \times 10^{-5}$  and an  $\text{H}_2\text{S}$  ratio of  $1.99 \times 10^{-5}$ . The defining feature of each model is not so much the absolute  $\text{NH}_3$  or  $\text{H}_2\text{S}$  abundance as it is the difference between the abundances. Thus a model with an  $\text{NH}_3$  ratio of  $1.0 \times 10^{-4}$  and an  $\text{H}_2\text{S}$  ratio of  $9.99 \times 10^{-5}$  would yield a curve similar to the solid curve of Figure 2.7.

It turns out that only models with an  $\text{H}_2\text{S}$  abundance lower than, but within 1% of, the  $\text{NH}_3$  abundance provide a good fit to the disk averaged data. There are two main reasons, however, this cannot be used as a firm estimate of the  $\text{H}_2\text{S}/\text{NH}_3$  ratio. The first is that disk averaged observations cannot reliably model chemical processes: areal averaging of abundances that vary spatially may yield a false picture of the chemical reactions occurring. For example, it will be found in Chapter 4 that when horizontal variations are accounted for, the  $\text{H}_2\text{S}$  and  $\text{NH}_3$  ratios can differ by up to 10% and still fit the data. The second reason to be cautious with this 1% value is that it is inversely proportional to the efficiency of formation of the  $\text{NH}_4\text{SH}$  cloud, which is not known (even clouds in the Earth's atmosphere cannot be accurately modeled).

While on the topic of the  $\text{H}_2\text{S}/\text{NH}_3$  ratio, mention must be made again of the work of de Pater *et al.* 1989 and 1991, which assume the  $\text{H}_2\text{S}/\text{NH}_3$  ratio is greater than 1 based on the planetary formation model of Pollack and Bodenheimer (1989), and then speculate on the cloud structures and opacity sources needed to fit the data. As discussed in the *Unmodeled Absorbers* part of Section 2.2.5, their interpretations are possible, but the perceived discrepancies between data and models can be accounted for most simply by the uncertainties in the models and the limitations of disk averaged observations.

The  $\text{H}_2\text{S}/\text{NH}_3$  ratio will be discussed further in Chapter 4, but for now it is reasonable to conclude that the presence of  $\text{H}_2\text{S}$  and the formation of  $\text{NH}_4\text{SH}$  can account for the observed opacity distribution with  $\text{NH}_3$  being the primary absorber above and below the  $\text{NH}_4\text{SH}$  cloud. The  $\text{H}_2\text{S}/\text{NH}_3$  ratio cannot be determined, however, primarily because of

difficulties in determining the nature of the  $\text{NH}_4\text{SH}$  cloud.

### 2.3.3 The Reference Model

This section describes a simple model of Uranus that will be used as a common reference point for high resolution observations made at different wavelengths and at different times. This aspect of its use will be described in Section 3.2.2. Here, the “reference model”, or “average model” will be used to present weighting functions and to explore the model sensitivities to various factors such as how absorption coefficients are calculated and uncertainties in the radio science temperature profile. The model chosen for this has already been presented, and corresponds to the solid curve of Figure 2.6. This model uses the standard temperature profile of Figure 2.1, has an  $\text{NH}_3$  mixing ratio of  $8.0 \times 10^{-7}$ , an  $\text{H}_2\text{O}$  ratio of  $1.0 \times 10^{-3}$ , and no  $\text{H}_2\text{S}$ . The water cloud is assumed to be liquid at temperatures greater than 273 K. This particular model does not necessarily provide the best fit to the unresolved data, but its simplicity is attractive. It has the features that almost certainly exist in the Uranian atmosphere (an absorber depleted upper troposphere and an absorber rich lower troposphere) but does not require any of the more speculative assumptions about  $\text{NH}_3$ - $\text{H}_2\text{S}$  chemistry, solution effects, or non-adiabatic temperature profiles.

Figure 2.8 shows weighting functions for this model. The weighting function is a useful concept that indicates how much of the observed total brightness arises from a given level of the atmosphere, and therefore indicates what regions of the atmosphere a particular wavelength is sensitive to. Expressing this mathematically using the definitions and discussion of Section 2.2.1, the total brightness observed out of the top of the atmosphere is

$$T_B = \int_{-\infty}^{\infty} T(z) W(z) dz,$$

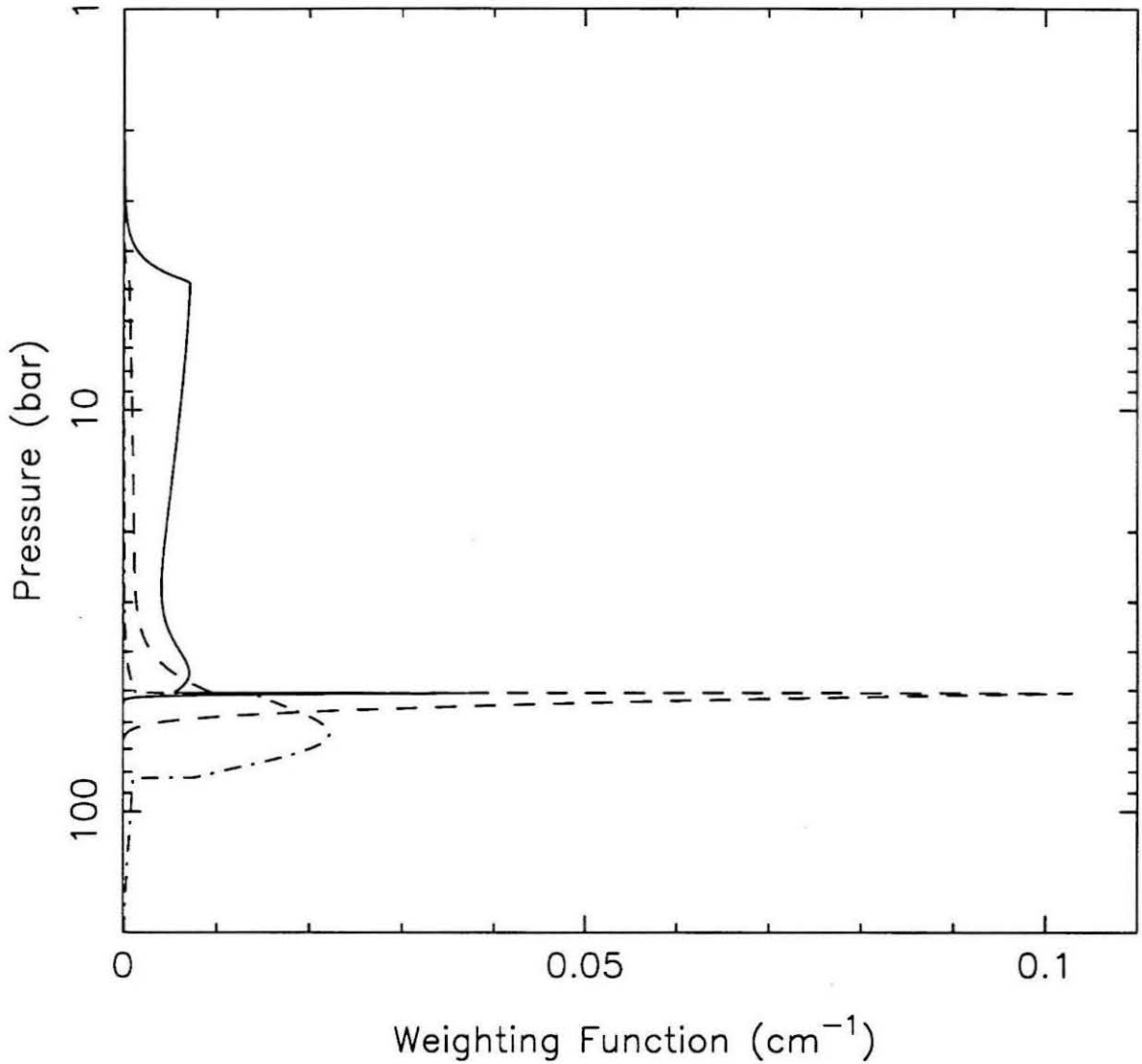


**Figure 2.8:** Weighting functions. These are 2, 6, and 20 cm weighting functions for normal incidence observations into an atmosphere described by the reference model (see text). The 2 cm observations (solid curve) are primarily sensitive to  $\text{NH}_3$  between its cloud top at 5 bars, and the 40 bar level. Between 40 and 50 bars there is a slight increase in the 2 cm weighting function due to the presence of water vapor, and at 50 bars there is a spike due to the abrupt increase in opacity associated with the liquid water cloud. This spike, however, has a negligible effect on the total brightness at 2 cm. The 6 cm weighting function (dashed curve) shows this wavelength is less sensitive to  $\text{NH}_3$  opacity than 2 cm data, and more sensitive to the presence of water. The 20 cm observations (dot-dashed curve) are dominated by the presence of the liquid water cloud.

where the weighting function, in units of  $\text{cm}^{-1}$ , is

$$W(z) = k_\nu(z) \exp \left[ - \int_z^\infty k_\nu(z') \frac{dz'}{\mu} \right].$$

The solid curve of Figure 2.8 is the 2 cm weighting function. It indicates that 2 cm observations are sensitive to a broad slice of the atmosphere between 5 and 50 bars. This is mostly due to  $\text{NH}_3$  absorption, but the small hump between 40 and 50 bars is due to water vapor, while the spike at 50 bars (which is so narrow it contributes a negligible amount to the total brightness) is due to the water cloud. The 6 cm weighting function (dashed curve) is much more sensitive to the water cloud, but it is not completely dominated by it. It has a broad shoulder at pressures less than 40 bars due to  $\text{NH}_3$  absorption, and begins to rise near 40 bars due to the presence of water vapor. 20 cm observations, however, are almost totally controlled by the water cloud in this model. This is shown by the dot-dashed curve, which rises sharply at the top of the liquid cloud at 50 bars, and drops near 80 bars, which is the base of the water cloud for this model's water mixing ratio. Figure 2.8 is calculated for a normal incidence viewing angle. Observations near the limb of the planet will, because of the longer path lengths through the atmosphere, not probe quite as deep, and will emphasize the higher altitudes slightly more. The general regional sensitivities shown, however, hold over most of the disk, and will apply to most of the models discussed in future chapters. Thus, one can generally say that short-centimeter observations of Uranus probe a broad region of the atmosphere corresponding to the absorber depleted zone of Gulkis *et al.* (1978). Observations near 6 cm are sensitive to the transition region between the upper atmosphere and the more strongly absorbing (or isothermal?) deeper atmosphere, while decimeter wavelength observations are almost totally controlled by the deep atmosphere.

The last thing to do before addressing the high-resolution observations is to show how the reference model responds to various perturbations in the way absorption coefficients are calculated and to the temperature profile. The purpose is to demonstrate the insensitivity of the results to these factors.

Section 2.2.5 described the absorption coefficients used in the radiative transfer calculations. For  $\text{NH}_3$ , the calculations use essentially a Ben Reuven (BR) line shape. While the Van Vleck-Weisskopf line shape (VVW) is inferior for use under Uranian conditions (Spilker 1990, Steffes *et al.* 1986, de Pater and Massie 1985), it can be used to provide an estimate of the uncertainty in the model results. Figure 2.9 shows the spectrum calculated using the VVW line shape exclusively, as well as the standard line shape. At centimeter wavelengths, the VVW profile has less absorption. Increasing the  $\text{NH}_3$  abundance by 60%, however, brings the VVW spectrum into agreement with the BR spectrum. This 60% abundance difference between VVW and BR line shape models also works for models of Uranus that resolve the planet and have  $\text{NH}_3$  abundances that vary with latitude. Thus we reach the important conclusion that the relative variations found in absorber abundances across the disk of Uranus are not effected by uncertainties in the  $\text{NH}_3$  line shape. The absolute value of the derived  $\text{NH}_3$  abundances, however, are uncertain by up to 60%.

To test the chosen expressions for  $\text{H}_2$  and  $\text{H}_2\text{O}$  vapor absorption, they are compared to alternate expressions in Berge and Gulkis (1976), taken from Goodman (1969). For  $\text{H}_2$  absorption, Goodman uses

$$k_{\text{H}_2} = 4.0 \times 10^{-11} P_{\text{H}_2} \left[ P_{\text{H}_2} \left( \frac{273}{T} \right)^{2.8} + 1.7 P_{\text{He}} \left( \frac{273}{T} \right)^{2.61} \right] \frac{1}{\lambda^2},$$

where  $k_{\text{H}_2}$  is in  $\text{cm}^{-1}$ , partial pressures are in atmospheres, and  $\lambda$  is the observing wavelength in cm. For  $\text{H}_2\text{O}$ , the expression is

$$k_{\text{H}_2\text{O}} = P_{\text{H}_2\text{O}} \left( \frac{273}{T} \right)^{13/3} \nu^2 \left\{ (1.45 \times 10^{-7}) \Delta\nu_1 + 9.07 \times 10^{-9} \left[ \frac{\Delta\nu_1}{(\nu/29.97 - 0.74)^2 + \Delta\nu_1^2} + \frac{\Delta\nu_1}{(\nu/29.97 + 0.74)^2 + \Delta\nu_1^2} \right] \right\},$$

where

$$\Delta\nu_1 = 9.88 \times 10^{-2} \left( \frac{273}{T} \right)^{2/3} [0.81 P_{\text{H}_2} + 0.35 P_{\text{He}}]$$

and pressures are in atmospheres,  $\nu$  is in GHz, and  $\Delta\nu_1$  and  $k_{\text{H}_2\text{O}}$  are in  $\text{cm}^{-1}$ . The results are shown in Figure 2.10. At millimeter wavelengths, the different expression for

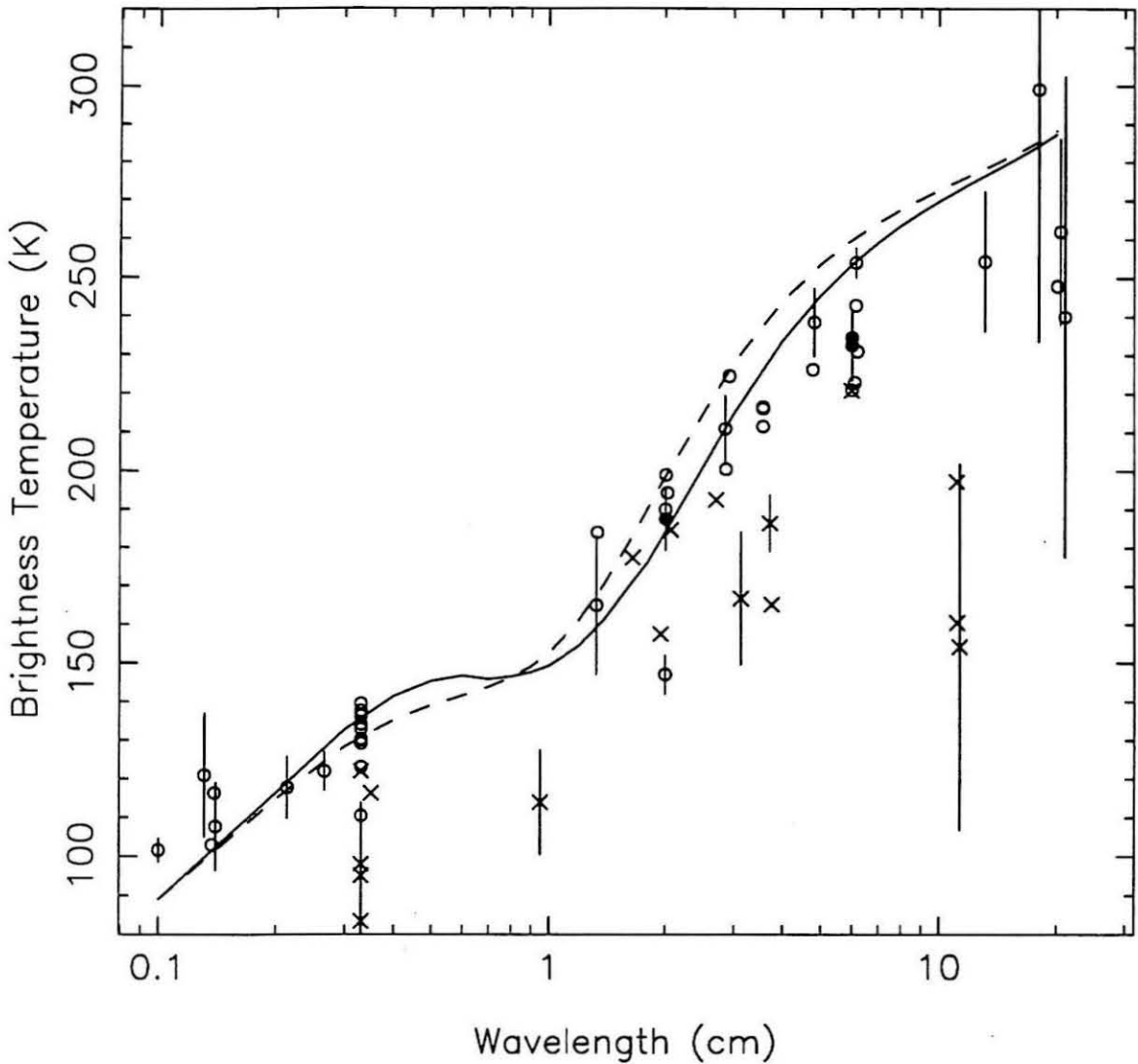


**Figure 2.9:** Uncertainties in the  $\text{NH}_3$  line shape. The solid curve is the calculated spectrum for the reference model described in the text. The dashed curve is the same model, except a Van Vleck-Weisskopf line shape is used to describe the  $\text{NH}_3$  absorption profile (see Section 2.2.5). This is an upper limit to the expected error in the calculated line shape. Increasing the  $\text{NH}_3$  abundance by 60% when using the VVW line shape brings the two curves to within 1 K of each other at all wavelengths between 1 and 20 cm.

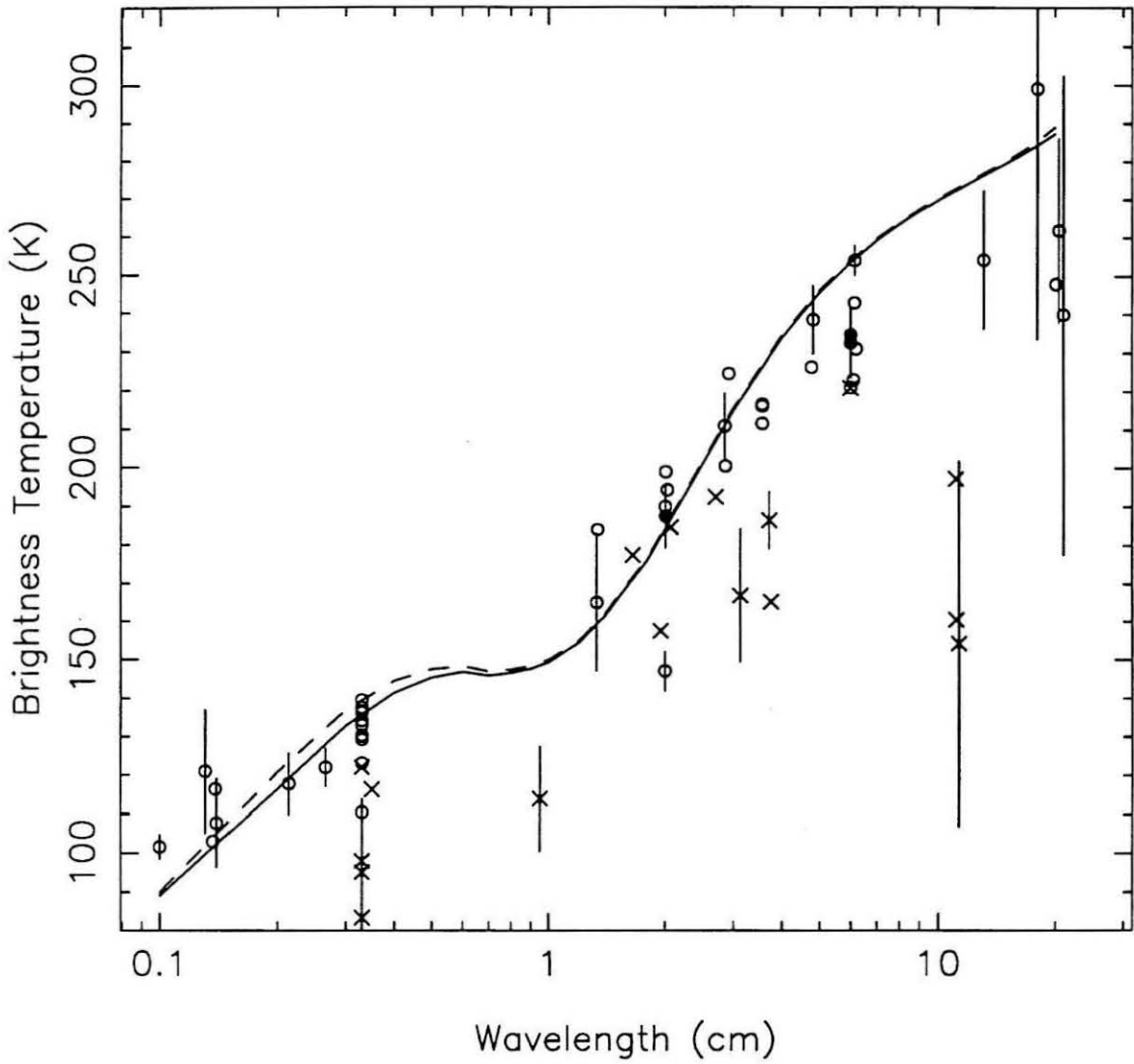


**Figure 2.10:** Uncertainties in the  $\text{H}_2$  and  $\text{H}_2\text{O}$  line shapes. The solid curve is the reference model, while the dashed curve is the same model, but using alternate expressions for  $\text{H}_2$  and  $\text{H}_2\text{O}$  vapor absorption taken from Goodman (1969) as quoted in Berge and Gulkis (1976). The differences between the curves are insignificant.

H<sub>2</sub> absorption results in brightness temperatures  $\leq 5$  K warmer, while at wavelengths near 20 cm, the different H<sub>2</sub>O absorption increases brightnesses by about 1 K. (The effect at long wavelengths is minimized because water cloud absorption screens much of the water vapor from view. Removing the water cloud from both models results in the alternate expressions yielding temperatures about 10 K warmer at 10 cm.) Since this work does not try to accurately model millimeter wavelengths, and since the error bars on the 10 cm and longer data are so large, the differences between these absorption coefficients are not very significant. It is of particular interest that calculations at 2 and 6 cm are changed by only 0.8 K when the alternate forms of the H<sub>2</sub> and H<sub>2</sub>O absorption coefficients are used.

As an additional test, the standard expressions for absorption by H<sub>2</sub> can be used, but with the *ortho* to *para* ratio constant at 3 : 1 (this is called “normal hydrogen”, and reflects the *ortho-para* ratio at temperatures above 300 K). Doing this decreases the disk averaged temperature by 5 K at 1 mm, but only by 0.2 K at 2 cm, and less at longer wavelengths. Therefore, the exact form of the H<sub>2</sub> *ortho-para* ratio is not critical when calculating absorption coefficients at centimeter and longer wavelengths.

Finally, Figure 2.11 shows the effects of altering the radio science temperature profile. As discussed in Section 2.2.3, uncertainties in the CH<sub>4</sub> abundance in the upper atmosphere create an uncertainty in the derived temperature at 2.3 bar of  $\pm 8$  K. Figure 2.11 shows the spectrum generated by the reference model using the nominal atmospheric temperature profile (solid curve), and a profile with the 2.3 bar temperature increased by 8 K (dashed curve)—which alters the adiabatic extrapolation. The dot-dashed curve is the nominal model with the 2.3 bar temperature decreased by 8 K. The longer wavelength data is least effected by shifts in the temperature profile because they are primarily sensitive to the liquid water cloud, which always (in the nominal model) begins at a temperature of 273 K. Comparing Figure 2.9 with 2.11 it can be seen that at centimeter and longer wavelengths, the uncertainty in the NH<sub>3</sub> absorption coefficient creates larger excursions

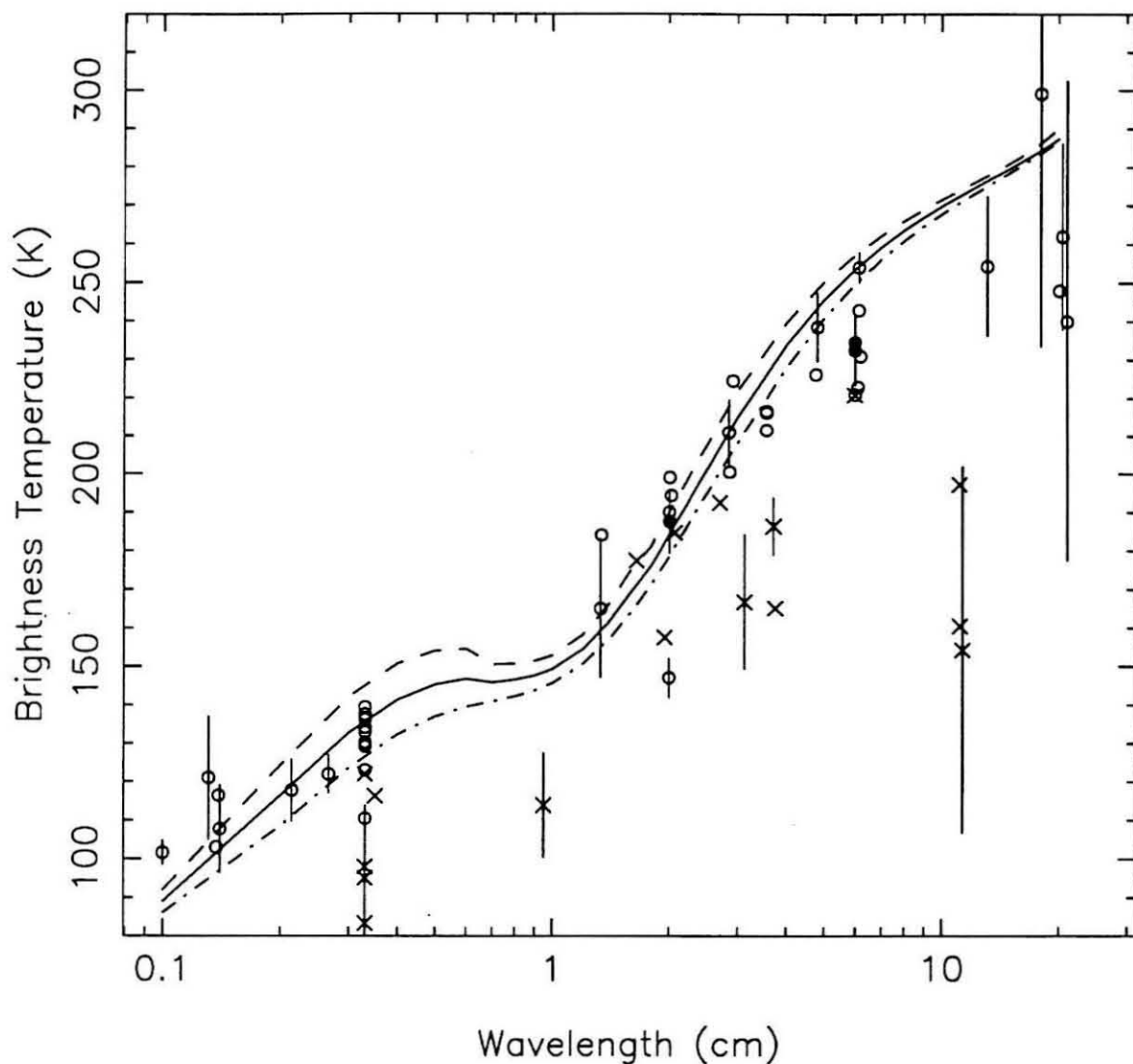


**Figure 2.11:** Uncertainties in the Voyager radio occultation temperature profile. The solid curve is the reference model, while the dashed curve is a similar model that has the Voyager occultation temperature at 2.3 bars increased 8 K from the nominal 100.9 K value. This offsets the entire temperature profile to higher temperatures at each pressure. Similarly, the dot-dashed curve uses a temperature profile that has the 2.3 bar temperature decreased by 8 K. The  $\pm 8$  K represents the uncertainty quoted by Lindal *et al.* (1987). A comparison with Figure 2.9 shows that at centimeter and longer wavelengths, the variation in brightness due to uncertainties in the  $\text{NH}_3$  line shape is greater than that due to uncertainties in the occultation temperature profile.

than the uncertainty in the temperature profile.

#### Section 2.3.4 Summary of Unresolved Observations

The important results from this initial analysis are:

- The model developed in this chapter yields results consistent with previous work.
- The upper troposphere (pressures less than 30 bars) is about 100 times less absorbing than would be expected for a near solar composition (see also Gulikis *et al.* 1978). This is very different from Jupiter or Saturn, whose spectra are well matched by near solar abundances.
- There is a region of the atmosphere where the temperature increases with depth from about 150 to 240 K. If the lapse rate is adiabatic, the pressures in this region run from about 5 to 30 bar, and the absorber mixing ratio is roughly constant (see also de Pater *et al.* 1989).
- Below this region, the atmosphere is very different. Either it is much more strongly absorbing (which is expected due to the presence of water vapor and clouds), or it becomes nearly isothermal (see de Pater and Massie 1985).

These results will be expanded upon in the high-resolution data analysis.

## Chapter 3

# High Resolution Observations

*"Invisible airwaves crackle with life,  
bright antennae bristle with the energy."  
— Rush*

The last chapter described how and why Uranus emits radio waves, and discussed disk-averaged observations of the planet. This chapter is first concerned with detecting radio emissions and turning them into maps that resolve the planet (Section 3.1). Three high resolution data sets are then presented (Section 3.2), along with some significant conclusions that can be drawn from these data with a minimal amount of analysis. The detailed analysis is left for Chapter 4. To map an object as small as Uranus (apparent size less than 4 seconds of arc) requires one of the most powerful telescopes in the world today. This instrument is the Very Large Array, or VLA. It is part of the National Radio Astronomical Observatory (NRAO), operated by Associated Universities, Inc. under contract with the National Science Foundation. Readers already familiar with the VLA and interferometers (and those not wishing to become familiar with them) can safely skip Section 3.1.

### 3.1 The VLA

#### 3.1.1 Physical Location and Layout

The VLA is located on the Plains of San Augustin, an hour's drive west of Socorro, New Mexico. This location was chosen based on the engineering requirements for a large, flat area to construct the instrument, the scientific sensitivity requirements that

called for a high altitude site isolated from man-made sources of radio interference, and the budgetary constraint of cheap land. The instrument itself consists of 27 antennas (plus one spare), each 25 meters in diameter, arranged in a 'Y' shape. There are four basic configurations for the antennas, distinguished primarily by the spacing between them. The A-array is the largest configuration, with antenna spacings (called baselines) as long as 36 km. The B, C, and D configurations are smaller, with longest baselines 12, 4, and 1.3 km, respectively. As will be seen in the next section, the longest baselines provide the highest resolution, while the shortest provide the greatest sensitivity. Hybrid array configurations are also used that consist of longer baselines in the North-South direction than in the East-West direction. This is useful for studying objects low in the sky, which is currently the case for Uranus.

### 3.1.2 Theory of Operation

The theory behind a synthesis array interferometer such as the VLA has been discussed elsewhere, two recent tutorials being Perley *et al.* (1986) and Thompson *et al.* (1986). An overview will be provided here so that the reader unfamiliar with the subject can have a basic understanding of the observing procedures and data reduction techniques to be discussed later. The notation follows that of Perley *et al.*

The basic unit of a microwave interferometer is a pair of antennas, electronically linked. The purpose of this linkage is to gain resolution. The high-resolution is achieved by essentially looking at the interference pattern generated by the antennas, which is extremely sensitive to the location of the source. Imagine two antennas, aimed at the same point in the sky. They are separated by a baseline vector,  $\mathbf{B}$ . (Vectors are denoted by bold-faced type, while the magnitude of a vector is given in normal type.) Consider for the moment monochromatic, sinusoidal radiation from the sky, which can represent one component of a Fourier decomposition of the actual source spectrum. There is a phase delay between the signals arriving at the antennas due to one antenna being closer

to the source than the other. For a point in the sky in the direction of the unit vector,  $\mathbf{s}$ , this geometric delay is

$$\tau_g = \frac{1}{c} \mathbf{B} \cdot \mathbf{s}, \quad (3.1)$$

where  $c$  is the speed of the radiation and the source is assumed to be far enough away that rays reaching the antennas are parallel. Instead of just adding the two signals to generate an interference pattern, most modern arrays use a multiplier followed by a time averaging circuit. This device, called a correlator, has less noise in the output than a straight additive correlator does. After multiplying the two sine functions from the antennas, one with a phase delay given by Equation 3.1, and then time averaging, which eliminates the high frequency terms, the correlator output is proportional to

$$F = \cos \left( 2\pi \frac{\nu}{c} \mathbf{B} \cdot \mathbf{s} \right), \quad (3.2)$$

which is a slowly varying function of time because  $\mathbf{B} \cdot \mathbf{s}$  changes as the Earth rotates. Equation 3.2 means that in the plane of the sky the instrument sensitivity is a series of stripes (called fringes) of positive and negative response separated by nulls. The fringes are perpendicular to the projection of  $\mathbf{B}$  on the sky.

In addition to the factor of Equation 3.2, the correlator output due to a solid angle  $d\Omega$  in the sky is proportional to the sky brightness, also called the intensity,  $I(\mathbf{s})$ , (measured in units of  $\text{W m}^{-2} \text{ Hz}^{-1} \text{ sr}^{-1}$ ), the effective antenna area,  $A(\mathbf{s})$ , the solid angle, and the frequency bandwidth,  $\Delta\nu$ . If we assume that  $\Delta\nu$  is small enough so that  $I(\mathbf{s})$  and  $A(\mathbf{s})$  are constant over  $\Delta\nu$ , the effects of different frequencies having different fringe patterns (as given by Equation 3.2) can be ignored. Furthermore, spatial incoherence of the radiation source can be assumed, which allows us to integrate the correlator response to a small piece of the sky over the entire sky to get the full correlator output:

$$r(\mathbf{B}, \mathbf{s}) = \Delta\nu \int A(\mathbf{s}) I(\mathbf{s}) \cos(2\pi \frac{\nu}{c} \mathbf{B} \cdot \mathbf{s}) d\Omega. \quad (3.3)$$

In practice, the antennas track a particular point in the sky, specified by the unit vector  $\mathbf{s}_0$ , and the sky brightness and antenna pattern are specified relative to this direction. Using

$\mathbf{s} = \mathbf{s}_0 + \mathbf{s}_1$ , Equation 3.3 becomes

$$\begin{aligned} \tau(\mathbf{B}, \mathbf{s}) = & \Delta\nu \cos(2\pi \frac{\nu}{c} \mathbf{B} \cdot \mathbf{s}_0) \int A(\mathbf{s}_1) I(\mathbf{s}_1) \cos(2\pi \frac{\nu}{c} \mathbf{B} \cdot \mathbf{s}_1) d\Omega \\ & - \Delta\nu \sin(2\pi \frac{\nu}{c} \mathbf{B} \cdot \mathbf{s}_0) \int A(\mathbf{s}_1) I(\mathbf{s}_1) \sin(2\pi \frac{\nu}{c} \mathbf{B} \cdot \mathbf{s}_1) d\Omega. \end{aligned} \quad (3.4)$$

What is measured is  $\tau(\mathbf{B}, \mathbf{s})$ , but what is desired is  $I(\mathbf{s}_1)$ , the sky brightness. To invert Equation 3.4 we can make use of the complex visibility, defined as

$$\mathcal{V}(\mathbf{B}, \mathbf{s}) = V e^{i\phi_V} = \int A(\mathbf{s}_1) I(\mathbf{s}_1) e^{-2\pi i \frac{\nu}{c} \mathbf{B} \cdot \mathbf{s}_1} d\Omega, \quad (3.5)$$

where  $V$  and  $\phi_V$  are the amplitude and phase of the complex visibility, and are both real.

Dividing this into real and imaginary parts, Equation 3.5 can be written as

$$V \cos \phi_V = \int A(\mathbf{s}_1) I(\mathbf{s}_1) \cos \left( 2\pi \frac{\nu}{c} \mathbf{B} \cdot \mathbf{s}_1 \right) d\Omega$$

and

$$V \sin \phi_V = - \int A(\mathbf{s}_1) I(\mathbf{s}_1) \sin \left( 2\pi \frac{\nu}{c} \mathbf{B} \cdot \mathbf{s}_1 \right) d\Omega.$$

To put some physical meaning to these components, realize that the real part of the visibility (the cosine term) is an even function, and describes the brightness distribution symmetric about  $\mathbf{s}_0$ , while the imaginary part (the sine term) describes the asymmetric components of the sky brightness. The significant thing about  $\mathcal{V}$  is that it forms a Fourier Transform Pair with  $A(\mathbf{s}_1)I(\mathbf{s}_1)$ .

Substituting the magnitude of the real and imaginary parts of Equation 3.5 into 3.4 yields

$$\tau(\mathbf{B}, \mathbf{s}) = \Delta\nu V \cos(2\pi \frac{\nu}{c} \mathbf{B} \cdot \mathbf{s}_0 - \phi_V). \quad (3.6)$$

In practice, to determine both the amplitude and phase of the visibility, two correlators are used. One correlator adds a  $90^\circ$  phase shift to one antenna's signal, giving a sine term similar to Equation 3.6. By comparing the two measurements, both  $V$  and  $\phi_V$  can be solved for. A correlator that makes these simultaneous measurements is called a complex correlator.

The standard coordinate system used to measure baselines is a  $(u, v, w)$  right-handed system with the origin at the phase reference position,  $s_0$ , and with each component measured in units of the central wavelength of the frequency bandpass.  $u$  and  $v$  are measured in the plane of the sky,  $u$  positive eastward,  $v$  positive northward, while  $w$  is measured along  $s_0$ . The sky position,  $s_1$ , is measured with direction cosines  $(l, m, n)$  referred to the  $u$ ,  $v$ , and  $w$  axis. Because the sky brightness we wish to solve for is the brightness on the “celestial sphere” a very large distance away,  $w$  and  $n$  are approximately zero near  $s_0$ . This means we need only consider two-dimensional quantities. Thus, Equation 3.5 and the associated Fourier Transform become:

$$\mathcal{V}(u, v) = \int_{-\infty}^{\infty} \int_{-\infty}^{\infty} A(l, m) I(l, m) e^{-2\pi i[ul+vm]} dl dm \quad (3.7a)$$

$$A(l, m) I(l, m) = \int_{-\infty}^{\infty} \int_{-\infty}^{\infty} \mathcal{V}(u, v) e^{2\pi i[ul+vm]} du dv. \quad (3.7b)$$

Equations 3.6 and 3.7 are the basic relationships governing interferometers. The task becomes to measure the visibility at enough  $(u, v)$  points (*i.e.*, on enough baselines) that the integral of Equation 3.7b can be performed to determine  $A(l, m)I(l, m)$ . Calibrations can then presumably be used to remove the antenna pattern,  $A$ , leaving the desired quantity, the sky brightness.

### 3.1.3 Mapping

The real world process by which the visibility data is converted to a map (called, oddly enough, mapping) is more involved than just doing the Fourier Transform of Equation 3.7b. The complications arise because not all visibilities are sampled. To account for this, a sampling function should be applied to the integrand of 3.7b which is 1.0 for measured visibilities and zero otherwise. The effect of this sampling is that the integral no longer yields the true sky brightness, but instead yields the sky brightness convolved with a function. This is a result of the convolution theorem, which states

that the Fourier Transform of the product of two functions equals the convolution of their Fourier Transforms. The convolving function, then, is just the Fourier Transform of the sampling function, and can be thought of as the effective antenna pattern of the synthesized array. It is usually called the “dirty beam,” while the resulting map of brightness is called the “dirty map.” The more complete the coverage in  $u$ - $v$  space, the more like a delta function the dirty beam will be, and hence the dirty map becomes more like the true sky brightness.

Because the dirty beam is known, there is hope for removing its effects from the dirty map and finding the true sky brightness. Note, however, that because of the incomplete  $u$ - $v$  sampling, there is a uniqueness problem. Some spatial frequencies are unsampled, and a brightness distribution having only these frequencies is undetectable. Thus, while the true sky brightness will be consistent with the data, so will be the true brightness plus an “invisible distribution.” Fortunately, with the extensive coverage provided by the 351 baselines at the VLA, and by making some assumptions about the real sky brightness, a unique solution can usually be found.

The most common way of determining the true sky brightness from a dirty map is probably the CLEAN algorithm (Hogbom 1974). This algorithm assumes that all the emission from the sky comes from a known, finite area, which restricts the possible invisible distributions. CLEAN picks the brightest point (in absolute value) on the dirty map within the specified area, and subtracts the dirty beam multiplied by the brightness of the point and a gain factor, from the dirty map centered on this point. The location of the point and the flux associated with it are recorded, and are called a clean component. The process is repeated on the modified dirty map until all points remaining on the map have a very small flux associated with them. The resulting list of clean components is a series of delta functions that presumably approximate the sky brightness. These delta functions are then smoothed with a “clean beam,” usually a Gaussian, and the residual map from the CLEANing process is added to it to get the final clean map. (The size of

the clean beam is usually chosen to be comparable to the resolution of the largest antenna spacing. In this way, the smoothing does not degrade the resolution of the instrument, while at the same time, it does not attempt to produce features so small that they are not adequately sampled by the instrument.)

Another common method to find a sky brightness from a dirty map and beam is the Maximum Entropy Method, or MEM. (An early discussion of this technique in the context of optical imaging is given by Frieden 1972. See Thompson *et al.* 1986 for further references.) This method assumes that the true sky brightness is as smooth as is consistent with the data. In other words, it chooses the invisible distribution that yields the most uniform map. As a test of the two most common inversion schemes, the 6 cm data presented in the next section were mapped using both CLEAN and MEM. The resulting maps were not significantly different.

Before turning to the actual data used in this thesis, mention should be made of the uniform cosmic background radiation, which is an invisible distribution. To see that this is the case, consider Equation 3.3 or 3.7a. If  $I$  is constant everywhere, the integral tends to zero because a sine or cosine is being integrated over essentially all space. (This assumes the primary antenna beam width, as represented by  $A$ , is much larger than the fringe spacing. This is always true because for  $A$  to be smaller than the fringe spacing, the diameter of a single antenna would have to exceed the spacing between antennas.) A more intuitive way to think of it is that an infinitely small baseline is needed to resolve an infinitely large source (this is the so-called zero-spacing problem). What this means is that the presence of the cosmic background effectively subtracts flux from the measurement of an opaque body by an interferometer. For example, an opaque object with a brightness temperature of 2.7 K would, against the 2.7 K background, not be seen, and an interferometer would measure a temperature of zero. Because of this, all the final brightnesses determined in this work have 2.7 K added to them. The situation is more complicated for non-opaque bodies, or ones that scatter the background radiation because

the interferometer responds to some of the background that is seen through the object, as well as the object's own emissions. See Grossman 1990 for a discussion of this.

### 3.1.4 Observing Procedures

When making observations, there are several factors to take into account and procedures to follow in order to maximize the data quality. In this section some of these will be discussed, namely:  $u$ - $v$  coverage, calibration, and tracking sources in the sky. The two main considerations in choosing baselines (equivalent to choosing a  $(u, v)$  point at which to measure the complex visibility) are resolution and coverage. The angular size of the smallest feature seen will be on the order of the fringe spacing. From Equation 3.2, the fringe frequency is highest (meaning highest resolution) for longer baselines. Thus, baselines must be long enough to resolve the features of interest. It is also necessary to cover enough  $(u, v)$  points that Equation 3.7b can be integrated. At the VLA this is achieved by using 27 antennas, each paired off with each of the other antennas and a complex correlator, yielding 351 separate baselines. Furthermore, when observing for several hours, the baselines change due to the Earth's rotation, increasing the sampling of  $(u, v)$  points. There will always be some points unsampled, however, and these unknown spatial frequencies mean some of the sky brightness features will be undetermined.

Calibration of both amplitude and phase is another important factor in successful observing. If one assumes that all the relatively constant effects on the received signal have been accounted for (such as antenna patterns and phase delays in electronic equipment) there remains the crucial calibration of time and position varying effects. These are primarily due to the Earth's atmosphere and primarily involving phase, though antenna gain variations as the telescopes move are significant as well. By observing a source of known brightness and position, these effects can be determined. Generally an unresolved, strong source is best for calibration, such as a quasar. A strong calibrator is desired for a high signal-to-noise ratio in a minimal amount of time, and an unresolved calibrator is

desired because its visibility function is simple: all baselines have the same amplitude and, if it is located at the phase center of the array (the aim point), all phases are zero. (To see this, consider the real and imaginary components of Equation 3.5 and realize that  $I(s_1)$  is zero for all  $s_1 \neq 0$ .) It is also important for the calibrator to be near the desired source in the sky because atmospheric effects (primarily on phase) can vary dramatically in different directions. Because many quasars are variable, it is relatively rare to find a strong, known source close to the desired object of study. To get around this problem, at least two calibrators are used. One of them, called the secondary calibrator, is chosen for having a well known position and for being as close as possible to the source to be studied. This calibrator's brightness need not be well known, but it must be constant over the observing run. The secondary calibrator will be observed repeatedly during the course of observations (typically every 20 minutes for the data at 6 cm). Once during the observing run an amplitude, or primary calibrator will be observed. The primary calibrator must have a well determined flux, but need not be especially close to the target. It is used to determine the flux of the secondary calibrator. To do this, both calibrators are observed when they are at the same elevation angle. (This is done so the total path length through the atmosphere is the same in both observations.) Once the flux of the secondary calibrator is known, it can be used to adjust both the amplitude and phase of source observations. For all the high resolution data discussed here, 3C286 is used as the primary calibrator. It is the primary flux reference for the VLA and is known to about 3%. 3C286 is not a point source, however, and the longest baselines of 6 cm observations can partially resolve it. For this reason, these baselines are not used when determining the secondary calibrator's flux. (Every antenna can still be calibrated on the secondary calibrator, however, as long as it is a point source.)

While on the subject of calibration, mention should be made of a potentially powerful technique called self-calibration. The technique uses the observed source itself as a calibrator. This has the advantage of allowing effects that change on short time or spatial

scales, such as weather, to be measured at the precise time and location of the observation. It works by assuming the basic sky brightness pattern is already known (usually a CLEAN map or, for a planet, a flat disk is a good start), and adjusting the phases to bring the observations as close to this known pattern as possible. For self-calibration to work, however, the signal to noise ratio must be high enough that single baselines over short time scales have enough of a signal to calibrate. Self-cal will not be discussed further because in the maps to be presented shortly, its application did not alter the results. This is partially due to very stable weather, which allowed standard calibration techniques to be effective, as well as a relatively low signal to noise ratio.

In the two most important data sets analyzed in the next chapter (Berge *et al.* 1988 and Hofstadter *et al.* 1990) the method used to track both Uranus and the calibrators is slightly non-standard, and deserves mention. At the VLA, the default assumption is that objects in the sky are fixed in their positions on the celestial sphere. While this is a valid assumption for the calibrators used, planets move relatively rapidly, and the VLA has a “proper motion” routine to handle this. To make sure the antennas are pointed at the planet and the calibrators in a consistent fashion, Berge *et al.* (1988) point out that even the fixed sources can be handled as if they were moving, with updates applied to their positions. This procedure was used by Berge *et al.* when making 2 cm observations in 1985, and by Hofstadter *et al.* (1990) when taking 6 cm data in 1989. For these observations, the positions of all targets at hourly intervals in geocentric right ascension and declination of date were kindly provided by E. M. Standish of the Jet Propulsion Laboratory, using the JPL DE-200 ephemeris.

## **3.2 The Data**

### **3.2.1 Summary of Observations**

There are three high resolution VLA data sets that will be used in our study of Uranus. They consist of 6 cm observations made in March of 1981 and January of

1989 (reported in Jaffe *et al.* 1984 and Hofstadter *et al.* 1990, respectively), and 2 cm observations made in April of 1985 (reported in Berge *et al.* 1988). The observations are summarized in Table 3.1. The map resolution column refers to the full-width-at-half-maximum (FWHM) of the circularly symmetric, Gaussian CLEAN beam used to map the data (see Section 3.1.3). These three data sets are used because each is believed to be well calibrated, each was taken under favorable weather conditions, and because the complete visibility data set of each is available (the 1989 6 cm observations were, in fact, undertaken specifically for this thesis). These data also have the advantage of covering the maximum possible time span: the 1981 observations, made when the VLA was first completed, are one of the first data sets to fully resolve Uranus, and the 1989 data are the most recent. The 1985 2 cm observations are conveniently located midway between the two 6 cm observing dates.

**Table 3.1**  
High Resolution Observations

Date	Wavelength (cm)	Array	Sub-Earth Latitude <sup>1</sup> (degrees)	Uranus Diameter (arcsec)	Map Resolution (arcsec)
7 March 1981	6	A	-71.1	3.81	0.5
30 April 1985	2	B	-82.5	3.87	0.5
17 January 1989	6	BnA <sup>2</sup>	-72.8	3.49	0.4

<sup>1</sup>Planetocentric

<sup>2</sup>This designates the A-B hybrid.

Each observing run consists of approximately 8 hours of observations. For other details about the observing, see Jaffe *et al.* (1984), Berge *et al.* (1988), and Hofstadter *et al.* (1990). The three visibility data sets are mapped using the CLEAN algorithm (Section 3.1.4). Both 6 cm data sets were also mapped with MEM, but this did not

significantly alter the maps, nor did self-calibration of the 1985 and 1989 data. The CLEAN maps are presented in Figure 3.1. The peak brightness in the 1981 6 cm map is 296.9 K, while that in the 1989 6 cm map is 292.3 K. The 2 cm peak brightness is 226.5 K. The contour increment in each map is 10% of the peak flux. (All brightnesses have 2.7 K added to them to account for the cosmic microwave background, as discussed in Section 3.1.3.) In the 1989 data, Uranus appears slightly smaller because the planet was further away and because the data has higher resolution, resulting in less smearing of the image.

To calculate the disk averaged brightness temperatures from the 6 cm data sets, it is assumed that the total flux found in the clean components of the CLEAN map is the total flux from Uranus. This total flux is then normalized to the apparent surface area to yield an average brightness. Assuming a radius of 25,559 km (the equatorial radius at 1 bar as determined by Lindal *et al.* 1987), the average brightness is  $234.6 \pm 6$  K in 1981 and  $232.6 \pm 5$  K in 1989, where the error bars do not include absolute calibration errors, which are probably less than 3%. (Since the radio data probe deeper than 1 bar, the assumed radius is not quite correct, but this results in an underestimate of the average brightness of less than 2%. The radius assumed for this calculation has no effect on the rest of the analysis.) The total flux is also estimated by fitting a uniform disk of unknown brightness directly to the visibility data (the appearance of a uniform disk in  $u$ - $v$  space is a Bessel Function). This method is less accurate, however, because Uranus appears strongly limb darkened and its brightness is asymmetric, so the uniform disk is a poor model. Using various values for the size and location of the disk that is fit to the data yields brightness values that bracket the CLEAN value. The maximum discrepancy between the two methods is used as an estimate of the error. The disk averaged brightness of the 2 cm data is  $185 \pm 8$  K, which is determined by Berge *et al.* (1988) from fitting of a limb darkened disk to the visibility data.

To study latitudinal structures on Uranus, it is necessary to locate the center of the

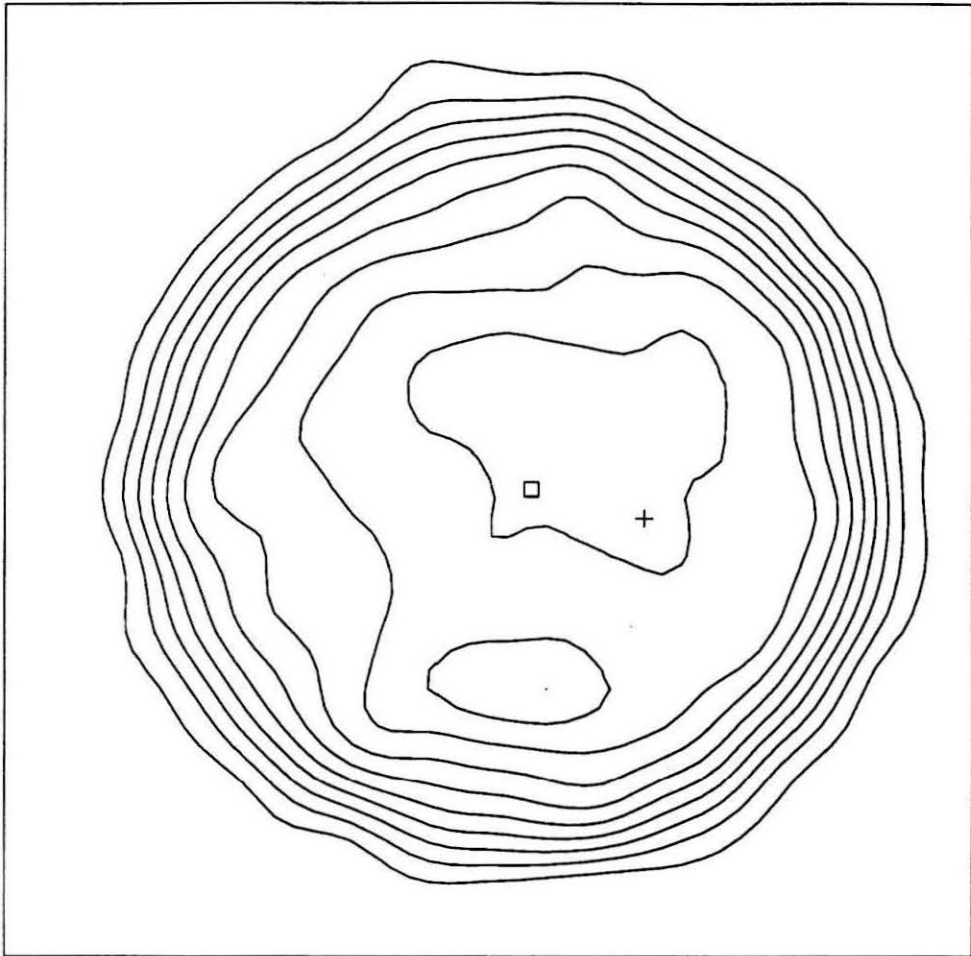


**Figure 3.1a:** Uranus as seen at 6 cm in 1981. The peak brightness is 296.9 K, and the contour interval is 10% of this value. The disk averaged brightness is  $234.6 \pm 6$  K. The square and cross mark the disk center and the South Pole, respectively. The box around the image is 5 arcsec on a side, and north is towards the top of the page. Note that the center of symmetry is not at the disk center, but is shifted towards the pole. The map is made from 8 hours of observations, so any longitudinal features are smeared by the planet's rotation.

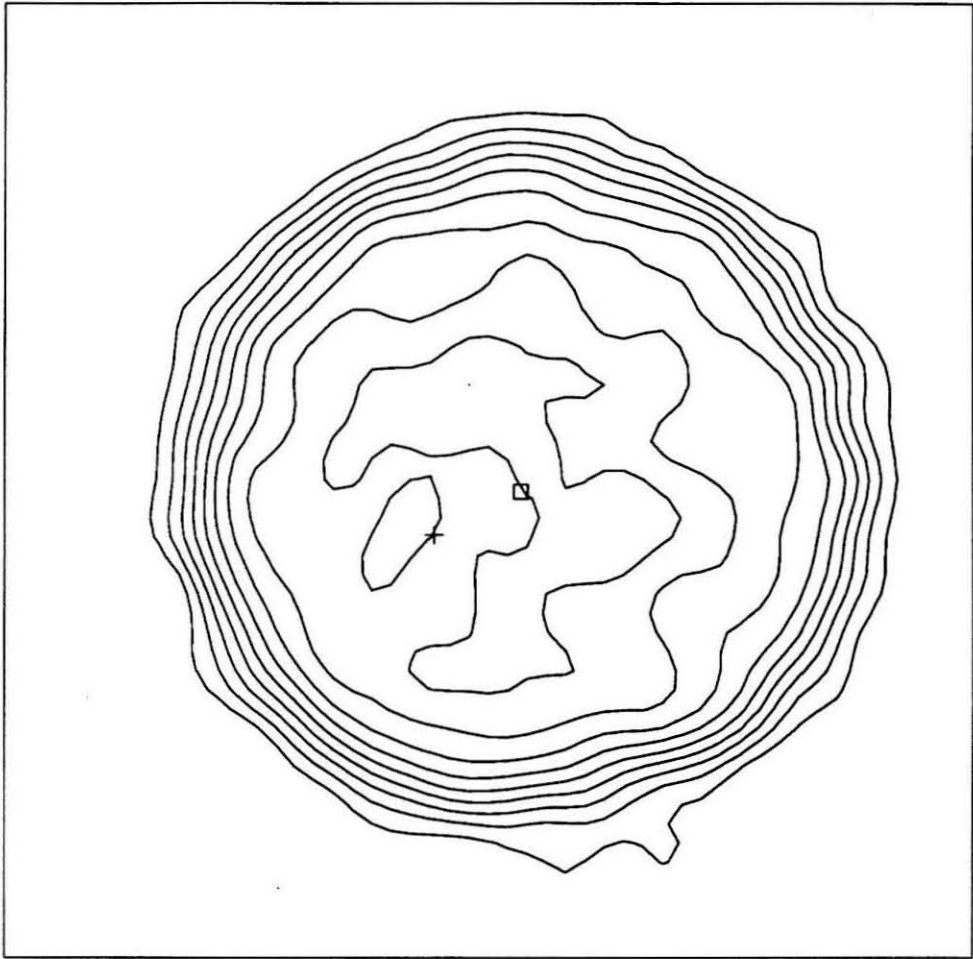


**Figure 3.1b:** The 1989 appearance of Uranus at 6 cm. The map orientation and size is the same as in 3.1a. The peak brightness in this map is 292.3 K, and the contour interval is 10% of this value. The disk averaged brightness is  $232.6 \pm 5$  K. As before, the square and cross mark the disk center and the South Pole, respectively. In the 8 years between the 6 cm observations, the South Pole has appeared to move across the planet, and the center of brightness has moved with it.

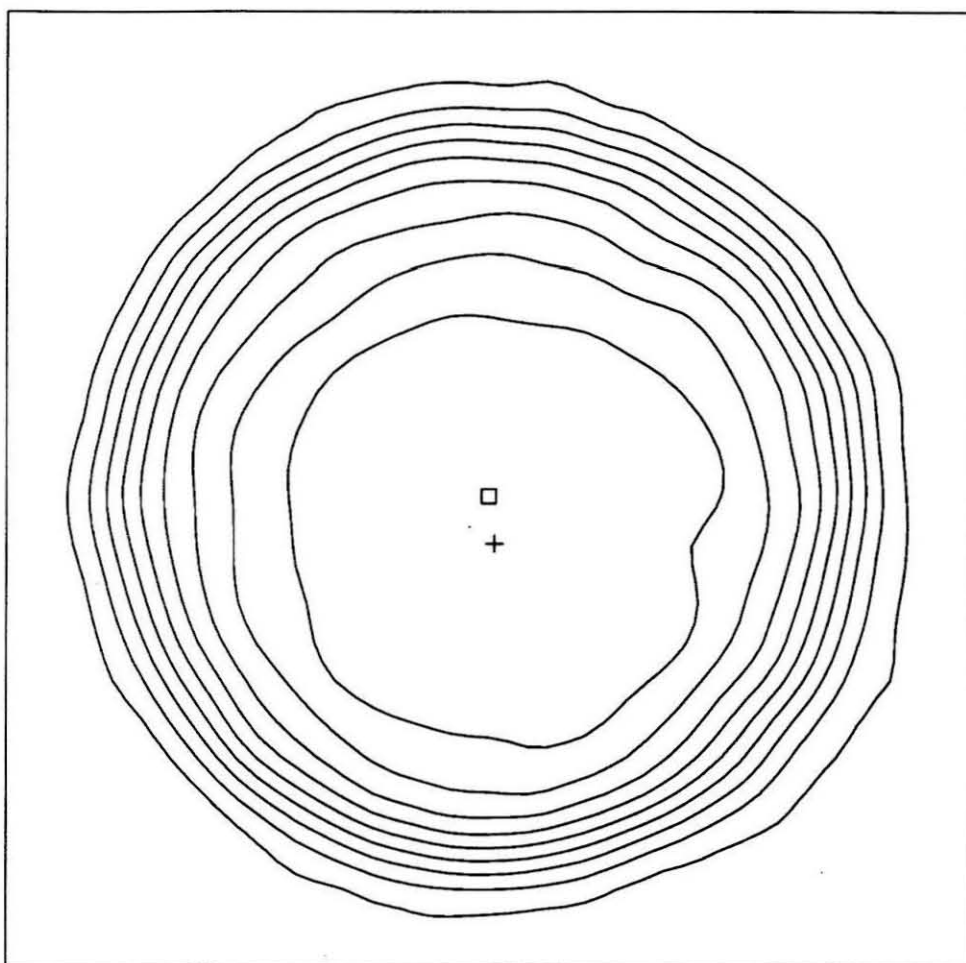


**Figure 3.1c:** This is the 2 cm appearance of Uranus in 1985, when the South Pole (marked by a cross) was very close to the disk center (marked by a square). The map orientation and size are the same as in the previous two figures. The peak brightness at 2 cm is 226.5 K, and the disk averaged temperature is  $185 \pm 8$  K. As before, the contour increment is 10% of the peak flux. While the effect is subtle, there is still a definite asymmetry to the appearance, with the center of brightness shifted towards the pole.

observed disk and the pole of the planet on the map. (It is not the absolute coordinates in the sky that are needed, but just the pixel location on the map.) The disk center of each 6 cm map is found by fitting a uniform disk of known brightness to the data (again, using a Bessel Function to fit directly to the visibility data). In this case, a uniform disk is a reasonably good model to use because the centroid is determined by the overall shape of the planet (the outer contours), which is circular, and not by details of the brightness distribution within that shape. Nonetheless, elliptical models, as well as circular models with various sizes and fluxes were also fit to the visibility data, from which the error in locating the disk center is estimated to be about 0.04 arcsec. The disk center in the 2 cm map is taken directly from Berge *et al.* (1988), who carefully used both uniform disk and limb darkened disk models as well as direct measurements of brightness contours on the CLEAN map of the planet to determine a location to within 0.03 arcsec. The location of the disk center relative to the center of the maps (the aim point of the array) is  $-0.32$  arcsec eastward and  $+0.05$  arcsec northward in the 1981 map,  $-0.40$  arcsec eastward and  $-0.04$  arcsec northward in the 1985 map, and  $-0.37$  arcsec eastward and  $-0.06$  arcsec northward in the 1989 map.

The location of the South Pole is also shown in each map of Figure 3.1. For the 1981 and 1985 data, the pole positions, relative to the disk centers, were taken from expressions in the Astronomical Almanac of the appropriate year. In 1981, the position of the South Pole, relative to the disk center, is  $-0.63$  arcsec eastward and  $-0.12$  arcsec northward, and in 1985 the position is  $-0.03$  arcsec eastward and  $-0.25$  arcsec northward. In the 1989 map, the apparent offset of the pole was kindly provided by P. Nicholson (personal communication) using some of the latest Voyager information available on the orientation of Uranus. The offsets of the South Pole from the disk center for these observations are 0.45 arcsec to the east and  $-0.23$  arcsec to the north.

Looking at the maps of Figure 3.1, the motion of the South Pole from west to east is clear. The 1985 observations correspond to the southern solstice, and the 1981 and

1989 data are equally spaced around it, so the sub-Earth latitudes are almost identical (Table 3.1). If the planet was horizontally uniform (no variations on surfaces of constant pressure), the disk center would be the brightest point and the center of symmetry. All maps, however, show that the center of brightness is shifted toward the pole. To study these maps further, the reference model of Section 2.3.3 is now called upon.

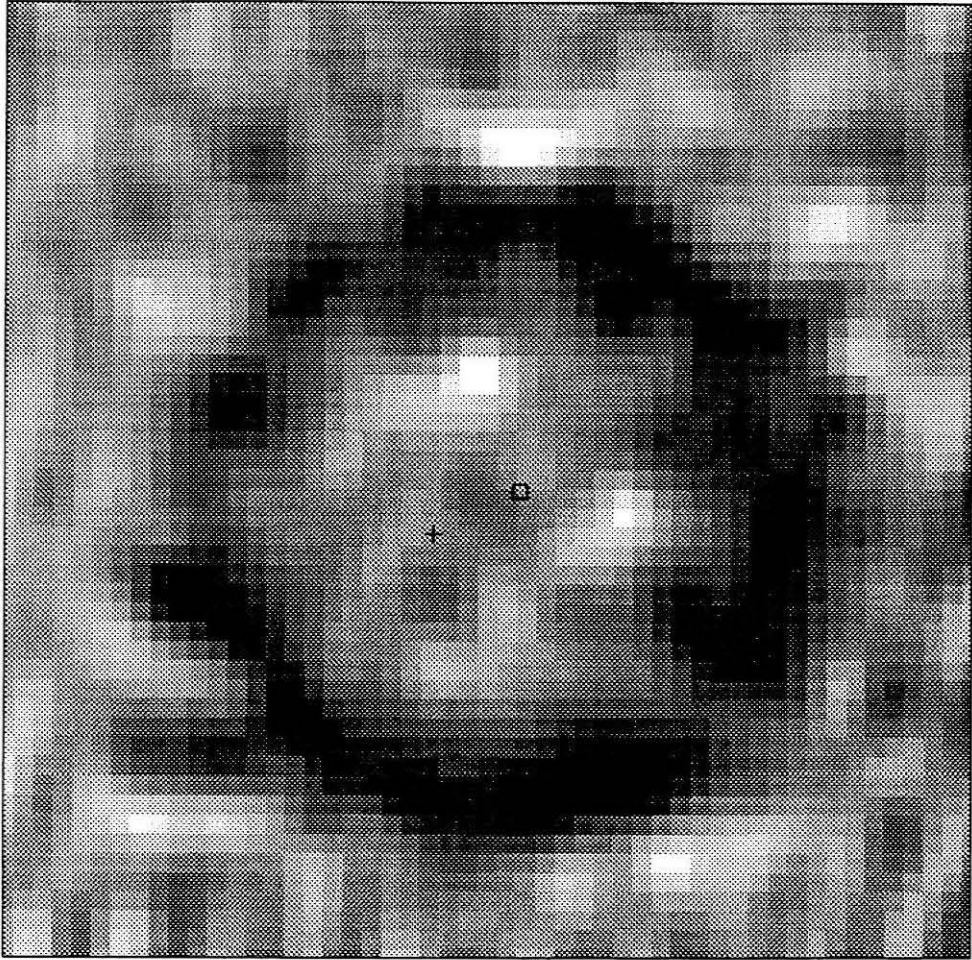
### 3.2.2 Intrinsic Brightness Structures

In Figure 3.1, three high resolution radio maps of Uranus are presented. Because they are made at different wavelengths and under differing viewing geometries, they cannot be directly compared. To see the intrinsic structure in the maps, limb darkening must be removed, and to compare the maps, each must be put in the same reference frame. (Limb darkening results from observations near the limb of the planet having a greater path length through the atmosphere, resulting in more absorption along the path between any pressure level and the telescope. This means that even in a perfectly uniform planet, observations near the limb will not probe as deeply as near the disk center. When sensing the troposphere, where temperature decreases with altitude, this makes the limb appear darker. Observations probing the stratosphere can be limb brightened.) Limb darkening effects can be estimated with the reference model of Section 2.3.3. This horizontally uniform model, which fits disk averaged data, is used to make maps at 2 and 6 cm with the same orientation as the data maps, and each is smoothed with a Gaussian identical to the “clean beam” of the map it imitates. If the model is then subtracted pixel by pixel from the data, any significant horizontal variations in the residuals are due to horizontal variations in the intrinsic brightness of the data—where intrinsic brightness means the brightness as determined by composition and temperature, not observing geometry. A constant offset of the data from the model would be an indication of data which have a uniform intrinsic brightness that is different from the reference model’s. (While it can be argued that errors in the reference model’s limb darkening or vertical structure will

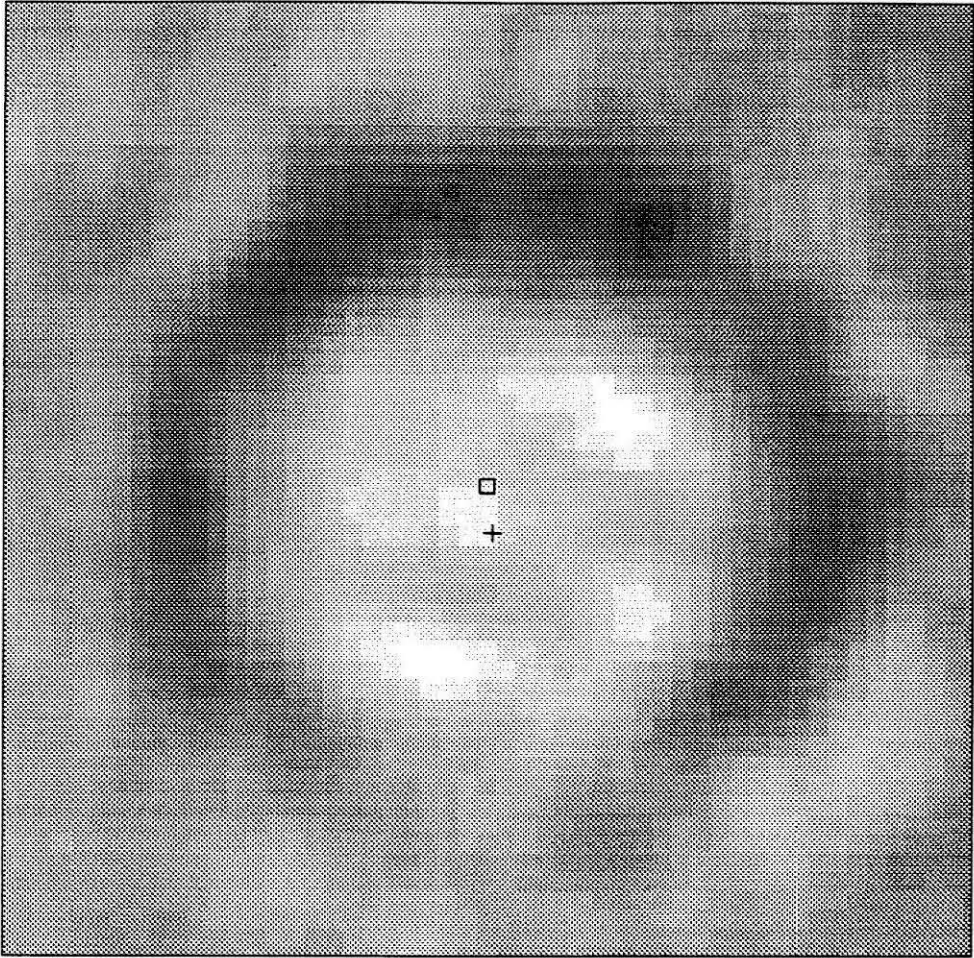
create false structures, the features found in the difference maps turn out to be too large in magnitude and too asymmetric to be accounted for by such errors.)

Figure 3.2a shows the resulting map when the reference model is subtracted from the 1989 6 cm data. Figure 3.2b does the same for the 1985 2 cm data. These gray scale maps indicate that at both wavelengths the region around the South Pole is brighter than average, while there appears to be a region closer to the equator that is unusually dim. To better understand these maps, a zonal average is taken. This has two desirable effects. The first is that by plotting intrinsic brightness as a function of latitude, all three data sets can be compared. The second desirable effect is that the zonal averaging reduces the noise level. Taking the zonal average assumes that the structures we are interested in seeing are symmetric about the axis of rotation, or close to it. We are justified in doing this for several reasons. One is that the optical features on all the major planets, including Uranus, are organized zonally. Another reason is that the dominant organizers of planetary atmospheres are the heat inputs (which need not be zonally symmetric) and the planetary rotation: since the heat inputs to the Uranian atmosphere are small, the (zonally symmetric) rotation becomes relatively more important. A final reason to assume axial symmetry is that the synthetic aperture radio maps used are made from about 8 hours of observations to maximize resolution and sensitivity, and the planet's own rotation period of about 17 hours smears all features zonally during this time.

The results of the subtraction and averaging are shown in Figure 3.3. (For later reference, a Voyager IRIS temperature profile is also shown.) This figure first appeared in Hofstadter *et al.* (1990). Since effects that are due to limb darkening and the differing observing dates are now removed, each curve shows the latitudinal structure of a data set. The solid curve is the newest 6 cm data set, while the dashed curve is the 1981 6 cm data. The dot-dashed curve is from the 2 cm observations. Each data set is averaged into latitude bins  $5^\circ$  wide. This is smaller than the beam size (which covers about  $15^\circ$  of latitude near the disk center) so as not to degrade the resolution. This means each



**Figure 3.2a:** Gray scale plot of the 1989, 6 cm data map, with the reference model subtracted from it (see text). Map orientation and scale are the same as in Figure 3.1b and, as before, the square marks the disk center and the cross the South Pole. The gray scale runs from -65 K (black) to 25 K (white). (The difference map carries values from -85 to 36 K, but this full range is not used so that Figure 3.2b can be plotted with the same scale.) The obvious feature is the dark band circling the planet. Note that it is not symmetric about the disk center.



**Figure 3.2b:** Gray scale plot of the 1985, 2 cm data map, with the reference model subtracted from it (see text). Map orientation and scale are the same as in Figure 3.1c. The square marks the disk center and the cross the South Pole. Map values vary between -24 and 27 K, but the gray scale runs from -65 K (black) to 25 K (white) so this figure can be compared directly to Figure 3.2a. The important features of this map are that the South Polar region is generally the brightest, and lower latitudes are the darkest. As in Figure 3.2a, the dark region is not symmetric about the disk center.

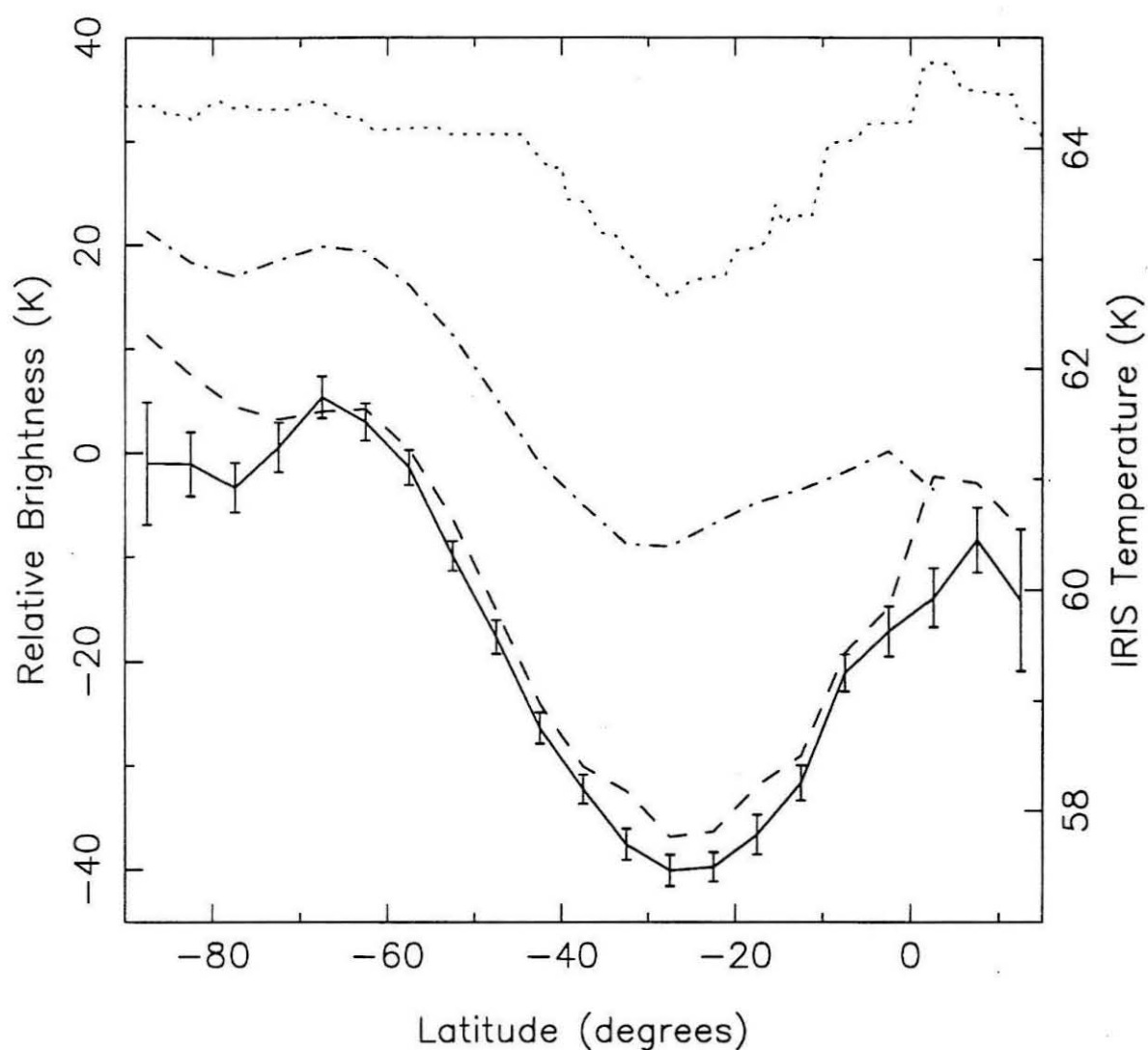


**Figure 3.3:** The intrinsic radio brightness of Uranus as a function of latitude, and upper atmospheric temperatures. The solid curve is the 1989 6 cm data and the dashed is the 1981 6 cm data. The dot-dashed curve is from the 1985 observations at 2 cm. Error bars are shown on the new 1989 data. The errors associated with the older 6 cm data are much larger, between  $\pm 5$  and  $\pm 10$  K. The 2 cm data have error bars slightly smaller than those shown. The dotted curve is the kinetic temperature near the 1 bar level as inferred from Voyager IRIS data by Hanel *et al.* (1986). Flasar *et al.* (1987) use additional IRIS data to find similar structures near the 100 mbar level.

data point in the zonal average is not an independent measurement, but is affected by the brightness of the neighboring latitudinal bins. (Averaging was also done in  $10^\circ$  bins with no significant change to the results.)

The error bars on the 1989 data are shown, and range from  $\pm 1$  to  $\pm 7$  K. The 2 cm error bars are smaller, ranging between  $\pm 1$  and  $\pm 2$  K (Hofstadter and Muhleman 1989), while the 1981 error bars are significantly larger, ranging from  $\pm 5$  K at equatorial and mid-latitudes, to  $\pm 10$  K near the pole. These error bars are determined from the background noise level of each data map, as described in Hofstadter and Muhleman (1989). The procedure is to pick 100 random points on the map far away from the planet, and take zonal averages as if each point were the disk center. The RMS value of the 100 temperatures for each latitude bin is used as the noise estimate for that bin. These error bars represent relative errors (errors on the shape of the curve). One source of error not accounted for in these estimates is the uncertainty in locating the disk center of Uranus in a map. Shifting the disk center by 0.04 arcsec (the estimated uncertainty in the location on the 6 cm maps) can change calculated brightnesses northward of  $-10^\circ$  latitude. The maximum uncertainty is about 20 K at  $+10^\circ$ . Errors associated with uncertainties in the pole position relative to the disk center are small enough to be ignored. Thus, points near the limb of the planet (latitudes northward of about  $-10^\circ$ ), must be considered uncertain by 10 to 20 K. Furthermore, errors in the absolute calibration may shift any curve up or down about 6 K, but will not alter its shape.

The unambiguous feature in Figure 3.3 is the deep depression of the curves between the equator and  $-45^\circ$  latitude. While the minimum is shifted slightly poleward in the 2 cm data, this may be due to noise. There is also some evidence for a warmer "collar" around the South Pole at a latitude of about  $-65^\circ$  as first reported in Jaffe *et al.* (1984). The amplitude of this feature is near the noise level, but since it occurs in all three data sets, it may be real. A very important feature of Figure 3.3 is the excellent agreement between the two 6 cm data sets (keeping in mind that the 1981 error bars are generally more than

twice those on the 1989 data). While there is a definite vertical offset between the curves, its magnitude is within the  $\sim 6$  K absolute calibration uncertainty of any one curve. Note that the shape of each curve is identical given the error bars shown. Because these two curves represent data taken 8 years apart and under different geometries, their agreement is a validation of the calibration, mapping, and limb darkening removal procedures.

The Voyager IRIS data is included in Figure 3.3 (dotted curve) because it has latitudinal structure very similar to that seen in the radio data. The curve shown, taken from Hanel *et al.* (1986) and Flasar *et al.* (1987), shows the kinetic temperature inferred for the atmosphere from IRIS data at  $325\text{ cm}^{-1}$ , which probes the atmosphere between about 0.5 and 1 bar. An IRIS data set that probes the atmosphere much higher, from 60 to 200 mbar, shows identical structure, with temperature variations larger by about a factor of 3 (Flasar *et al.*). Thus, a different instrument, sensitive to different physical properties of the atmosphere, sees structures correlated with the radio data. The implications of this will be discussed below and in Chapter 4. It should be noted that the radio data of Figure 3.3 show a much broader depression than the IRIS data only because the radio resolution is poorer.

There are several significant conclusions that can be drawn from Figure 3.3. They are:

- The deep atmosphere is less bright than the upper atmosphere, relative to the reference model. This is shown by the offset between the 2 and 6 cm curves, and the fact that the 6 cm data is probing deeper than the 2 cm data (see the weighting functions of Figure 2.8). This property of the atmosphere was already recognized in disk averaged data, discussed in Chapter 2.
- The pole is brighter than mid-latitudes over a wide altitude range, and the contrast increases with depth. This is indicated by the 6 cm data having a larger brightness dip than the 2 cm data.
- The same mechanism is acting, or several mechanisms are strongly coupled, over

a wide altitude range to create the latitudinal structure. The similarity of the shapes of the radio and IRIS curves indicates they are being influenced by the same process. The 6 cm data, however, is sensing as deep as about 50 bar, while the 2 cm is sensing as high as 5 bar and the IRIS data is probing higher still, up to 100 mbar.

- The brightness structure has not changed appreciably between 1981 and 1989. The agreement between the 1981 and 1989 6 cm data, as well as the fact that the shape of the 1985 2 cm data is quite similar, indicates no significant changes have occurred.

The robustness of the above conclusions must be emphasized. They are independent of most assumptions about the atmospheric structure or composition. The only point where such assumptions enter is in the use of the reference model to remove limb darkening—but none of the models discussed in Chapter 2, if used as a reference, would change the above conclusions. The data clearly show features that a horizontally uniform model cannot create. In Chapter 4 these conclusions will be expanded upon.

Before doing this, other high resolution observations found in the literature should be compared to the ones presented here. Most maps made at centimeter wavelengths have shown that the brightness of the planet is not symmetric about the disk center (Gulkis and de Pater 1984, de Pater and Gulkis 1988), in agreement with what was found here. The observations of Briggs and Andrew (1980) deserve special mention. They used the partially completed VLA to get visibility data on Uranus. While the data are insufficient to map the planet (only 9 essentially co-linear antennas were available), a careful analysis of the visibilities indicates a pole to equator brightness gradient of  $55 \pm 20$  K existed at a wavelength of 6 cm. While they do not explicitly attempt to remove limb darkening from the data, the geometry of their observations essentially does this for them. Because the sub-Earth latitude was near  $-45^\circ$ , both pole and equator were roughly equa-distant from the limb, and therefore had comparable limb darkening. The 55 K gradient is then,

to first order, an intrinsic one. This is in very good agreement with the total variation of about 40 K in the 6 cm data of Figure 3.3.

De Pater *et al.* (1989) also attempted to estimate intrinsic brightness variations on the planet. Using 2 and 6 cm observations made between 1982 and 1984, they found horizontal variations of about 60 K at 6 cm and 80 K at 2 cm. They also reported that the brightness distribution was changing on time scales of less than a year, and perhaps as short as a few weeks. It is difficult to judge the significance of the variations they report, however, because no description of how models were fit to the data is given, nor is there any estimate of errors. Also, while their 6 cm models were symmetric about the South Pole, de Pater *et al.* were unable to explain their 2 cm data in this way. Instead, they chose the 2 cm center of symmetry to be at roughly  $-80^\circ$  latitude in 1982, and at  $-87^\circ$  in 1984, but in both cases to be moving in longitude during the course of the observations (3 to 4 hours) so as to always be on the line between the sub-Earth point and the South Pole. No attempt is made to explain or justify this physically. The fact that the data presented in the current work have higher resolution and sensitivity than those of de Pater *et al.* (by virtue of longer observing runs and careful calibration), and the fact that the data sets presented here are consistent with each other, suggests the current analysis should be favored.



## Chapter 4

# Data Analysis

*"It ain't science but it works for me."*  
— .38 Special

This chapter will use the radiative model developed in Chapter 2 to explain the features seen in the high resolution radio data. The first section discusses the compositional and temperature variations needed to fit the observations. Arguments are presented for compositional effects being the dominant factor, and (in Section 4.1.2) a model that specifies the composition and circulation of the observed atmosphere is presented as the most likely interpretation of available data. The second section uses a simple dynamical model to prove the plausibility of the inferred circulation pattern, and to suggest that water condensation has an important role in controlling the depth of this circulation. The final section discusses the time variability of Uranus' radio brightness. While the high resolution data show no significant variability over the last 10 years, seasonal variations are expected on longer time scales.

## 4.1 Generating Observed Features

### 4.1.1 Absorber Gradients

As discussed in the previous chapter, the data call for both horizontal and vertical gradients in the atmospheric properties that control the radio brightness (Figure 3.3). This means there are variations in either the absorber abundance or the kinetic temperature, or both. In this section, it is assumed that composition is the only latitudinally varying

parameter and that the vertical temperature gradient is given by the pseudo-adiabat used in the standard temperature profile (Figure 2.1). As done before with disk-averaged observations, the high-resolution data will first be fit by explicitly setting the  $\text{NH}_3$  mixing ratio as a function of latitude and height, with no  $\text{H}_2\text{O}$  or  $\text{H}_2\text{S}$  in the atmosphere. This allows a determination of the absorber distribution without making assumptions about chemical or cloud processes, or even what the absorbing species is. (It can be argued that the actual absorber may have a drastically different wavelength dependence than  $\text{NH}_3$  does, and these results are then not truly general. A counter-argument, however, is that at the relatively high pressures dealt with here [5 to 100 bar], pressure broadening drives all absorbers towards having a constant strength over wide wavelength ranges. In either case, since  $\text{NH}_3$  is likely to be the primary opacity source [Section 2.2.5], the approach seems reasonable.) Once the required distribution is determined, we will explore details of how the  $\text{NH}_3$ ,  $\text{H}_2\text{S}$ , and  $\text{H}_2\text{O}$  abundances, as adjusted by chemical interactions and condensation, can create this distribution.

As a starting point, we can estimate the absorber distribution in the “upper” atmosphere, where upper is defined as the region to which the 2 cm data is sensitive. (This analysis is very similar to one carried out in Hofstadter and Muhleman 1987, 1989.) Figure 4.1 shows the zonal averaged temperatures of the 2 cm data (discussed in Section 3.2.2) and two models. The dashed curve is the reference model, whose spectrum was shown in Figure 2.6. (The reference model has an  $\text{NH}_3$  molar mixing ratio of  $8.0 \times 10^{-7}$ , an  $\text{H}_2\text{O}$  ratio of  $1.0 \times 10^{-3}$ , and accounts for absorption in a water cloud.) It is no surprise at this point to find that the polar regions in the model need to be made warmer (brighter), while lower latitudes need to be cooler. It turns out that using a lower absorber abundance poleward of  $-45^\circ$  latitude and a slightly higher abundance at all other latitudes provides a much better fit to the data, as shown by the solid curve of Figure 4.1. This curve is a model that has no  $\text{H}_2\text{O}$ , and uses an  $\text{NH}_3$  mixing ratio of  $7.0 \times 10^{-7}$  over the South Pole, and  $1.2 \times 10^{-6}$  elsewhere. It is particularly interesting to note that in the region

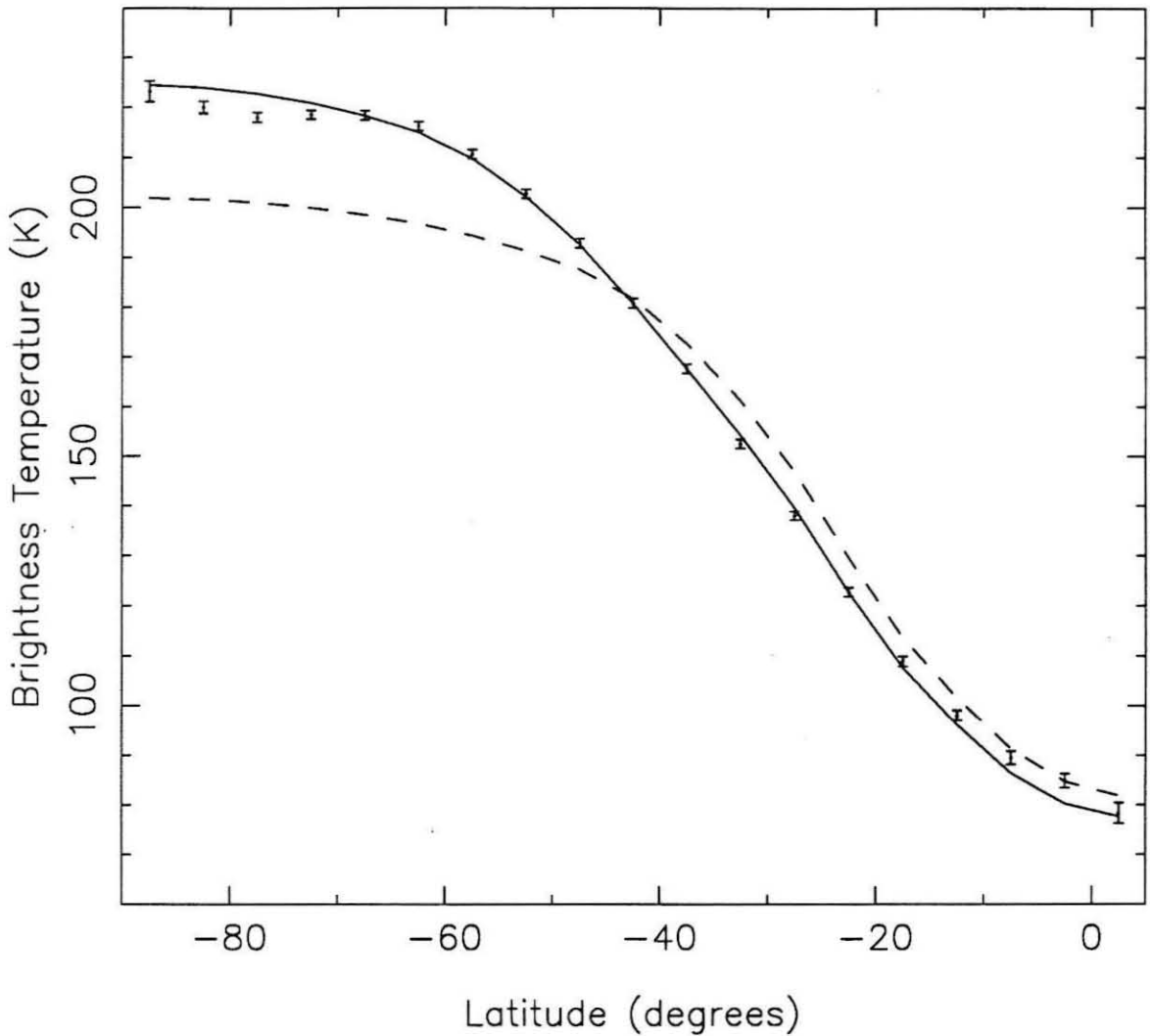


**Figure 4.1:** Zonal averaged brightness at 2 cm. The data points (with error bars) are the 1985 2 cm observations from Chapter 3. The dashed line is the reference model, presented in Section 2.3.3, which provides a good fit to unresolved observations, but not the high-resolution ones presented here. The solid curve is a model demonstrating that a simple, bi-modal absorber distribution provides a much better fit. It has an  $\text{NH}_3$  mixing ratio of  $7.0 \times 10^{-7}$  from  $-45^\circ$  to  $-90^\circ$  latitude, and  $1.2 \times 10^{-6}$  elsewhere. As discussed in the text, this model does not include any water or  $\text{H}_2\text{S}$ .

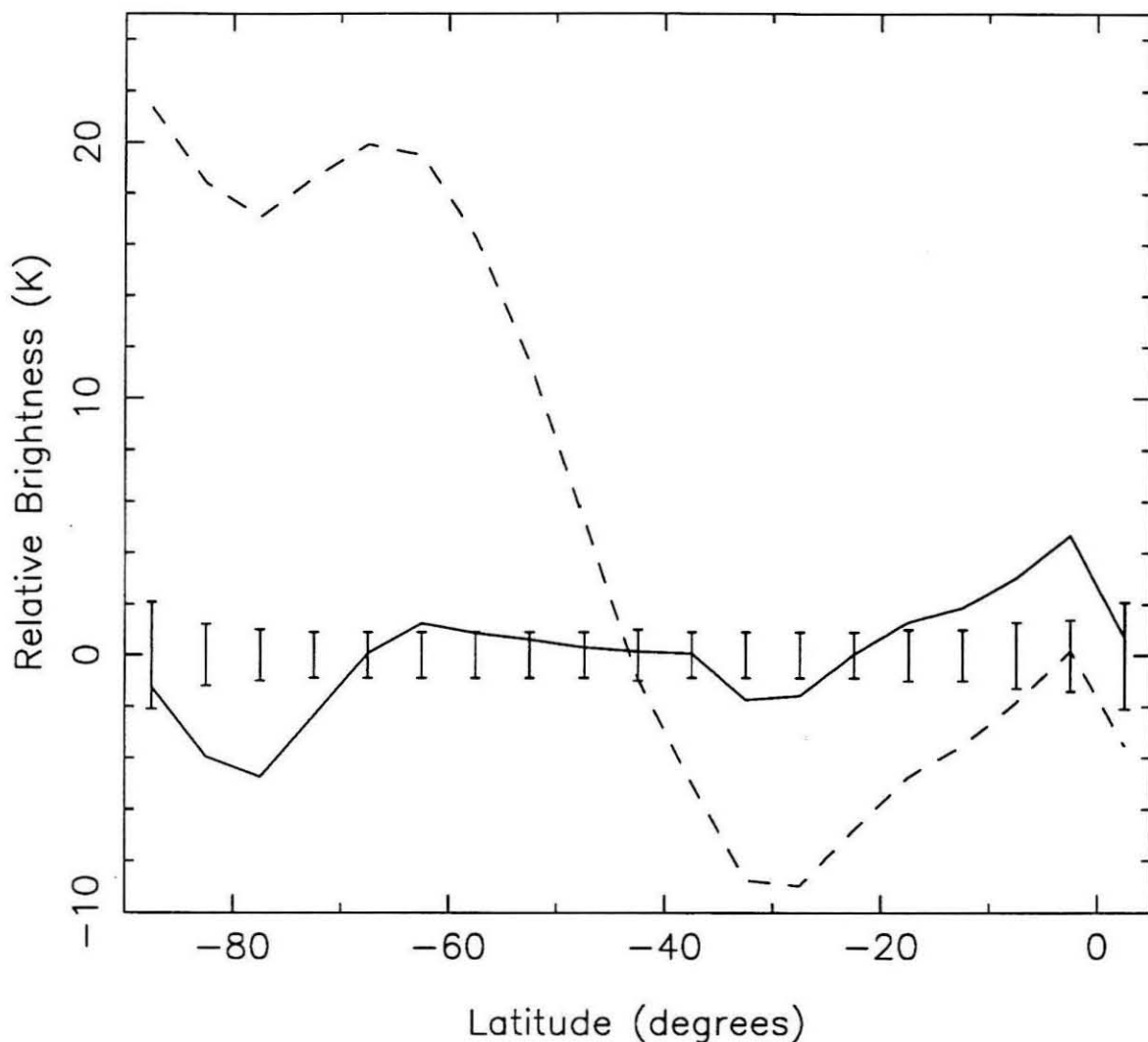


**Figure 4.2:** Difference plot of the 2 cm data. This “data-minus-model” plot presents the same information as Figure 4.1, but here the model brightness is subtracted from the data temperature, which highlights the discrepancies. The data’s error bars are plotted along the line of 0 K brightness, and a model that fits the data will yield a curve that stays within these error bars. The root-mean-square (RMS) value of each curve is a measure of the discrepancy between data and model. The dashed curve has an RMS deviation of 12.4 K, while the solid curve’s is 2.2 K.

from  $-35^\circ$  to  $-55^\circ$ , the solid curve provides an excellent fit to the data. Since the model has an abrupt change in absorber abundance here, this suggests the actual transition from absorber depleted pole to absorber rich equatorial region occurs in an area smaller than the resolution of the data (the CLEAN beam size, covering about  $15^\circ$  latitude).

Figure 4.2 introduces a new way of plotting the data that will prove more useful. It shows the difference between the data and model temperatures, so a perfect fit model would yield a horizontal line at 0 K brightness. The error bars along this line are the error bars of the data. The dashed and solid curves correspond to the same data and models as in Figure 4.1. The major deviations of the “bi-modal model” (solid curve) are near the equator, where the data are brighter than the model (suggesting the equatorial region may be absorber depleted just as the pole is), and near the South Pole, where the data are less bright than the model. Details such as these will be addressed after the 6 cm observations have been included in the analysis, a task to which we now turn.

As discussed in Chapter 3, the agreement between the 1981 and 1989 6 cm observations is high enough that we need only consider the newer data, which have less noise. Figure 4.3 shows the data minus model curves for the 2 and 6 cm data, using the same bi-modal model of Figure 4.2. (Note that when plotting both 2 and 6 cm data, the error bars shown will be from the 6 cm data because they are the larger of the two.) It is clear that at 6 cm the atmosphere is everywhere much less bright than the model, a fact previously determined when disk averaged observations were found to require a deep absorbing layer in the model (Chapter 2). It is also clear that the horizontal absorber gradient just found to fit the 2 cm observations is insufficient to flatten out the 6 cm curve.

To improve the fit to the 6 cm data, additional absorption must be provided at all latitudes, and the pole to equator gradient must increase. This enhancement must not, however, make the horizontal brightness variations at 2 cm too large. It is possible to satisfy these constraints because the 6 cm data probe deeper than the 2 cm (see the

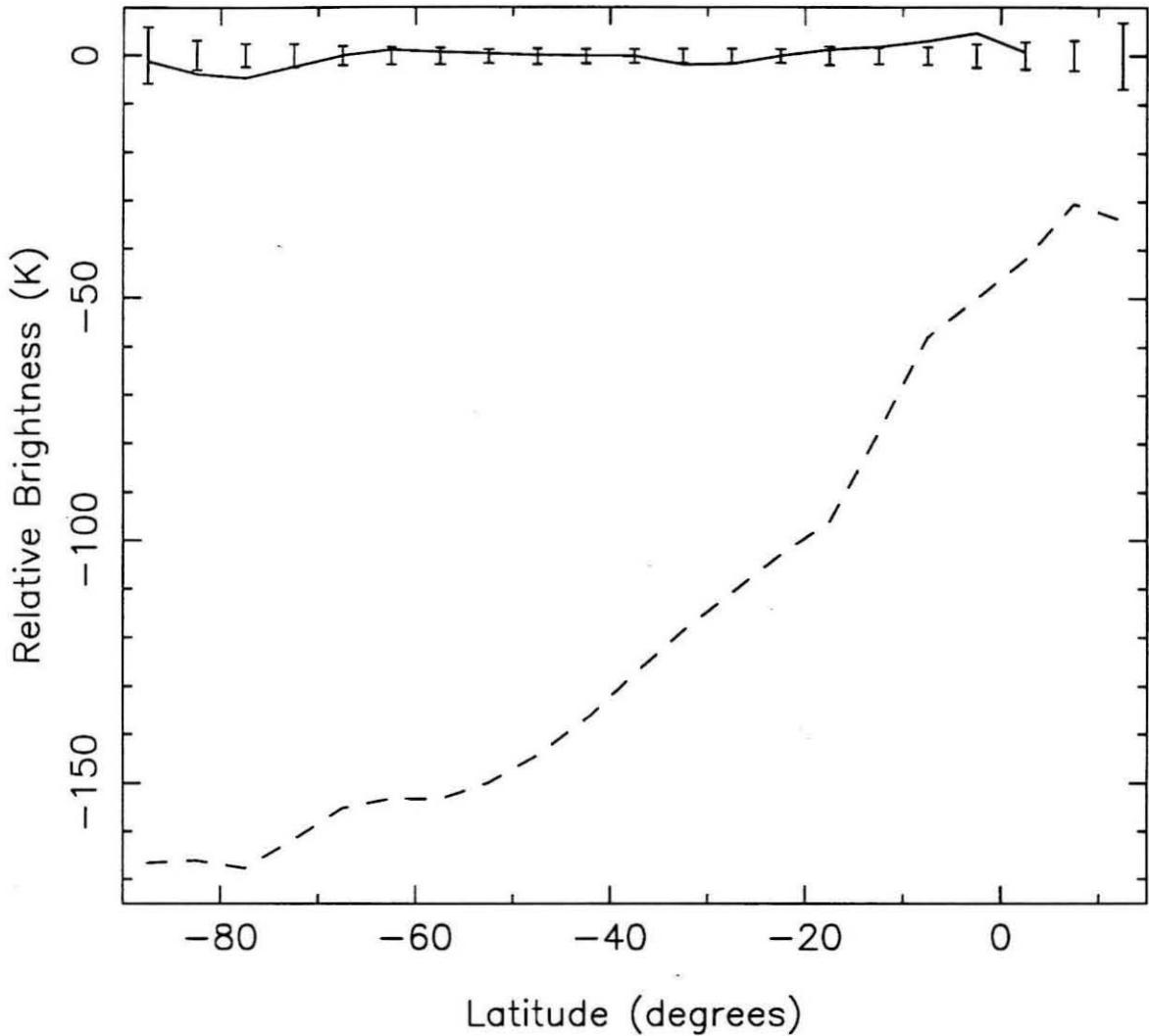


**Figure 4.3:** Difference plot (data-minus-model) of the 2 and 6 cm data. One advantage of using the difference plots is that the different wavelengths can be directly compared. The solid curve is the 2 cm data differenced with the bi-modal model, and the dashed curve is the 1989 6 cm data differenced with the same model absorber distribution. The error bars shown when the two wavelengths are plotted together are from the 6 cm data set.

weighting functions of Figure 2.8). Figure 4.4 presents a model similar to the bi-modal one just discussed, but with an added strong opacity source (a solar  $\text{NH}_3$  mixing ratio of  $1.4 \times 10^{-4}$ ) at depth. Poleward of  $-45^\circ$  the extra absorption is at pressures greater than 46 bar, while at other latitudes it is brought up to 22 bar. In addition, the absorber abundance in the upper atmosphere is slightly decreased to offset the small effect the deep absorbing layer has on the 2 cm data. This new model is a much better fit to both the 2 and 6 cm observations. It is very interesting that deviations from the data are highly correlated at the two wavelengths. This suggests we are seeing the small scale structure of the planet rather than noise in the maps. We will return to this point later. For now we will address only the largest deviation, which occurs in the 6 cm data set near the equator. In Figure 4.5 we see that the fit is improved if the Northern Hemisphere is given the same opacity distribution as the South Pole. This result is speculative, however, because uncertainties in locating the disk center in the 6 cm map create large uncertainties in the data northward of  $-10^\circ$  latitude (see Section 3.2.2. This source of error is not included in the error bars shown).

The model just described is a two-layer model. At any latitude the atmosphere is divided into upper and lower regions, each with its own absorber abundance. While the actual atmosphere will have more structure than this, we cannot unambiguously determine it using only two observing wavelengths without making further assumptions. While these more detailed solutions will be presented shortly (making use of assumptions as well as unresolved data at additional wavelengths), for now it is desirable to maintain as much generality as possible, and therefore we will constrain ourselves to using two-layer models. The quoted absorber abundance in each layer should be taken to be the average value over the height of the layer. In the following discussion, the deeper layer will usually be referred to as the deep absorbing layer, while the higher layer will be referred to as the upper atmosphere.

For current purposes, the model shown in Figure 4.5 is an acceptable fit to the data.

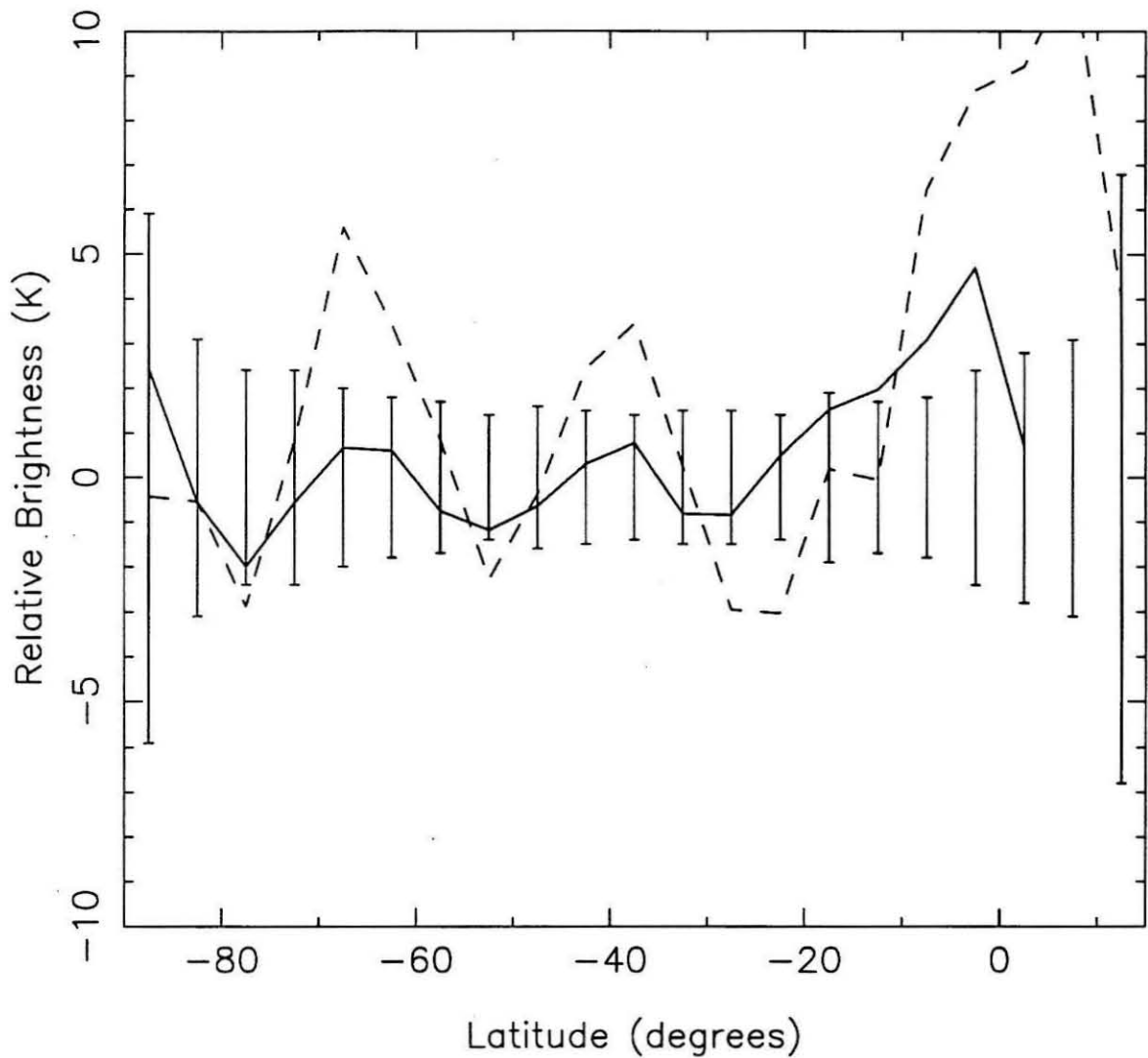


**Figure 4.4:** Simultaneous fitting of 2 and 6 cm data. The model absorber distribution used here is that poleward of  $-45^\circ$  the  $\text{NH}_3$  mixing ratio is set to  $1.4 \times 10^{-4}$  at pressures greater than 46 bars and  $4.5 \times 10^{-7}$  above this. At all other latitudes the  $\text{NH}_3$  ratio is  $1.4 \times 10^{-4}$  deeper than 22 bars and  $1.1 \times 10^{-6}$  above this. The solid curve corresponds to 2 cm temperatures, the dashed to 6 cm. The RMS deviation at 2 cm is 1.7 K and at 6 cm it is 4.6 K.

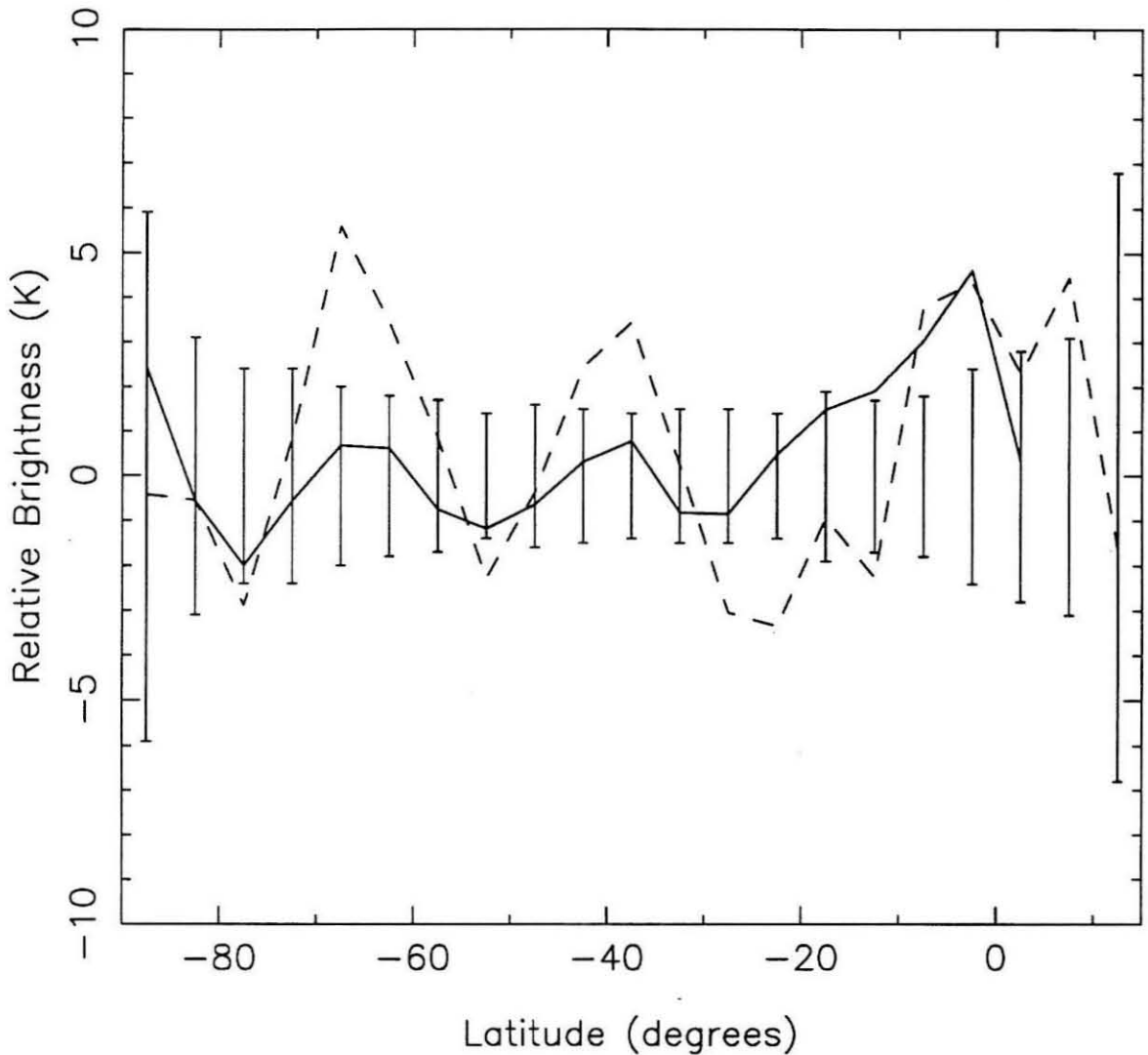


**Figure 4.5:** Removing absorber from the Northern Hemisphere. These curves are for a model identical to that shown in Figure 4.4, except that now all northern latitudes have the same absorber abundance as the South Pole. Again, the solid curve is for 2 cm observations, the dashed is for the 6 cm data. Clearly the 6 cm data favors absorber depleted low northern latitudes. Uncertainties in locating the disk center in the 6 cm data map (discussed in Section 3.2.2), which are not included in the error bars shown, make this conclusion speculative. Note that the 2 cm data also suggests a low absorber abundance near the equator. The RMS deviations are 1.7 K at 2 cm and 2.8 K at 6 cm.

This model can be used to explore the sensitivity of the data to the location and strength of the absorber in each atmospheric region. For a given deep absorber mixing ratio, the 6 cm data is extremely sensitive to the pressure level of the layer (actually it is the temperature at this level that is the significant parameter). For example, moving the deep layer in polar regions from 46 to 40 bars decreases calculated brightness temperatures at 6 cm by 9 K poleward of  $-60^\circ$ . Therefore, to bring the deep absorbing layer to higher altitudes requires decreasing the absorber abundance in it (and in the upper atmosphere as well). There is a limit to how high the layer can go, however, because eventually it will start creating brightness gradients at 2 cm greater than those observed. Similarly, pushing the layer deeper requires it to be more strongly absorbing, with a limit on its depth set by the requirement that it must be high enough for 6 cm observations to “see” it.

To achieve fits to the data comparable to that shown in Figure 4.5, the top of the deep layer over the South Pole must be between 25 and 50 bars, and the top of the layer at lower latitudes must be between 10 and 25 bars. Figures 4.6 and 4.7 demonstrate how these limits are determined. Basically, the deep layer is moved vertically and then absorber abundances are adjusted to try to fit the data. Eventually, an altitude is reached at which no possible adjustment will work. Figure 4.6 shows an attempt to place the deep absorbing layer at low latitudes at 5 bars. The 2 cm data (solid curve) are brighter than the model equatorward of  $-45^\circ$ , suggesting less absorber is needed in the model. The model, however, already has all the absorber (other than  $H_2$ ) above 5 bars removed. This then requires lessening absorption in the deep layer. Doing that, however, will increase the 6 cm model brightness—and the 6 cm model is already much too bright to fit the data (dashed curve). Thus the model cannot be made to fit the data with the deep absorbing layer as high as 5 bars. Similarly, Figure 4.7 shows the limit of how deep the layer can be forced over the pole. In this case, the 6 cm data (dashed curve) are cooler than the model, which has the deep layer at 55 bars over the pole. Increasing absorption in the

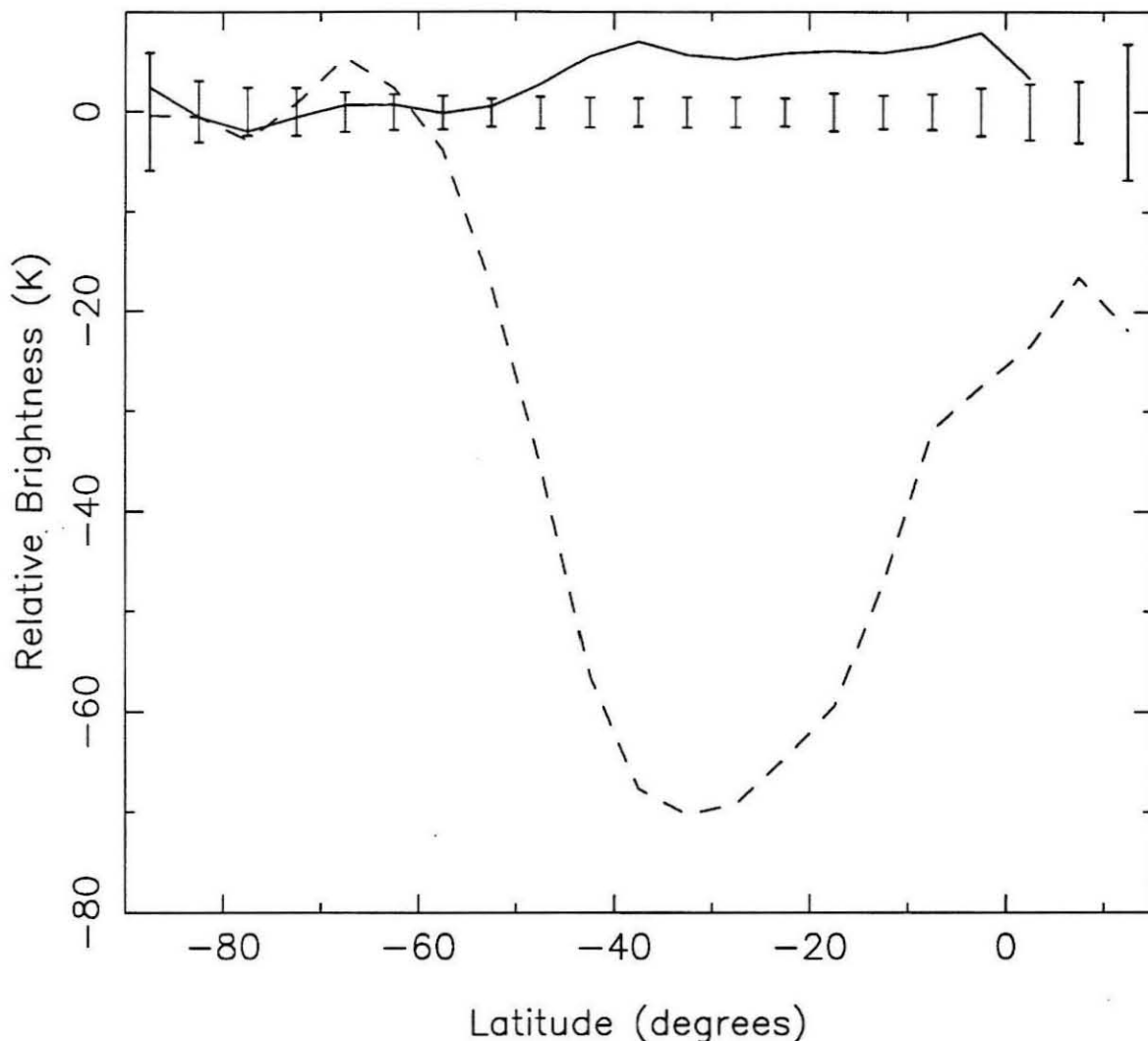


**Figure 4.6:** Setting limits on absorber altitude. These curves demonstrate what happens when the “deep absorbing layer” at low latitudes is placed at the 5 bar level. Poleward of  $-45^\circ$  and in the Northern Hemisphere, the absorber distribution is the same as in the previous model (Figure 4.5). Between  $-45^\circ$  and  $0^\circ$ , however, the  $\text{NH}_3$  abundance at altitudes above the 5 bar level is set to zero, while below 5 bars it is at  $2.0 \times 10^{-6}$ . The 2 cm data (solid curve) are slightly brighter than the model at low latitudes, calling for decreased model absorption in this region. Since the upper atmosphere has essentially all the absorber already removed, the deep layer must be depleted to fit the 2 cm observations. The 6 cm data (dashed curve) are, however, already much dimmer than the model, and decreasing model absorption would only degrade the fit further. Thus, a two-layer model cannot fit the data if the transition level is as high as 5 bars.

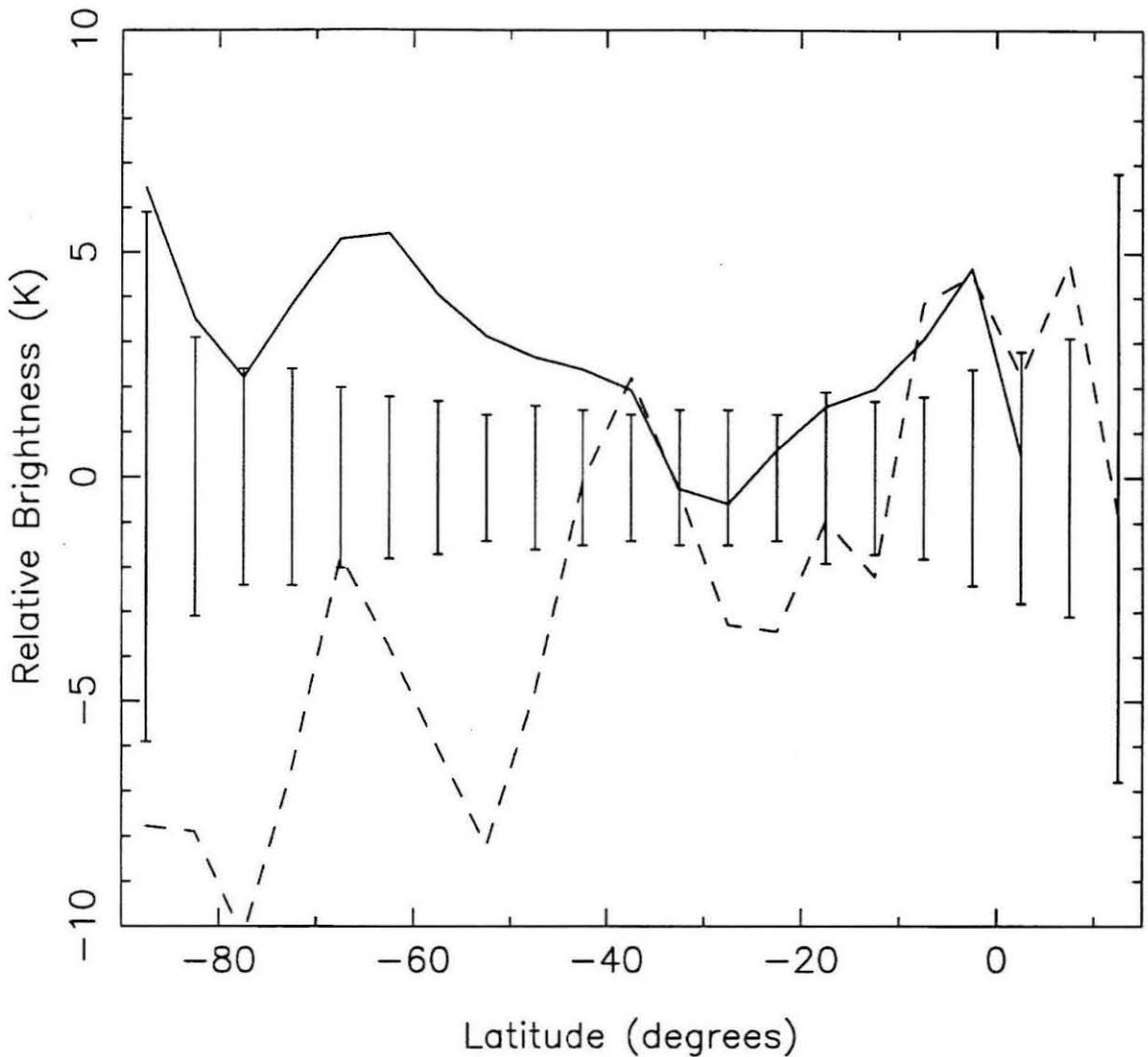


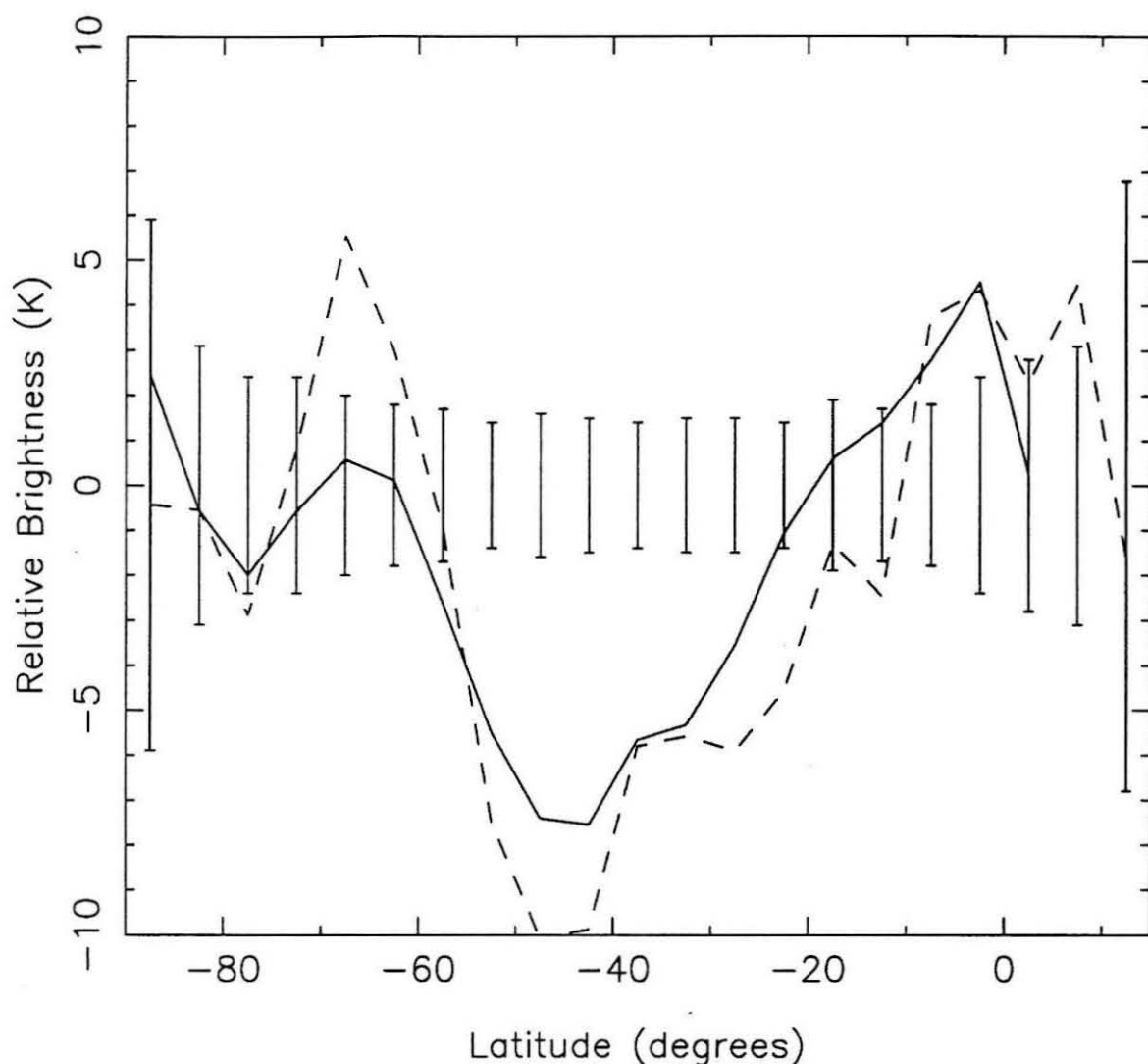
**Figure 4.7:** Setting more limits on absorber altitude. These curves show the lower altitude limit for the deep absorbing layer over the South Pole. This time, latitudes northward of  $-45^\circ$  are the same as the model shown in Figure 4.5, but southward of this, the  $\text{NH}_3$  ratio is  $5.9 \times 10^{-7}$  at altitudes higher than the 55 bar level, and  $1.4 \times 10^{-2}$  below this level. The deep absorber abundance is so high that this region of the atmosphere is opaque, and adding more absorber here will not change calculated brightness temperatures. To fit the 6 cm data (dashed curve), which is cooler than the model, absorber must therefore be added to the upper atmosphere. The 2 cm data (solid curve) is already brighter than the model, and adding absorber in this region degrades the 2 cm fit even further. This indicates the model cannot be made to simultaneously fit both data sets if the deep layer is as deep as 55 bars over the pole.

deep layer has no effect on 6 cm model brightnesses because it is already opaque, so the extra opacity needed to decrease the 6 cm model temperatures must be placed in the upper atmosphere. The 2 cm observations (solid curve), however, are already brighter than the model, so increasing absorption in the upper atmosphere will degrade the 2 cm model fit. Thus, it appears a model with the deep absorbing layer as deep as 55 bars will not work.

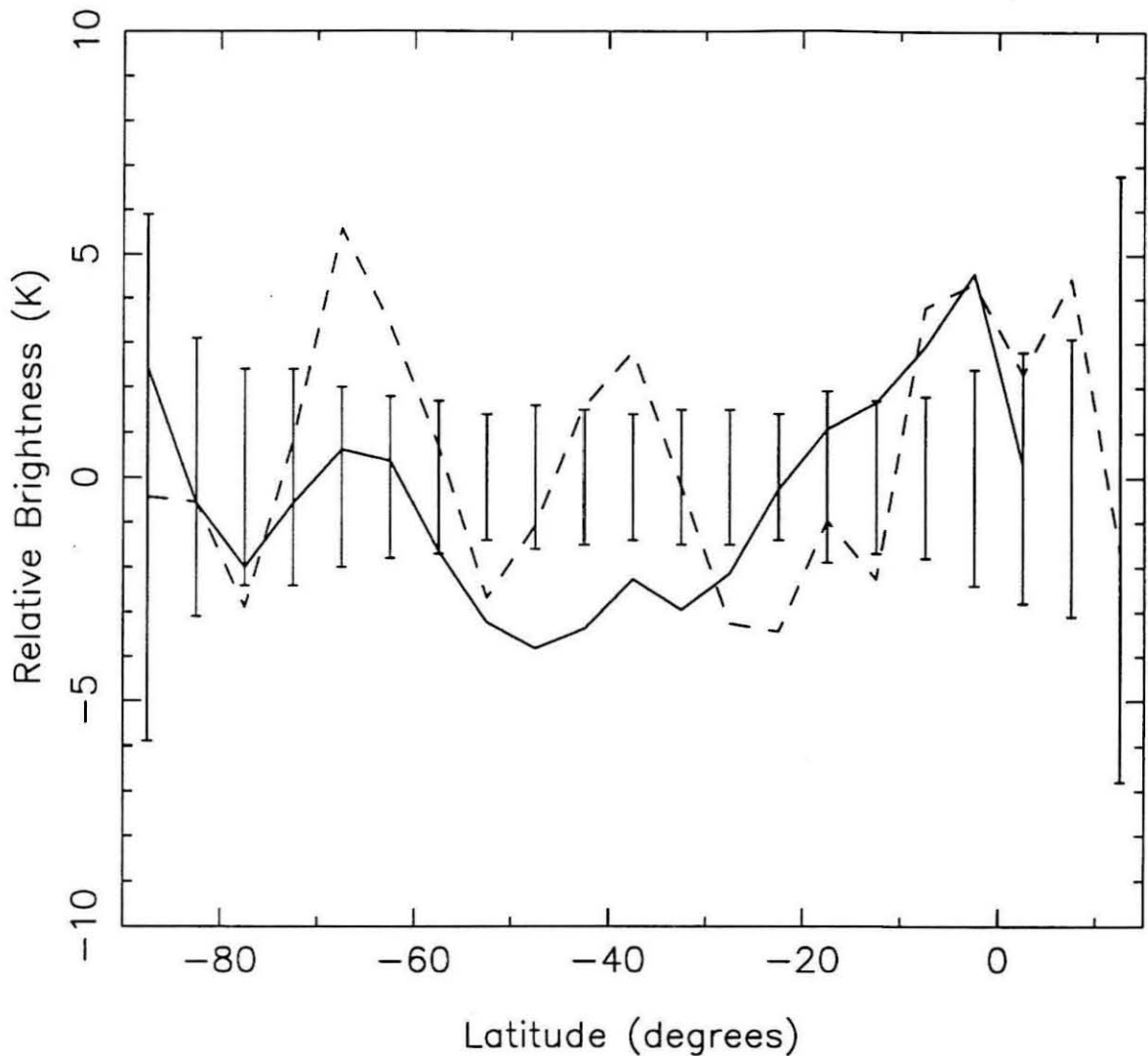
The model of Figure 4.5 can also be used to explore the sensitivity of the data to the latitude of transition between the relatively absorber-rich low-latitudes and absorber-depleted pole. Figure 4.8 shows the effect of moving the transition equatorward only  $5^\circ$ , to  $-40^\circ$  latitude. The models are far from the data at mid-latitudes, and adjusting the absorber abundance to fit these latitudes would destroy the fit over the poles and equator. The magnitude of the disturbance is identical if the transition is shifted poleward  $5^\circ$  to  $-50^\circ$  latitude. Attempting to shift the deep layer's transition latitude  $5^\circ$  while keeping the upper atmosphere's transition at  $-45^\circ$  also results in an inability to fit the data at 6 cm, though a marginal fit at 2 cm can still be maintained. When shifting the upper atmosphere's transition while keeping the deep layer transition at  $-45^\circ$ , again a  $5^\circ$  shift poleward yields an unacceptable fit, but now there is a slight bit of room to shift things equatorward. Figure 4.9 shows that an upper atmospheric transition at  $-40^\circ$  is still a marginal fit to the data, but shifting it further is unacceptable. This slight uncertainty in the upper transition location is probably attributable to the 2 cm data having a slightly poorer resolution near the equator than the 6 cm data does. (This is due to the differing observing geometries.)

Figure 4.10 summarizes the results of fitting the 2 and 6 cm observations by varying the absorber abundance. The three main conclusions are:

- Polar regions are absorber depleted relative to lower latitudes at least down to 25 bars.
- The absorber gradient between pole and mid-latitudes increases with depth until



**Figure 4.8:** Setting limits on transition latitude. These curves use the model of Figure 4.5, but shift the latitude of the transition from absorber depleted pole to absorber rich mid-latitudes equatorward  $5^\circ$ . Clearly the temperatures are very sensitive to the location of this transition, and placing it at  $-40^\circ$  is not acceptable. A similar result is found when the transition is moved to  $-50^\circ$ . Keep in mind that because the data resolution is about  $15^\circ$  in latitude, this indicates the center of the transition region is within  $5^\circ$  of  $-45^\circ$  latitude, but the transition region itself may be larger.



**Figure 4.9:** Setting further limits on the transition latitude. These curves show the effect of shifting the upper atmosphere's transition latitude while holding the deep transition latitude fixed. Here, the upper transition occurs at  $-40^\circ$ . This shift still yields a marginal fit to both data sets. Shifting the transition to  $-50^\circ$  or  $-35^\circ$  results in unacceptable fits similar to the one shown previously. Thus, the data does not constrain the upper atmosphere's transition latitude quite as tightly as it does the lower, but both are required to be close to  $-45^\circ$ .

the polar deep absorbing layer is reached, which occurs somewhere between 25 and 50 bars.

- The transition between absorber rich and depleted regions is centered at  $-45 \pm 5^\circ$  latitude, and the transition occurs over a narrow region (less than  $15^\circ$  in latitude, or about 6500 km across).

It also appears likely that the small region of the Northern Hemisphere that is visible is depleted in absorbers relative to mid-southern latitudes. In Figure 4.10, the deep absorbing layer is shown having the same absorber abundance at all latitudes. This is true only when the layer is at the high pressure end of the allowed range (roughly 40 to 50 bars over the pole, 20 to 25 bars at lower latitudes). Assuming that this is the case, however, allows the data to be fit with fewer free parameters, which is pleasing from a simplicity standpoint, and survives the test of Occam's razor. Furthermore, placing the deep layer at higher pressures requires it to have a high opacity. This allows for the same model to fit longer wavelength, disk-averaged data without adding free parameters. This is shown in Figure 4.11, which presents the spectra of two models that both fit the high-resolution 2 and 6 cm data. The dashed curve has the deep layer at relatively low pressures, the solid curve places it at high pressures. The first model clearly requires an additional opacity source below the "deep layer" to fit the data near 20 cm, while the second does not. Thus, while we cannot exclude the possibility of the deep layer being at relatively low pressure levels in the atmosphere, it is preferable to place it at higher pressures.

#### 4.1.2 Explaining the Absorber Gradients

Returning to Figure 4.10, it is appropriate now to question how such an opacity distribution could arise. Three options considered are photochemistry, the infall of ring particles, and atmospheric dynamics. Due to the unusual obliquity of Uranus, its polar regions receive, on an annual average, about a factor of  $\sqrt{2}$  more sunlight than the

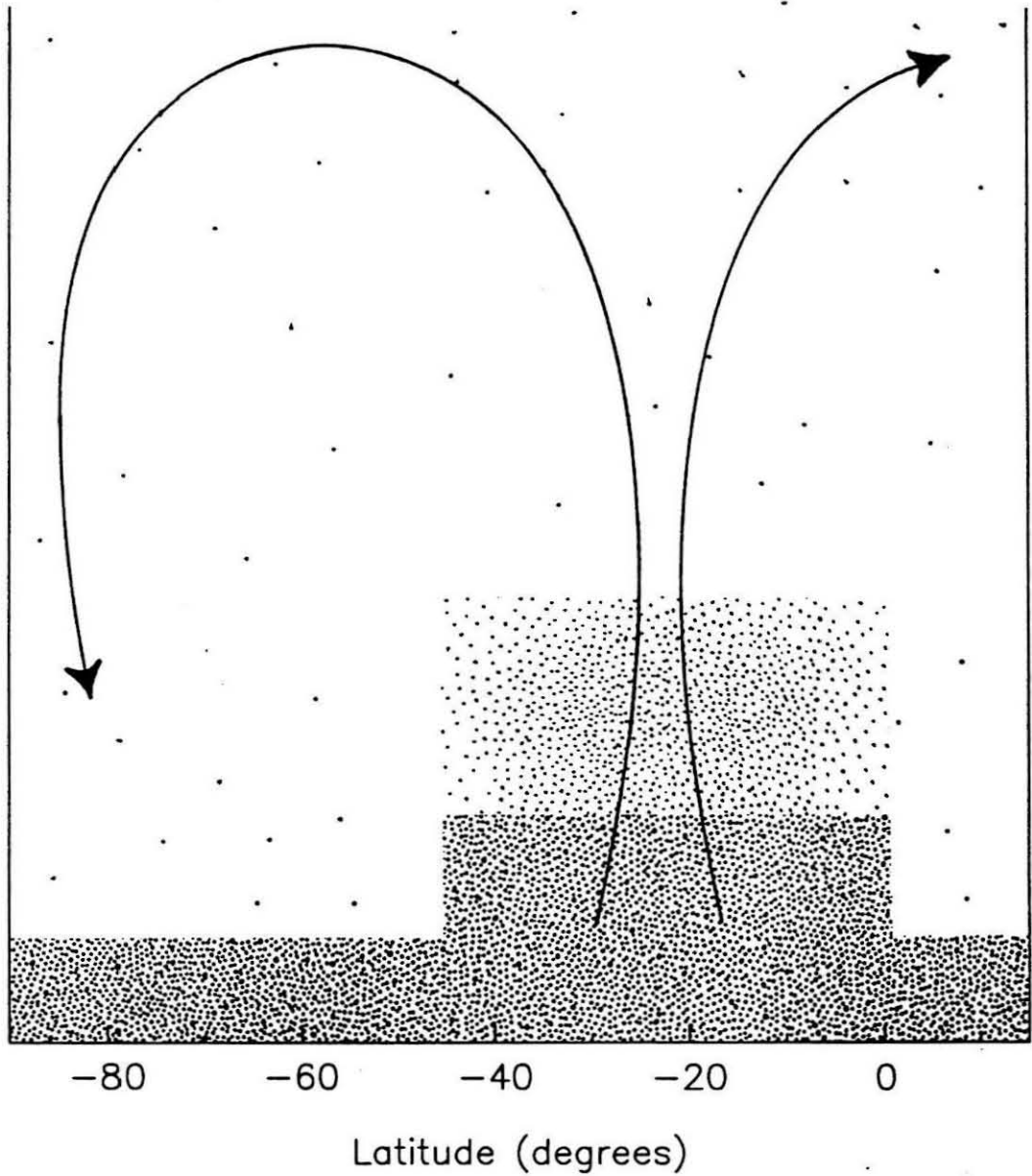


**Figure 4.10:** Schematic diagram of the gross structure of the atmosphere, as inferred from radio data. The density of dots in any region is indicative of the absorber abundance. No vertical scale is shown, but the transition between absorber-rich deep atmosphere and depleted upper atmosphere occurs somewhere between 25 and 50 bars over the South Pole, and between 10 and 25 bars at lower southern latitudes. The arrows indicate a circulation pattern that might explain the absorber distribution. This is discussed later in the text. The text also points out that the deep absorbing layer need not have the same absorber abundance at all latitudes.

equator. It is unlikely, however, that photo-destruction of absorbing species could cause the observed distribution because sunlight does not penetrate deeper than 5 bars (Rages and Pollack 1988). Furthermore, this mechanism would not (by itself, anyway) generate a uniformly depleted polar region that transitions abruptly to undepleted lower latitudes. Ring particles (which are primarily water ice, but can also contain  $\text{NH}_3$  trapped as a hydrate) falling into the atmosphere could enrich equatorial regions in absorbers. The excess mass of absorber (assuming it to be  $\text{NH}_3$  or  $\text{H}_2\text{O}$ ) that exists at low latitudes relative to polar latitudes is much larger, however, than the total current mass of the  $\epsilon$  ring, so this does not seem a plausible explanation either.

Atmospheric dynamics, on the other hand, can not only explain the absorber distribution, but there also is supporting evidence for just the type of circulation suggested by the radio data. The atmospheric pattern proposed is a large-scale upwelling at latitudes that appear absorber rich ( $0^\circ$  to  $-45^\circ$ ). The rising air parcels lose their entrained absorber in a two-stage process. The first, more dramatic depletion, occurs somewhere between 25 and 10 bars, and marks the boundary between the deep absorbing layer and upper atmosphere at these latitudes. (Based on the modeling previously described, the absorber mixing ratio decreases by a factor of 10 to 100 between these altitudes.) As parcels continue to rise and spread horizontally, they lose additional absorber somewhere above the 5 bar level. These absorber depleted air parcels then descend over the South Pole (and perhaps low Northern Latitudes), leaving the regions of subsidence depleted in absorbers by a further factor of 2 or 3 from the "upper layer" abundance in the upwelling. These absorber poor subsiding air parcels dominate the atmospheric composition over the South Pole to somewhere between 25 and 50 bar, below which the absorber abundance sharply increases again, this transition marking the boundary between the deep layer and upper layer at polar latitudes.

The likely mechanism to deplete absorbers in the upwelling is condensation. If  $\text{NH}_3$  is the primary opacity source, the first, major depletion can result from the condensation

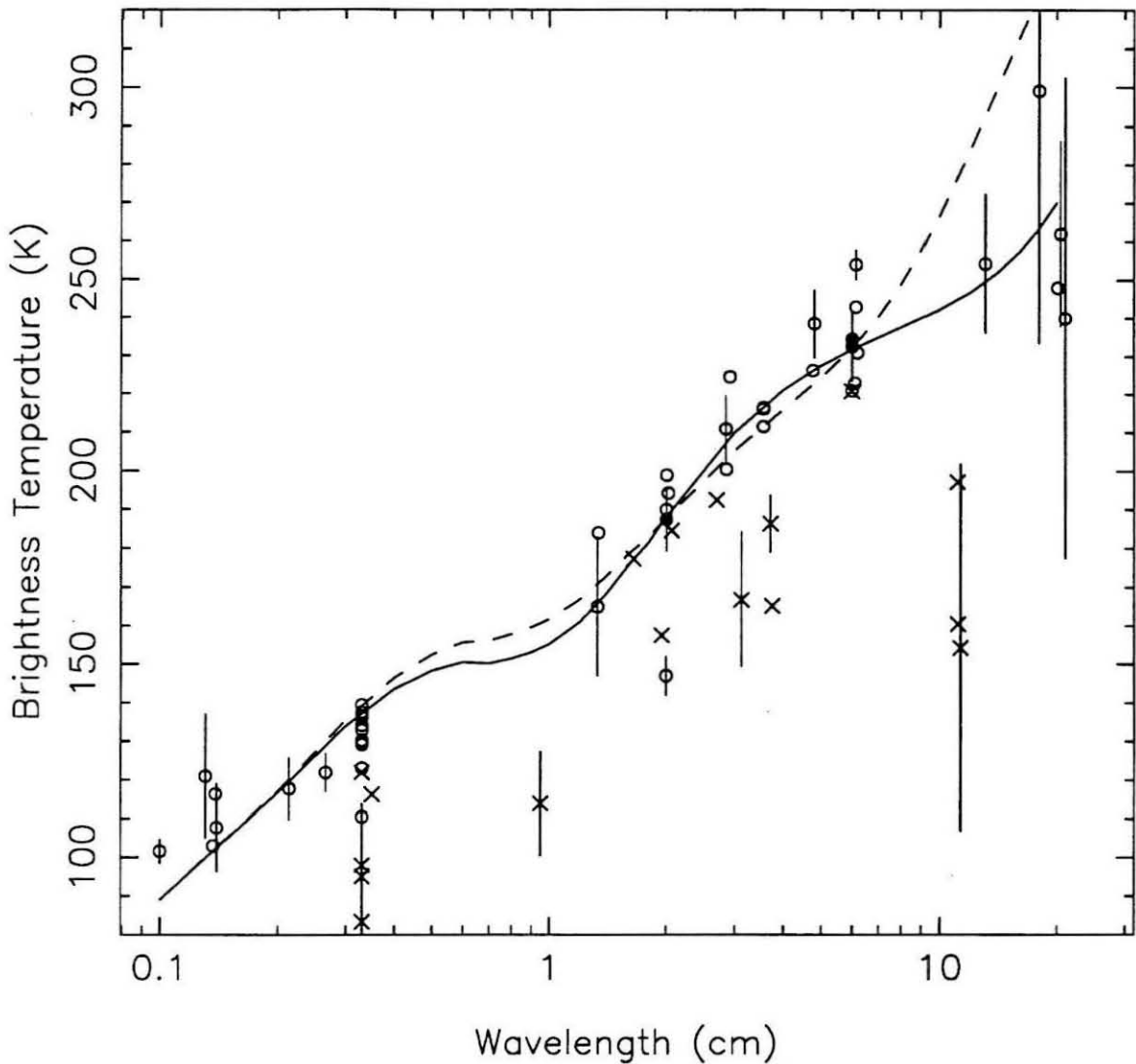


**Figure 4.11:** Using disk averaged observations to constrain the high resolution model. These curves demonstrate that placing the deep absorbing layer at the high pressure end of the range allowed by the disk resolved data will simultaneously fit unresolved observations. Placing it at lower pressures does not. The solid curve represents a model that poleward of  $-45^\circ$  and in the Northern Hemisphere, has an  $\text{NH}_3$  molar mixing ratio of  $4.5 \times 10^{-7}$  above 46 bars, and a ratio of  $1.4 \times 10^{-4}$  below this level. At low Southern latitudes, the upper atmospheric  $\text{NH}_3$  ratio is  $1.1 \times 10^{-6}$ , while below 22 bars it is  $1.4 \times 10^{-4}$ . The dashed curve is similar at low southern latitudes, but over the pole its  $\text{NH}_3$  mixing ratio is  $2.4 \times 10^{-7}$  above 30 bars, and  $1.6 \times 10^{-5}$  below it. Both curves provide a good fit to the high-resolution data, with RMS deviations of about 1.8 K and 3.0 K at 2 and 6 cm, respectively.

of  $\text{NH}_4\text{SH}$ , which has already been suggested as an  $\text{NH}_3$  depleting mechanism to explain disk averaged observations (see Section 2.3.2 and references therein). The secondary depletion near 5 bars is then condensation of  $\text{NH}_3$  ice. Alternatively, the deep absorbing layer could be defined by a super-cooled, super-dense, liquid water cloud. Section 2.2.4 discussed how various contaminants (such as  $\text{NH}_3$ ) placed in solution can depress the freezing point of water to as low as 200 K (which corresponds to the 18 bar level of the nominal profile. The freezing point of pure water, about 273 K, is reached at the 50 bar level). Thus, a dense liquid cloud could be the “deep absorber” in the upwelling, and the transition between deep absorbing layer and upper atmosphere marks the altitude where the liquid solution freezes. A small  $\text{NH}_3$  abundance would then provide the upper atmosphere’s absorption, with  $\text{NH}_3$  condensation near 5 bars again resulting in the second-stage depletion of air parcels. One difficulty in using a liquid water cloud as the opacity source at these altitudes is that the cloud needs to be ten times denser than calculated by the method of Weidenschilling and Lewis (1973) to provide enough absorption (neglecting absorption by aqueous  $\text{NH}_3$ ). When discussing cloud densities in Chapter 2, however, it was pointed out that the model cloud densities are probably an upper limit to the actual densities, so it seems preferable to interpret the absorber as  $\text{NH}_3$ .

Thus, qualitatively at least, mechanisms exist to condense out the likely absorbers at the appropriate altitudes. To show this quantitatively, a model that includes  $\text{H}_2\text{O}$  and  $\text{H}_2\text{S}$  in the atmosphere can be fit to the high-resolution data. All water cloud absorption at temperatures less than 273 K is neglected based on the assumption that any cloud at these altitudes will have a low density. The relatively strong opacity source at pressures less than 50 bars that was found to exist at mid-latitudes must then be  $\text{NH}_3$ , and its depletion by a factor of about 100 at higher altitudes requires the  $\text{H}_2\text{S}$  abundance to be within 1% of the  $\text{NH}_3$  mixing ratio if the nominal cloud model is used. In the deep absorbing layer, the  $\text{NH}_3$  abundance is required to be the same at all latitudes because these are assumed to be well-mixed regions of the atmosphere. Using an approach identical to the

one used previously to determine the most general form of the opacity distribution, a good fit to the data is found with a model having a deep  $\text{NH}_3$  mixing ratio of  $1.4 \times 10^{-4}$ , and an  $\text{H}_2\text{S}$  ratio of  $1.396 \times 10^{-4}$ . The downdraft over the South Pole persists as deep as 48 bars, and has an  $\text{NH}_3$  mixing ratio of  $4.2 \times 10^{-7}$ . The  $\text{H}_2\text{O}$  abundance is not well constrained by the high resolution data because they do not probe deep enough to see the cloud base. From the discussion of disk-averaged observations at wavelengths as long as 20 cm, however, the  $\text{H}_2\text{O}$  ratio is expected to be at least  $1.0 \times 10^{-3}$ , so this value is adopted for the current model. (The high-resolution data sees any value greater than about  $10^{-4}$  as the same.) This model will be referred to as the “nominal model.”

Figure 4.12 shows the composition of this model as a function of height in the upwelling region, while Figure 4.13 shows its fit to the data. There are several areas where the model and data deviate. Most of them are relatively small, but while ripples near the noise level in any one map might be suspect, the fact that these appear at the same latitudes in different data sets taken at different times under different viewing geometries, and even when maps are made using different algorithms (Section 3.1.3), suggests they are real. There is also a significant deviation of the 6 cm data from expected values between  $-20^\circ$  and  $-30^\circ$  latitude. (This corresponds to the center of the presumed upwelling.) These structures could be due to variations in the absorber abundance, variations in the altitude at which the absorber-rich deep layer is found, or variations in kinetic temperature. A discussion of the latter possibility is deferred to the next section, but kinetic temperature variations of 5 to 10 K along surfaces of constant pressure, at pressures of tens of bars, could create the observed structures. If varying absorber abundances are responsible for the features, they represent substantial deviations from the general circulation discussed, and factor of a few differences from the nominal model’s absorber abundance exist in small regions. Alternatively, small variations in the altitude of the  $\text{NH}_4\text{SH}$  cloud base or in the depth of penetration of subsiding air parcels can also create the features. The magnitude of the altitude variations required is about 5 bar

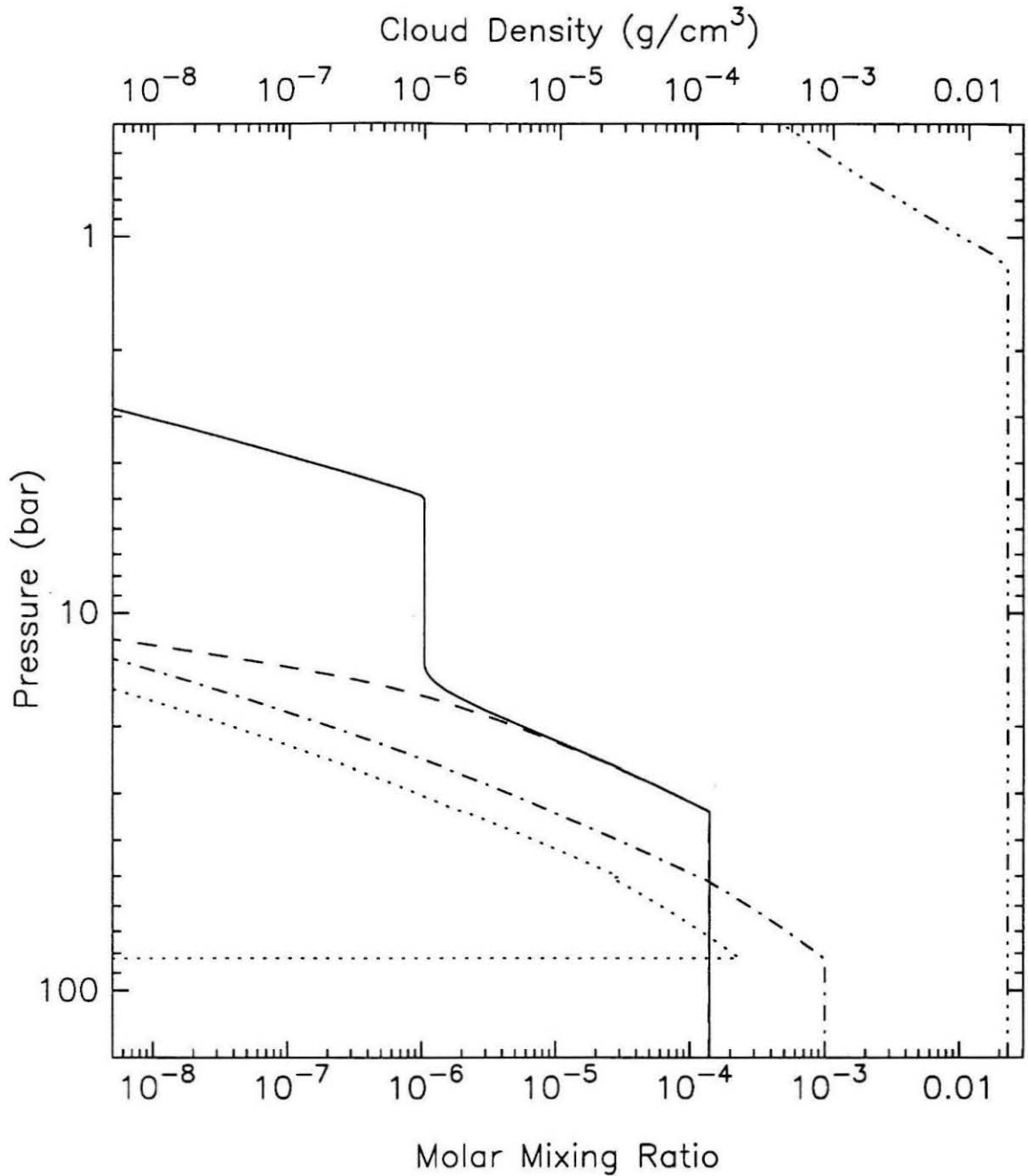


**Figure 4.12:** Atmospheric structure of the nominal model (shown also in Figure 2.2). This figure shows the abundance of various atmospheric species as a function of height in the upwelling region of the nominal model. The  $\text{NH}_3$  molar mixing ratio is given by the solid curve, the  $\text{H}_2\text{S}$  ratio by the dashed curve, and the  $\text{H}_2\text{O}$  vapor mixing ratio by the dot-dashed curve. The dash-triple-dotted curve is the  $\text{CH}_4$  mixing ratio, while the dotted curve is the water cloud density in  $\text{g cm}^{-3}$ .

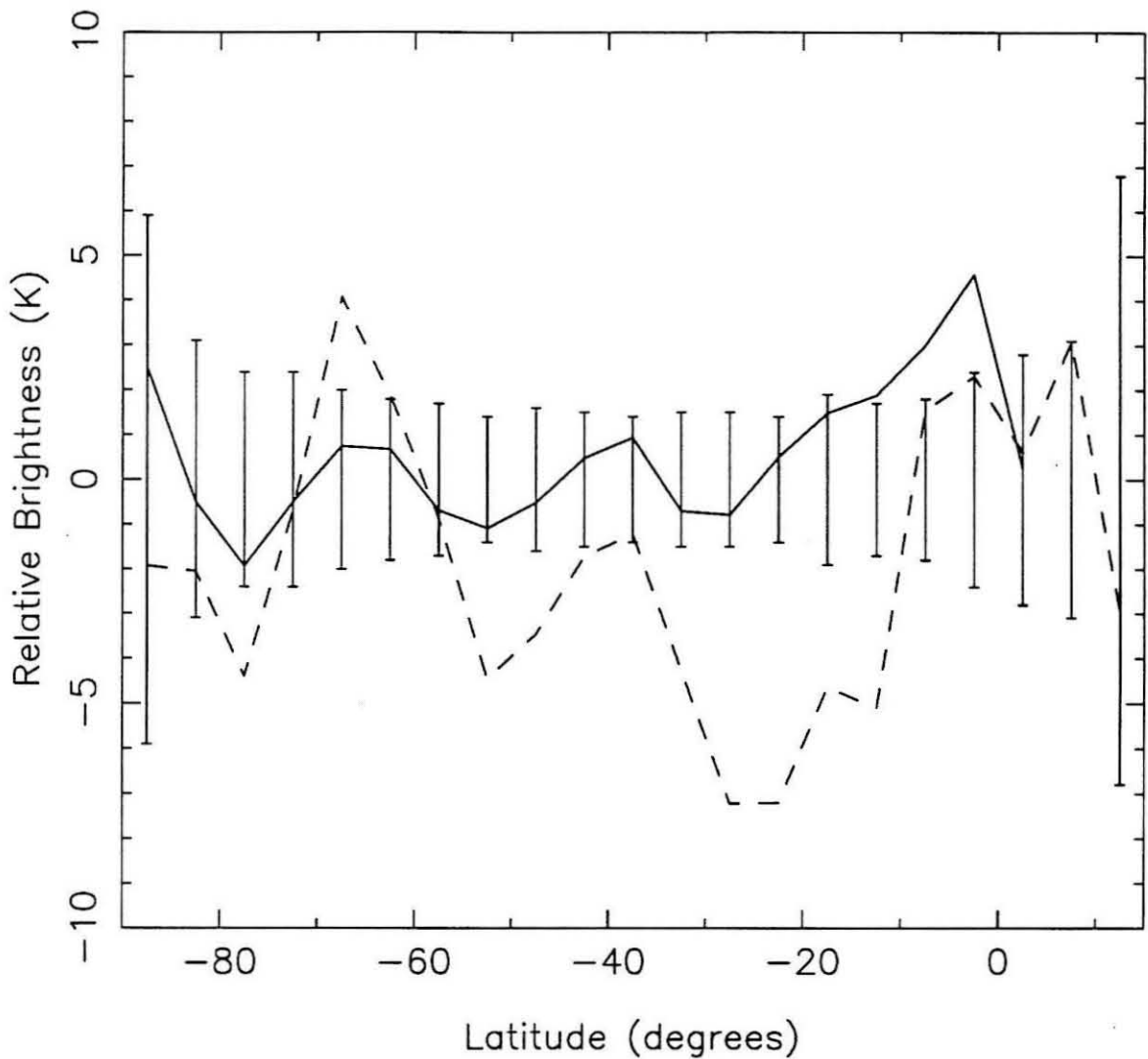


**Figure 4.13:** Deviations of the nominal model from the data. These are “data-minus-model” curves. The model, described in the text, uses  $\text{NH}_3$  and  $\text{H}_2\text{S}$  chemistry, cold-trapping of absorbers at high altitude, and an assumed meridional circulation pattern to fit the observations. The solid curve is the difference between the 2 cm data and the model, while the dashed curve is the 6 cm difference. The RMS deviations are 1.6 K and 3.7 K, respectively. The error bars represent the noise in the 1989, 6 cm data set.

(corresponding to 10 km in the depth of penetration of subsiding air parcels, or 14 km in the  $\text{NH}_4\text{SH}$  cloud base). It seems unavoidable that variations of this magnitude would exist over planetary scales. Whichever mechanism is causing the features, it is intriguing that the variations seemed to remain fixed in latitude over the 4 years between the 2 and 6 cm observations. These features are reminiscent of Jupiter's zone-belt structure, which has optical banding that correlates with variations in radio brightness (de Pater 1986). It is, however, beyond the scope of this work to interpret these small scale features.

Figure 4.14 presents a schematic diagram of the model just discussed. While smaller scale features exist on the planet, this seems to be a reasonable model of the large-scale structure of the atmosphere. Keep in mind, however, that the depth of the downwelling over the pole and the identity of the absorber in the updraft are not unquestionable. If the deep  $\text{NH}_3$  abundance below the polar downdraft is  $\sim 1/10$  solar, the downdraft persists only to about 25 bars. (To make such a model fit disk-averaged observations near 20 cm, however, requires more opacity near 50 bars than is provided by the nominal water vapor and cloud profiles of the model.) Also, the region of upwelling could be absorber rich due to solution effects maintaining a liquid water cloud at temperatures as low as 210 K rather than the presence of a near solar  $\text{NH}_3$  abundance. (This interpretation also requires cloud densities greater than predicted by the model of Weidenschilling and Lewis.)

Another grey area of this model is the  $\text{H}_2\text{S}$  abundance. Some researchers have questioned the plausibility of the  $\text{H}_2\text{S}/\text{NH}_3$  ratio being so close to 1.0 (de Pater *et al.* 1989). For the model of Figure 4.14, with a near solar  $\text{NH}_3$  mixing ratio of  $1.4 \times 10^{-4}$ , the  $\text{H}_2\text{S}/\text{NH}_3$  ratio needs to be between 1.0 and 0.996. If, however, the  $\text{NH}_3$  ratio is assumed to be closer to  $1.4 \times 10^{-5}$  (which raises the level of the deep absorbing layer), the  $\text{H}_2\text{S}$  to  $\text{NH}_3$  ratio can go as low as 0.9 and still fit the data, so there is some flexibility in its value. Uncertainties in the equilibrium constant governing the  $\text{H}_2\text{S}$  and  $\text{NH}_3$  reaction (Equation 2.9), and the possibility of  $\text{NH}_3$  being sub or super-saturated over the  $\text{NH}_4\text{SH}$  cloud also widen the allowed range of  $\text{H}_2\text{S}$  abundances. Thus, while the nominal model

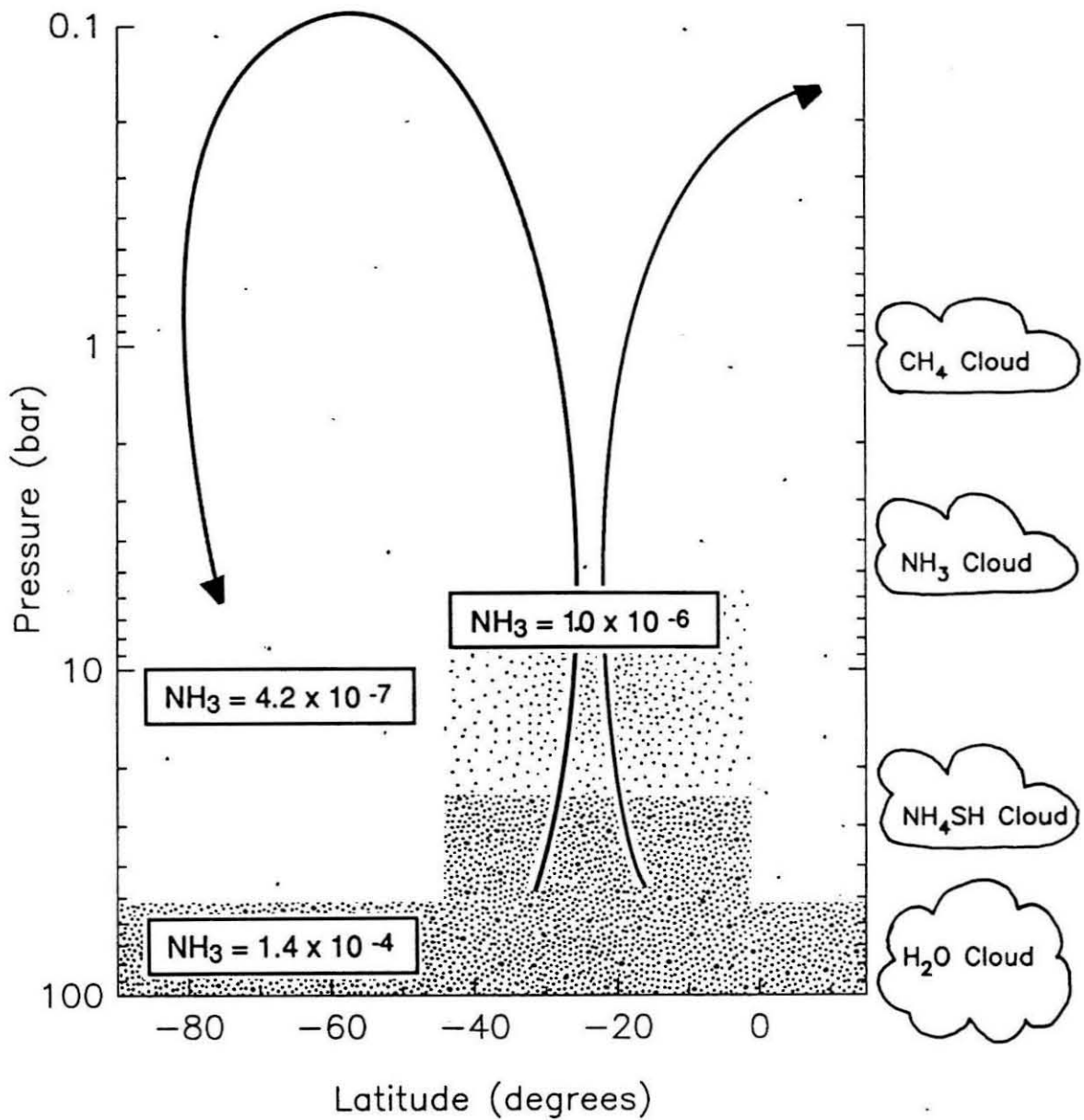


**Figure 4.14:** Schematic diagram of the nominal model. The density of dots indicates the absorber (NH<sub>3</sub>) abundance. The arrows show the circulation pattern believed to maintain the absorber distribution. The various cloud levels are shown on the right margin. The upwelling brings absorber-rich air parcels to higher and colder regions. Condensation removes the absorbers from the parcel, so that regions dominated by subsidence are clear. The Northern Hemisphere is not as well resolved as the Southern, but it appears to be as depleted as the South Pole.

sets a very specific value for the  $\text{H}_2\text{S}$  abundance, the uncertainties in the model prevent a true determination of its value. While on the subject of the  $\text{H}_2\text{S}/\text{NH}_3$  ratio, it is interesting to note that  $\text{NH}_3$  is more soluble in water than  $\text{H}_2\text{S}$  (Fegley *et al.* 1991), so that the atmosphere above the water cloud is likely to have a larger ratio than exists below the cloud. This means, for example, an initial solar ratio of 0.2 would be driven towards 1.0.

The final points to make about the model represented by Figure 4.14 regard the circulation pattern. While the radio data do not constrain the high altitude portion of the flow, in Section 3.2.2 and Figure 3.3 (for convenience repeated as Figure 4.15), it is shown that the Voyager IRIS instrument, probing as high as the 60 mbar level, finds a region of depressed kinetic temperatures at the latitudes that appear rich in microwave absorbers (Hanel *et al.* 1986, Flasar *et al.* 1987). Furthermore, Flasar *et al.* have interpreted these infrared measurements as indicating an upwelling exists, centered near  $-25^\circ$  latitude, with subsiding air to either side. Thus, a different instrument, sensitive to different physical properties of the atmosphere, finds the same circulation pattern at the tropopause as the radio data finds much deeper. This not only supports the model developed here, it also indicates that the vertical extent of the circulation pattern is from at least as high as the 100 mbar level (about 55 km above the  $\text{CH}_4$  cloud tops at 1 bar), down to somewhere between 25 and 50 bar, with the preferred model being 50 bar. This is a total extent of from 200 to 275 km. Section 4.2 will discuss the proposed circulation pattern in more detail, making use of a simple dynamical model to demonstrate that such a pattern is possible and is consistent with all available data. Before doing this, however, a different way of explaining the observed radio features will be explored.

### 4.1.3 Temperature Gradients

In this section, horizontal and vertical temperature gradients are explored as a means to fit the radio data, under the assumption that the atmospheric composition does not

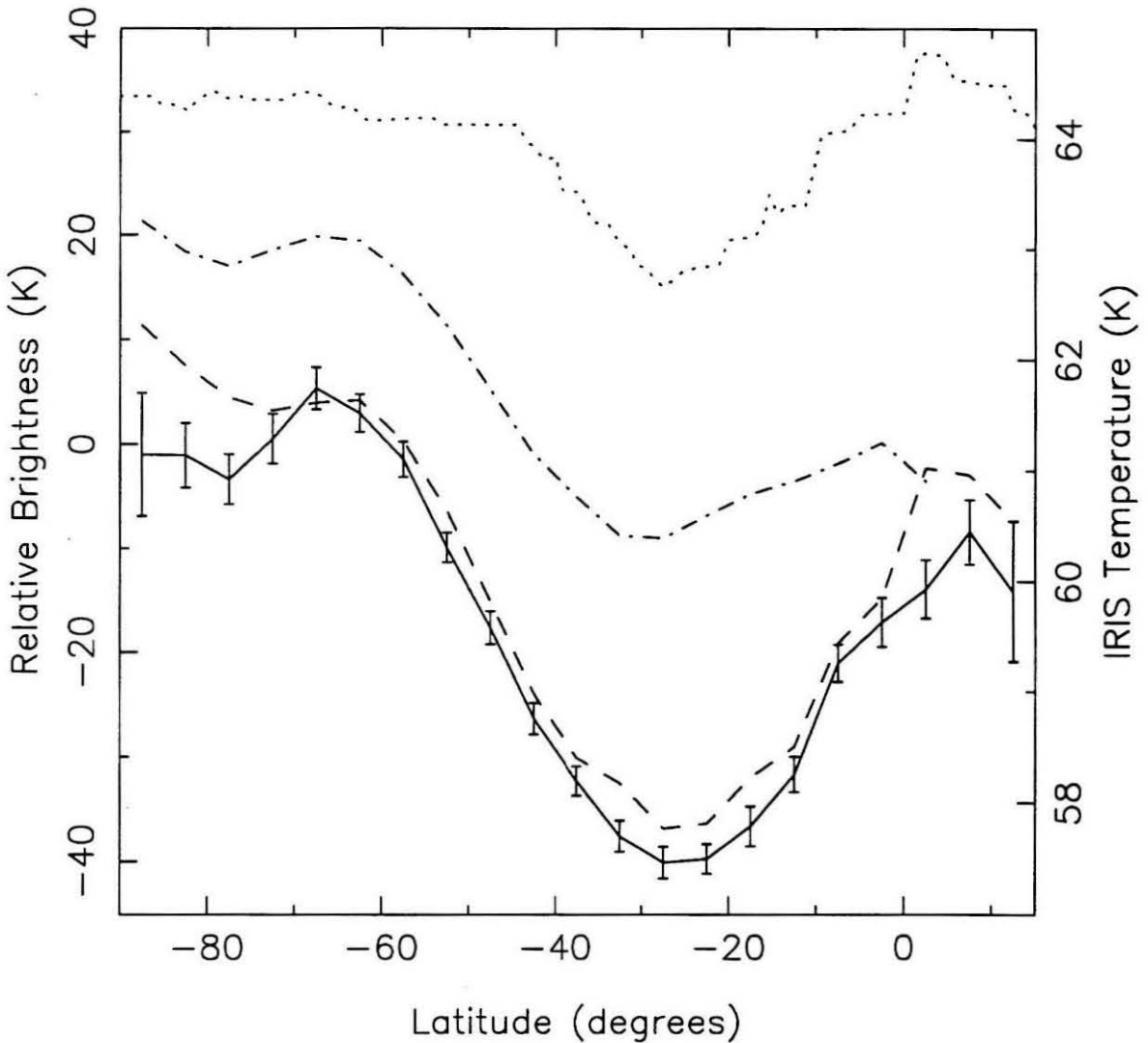


**Figure 4.15:** The intrinsic radio brightness of Uranus as a function of latitude, and upper atmospheric temperatures. This is Figure 3.3 again, and Section 3.2.2 should be referred to for a discussion of how these curves were arrived at. The solid curve is the 1989 6 cm data set and the dashed is the 1981 6 cm set. The dot-dashed curve is from 1985 observations at 2 cm. The dotted curve is the kinetic temperature near the 1 bar level as inferred from Voyager IRIS data at  $225\text{ cm}^{-1}$  by Hanel *et al.* (1986). Flasar *et al.* (1987) use IRIS data at  $325\text{ cm}^{-1}$  to find similar structures near the 100 mbar level. The similarity in shape of the curves suggests they are all caused by the same mechanism, which is believed to be an atmospheric upwelling. Since the 6 cm radio data probe as deep as 50 bars, and the infrared data as high as 100 mbar, this indicates the vertical extent of the atmospheric circulation.

vary with latitude. Based on the previous analysis, it can immediately be said that the polar regions will need to be warmer than lower latitudes, and the gradient between pole and equator will have to increase with depth in at least the upper few tens of bars of the atmosphere. Furthermore, based on Figure 4.15, pole to equator temperature gradients are likely to average about 20 K in the regions the 2 cm data are sensitive to, and 40 K where the 6 cm data probe. We can start by choosing the atmospheric composition to be the one that fits the data in the polar regions when the standard temperature profile of Figure 2.1 is used. At lower latitudes the temperature profile is then altered until a reasonable fit to the entire data set is achieved, keeping in mind that Voyager IRIS observations constrain variations in temperature with latitude to be less than  $\sim 2$  K at the 1 bar level (Hanel *et al.* 1986). The main features of the temperature structure derived in this way are representative of all models that fit the data.

As shown in Figure 4.16, using the standard temperature profile with an  $\text{NH}_3$  molar mixing ratio of  $1.1 \times 10^{-6}$ , an  $\text{H}_2\text{S}$  ratio of  $1.0 \times 10^{-6}$ , and a water ratio of  $1.0 \times 10^{-3}$  creates the right absorber distribution to simultaneously fit both the 2 cm and 6 cm data in the polar regions. Lower latitudes, however, appear much cooler. To match these latitudes, it appears a temperature profile with a lapse rate smaller in magnitude than that over the pole is needed. This keeps temperatures near their relatively cool, upper tropospheric values, and also creates a pole to equator gradient that increases with depth. One way to decrease the lapse rate is to use equilibrium instead of frozen equilibrium  $\text{H}_2$  (see Section 2.2.2). While doing this improves the fit at 2 cm, the 6 cm data require a much stronger deviation from the nominal profile. In fact, lapse rates must be cut roughly in half to provide the necessary gradients. Figure 4.17 shows the type of temperature structures required to fit the data. The solid curve is the temperature profile over the pole, corresponding to the nominal profile of Figure 2.1. The dashed curve is a variation that can fit the polar data as well. (Making the atmosphere isothermal at depth has an effect on the radio brightness equivalent to that of a deep absorbing layer, so the dashed profile

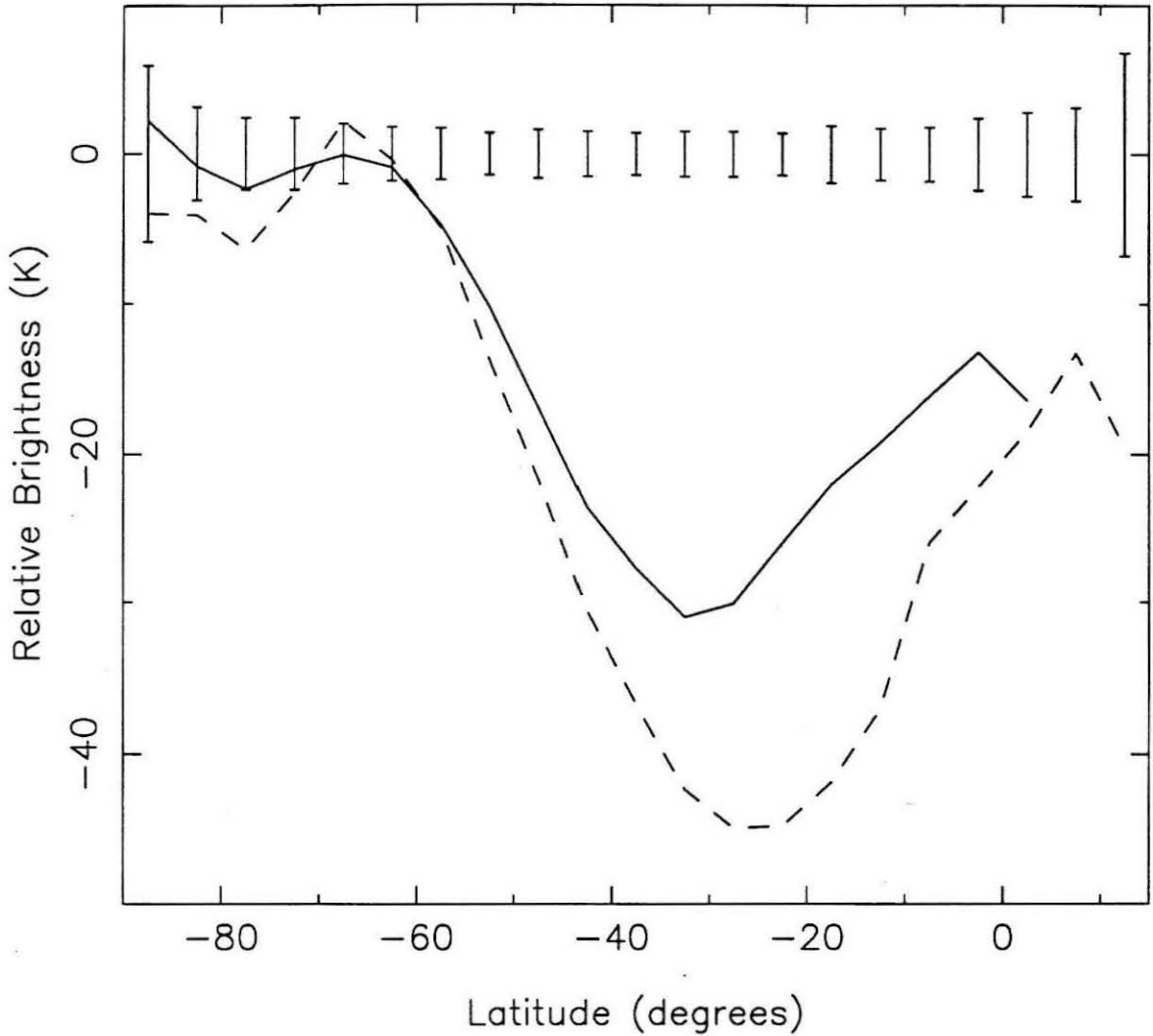


**Figure 4.16:** Fitting polar regions using the nominal temperature profile. These are data minus model plots at 2 cm (solid curve) and 6 cm (dashed curve) for a model using the nominal temperature profile, and having an  $\text{NH}_3$  molar mixing ratio of  $1.1 \times 10^{-6}$ , an  $\text{H}_2\text{S}$  ratio of  $1.0 \times 10^{-6}$ , and a water ratio of  $1.0 \times 10^{-3}$ .

does not require the  $\text{H}_2\text{S-NH}_3$  reactions that are needed when the solid profile is used.) The dot-dashed curve is an example of a temperature profile at low to mid-latitudes that fits the data. It is identical to the nominal profile at altitudes above 0.4 bar, but below this it follows an adiabatic extrapolation using equilibrium  $\text{H}_2$ . The starting pressure for this extrapolation is chosen to maximize horizontal temperature gradients at depth, while keeping them near 2 K between 0.6 and 0.8 bar, as required by Voyager IRIS data. Below 10 bar, the lapse rate is reduced in magnitude from calculated values by  $0.5 \text{ K km}^{-1}$  in order to fit the 6 cm data. (The unadjusted lapse rate is near  $1.0 \text{ K km}^{-1}$  at these levels). The dot-dashed curve could also be modified to become isothermal at some point below 10 bars, but the temperature required is different from the polar isothermal temperature that fits the data. An attractive feature of using a polar profile given by the dashed curve along with a mid-latitudinal profile given by the dot-dashed curve is that at depth, atmospheric temperatures become horizontally uniform. Using an isothermal temperature at depth over the pole also provides a better fit to the long wavelength, unresolved radio observations than the purely adiabatic case does.

These curves demonstrate the basic temperature structures needed to fit the data:

- Polar latitudes are warmer than mid-latitudes.
- The pole to equator temperature gradient increases with depth over most of the observed atmosphere.
- Lapse rates in the deep atmosphere are significantly sub-adiabatic.

Also, it should be kept in mind that low northern latitudes appear to have the same structure as the South Pole does. Interpreting the data in terms of kinetic temperature variations has some attractive points. The idea that the deep atmosphere of Uranus might be sub-adiabatic, or even isothermal, is reasonable given Uranus' low internal heat source (Pearl *et al.* 1987, 1990). Furthermore, if Uranus preferentially directs what internal heat it has towards polar latitudes (as Jupiter and Saturn are believed to do), it would be expected that convection driven by this heating from below would make the temperature

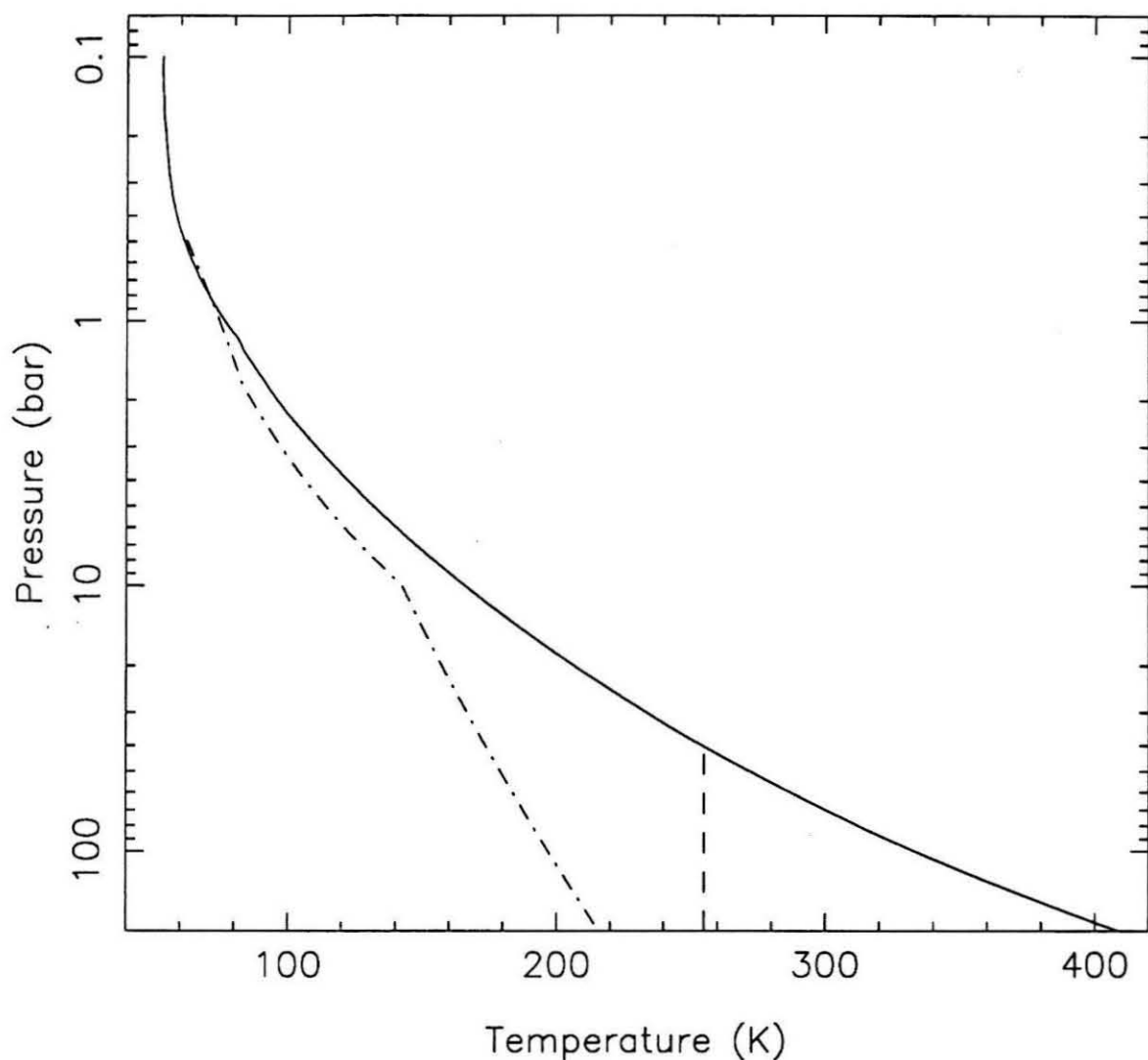


**Figure 4.17:** Representative polar and mid-latitude temperature profiles. The solid curve is the nominal temperature profile, also shown in Figure 2.1. It can yield a fit to both the 2 cm and 6 cm data over the South Pole with an appropriate atmospheric composition (see text). Alternatively, profiles that become isothermal deep in the atmosphere also provide a fit, as shown by the dashed curve. The dot-dashed curve is representative of temperature profiles at lower latitudes that fit the data. It uses an adiabatic extrapolation with equilibrium  $\text{H}_2$  to provide horizontal temperature gradients high in the atmosphere. Below 10 bars, in an attempt to provide the stronger gradients called for by the 6 cm data, the calculated lapse rate is arbitrarily reduced by  $0.5 \text{ K km}^{-1}$ .

profile at the pole more adiabatic than at lower latitudes, which is the case in Figure 4.17. It appears, however, that there are more problems with this structure than there are good points. For example, Jupiter and Saturn are believed to direct their internal energy towards polar latitudes because their equators, heated from above by the sun, inhibit convective transport from the interior (Ingersoll 1976, Ingersoll and Porco 1978). On Uranus, it is the poles that receive most of the sun's energy, and one would therefore expect most internal heating, and the most adiabatic conditions, to be directed equatorward. Another uncomfortable aspect of interpreting the radio data in terms of sub-adiabatic temperature profiles is that Neptune's microwave spectrum is similar to Uranus' (see, for example, de Pater and Massie 1985), and one would therefore like to interpret it in a similar way. Neptune, however, has an internal heat source, so it is unlikely to have a significantly sub-adiabatic temperature profile.

Another difficulty with interpreting the radio data in this way is that the resulting temperature structure, while possible, does not seem consistent with other observations. For example, IRIS observations of the stratosphere indicate an upwelling exists at low latitudes (Flasar *et al.* 1987)—but the temperature structure just derived portrays these latitudes as being more sluggish and stable than polar latitudes. Similarly, almost all of the cloud plumes seen on Uranus (Smith *et al.* 1986), which Del Genio (1989) has interpreted as being driven by moist convection from deep in the atmosphere, occur between  $-20^\circ$  and  $-40^\circ$  latitude, and it is surprising that they would be found in the most stable region of the atmosphere. Another interesting point is that if one applies the thermal wind equation (see Section 4.2.1), the temperature gradients at 20 bars found in Figure 4.17 yield wind shears of  $-100$  m/s per scale height near  $-45^\circ$ . (This means winds increase with depth.) Since the observed cloud top winds at this latitude are near 200 m/s, the zonal winds at depth would be extremely high. Finally, later in this chapter we shall discuss the time variability of Uranus' microwave spectrum, and suggest that the radio brightness features change on time scales of 20 years. It would seem difficult to

drive changes in the temperature of a deep, isothermal atmosphere on these time scales. Thus, while it is possible for temperature effects to explain the radio data, the previous interpretation involving compositional gradients seems more consistent with the available data.

## 4.2 Dynamical Modeling

### 4.2.1 Overview

Having decided that the most likely interpretation of the radio data involves compositional gradients maintained by atmospheric circulation, it needs to be demonstrated that the required circulation is physically reasonable. To do this a simple, zonally averaged, linear model based on the work of Gierasch *et al.* (1986), Flasar *et al.* (1987) and Conrath *et al.* (1990) is used. (The modeling described by these works is commonly referred to as the “IRIS model.”) The parameters defining the background atmosphere (the atmosphere before modifications due to dynamics) are assumed to be constant in latitude and time. Unlike Flasar *et al.*, variations are allowed with altitude. The model specifies the relationships between the temperature and wind fields in the atmosphere. Since the mechanism by which atmospheric motions are driven is not known, a zonal wind profile is assumed at the base of the model, and this is used to force the system of coupled equations to a solution. This solution is then compared to the idealized circulation pattern of Figure 4.14, as well as to various Voyager observations, to determine whether a consistent, physically reasonable picture of the atmosphere can be assembled. An interesting part of this modeling will be the estimation of various dynamical parameters for the atmosphere.

The observed quantities the model needs to recreate are:

- Southern Hemisphere zonal wind speeds near 1 bar (Figure 4.18), as determined from optical tracking of cloud features (Smith *et al.* 1986) and the Voyager radio occultation analysis of Lindal *et al.* (1987).
- Meridional temperature profiles at 0.1 and 0.8 bar (Figure 4.19) that are derived

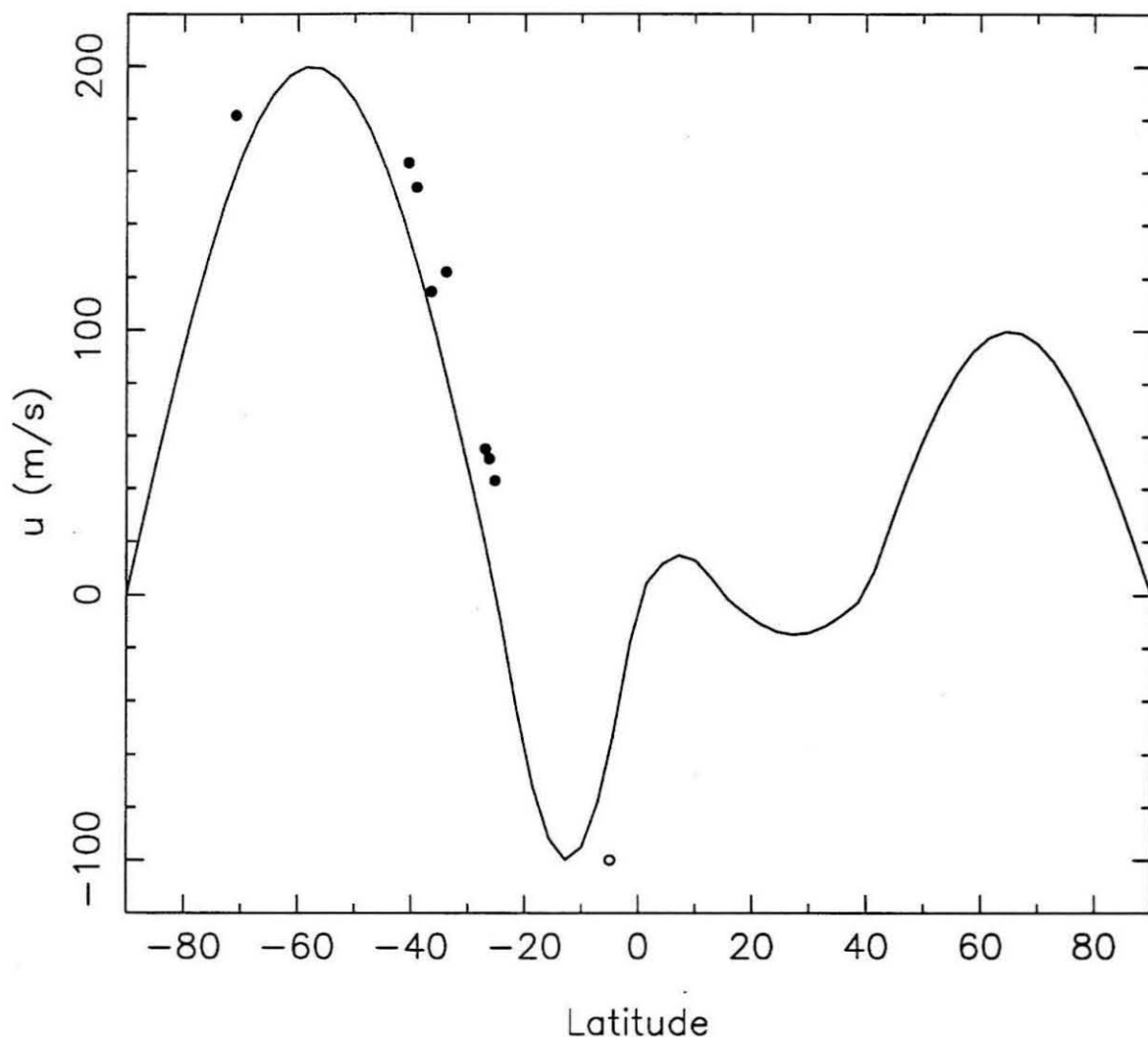


**Figure 4.18:** Observed and model cloud top winds. The solid circles represent zonal winds as determined by Smith *et al.* (1986) from optical tracking of cloud plumes. The open circle is the wind speed determined by Lindal *et al.* (1987) from the Voyager radio occultation experiment. The curve shows the zonal wind profile used in the model to approximate the observations. It consists of several segments of sine functions. In order to comply with assumptions made in the model, the wind speed is zero at the poles, the equator, and at the temperature extrema found in the Voyager IRIS data (Figure 4.19). Because the IRIS data and wind speeds are highly correlated in the Southern Hemisphere, the IRIS temperature data in the north are used to estimate the zonal winds there, where no direct observations exist.

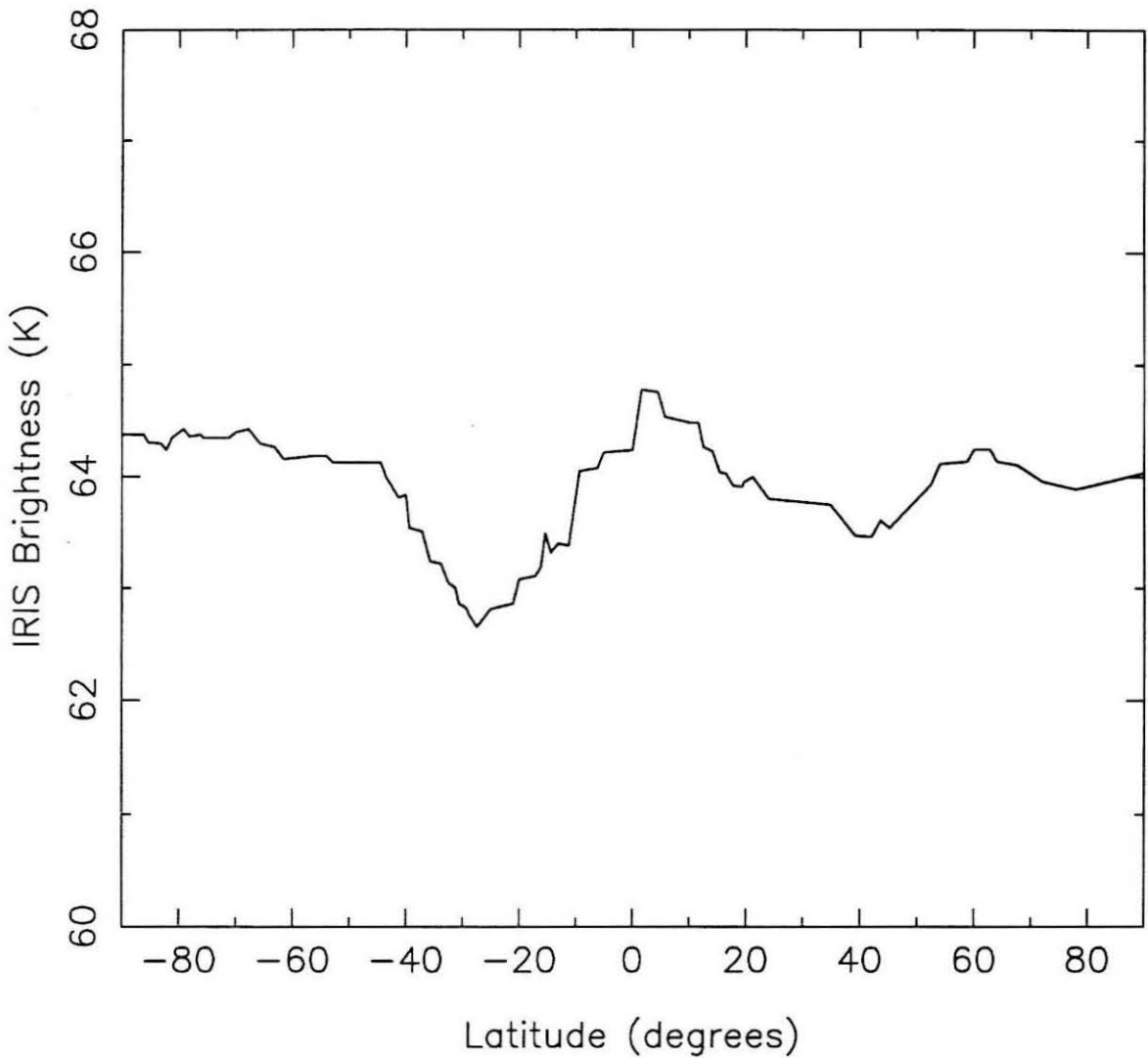


**Figure 4.19:** Voyager IRIS temperature profile near 0.8 bar. This curve is taken from Flasar *et al.* (1987), and shows the temperature retrieval based on  $325\text{ cm}^{-1}$  infrared observations of Uranus. These observations are probing the 0.5 to 1.0 bar region of the atmosphere. Data are also available that probe the 0.06 to 0.2 bar region, but they are much noisier (Flasar *et al.*). In the higher altitude data set, the temperature minima appear at the same latitudes as in the profile shown here, but the meridional variations are larger by about a factor of three.

from analyses of Voyager IRIS observations by Hanel *et al.* (1986) and Flasar *et al.* (1987).

Features desirable based on the radio data:

- A general upwelling equatorward of  $-45^\circ$ .
- Strong downdrafts over the pole, and perhaps near the equator.
- The polar downdraft dominating the atmospheric composition from above 5 bar at least down to 25 bar, and most likely down to 50 bar. The downdraft does not control the composition below 50 bar, however.
- Coupling of stratospheric and tropospheric motions.

Flasar *et al.* (1987) have already modeled the atmosphere above 1 bar and demonstrated that the IRIS model can match the Voyager observations. The present task is to maintain the agreement in the upper atmosphere while extending the model to include the deeper atmosphere probed by the radio observations.

## 4.2.2 The Model

### Governing Equations

Following the IRIS model, atmospheric motions are taken to be governed by five relations. The first is that zonal flow is maintained against friction by the Coriolis force acting on the meridional winds:

$$f v = \frac{u}{\tau_f}, \quad (4.1)$$

where  $v$  is the meridional velocity, measured positive northward, and  $f$  is the Coriolis parameter,  $f = 2\Omega \sin \theta$ , with  $\Omega$  being the angular velocity of rotation of the planet, and  $\theta$  being latitude. On the right,  $u$  is the zonal velocity, measured positive in the direction of the planet's rotation, and  $\tau_f$  is a frictional damping time. The second relationship is the thermal wind equation (Wallace and Hobbs 1977). This is based on the geostrophic approximation, which assumes that forces resulting from gravitational potential gradients on surfaces of constant pressure are balanced by the Coriolis force acting on the wind

field. Looking at the change of each of these quantities with height, and using the fact that, in hydrostatic equilibrium, changes in geopotential with height are proportional to the mean temperature of that altitude range, the following relation between meridional temperature gradients and zonal winds can be derived:

$$f \frac{\partial u}{\partial z} = -\frac{R}{a} \frac{\partial T}{\partial \theta}, \quad (4.2)$$

where  $z$  is dimensionless height, measured as a log pressure coordinate ( $z = z_0 + \ln \frac{P_0}{P}$ ),  $R$  is the gas constant (not the Universal Gas Constant),  $T$  is temperature, and  $a$  is the planetary radius.

Another coupling between temperature and winds is the assumption that, if  $T_E$  is the equilibrium temperature in the absence of any circulation, deviations from this are caused by the adiabatic heating or cooling of subsiding or rising air. Expressing this as a balance between the heat flux carried into a region by the wind field and the heat dissipated by other means:

$$\frac{N^2 H}{R} w = -\frac{T - T_E}{\tau_r}, \quad (4.3)$$

where  $w$  is the vertical velocity in scale heights per second ( $w = H \frac{dz}{dt}$ ,  $t$  being time),  $H$  is the scale height ( $H = \frac{RT}{g}$ ),  $N$  is the Brunt-Vaisala frequency (a measure of the stability of the atmosphere), and  $\tau_r$  is a time constant for the dissipation of heat.

The final two equations are just a conservation of mass requirement, expressed using a stream function,  $\psi$ ,

$$v = \frac{1}{H \rho \cos \theta} \frac{\partial \psi}{\partial z} \quad (4.4)$$

and

$$w = \frac{-1}{a \rho \cos \theta} \frac{\partial \psi}{\partial \theta}, \quad (4.5)$$

where  $\rho$  is the atmospheric density, calculated using the ideal gas law. These equations express the requirement that any mass carried into a region by the meridional wind,  $v$ , must be balanced by mass carried out by a vertical wind,  $w$ . (The zonal wind carries no net mass because this is a zonally averaged model.) The main reason for introducing

the stream function is that it will allow the equations to be expressed in an easy to solve form.

To combine the above expressions into a single equation of motion, start by substituting Equation 4.4 into 4.1, and take the vertical derivative. This yields

$$\frac{\partial u}{\partial z} = \frac{fg\tau_f}{P \cos \theta} \left\{ \frac{\partial^2 \psi}{\partial z^2} + \frac{\partial \psi}{\partial z} \left[ 1 + \frac{1}{\tau_f} \frac{\partial \tau_f}{\partial z} \right] \right\}, \quad (4.6)$$

where  $g$  is assumed constant with height, and we use the fact that  $\frac{\partial P}{\partial z} = -P$ . Similarly, substituting Equation 4.5 into 4.3 and differentiating with respect to  $\theta$  yields

$$\frac{\partial T}{\partial \theta} = \frac{\tau_r RN^2 T^2}{Pa g \cos \theta} \left[ \frac{\partial^2 \psi}{\partial \theta^2} + \frac{\sin \theta}{\cos \theta} \frac{\partial \psi}{\partial \theta} \right]. \quad (4.7)$$

Substituting Equations 4.6 and 4.7 into 4.2, yields the final equation (which, for those big on naming such things, is a second order, elliptical equation):

$$\begin{aligned} \frac{f^2 g \tau_f \cos \theta}{RT} \left\{ \frac{\partial^2 \psi}{\partial z^2} + \frac{\partial \psi}{\partial z} \left[ 1 + \frac{1}{\tau_f} \frac{\partial \tau_f}{\partial z} \right] \right\} + \\ \frac{\tau_r N^2 RT}{ga^2} \left[ \cos \theta \frac{\partial^2 \psi}{\partial \theta^2} + \sin \theta \frac{\partial \psi}{\partial \theta} \right] = 0. \end{aligned} \quad (4.8)$$

For numerical solution, the stream function is gridded,  $\psi = \psi_{j,l}$ , the  $j$  coordinate being a measure of latitude (grid spacing  $\Delta\theta$ ) and the  $l$  representing height (grid increment  $\Delta z$ ). The partial derivatives are expressed using center finite differencing,

$$\begin{aligned} \frac{\partial \psi_{j,l}}{\partial z} &= \frac{1}{2\Delta z} \{ \psi_{j,l+1} - \psi_{j,l-1} \} \\ \frac{\partial^2 \psi_{j,l}}{\partial z^2} &= \frac{1}{\Delta z^2} \{ \psi_{j,l+1} - 2\psi_{j,l} + \psi_{j,l-1} \} \end{aligned}$$

with similar expressions for  $\frac{\partial}{\partial \theta}$ . The resulting equation is solved using a simultaneous over-relaxation routine from the Numerical Recipes handbook (Press *et al.* 1986), with a slight modification to allow the specification of a derivative of  $\psi$  as the upper or lower boundary condition. (The boundary conditions are described below in a separate sub-section.)

In the equation of motion (4.8), there are several atmospheric parameters that need to be determined: none of which, it should be remembered, is a function of latitude.

The background temperature profile used is the standard one shown in Figure 2.1, but extended upward as high as 0.5 mbar to include all the radio occultation data points of Lindal *et al.* (1987). The gas constant,  $R = R^*/\mu$  (where  $R^*$  is the Universal Gas Constant and  $\mu$  is the mean molecular weight of the atmosphere), is a function of height due to condensation effects. To determine  $R$ , the expressions of Section 2.2.2 and 2.2.4 are used to find the partial pressures of all constituents as a function of height, which leads to  $\mu$ , and hence  $R$ .

The remaining parameters,  $N$ ,  $\tau_r$ , and  $\tau_f$ , are less straightforward to determine, and several ways of parameterizing them will be explored. The Brunt-Vaisala frequency,  $N$ , is the frequency of oscillation of an air parcel displaced from its current position. (Actually, it is a frequency only in a stable atmosphere.  $N$  is imaginary in an unstable atmosphere.) The standard way to calculate it is to imagine an air parcel in equilibrium with its surroundings, that is displaced adiabatically in the direction of increasing temperature. The composition of the parcel does not change in this move. The background atmosphere at the new level, however, can have a different composition. (In the troposphere, condensible species saturated at the initial point will have a higher abundance at the new level where the temperature is higher. In the stratosphere, this is not the case because of cold-trapping.) The ambient temperature at the new level will also generally be different than the (dry-adiabatically) displaced parcel's because, in the troposphere, the atmosphere follows a wet adiabat, and in the stratosphere, radiative processes dominate its profile. Assuming both parcel and background behave as ideal gases, the force per unit volume on the displaced parcel can be calculated. It is due to the differing density of parcel and background:

$$F_p = g(\rho_p - \rho_a), \quad (4.9)$$

where the subscripts  $p$  and  $a$  refer to the parcel and ambient air, respectively, and the force is measured positive in the direction of positive pressure change (downward). This equation of motion can be solved and  $N$  determined. Details of this calculation are

presented in the Appendix. It turns out that  $N$  calculated in this way is very small over large portions of the atmosphere (Figure 4.20, solid curve). To explore the effects of a more stable atmosphere on the circulation, various modifications to  $N$  are tried. The most simple is scaling the just described value by a constant factor at all altitudes.  $N$  is also calculated assuming the displaced parcel is perfectly dry (having no condensibles in it), containing only 85%  $H_2$  by number and 15% He. The value of  $N$  calculated in this way will be referred to as the “perfectly dry” value, and it will demonstrate the effect of having a relatively stable atmosphere even between cloud layers (Figure 4.20).

The final two parameters to determine are  $\tau_f$  and  $\tau_r$ . As with  $N$ , there are two ways used to calculate  $\tau_f$ , which represents a small scale dynamical overturn or frictional time. If we consider a freely convecting atmosphere (appropriate for the troposphere), the energy flux carried vertically through any level of the atmosphere should be constant with height,

$$\rho w^3 \sim c_0.$$

Scaling  $\tau_f$  as the time for parcels to move a scale height,

$$\tau_f \sim H/w.$$

Combining these equations and solving for  $\tau_f$ ,

$$\tau_f = c_1 \frac{R^{2/3}}{g} (PT^2)^{1/3}, \quad (4.10)$$

where  $c_1$  is a proportionality constant (incorporating  $c_0$ ) to be determined. An identical equation results from a scaling of  $\tau_f$  by the eddy diffusion coefficient,  $K$ ,

$$\tau_f \sim H^2/K,$$

where  $K \sim Hn^{1/3}$  and  $n$  is the number density of the atmosphere (Stone 1976). There is an alternative formulation for  $\tau_f$  that is more applicable to the stratosphere. Using the eddy diffusion coefficient for a low-density, sub-adiabatic atmosphere,  $K \propto 1/\sqrt{n}$

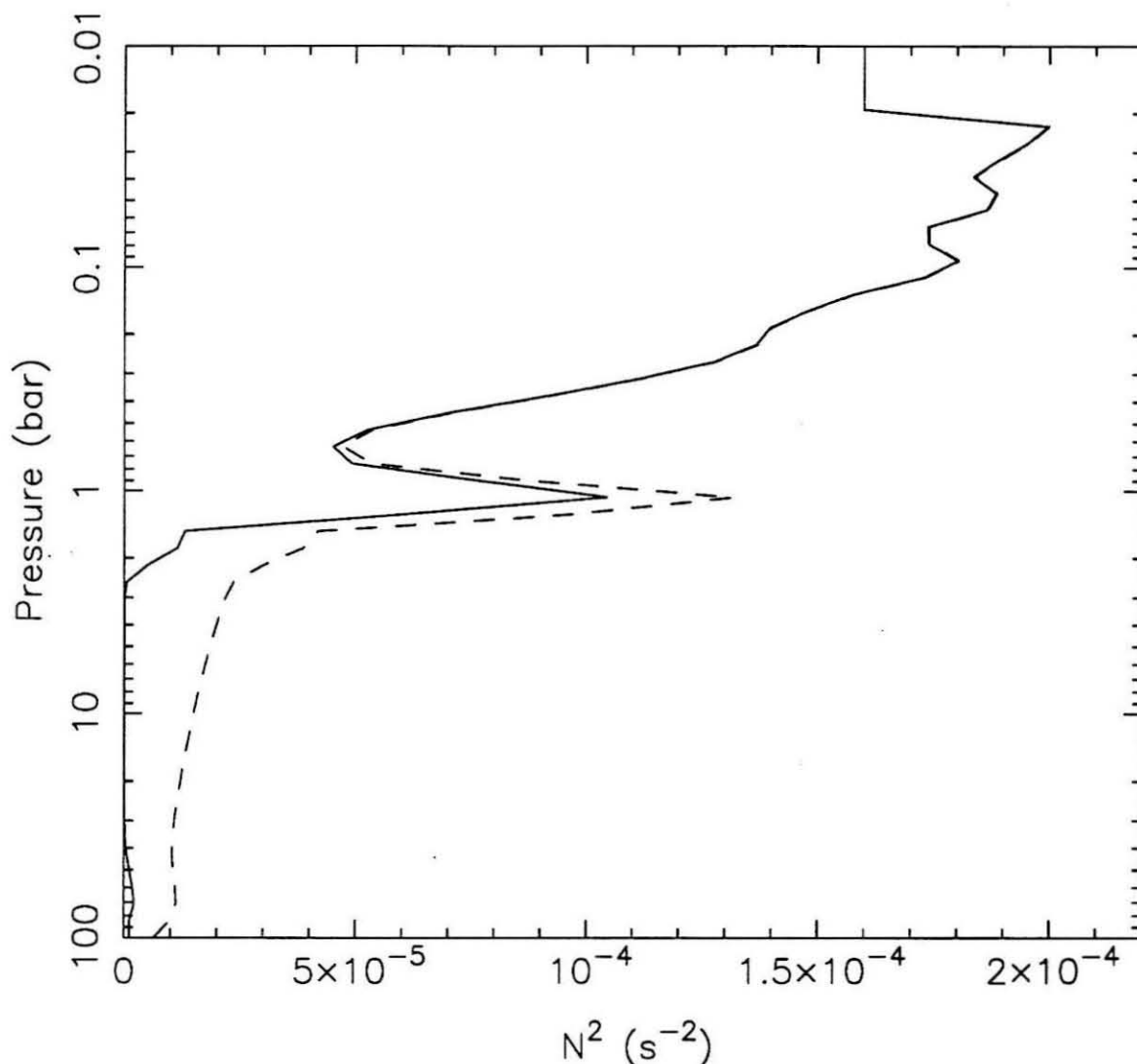


**Figure 4.20:** The atmospheric stability. These curves indicate the square of the Brunt-Vaisala frequency as a function of height in the nominal atmosphere. (This is a measure of the stability of the atmosphere.) The solid curve is for the standard  $N^2$ , as calculated in the Appendix. The dashed curve is for the “perfectly dry” case (see text). At pressures less than 0.02 bar,  $N^2$  is held constant to remove some significant oscillations that, since they are near the boundary of the model, might interfere with the numerical solution. (The oscillations are due to variations in the radio science temperature profile, and are possibly related to hydrocarbon condensation, Lindal *et al.* 1987.) The peak near 1 bar is due to  $\text{CH}_4$  condensation, while the bump near 80 bars is due to the water cloud.  $\text{NH}_3$  and  $\text{NH}_4\text{SH}$  cloud effects are too small to appear.

(Lewis and Prinn 1984), leads to

$$\tau_f = c_2 \sqrt{PT^3}, \quad (4.11)$$

where  $c_2$  is another constant. The proportionality constants  $c_1$  and  $c_2$  are determined from Flasar *et al.* (1987), where it is estimated that at the 1 bar level,

$$\tau_f \sim \tau_r \sim 4 \times 10^9 \text{ s.}$$

(This value is a radiative time constant calculated for Uranus, and the assumption is made that at this altitude  $\tau_r$  is due to radiative damping.  $\tau_f$  is also equated to this radiative time constant because, as discussed in Flasar *et al.*, IRIS data indicates at these levels  $\tau_f \simeq \tau_r$ .) The difference between the two values of  $\tau_f$  in the stratosphere turns out to be unimportant for our purposes, and generally Equation 4.10 is used at all altitudes.

The dissipative term  $\tau_r$  is assumed to be proportional to  $\tau_f$ , and the proportionality constant is usually taken to be 1, though in the analysis to follow ratios between 0.1 and 10 are considered. The reasons for assuming a proportionality are first, in the stratospheres of Uranus and Jupiter, good agreement with observation is found for  $\tau_r \simeq \tau_f$  (Gierasch *et al.* 1986, Flasar *et al.* 1987), and second, in the troposphere, radiative damping is minimal, and the dissipation of heat expressed in Equation 4.3 is caused by the same sort of turbulence as is imagined to account for the damping in Equation 4.1, so  $\tau_r$  is identical to  $\tau_f$ .

Figures 4.20 and 4.21 show plots of  $N^2$  and  $\tau_f$  for the nominal temperature profile and composition, as given in Table 2.1. In the  $N^2$  plot, the more stable regions caused by condensation of  $\text{CH}_4$  near 1 bar and, to a lesser extent,  $\text{H}_2\text{O}$  condensation near 80 bar, as well as the strong stable stratification of the stratosphere, are clear.

### Boundary Conditions

The atmospheric grid has boundaries referred to as the “top” and “bottom”, meaning highest and lowest altitudes, and the “sides,” which refer to the poles. It is the conditions

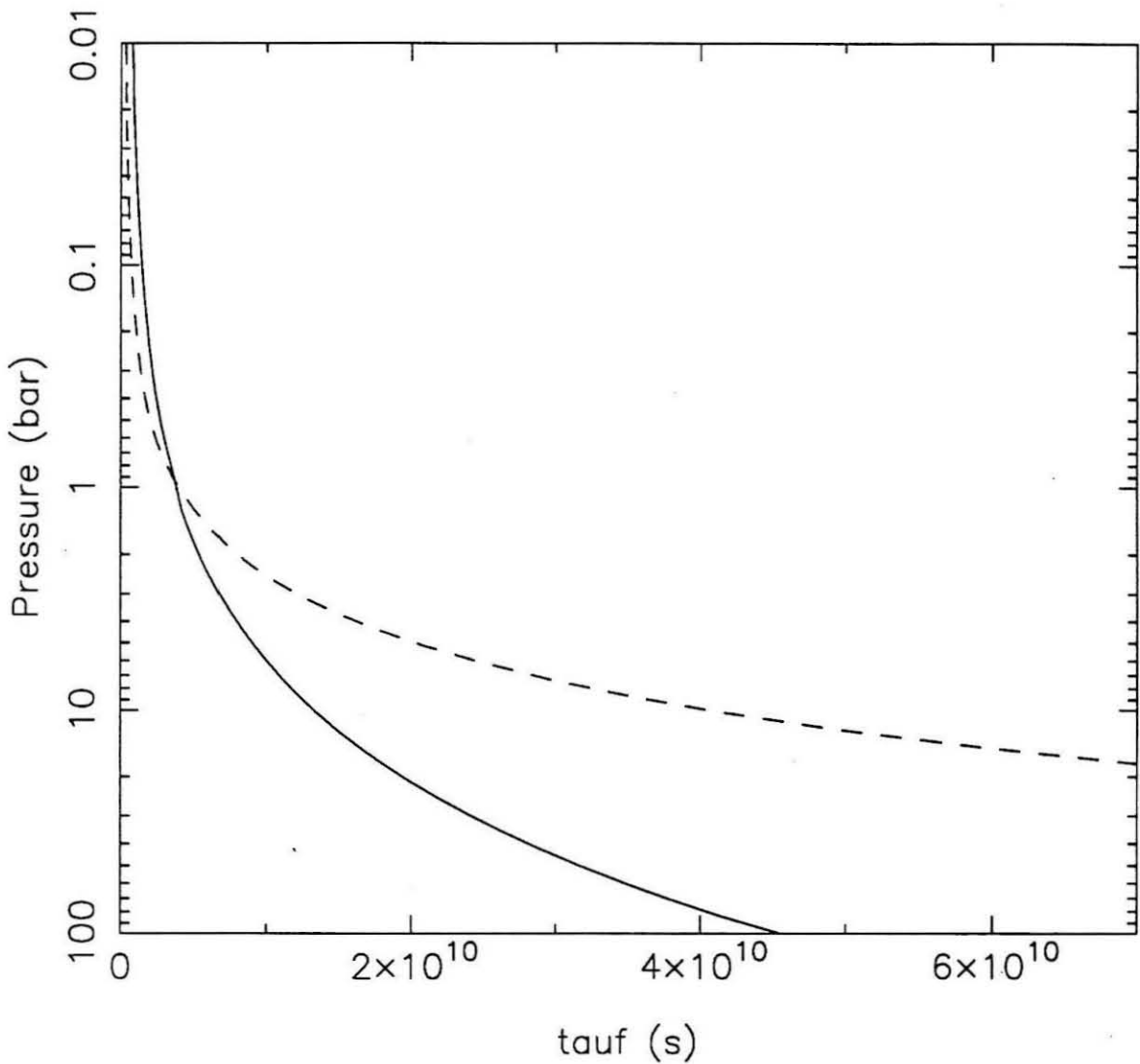


**Figure 4.21:** The frictional damping time,  $\tau_f$ . The solid curve is the damping time estimated for a freely convecting atmosphere, and should be appropriate for use in the troposphere. The dashed line is more appropriate for conditions in the stratosphere. See the text for a discussion of how these curves are calculated. Both curves are normalized to the same value at 1 bar,  $4 \times 10^9$  s, which is taken from Flasar *et al.* (1987).

along these boundaries that drive the model circulation. Along the sides, the condition is zero mass flux through the boundary at all altitudes, meaning  $v = 0$  or  $\psi = \text{constant}$ . (This is physically the requirement that, in a zonal average sense, flow cannot occur southward from the South Pole or northward from the North Pole.) Since  $\psi$  is defined in a way that allows an arbitrary constant to be added to it, without loss of generality we can take  $\psi = 0$  here. Along the top, zero mass flux ( $w = 0$ , implying  $\psi = 0$ ) is also used because this region represents the uppermost reaches of the atmosphere, and it is unphysical to be losing or gaining mass from space via the general circulation. (While exploring the model's responses, boundary conditions of specified  $w$  or  $u$  were also tried here, in which case a zero net mass flux across the boundary is the requirement, see below.) Along the bottom of the model, the usual approach is to specify  $u$ , the zonal winds, and let this drive the atmospheric circulation. To use  $u$  as a condition on  $\psi$ , combine equations 4.1 and 4.4 to express  $\frac{\partial\psi}{\partial z}$  in terms of  $u$ , which makes specification of  $u$  equivalent to specifying the vertical derivative of  $\psi$  on the boundary.

$$\frac{\partial\psi}{\partial z} = \frac{u}{f\tau_f} H\rho \cos\theta.$$

If  $l = 1$  represents the lower boundary, then this derivative condition can be expressed as

$$\psi_{j,1} = \psi_{j,2} - \frac{\partial\psi}{\partial z} \Delta z.$$

Substituting this into the finite difference equation along the  $l = 2$  line, and then proceeding with the solution as normal, incorporates the  $u$  field into the solution. An alternative boundary condition is to use a specified temperature perturbation along the bottom, which by virtue of Equation 4.3, is equivalent to specifying a vertical wind speed. Using Equation 4.5, this in turn specifies the derivative of  $\psi$  with latitude.

$$\frac{\partial\psi}{\partial\theta} = -aw\rho \cos\theta.$$

Since

$$\psi_{j,1} = \psi_{j-1,1} + \frac{\partial\psi}{\partial\theta} \Delta\theta \quad \text{for } j > 1,$$

and the value of  $\psi_{1,1}$  is known to be zero from the side boundary condition, all values of  $\psi$  can be determined along the bottom. When specifying  $w$  (or  $T$ ), care must be taken to ensure that the net flux across the entire boundary is zero—otherwise the system keeps gaining or losing mass, and a steady state is never reached.

### 4.2.3 Results

We can now discuss the atmospheric circulation that results from the model just described. Figure 4.22 shows the stream function (units of  $\text{kg m}^{-1} \text{s}^{-1}$ ) for a model with a lower boundary at 50 bars and the zonal wind specified on this boundary to be the same as the cloud top winds (Figure 4.18).  $N^2$  is calculated in the standard way (the solid curve of Figure 4.20),  $\tau_f$  is calculated for a freely convective atmosphere, and  $\tau_r = \tau_f$ . The direction of motion along stream lines is indicated. The dominant feature is clearly an upwelling centered at  $-25^\circ$  latitude, with subsidence over the South Pole and low northern latitudes. There is also a smaller upwelling at  $+40^\circ$ , but its intensity falls below most contour levels plotted. From Equation 4.3, it is expected that these upwelling regions will have relatively low temperatures, which is shown to be the case in Figure 4.23.

To compare these results to the Voyager observations, Figure 4.24 shows the zonal wind horizontal profile at several heights, and Figure 4.25 does the same for vertical profiles at several latitudes. From these figures, it can be seen that no appreciable damping of the winds occurs between 50 and 1 bar. This is because the atmosphere is essentially neutrally stable between the water and methane clouds, so there is little resistance to the motions forced from below. At the  $\text{CH}_4$  cloud the atmosphere becomes substantially stable, and wind speeds drop. At 0.8 bar (just above the cloud tops), however, the basic zonal wind profile is still observed. This means the observed Voyager winds at the cloud tops can be recreated by this model. The second set of Voyager observations that must be satisfied are temperatures measured by the IRIS instrument

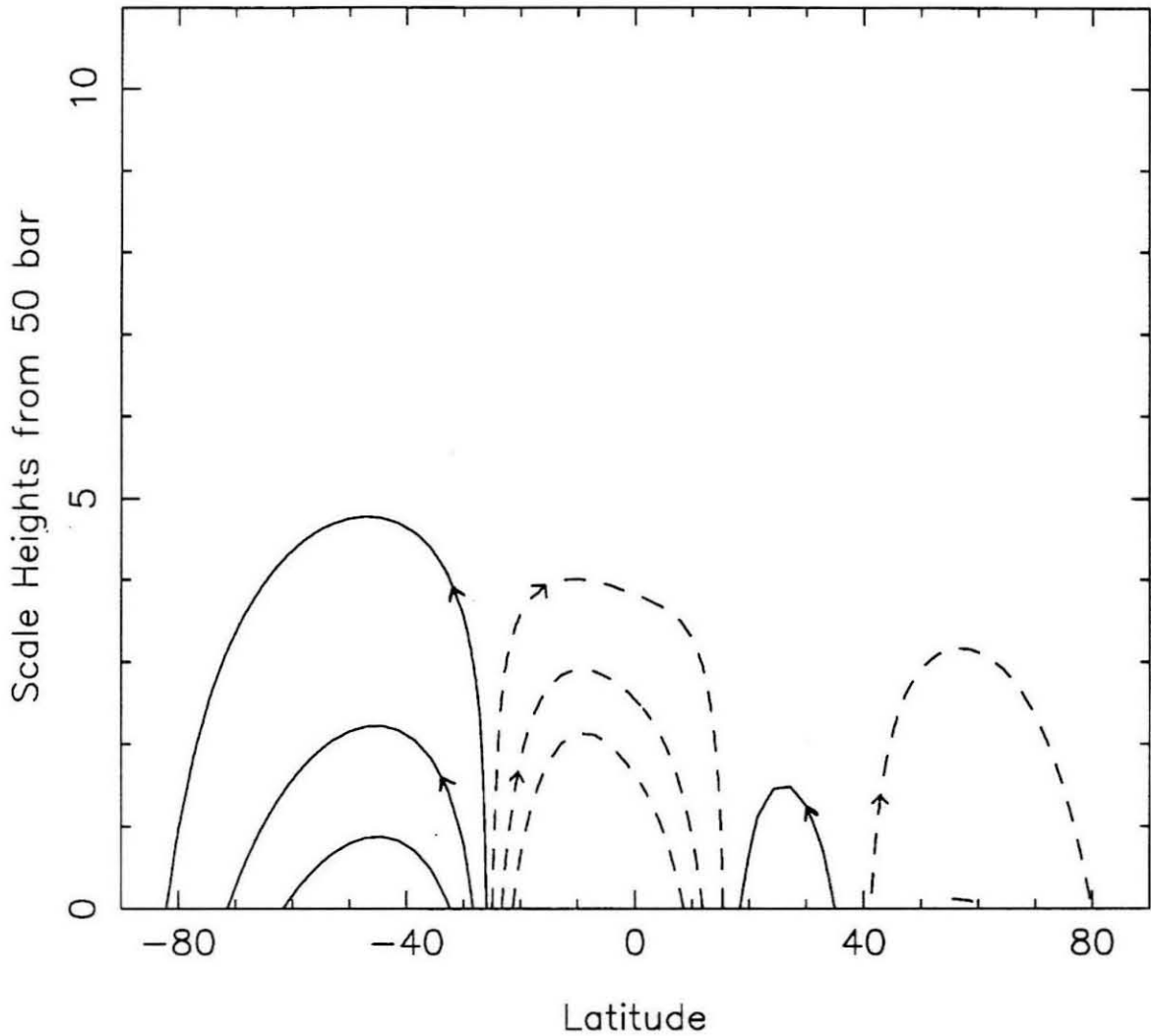


**Figure 4.22:** Contour plot of the stream function,  $\psi$ , in  $\text{kg/m/s}$ . Positive (solid) contours indicate circulation in a right hand sense, as indicated by the arrows. Applying the zonal winds observed at the cloud tops (Figure 4.18) as a forcing function at the 50 bar level drives a strong upwelling centered at  $-25^\circ$  latitude, and a weaker one near  $40^\circ$ . The 1 bar level is about 4 scale heights above 50 bars. Contours are plotted at  $\pm 2$ ,  $\pm 10$ , and  $\pm 20$   $\text{kg/m/s}$ .

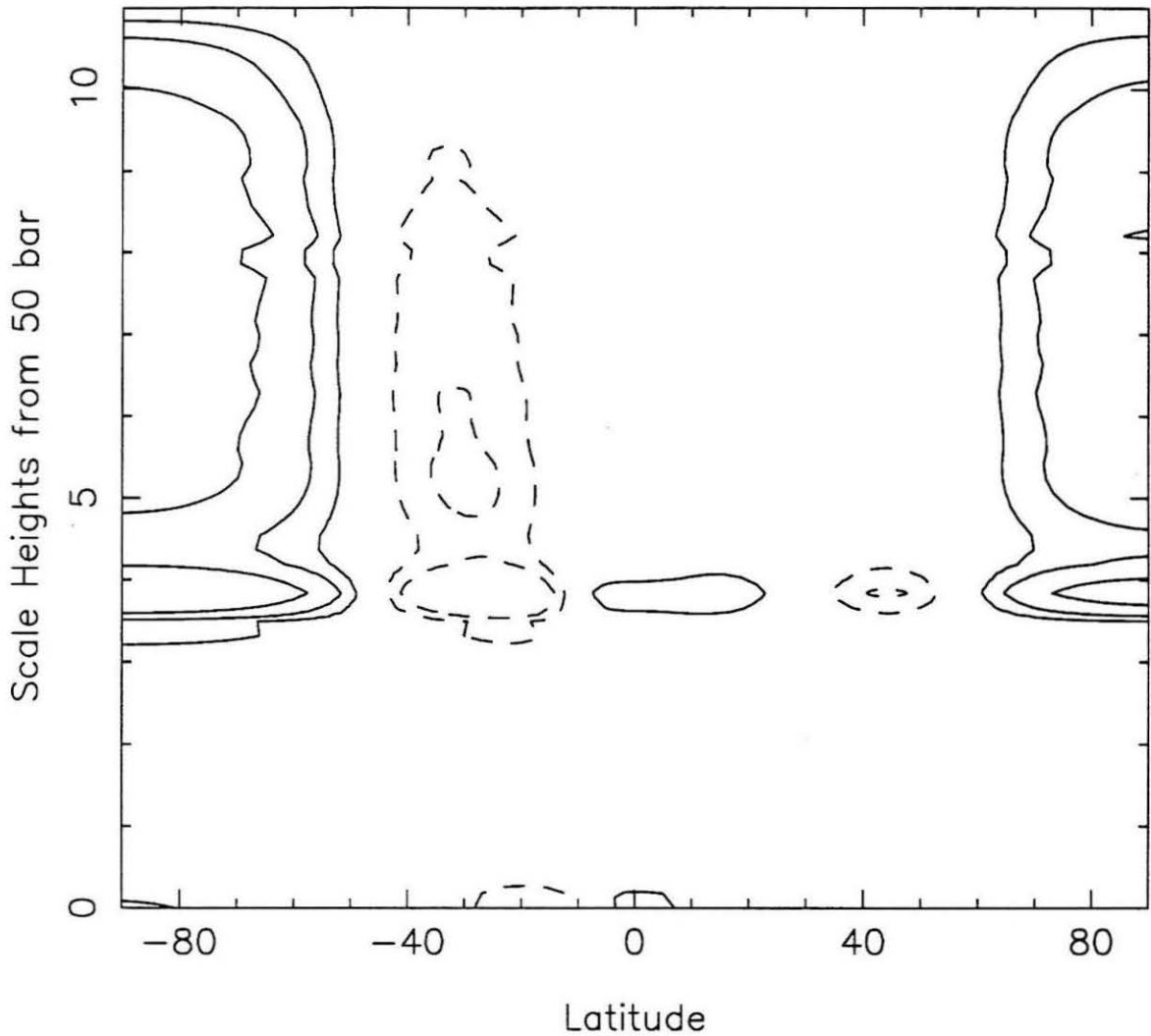


**Figure 4.23:** Contour plot of the temperature perturbations due to the general circulation,  $T - T_E$ . The 1 bar pressure level is at approximately 4 scale heights, and the 10 scale height point is equivalent to 2 mbar. The upwellings cool the atmosphere due to adiabatic expansion (dashed contours), while areas of subsidence are marked by warmer temperatures (solid contours). The region above the  $\text{CH}_4$  cloud (which is near 4 scale heights) has a sub-adiabatic temperature profile, so air parcels moved adiabatically end up having temperatures quite different from their surroundings, accounting for the concentration of contours at high altitude. Contour levels are  $\pm 1$ ,  $\pm 2$ , and 4 K.

near 0.8 and 0.1 bar, shown in Figure 4.19. We shall focus on the temperatures in the Southern Hemisphere because the forcing function used in the Northern Hemisphere is not well constrained by observations. Figure 4.26 shows model temperatures, relative to the equilibrium temperature in the absence of dynamics,  $T - T_E$ , at 10, 0.8, and 0.1 bar. At 0.8 bar, the model temperature has a 2 K dip centered near  $-25^\circ$ , which matches very well with the one observed. The relatively constant equatorial temperatures also match observations. The temperature maxima seen over both poles, however, is not observed. This discrepancy may be due to the fact that the model equilibrium temperature ( $T_E$  in Equation 4.3) is assumed constant with latitude, and is based on the observed temperature profile near  $-5^\circ$  latitude (the Voyager radio occultation ingress latitude). It was already pointed out, however, that the  $98^\circ$  obliquity of Uranus means the poles receive more sunlight than the equator, and therefore  $T_E$ , (and probably other parameters as well) can be different here. Thus, it is suggested that limitations of the model can create this discrepancy. Overall, the fact that the total variation in model temperatures is about 6 K at 0.8 bar, while the data vary by 2 K, is encouraging because these values are quite close given the uncertainties involved in the calculations. Similarly, the fact that model temperatures at 0.1 bar vary by about 8 K, while the data vary by 6 K is quite good. Note that in agreement with the observations, temperature variations seem to increase with altitude in this region. A problem with the model temperatures is that at the 0.1 bar level, the minimum at  $-25^\circ$  is only a third of what the data call for. Given the fact that the calculated temperature deviation is proportional to both  $N^2$  and  $\tau_r$ , this factor of three can be accounted for by uncertainty in the model parameter values.

Having found that the model can be made to fit the Voyager data (which repeats the work of Flasar *et al.* 1987), can it also match the radio data? In Section 4.2.1, features called for by the data are specified, and it appears all can be present in the model. There is an upwelling at  $-45^\circ$  with subsidence over the pole and equator. Furthermore, there is a strong coupling of atmospheric motions between 50 and 0.1 bar. The remaining

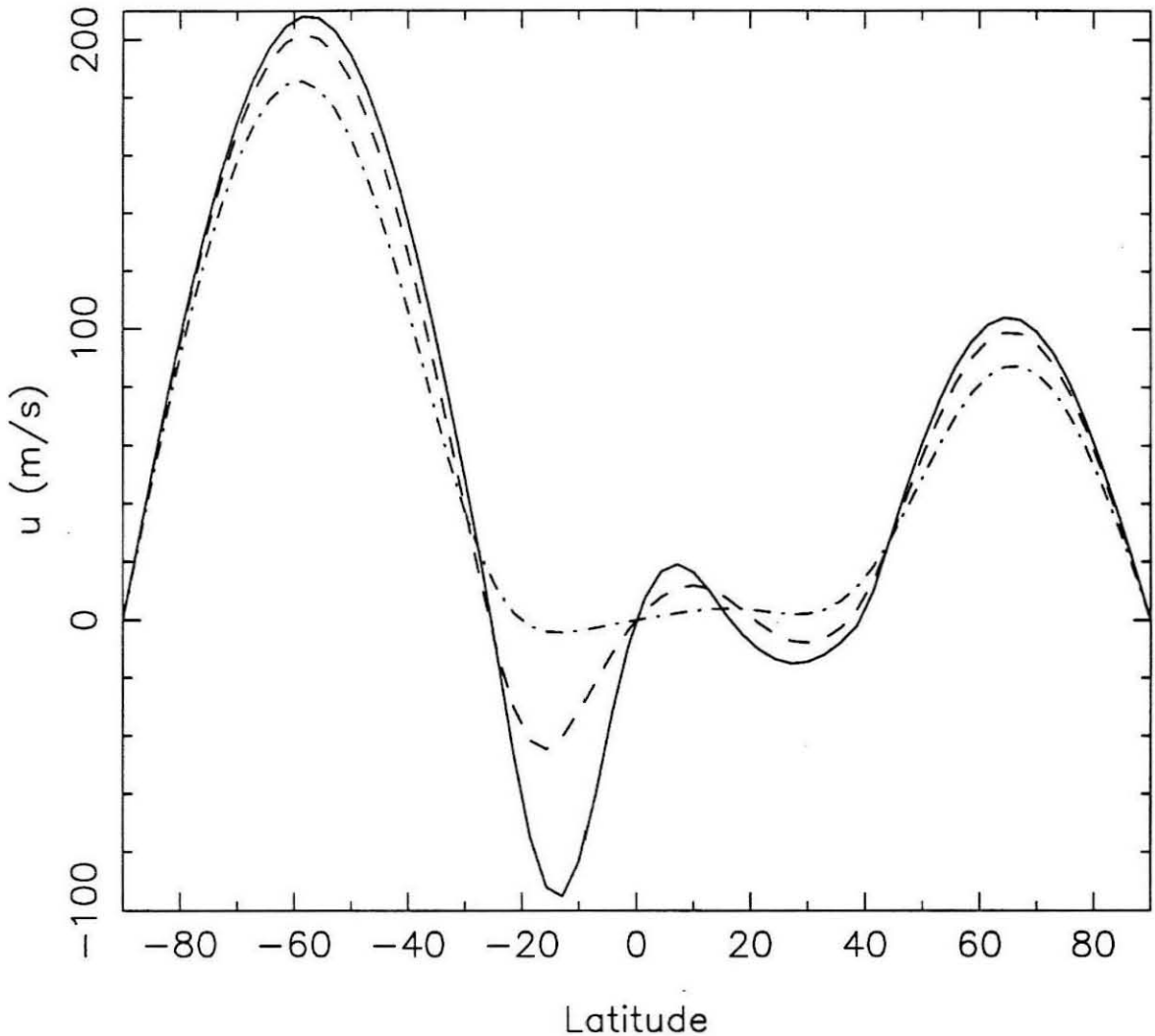


**Figure 4.24:** Model zonal wind speeds,  $u$ . These curves show the calculated zonal wind profiles at the 10 bar level (solid curve), 0.8 bar level (dashed curve), and 0.1 bar level (dot-dashed). There is very little damping of the zonal winds between 50 and 1 bar, so the profile at 10 bars is essentially the same as what is forced at 50 bars. At 0.8 bar, which is near where the winds observed by Voyager are, the basic structure of the winds are the same, though there is evidence of damping near the equator. Higher up, the winds near the equator are almost completely damped out, and only the polar jets remain. As discussed by Gierasch *et al.* (1986), the decay scale height of the zonal winds is proportional to the sine of the latitude as well as the width of the zonal banding. It is therefore a general feature of all the models considered here that the broad, high latitude zonal wind features persist at altitude.

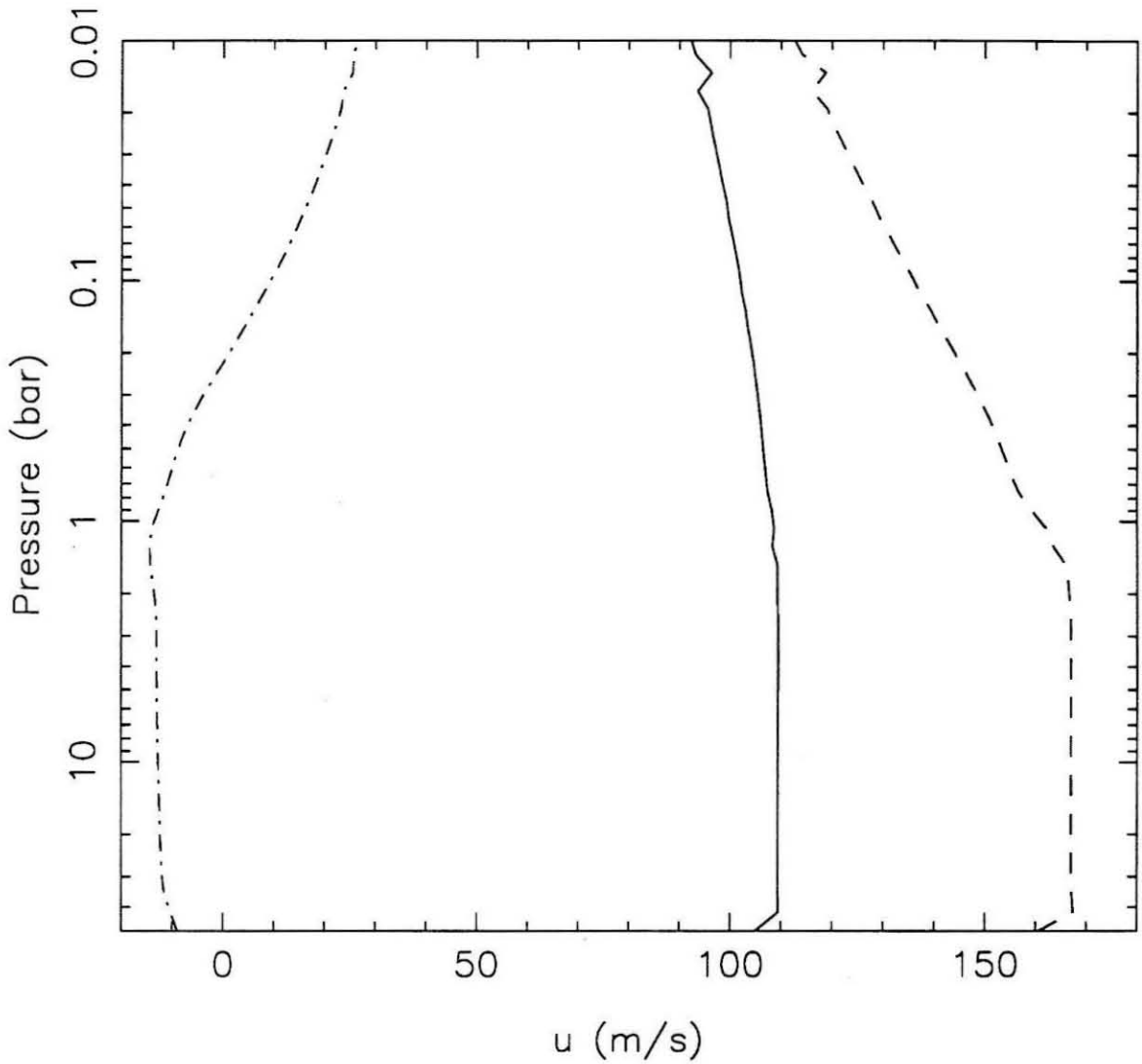


**Figure 4.25:** Vertical profiles of model zonal winds. The solid curve indicates the zonal wind as a function of height at  $-80^\circ$  latitude, which corresponds to the center of the region of subsidence. The dashed curve is at a latitude of  $-45^\circ$ , near the maximum in the zonal wind profile. The dot-dashed curve is in the updraft, at  $-25^\circ$  latitude. The damping of motions at altitudes above 1 bar is clearly seen.

requirement of the radio data, that the subsiding column of air dominate the composition from at least as high as 5 bar to at least as deep as 25 bar (but not below 50 bar) is more difficult to test. While it is easy to see that the dominant motion is subsidence in this region (Figures 4.22 and 4.27), the question that remains is, are these motions and the mass transport they imply enough to dominate the composition? This is not entirely clear. The reason for this is that even though the model circulation does not have any mixing between polar subsiding regions and the low-latitude upwelling ( $v = 0$  at the transition latitude between rising and falling parcels), there is undoubtedly some smaller scale mixing that occurs due to turbulence. It is beyond the scope of this thesis to carry out a detailed estimation of this effect. The crude approximations presented below suggest the composition of the south polar region is indeed controlled by the general circulation, but this conclusion could be altered depending on the nature of the turbulence.

As a rough estimate of turbulent mixing, a “turbulent velocity” can be found by dividing an atmospheric length scale by a mixing time, such as

$$v_t \sim H/\tau_f.$$

Comparing this velocity directly to the vertical wind speed,  $w$ , is of limited value because the total mass fluxes depend on the density of the moving air masses, and the area across which the transport occurs. For example, consider the absorber depleted polar regions to be a box, with vertical sides running between 5 and 50 bar, and a horizontal top extending from  $-45$  to  $-90^\circ$  latitude. At the top of this box, the total absorber depleted mass flux entering due to  $w$  is about ten times greater than the total mass flux in through the equatorward facing side as a result of  $v_t$ . This would indicate that the subsiding air does dominate the composition. A different conclusion is reached if one considers the source of contamination to be the base instead of the side. Now, the area across which  $w$  and  $v_t$  bring mass into the region is the same, so the ratio of subsiding air mass to turbulent air mass goes as the density at 5 bars times  $w$  at 5 bars, divided by the density and  $v_t$  at 50 bars. In this case, the ratio is 0.1, which indicates the subsiding air does

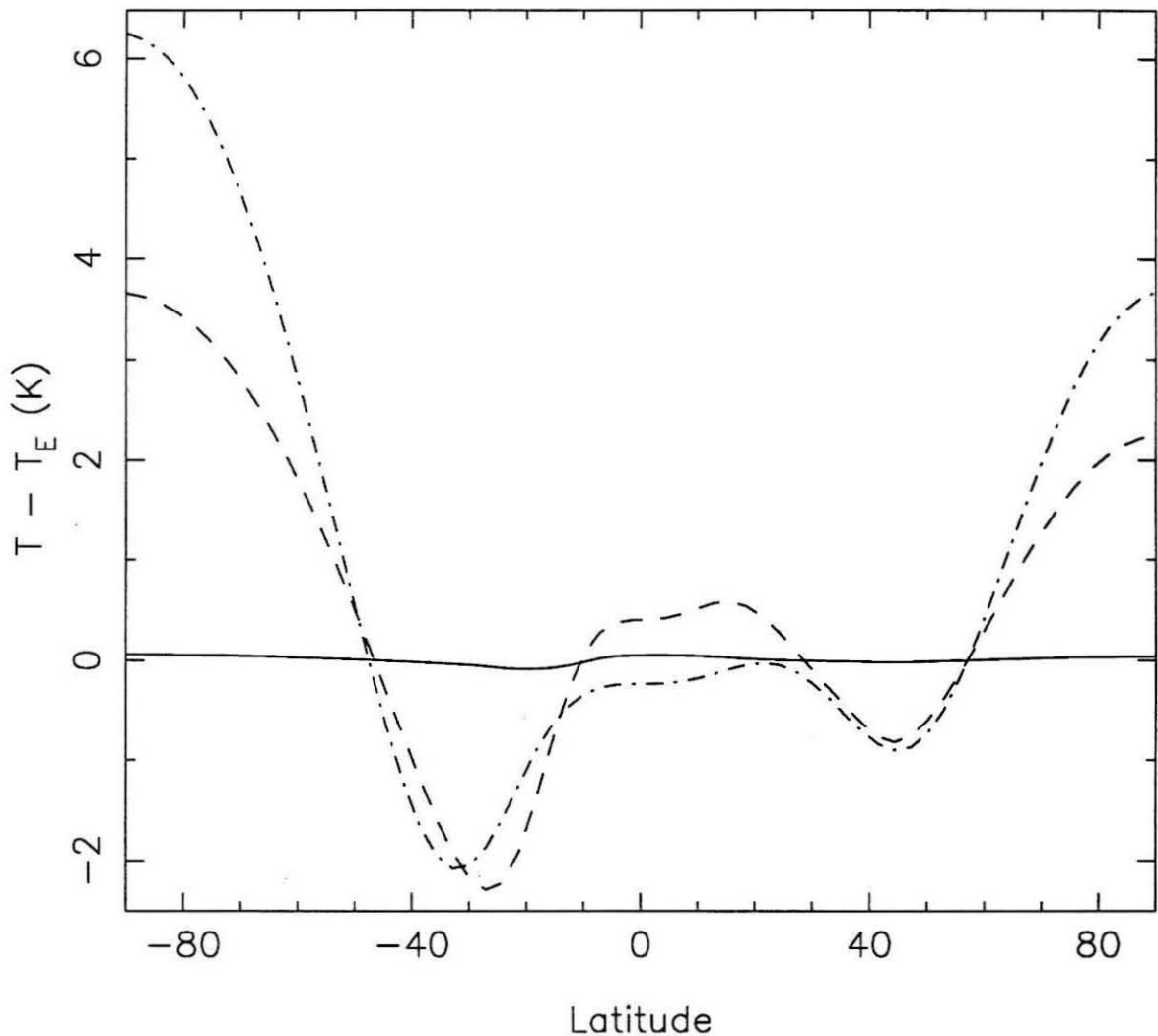


**Figure 4.26:** Meridional temperature profiles. These curves should be compared to the Voyager IRIS data of Figure 4.19, and show deviations of temperature due to dynamical effects as a function of latitude. At 10 bars, temperature variations are small, as shown by the solid curve. At 0.8 and 0.1 bar, the dashed and dot-dashed curves indicate a temperature minimum of about 2 K exists between  $-20^\circ$  and  $-40^\circ$ . This is in excellent agreement with the IRIS data 0.8 bar, but the 0.1 bar minima seems to be too shallow in the model. Over the pole, the model shows large temperature deviations that do not appear in the data. As discussed in the text, the discrepancies between model temperatures and IRIS data may be due to the model being overly simplified.

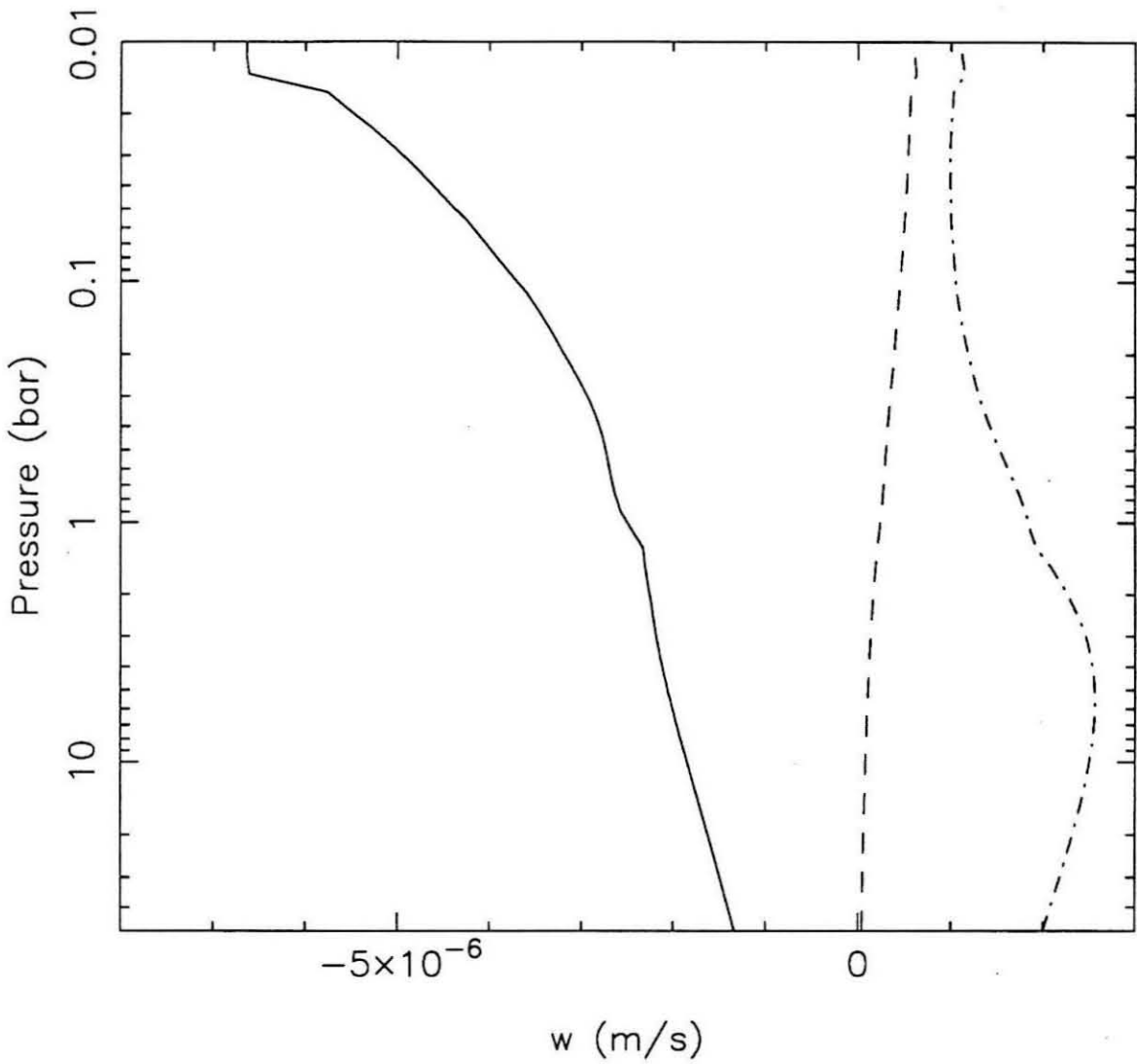


**Figure 4.27:** Vertical profile of vertical winds,  $w$ . These curves show how  $w$  varies with height in the region of subsidence ( $-80^\circ$ , solid curve), in the upwelling ( $-25^\circ$ , dot-dashed curve), and between the two regions ( $-45^\circ$ , dashed curve).

not dominate. Because the general circulation of the model creates no meridional flow at the sides of the hypothetical box to resist mixing, while at the base of the box, upward turbulent mixing is working directly against the general flow, it seems reasonable to expect most turbulent mixing to come from the side. It therefore appears that the model can satisfy the compositional constraint as well.

One aspect of the radio data not yet directly addressed is that the subsiding air must cease dominating the composition somewhere between 25 and 50 bars. There are two ways this can be accomplished. One is to drive the forcing from this altitude range. In this scenario, the region of subsidence quickly dies out below the forcing level, and well-mixed, absorber-rich atmosphere prevails. Another possibility is that the turbulence just discussed is the controlling factor. Because the turbulent mass flux brought in from the sides is proportional to the atmospheric density, at deeper levels this flux can eventually dominate over what is supplied at the “top”.

Before ending this brief foray into atmospheric dynamics, it is useful to consider classes of models that do not fit the observations. If the base level of the model is moved from 50 to 100 bar, zonal winds near the equator begin to be damped out by the time the cloud tops are reached, and to avoid disagreement with the radio occultation wind speed estimate near  $-5^\circ$ , the wind speed forced at the base of the model must be significantly larger than that observed at the cloud tops. Now that models that include regions below 80 bar are being considered, the  $\text{H}_2\text{O}$  abundance used must be reconsidered. Up until now, a  $\text{H}_2\text{O}$  mixing ratio of  $1.0 \times 10^{-3}$  has been assumed. This is the lower limit to the water abundance, based on radio observations. Using the lower limit was acceptable because the model did not include levels deep enough to be affected by the additional water at depth. This is no longer the case. For example, if the  $\text{H}_2\text{O}$  mixing ratio is increased to 4% (which is comparable to the factor of 20 enhancement observed in  $\text{CH}_4$  over a solar abundance), and the atmospheric forcing level is set at 500 bar, the stability caused by the water cloud is enough to significantly decouple the forcing region from

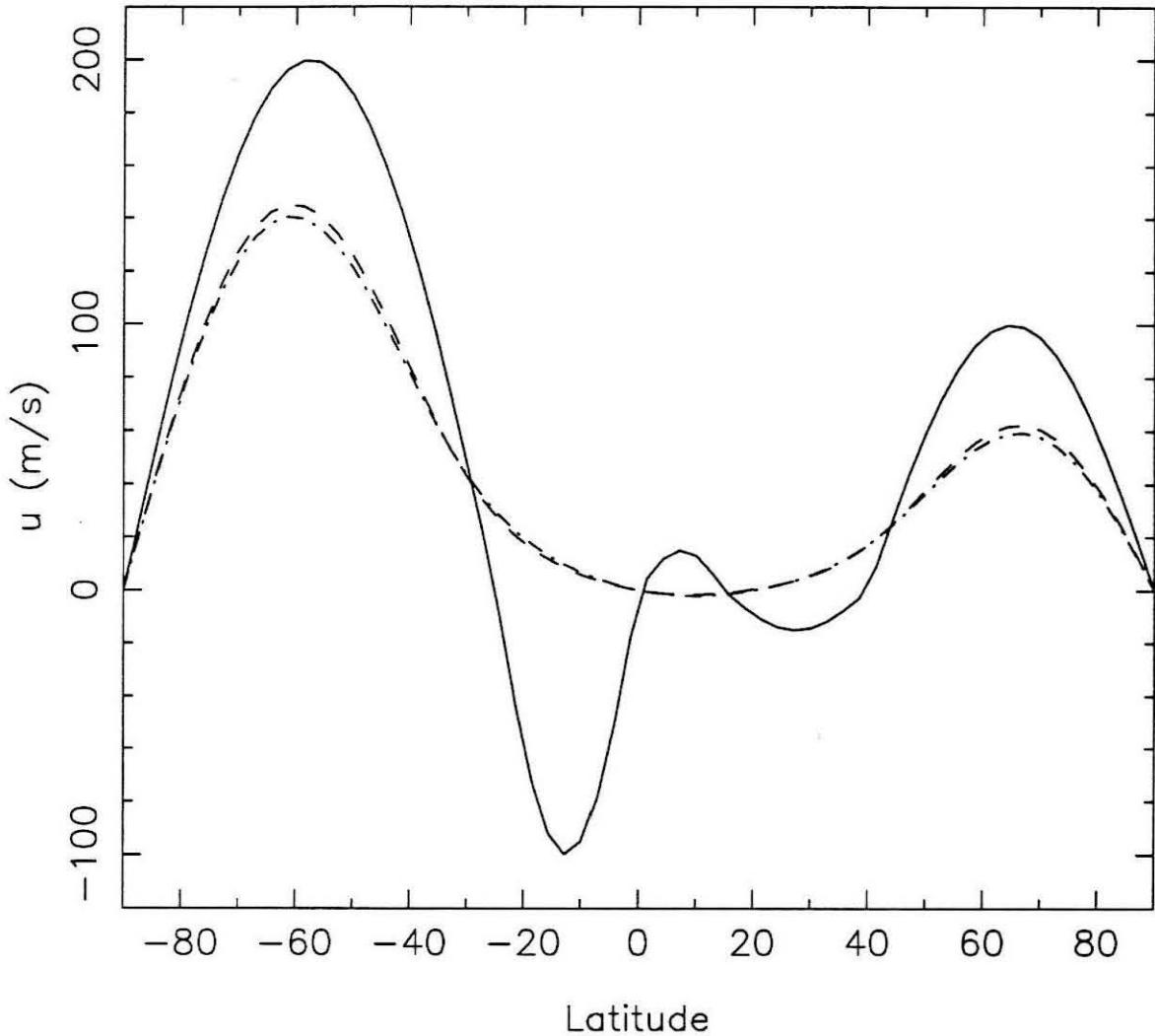


**Figure 4.28:** Decoupling the forcing region from the cloud tops. These curves show zonal wind profiles for a model that has motions forced at the 500 bar level, and has a 4%  $\text{H}_2\text{O}$  molar mixing ratio. The combination of stability created by the water cloud and deep forcing causes winds near the equator to damp out far below the cloud tops. The solid curve shows the zonal winds at the base of the model (500 bars), while the dashed and dot-dashed curves show the profiles at 10 and 0.8 bars, respectively.

the cloud tops. This is shown in Figure 4.28, which shows that the zonal winds near the equator are completely damped out, leaving only the strong polar jets. This model also shows no temperature variability above 1 bar at latitudes between  $-40$  and  $40^\circ$ , in disagreement with Voyager IRIS results.

Another way to decouple the upper atmosphere from motions generated at depth is to increase  $N^2$  by a factor of 10 at all altitudes, or to use the “perfectly dry” model when calculating the Brunt-Vaisala frequency (see Equation 4.9 and the associated discussion). In this case, even if motions are forced as high as 50 bar, the results are comparable to those found when forcing was as deep as 500 bar with the “standard”  $N$  (Figure 4.28). Enhancing the  $\text{CH}_4$  mixing ratio to 10% also creates enough stability to decouple the upper and lower atmospheres. Altering the ratio between  $\tau_r$  and  $\tau_f$  can have a significant effect on the model atmosphere as well. If  $\tau_r$  is made to be ten times as large as  $\tau_f$ , all equatorial structure in the zonal wind and temperature profiles is lost, similar to what is seen in Figure 4.28. If  $\tau_r/\tau_f$  is set to 0.1, the wind field above the clouds is correct, as is the shape of the temperature profile, but now the amplitude of the temperature variations are much smaller, only about 1 K at both 0.8 and 0.1 bar.

The conclusion to be drawn from the above discussions is that, given the flexibility allowed by an imprecise knowledge of basic atmospheric parameters, it appears possible to develop a model that is consistent with Voyager observations, the ground-based radio data, and atmospheric physics. It is also interesting that using some standard assumptions,  $N^2$  is very low between the  $\text{CH}_4$  and  $\text{H}_2\text{O}$  clouds, indicating the atmosphere is almost neutrally stable between 2 and 50 bars. Within the framework of the so-called “IRIS model,” it appears that the circulation of the stratosphere and upper troposphere is being driven from somewhere between 25 and a few hundred bars. The increase in atmospheric stability caused by water condensation is an important factor in determining the allowed range of altitudes from which the observed motions can be driven.

### 4.3 Time Variability

In Section 2.3.1, when unresolved observations of Uranus were first presented, it was seen that Uranus brightened between 1965 and the present. Klein and Turegano (1978) were the first to recognize this trend in the data, and additional discussion of it appears in Briggs and Andrew (1980), Gulkis *et al.* (1983), Jaffe *et al.* (1984), Gulkis and de Pater (1984), and Hofstadter and Muhleman (1989). The disk averaged data, along with some model spectra that will be discussed shortly, are presented again in Figure 4.29. While many of the older data are of low quality and earn the full range of their error bars, the conclusion seems inescapable that something has been changing. One interpretation of this is that the temperature or composition of the observed part of Uranus has actually been changing over the last 25 years, perhaps due to seasonal effects. Another possibility is that a static brightness distribution exists on the planet, but as the observing geometry changes over the years (bringing different latitudinal regions into view), the average brightness changes.

As the first disk resolved observations became available (Briggs and Andrew 1980, Jaffe *et al.* 1984, Gulkis and de Pater 1984), it was clear that a pole to equator brightness gradient did indeed exist, and it could explain some of the observed variability by geometric effects. It is still unclear whether this can explain all of the variability: part of the problem being uncertainty in how much of the variability is real and how much might be tied to bad data. Using the model developed in this thesis and clues provided by the Voyager IRIS instrument, it appears that most of the variability seen in the range from 1 to 20 cm can be explained by a static distribution, but that some seasonal variations are expected as well. In the discussion to follow, models will be presented that use  $\text{NH}_3$  gradients to explain the observed brightness features. It will not change the discussion or conclusions, however, to use models with alternate absorbers, or ones that use temperature gradients to fit the high-resolution data.

The solid curve of Figure 4.29 shows the spectrum of the nominal model that was

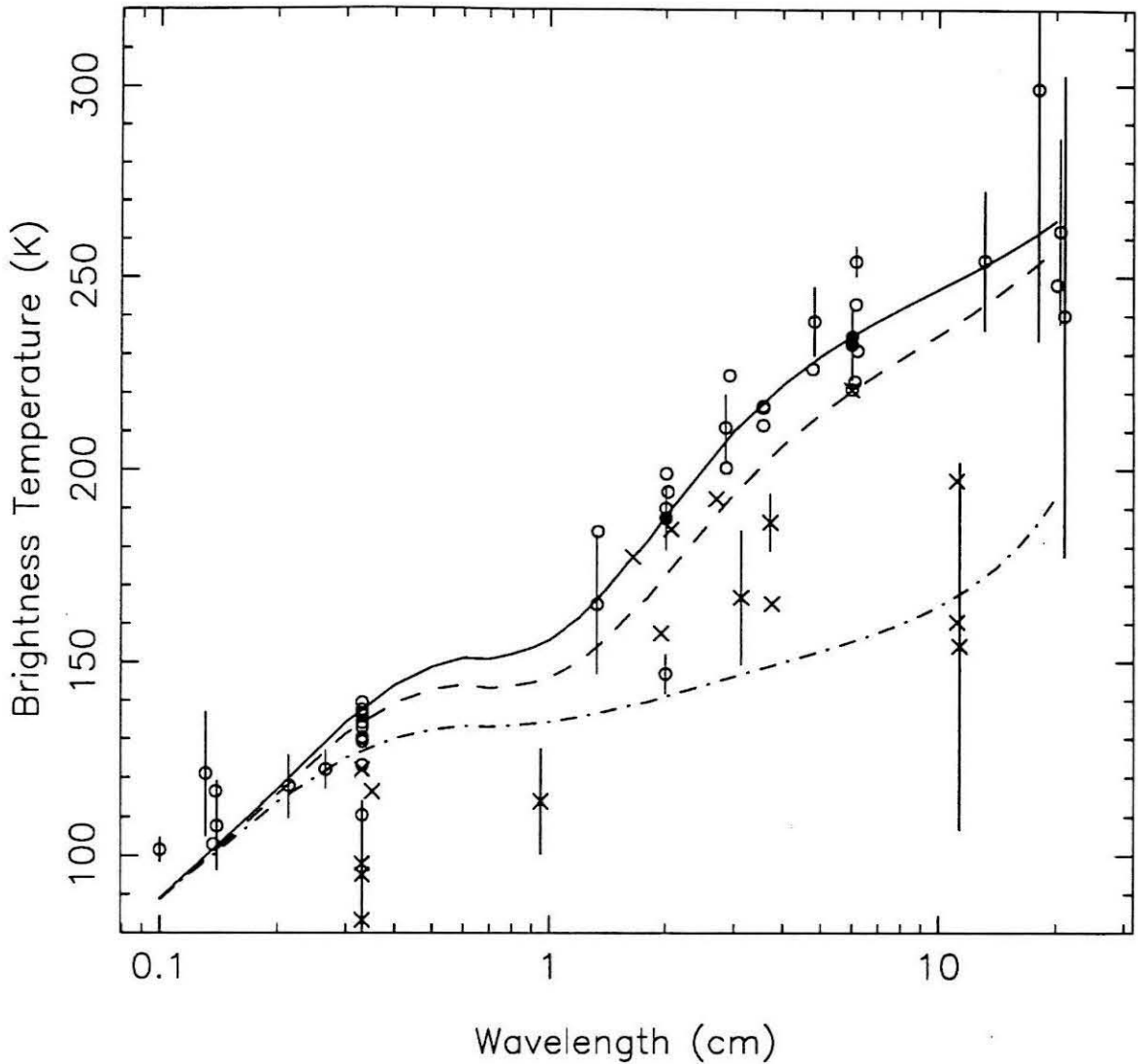


**Figure 4.29:** Time variability of Uranus' microwave spectrum. The open circles represent observations of Uranus made since 1973, while crosses indicate older data. The three filled circles mark the high-resolution data sets presented in Chapter 3. (See Chapter 2 for a more complete discussion of this compilation of unresolved data.) Older observations are clearly less bright than the newer ones. The solid curve shows the spectrum of the nominal model derived in Section 4.1.2, for observations that look down upon the pole of the planet. The dashed curve is the spectrum for the same model when the equator is at the sub-Earth point. It is assumed that the Northern and Southern Hemispheres have symmetric brightness distributions that do not vary with time. The dot-dashed curve is the brightness of a model that has an  $\text{NH}_3$  molar mixing ratio of  $1.4 \times 10^{-4}$  at all latitudes, and no  $\text{H}_2\text{S}$ .

presented in Section 4.1.2, and shown in Figures 4.12, 4.13, and 4.14. For this calculation, the pole is assumed to be at the disk center (roughly corresponding to the current geometry). To calculate what the spectrum might look like for the case when the equator is near the sub-Earth point (corresponding to observations made closer to 1965), it is necessary to determine the opacity distribution of the Northern Hemisphere. Three northern brightness patterns are considered. The first is symmetric with the Southern Hemisphere, while the second attempts to maximize the time variability by assuming the entire Northern Hemisphere is similar to the absorber rich upwelling in the south. The third model makes use of the fact that the Voyager IRIS instrument has pole to pole coverage on Uranus (Figure 4.19), and that the radio brightness in the south is highly correlated with the IRIS temperatures. This third model therefore places an absorber rich upwelling in the north between  $10^\circ$  and  $50^\circ$  latitude (where an IRIS temperature minimum is observed), and models the rest of the Northern Hemisphere as a region of subsidence. While these three models would appear dramatically different in disk resolved images, they are quite similar when only disk-averaged information is available. The dashed curve of Figure 4.29 shows the spectrum for the model in which the Northern and Southern Hemispheres are symmetric about the equator, under 1965 viewing conditions (the equator is at the sub-Earth point). The other models are all within 4 K of this curve.

The apparent time variations for these models are in the 10 to 20 K range at wavelengths between 1 and 20 cm. It is difficult to determine just what the magnitude of the data variations are because there is tremendous scatter in the observations, particularly the older ones. It seems that about the best that can be said at this point is that a static brightness distribution may explain the time variability between 1 and 6 cm, though the fit would definitely be improved with more variability in the model. At the longer wavelengths, there is a bit of a dilemma. Taken at face value, the older 11 cm data require two orders of magnitude more absorption in both the north and south than the newer

data do, equivalent to a solar  $\text{NH}_3$  abundance without any depleting reactions such as were postulated to occur with  $\text{H}_2\text{S}$ . This is shown by the dot-dashed curve. This model, however, appears too cold to simultaneously match the shorter wavelength older data. A reasonable overall fit to the older data is found by using the nominal absorber distribution in the Southern Hemisphere, and the factor of 100 absorber enrichment only in the Northern Hemisphere. This model's spectrum would fall midway between the dashed and dot-dashed curves of Figure 4.29. Thus, to explain the older data at decimeter wavelengths requires either a static but extremely large asymmetry between the hemispheres, or dramatic seasonal variations. It must be acknowledged, however, that the data can be in error, and it would seem imprudent to base very much on the three data points at 11 cm.

Given the limitations of the current data set, there does not appear to be a requirement for Uranus' intrinsic radio brightness, and hence atmospheric structure, to vary seasonally. This does not, however, preclude the existence of some variability. In fact, even though the 1981 and 1989 6 cm observations presented in Chapter 3 convincingly demonstrate no major changes occurred over this time span, the fact that the Voyager IRIS temperatures show differences between the Southern (summer) Hemisphere and Northern (winter) one, is suggestive of some changes. In particular, the circulation in the winter appears weaker than that in the summer, and the upwelling shifts poleward (Figure 4.19). Since the stratospheric temperatures in the south seem coupled to deep atmospheric motions, it is reasonable to expect that seasonal variations will occur throughout the altitude range probed by the radio data on time scales of 40 years (half a Uranian year). If the 11 cm data are accurate, the case for large seasonal effects is strengthened: while the Northern Hemisphere could be permanently much more absorbing than the Southern, there is no reason to suspect such an asymmetry would be maintained throughout the year. In this case it appears more likely that the fall or winter hemisphere (or both) is much more absorbing than the summer hemisphere.

To summarize this discussion of time variability, it appears that a static brightness distribution of the type currently observed in the Southern Hemisphere can explain most of the variability seen over the last 20 years. If the oldest 11 cm data are to be believed, however, some dramatic seasonal variations are expected. The fact that the Voyager IRIS instrument did see some hemispherical asymmetries suggests seasonal effects do occur, though no major changes have been observed over the 10 years that high resolution radio data have been available. Continued observations in the coming 15 years will resolve most of the questions raised here because the Northern Hemisphere can be observed as it passes from spring into summer, while the Southern Hemisphere transitions from fall to winter.



## Chapter 5

### Summary

*“Those summer nights are calling...”*  
— Journey

In this thesis, the first detailed analysis of high resolution radio maps of Uranus is presented. Microwave instruments are an extremely powerful tool for observing the solar system, and the data discussed here probe the atmosphere deeper than has ever been seen on any giant planet. While it may have been obscured by all the technical minutiae, the overriding force behind this work is the thrill of looking up and seeing something new.

What is seen on Uranus, using VLA maps at 2 cm and 6 cm, is that the Southern Hemisphere appears to be dominated by a single meridional circulation cell, spanning vertically 250 km, from the 50 to 0.1 bar pressure levels. This means stratospheric motions are coupled to those in the deep troposphere. The circulation cell divides the hemisphere into two distinct regions: an absorber rich upwelling between the equator and  $-45^\circ$ , and an absorber depleted downdraft from  $-45^\circ$  to  $-90^\circ$ . The transition between the regions is sharp (less than  $15^\circ$  in latitude) and centered at  $-45 \pm 5^\circ$ . As parcels rise in the upwelling, the absorber mixing ratio drops by a factor of about 200, presumably due to condensation. The depletion occurs in a two-stage process, with a factor of 100 loss occurring between 25 and 10 bar, and a smaller depletion occurring at or above 5 bar. The absorber depleted air parcels then move poleward and descend, keeping latitudes poleward of  $-45^\circ$  relatively absorber free down to about the 50 bar level. Below this, the subsiding air no longer dominates the composition, and the atmosphere appears strongly

absorbing again.

Based on simple dynamical modeling, it appears this circulation pattern is consistent with Voyager observations of the zonal winds and latitudinal temperature structure. This modeling also indicates that for stratospheric and tropospheric motions to be coupled, as indicated by observations, the forcing driving the atmospheric motions should occur above the 500 bar level (which means within 500 km of the observed cloud tops). Furthermore, if the deep atmosphere is adiabatic, water condensation effects can be an important factor in determining the atmospheric stability below 50 bars.

High resolution observations span 8 years, from 1981 to 1989. In this time span there has been no appreciable change in the appearance of Uranus. Because each season on Uranus lasts 21 years, however, seasonal effects probably take longer to manifest themselves. Voyager IRIS data indicate that, at least near the tropopause, detectable variations in atmospheric structure, presumably tied to the circulation pattern, do exist between the summer and winter hemispheres. Unresolved radio observations of Uranus made between 1965 and the present also favor seasonal variations in the deeper atmosphere, but this result is highly uncertain given the quality of the older, single dish measurements.

Finally, superimposed on the large scale, bi-modal brightness distribution of Uranus (the bright, absorber depleted pole and dark, absorber rich upwelling) are much smaller oscillations, reminiscent of the belts and zones of Jupiter. These features are narrow, covering generally less than  $15^\circ$  in latitude, and have not changed position between 1981 and 1989. While a complete analysis of these features is beyond the scope of this work, it has been determined that variations in the altitude at which clouds form could easily cause them.

Having completed an initial analysis of the radio data, there are several areas that deserve further study. One of the most straightforward tasks remaining is to continue observing Uranus in order to study its seasonal variability. Additional observations, along with a more detailed analysis of the existing data, may also determine the nature of the

small scale structures seen in the atmosphere. High resolution observations at wavelengths longer than 6 cm would be an ideal way to probe the atmosphere deeper than 50 bar, though no telescope currently has the capability to do this properly. (While the VLA can operate near 20 cm, the resolution at these wavelengths is not high enough to map Uranus. Possible ways around this are to use elements of the VLBA array in conjunction with the VLA to increase resolution, or to come up with the funds to equip the VLA with 13 cm receivers.) Placing a spaceborne microwave radiometer into orbit around Uranus (or any giant planet) would also yield an unprecedented high resolution, global look at the deep atmosphere. Another area for future work is to create more realistic dynamical and chemical models, including such things as latitudinally varying atmospheric parameters and aqueous solution effects on the composition. Last of all, VLA observations of Neptune are planned that will allow a similar analysis of its atmosphere. Since Neptune resembles Uranus without a high obliquity and with an internal heat source, these data will not only probe a new planet, but will also aid in our understanding of the general way in which both atmospheres work.



## Appendix

### Calculating the Brunt-Vaisala Frequency

Consider the forces on an air parcel, initially in equilibrium with its surroundings, that is displaced adiabatically a small height in the direction of increasing temperature. From Equation 4.9, the buoyancy force on the parcel is

$$F_p = g(\rho_p - \rho_a),$$

where the subscript  $p$  refers to the parcel, and  $a$  to the ambient atmosphere. Using the fact that the densities of parcel and air are the same at the initial point, and expressing the force as mass times acceleration in pressure coordinates, this becomes

$$\frac{d^2 P}{dt^2} = -g^2 \frac{\rho_a}{\rho_p} \left[ \frac{d\rho_a}{dP} - \frac{d\rho_p}{dP} \right] dP = -N^2 dP,$$

which is a common expression for oscillatory motion of frequency  $N$  when  $N^2 > 0$ , and for exponential growth (instability) when  $N^2 < 0$ . To calculate the total derivatives in  $N^2$ , use the ideal gas law to express each one in the form

$$\frac{d\rho}{dP} = \left( \frac{\partial \rho}{\partial P} \right)_{T, f_i} + \left( \frac{\partial \rho}{\partial T} \right)_{P, f_i} \frac{dT}{dP} + \sum_i \left( \frac{\partial \rho}{\partial f_i} \right)_{T, P} \frac{df_i}{dP}. \quad (\text{A.1})$$

In this expression,  $f_i$  refers to the molar mixing ratio of species  $i$ , the summation is over all atmospheric constituents, and the parenthesis around each partial derivative carry subscripted values of the parameters to be held constant.

With the exception of the summation term, these values are straightforward to calculate. The partial derivatives come from the ideal gas law, and the temperature lapse rate comes from Equation 2.4 for the ambient air, and from a dry adiabat for the parcel (which

is just Equation 2.4 without any species being saturated). To calculate the summation term, first note that all the  $\frac{df_i}{dP}$  terms are zero for the displaced parcel (its composition does not change), so the summation only appears in the term for  $\rho_a$ . In what follows, therefore, all parameters will refer to the ambient air, though the 'a' subscript will be left off for brevity. Looking at the summation in Equation A.1,  $\frac{df_i}{dP}$  is found from a finite differencing of partial pressures as a function of height based on the expressions of Section 2.2.4. The last term needed,  $\frac{\partial \rho}{\partial f_i}$ , requires some manipulations to calculate, which were kindly demonstrated by R.K. Achterberg (personal communication). From the ideal gas law, and the definition of partial pressures,

$$\frac{\partial \rho}{\partial f_i} = \frac{P}{R^*T} \sum_j \mu_j \frac{\partial f_j}{\partial f_i},$$

where  $\mu_j$  is the molecular weight of species  $j$ .

To find  $\frac{\partial f_j}{\partial f_i}$ , note that  $\sum f_j = 1$ , so that

$$\sum_j \frac{\partial f_j}{\partial f_i} = 0,$$

which, assuming  $i \neq \text{H}_2$ , can be written as

$$\frac{\partial f_{\text{H}_2}}{\partial f_i} + \sum_{j \neq i, \text{H}_2} \frac{\partial f_j}{\partial f_i} = -1. \quad (\text{A.2})$$

Now, assume that as  $f_i$  changes, the relative abundances of all other species are unchanged, so that  $f_j/f_k$  is constant for all  $j, k \neq i$ . This means all mixing ratios can be referenced to one species, say  $\text{H}_2$ , by

$$M_j = f_j/f_{\text{H}_2},$$

which, because  $M_j$  is constant for  $i \neq j$  and  $i \neq \text{H}_2$ , can be written as

$$\frac{\partial f_j}{\partial f_i} = M_j \frac{\partial f_{\text{H}_2}}{\partial f_i}. \quad (\text{A.3})$$

The two equations, A.2 and A.3, have two unknowns,  $\frac{\partial f_{\text{H}_2}}{\partial f_i}$  and  $\frac{\partial f_j}{\partial f_i}$ , which can be solved for. Doing this and noting that  $M_{\text{H}_2} = 1$ ,

$$\frac{\partial f_j}{\partial f_i} = \frac{-M_j}{\sum_{k \neq i} M_k} \quad i \neq j, \text{H}_2.$$

Substituting in the definition of  $M_j$  and cancelling the  $f_{H_2}$  factors, the final answer is

$$\frac{\partial f_j}{\partial f_i} = \begin{cases} \frac{-f_j}{\sum_{k \neq i} f_k} & \text{for } i \neq j; \\ 1.0 & \text{for } i = j. \end{cases} \quad (\text{A.4})$$

Note that in Equation A.4, the restriction on  $i \neq H_2$  is lifted. This is because the same derivation can be carried out for  $i = H_2$  if a different species is used as the reference for  $M_j$ , and the same result will be found.



## References

- Astronomical Almanac* 1981, 1989. U.S. Government Printing Office, Washington D.C.
- Atreya, S.K. 1986. *Atmospheres and Ionospheres of the Outer Planets and their Satellites*. Springer-Verlag, Berlin.
- Atreya, S.K., and P.N. Romani 1984. Photochemistry and clouds of Jupiter, Saturn, and Uranus. In *Recent Advances in Planetary Meteorology* (G.E. Hunt, Ed.), pp. 17–68. Cambridge University Press, Cambridge.
- Bachet, G., E.R. Cohen, P. Dore, and G. Birnbaum 1983. The translational-rotational absorption spectrum of hydrogen. *Can. J. Phys.* **61**, 591–603.
- Berge, G.L., and S. Gulkis 1976. Earth-based radio observations of Jupiter: Millimeter to meter wavelengths. In *Jupiter* (T. Gehrels, Ed.), pp. 621–692. Univ. of Arizona Press, Tucson.
- Berge, G.L., D.O. Muhleman, and R. Linfield 1988. Very Large Array observations of Uranus at 2.0 cm. *Astronomical Jour.* **96**, 388–395.
- Briggs, F.H. and B.H. Andrew 1980. Microwave radiometry and interferometry of Uranus. *Icarus* **41**, 269–277.
- Briggs, F.H. and P.D. Sackett 1989. Radio observations of Saturn as a probe of its atmosphere and cloud structure. *Icarus* **80**, 77–103.

- Cameron, A.G.W. 1982. Elemental and nuclidic abundances in the solar system. In *Essays in Nuclear Astrophysics* (C.A. Barnes, D.D. Clayton, and D.N. Schramon, Eds.) pp. 23–43. Cambridge University Press.
- Carlson, B.E., M.J. Prather, and W.B. Rossow 1987. The role of aqueous chemistry in determining the composition and cloud structure of the upper troposphere on Uranus. *Ap. J.* **321**, L97–L101.
- Carlson, B.E., W.B. Rossow, and G.O. Orton 1988. Cloud microphysics of the giant planets. *J. Atmos. Sci.* **45**, 2066–2081.
- Chandrasekhar, S. 1960. *Radiative Transfer*. Dover Publications, Inc., New York.
- Cohen, E.R., L. Frommhold, and G. Birnbaum 1982. Analysis of the far infrared H<sub>2</sub>-He spectrum. *J. Chem. Phys.* **77**, 4933–4941.
- Conrath, B.J., P.J. Gierasch, and S.S. Leroy 1990. Temperature and circulation in the stratosphere of the outer planets. *Icarus* **83**, 255–281.
- De Pater, I. 1986. Jupiter's zone-belt structure at radio wavelengths II. Comparison of observations with model atmosphere calculations. *Icarus* **68**, 344–365.
- De Pater, I., and S. Gulkis 1988. VLA observations of Uranus at 1.3–20 cm. *Icarus* **75**, 306–323.
- De Pater, I., and S.T. Massie 1985. Models of the millimeter-centimeter spectra of the giant planets. *Icarus* **62**, 143–171.
- De Pater, I., P.N. Romani, and S.K. Atreya 1989. Uranus deep atmosphere revealed. *Icarus* **82**, 288–313.
- De Pater, I., P.N. Romani, and S.K. Atreya 1991. Possible microwave absorption by H<sub>2</sub>S gas in Uranus' and Neptune's atmospheres. *Icarus* **91**, 220–233.

- Del Genio, A.D. 1989. Moist convection in the atmospheres of Uranus and Neptune. *Bull. Amer. Astron. Soc.* **21**, 917–918. [Abstract]
- Dore, P., L. Nencini, and G. Birnbaum 1983. Far infrared absorption in normal H<sub>2</sub> from 77 to 298 K. *J. Quant. Spectrosc. Radiat. Transfer* **30**, 245–253.
- Farkas, A. 1935. *Orthohydrogen, Parahydrogen, and Heavy Hydrogen*. Cambridge University Press.
- Fegley, B., D. Gautier, T. Owen, and R.G. Prinn 1991. Spectroscopy and chemistry of the atmosphere of Uranus. In *Uranus* (J. Bergstralh, E. Miner, and M.S. Matthews, Eds.), pp. 147–203. University of Arizona Press, Tucson.
- Flasar, F.M., B.J. Conrath, P.J. Gierasch, and J.A. Pirraglia 1987. Voyager infrared observations of Uranus' atmosphere: Thermal structure and dynamics. *J. Geophys. Res.* **92**, 15011–15018.
- Fox, K. 1974. On the microwave spectrum of methane in the atmospheres of outer planets. In *Exploration of the Planetary System* (A. Woszczyk and C. Iwaniszewska, Eds.), IAU Symposium No. 65, 359–365.
- Frieden, B.R. 1972. Restoring with maximum likelihood and maximum entropy. *J. Opt. Soc. Am.* **62**, 511–518.
- Friedson, J. and A.P. Ingersoll 1987. Seasonal meridional energy balance and thermal structure of the atmosphere of Uranus: A radiative-convective-dynamical model. *Icarus* **69**, 135–156.
- Gierasch, P.J. and B.J. Conrath 1987. Vertical temperature gradients on Uranus: Implications for layered convection. *J. Geophys. Res.* **92**, 15019–15029.
- Gierasch, P.J., B.J. Conrath, and J.A. Magalhaes 1986. Zonal mean properties of Jupiter's upper troposphere from Voyager infrared observations. *Icarus* **67**, 456–

483.

- Gill, A.E. 1982. *Atmosphere-Ocean Dynamics*. Academic Press, Inc., Orlando, Florida.
- Goodman, G.C. 1969. Models of Jupiter's atmosphere. Unpublished Ph.D. thesis, University of Illinois.
- Grossman, A.W. 1990. Microwave imaging of Saturn's deep atmosphere and rings. Ph.D. thesis, California Institute of Technology.
- Gulkis, S., and I. de Pater 1984. A review of the millimeter and centimeter observations of Uranus. In *Uranus and Neptune* (J.T. Bergstrahl, Ed.), NASA Conference Publication 2330, pp. 225–262.
- Gulkis, S., M.A. Janssen, and E.T. Olsen 1978. Evidence for the depletion of ammonia in the Uranus atmosphere. *Icarus* **34**, 10–19.
- Gulkis, S., E.T. Olsen, M.J. Klein, and T.J. Thompson 1983. Uranus: Variability of the microwave spectrum. *Science* **221**, 453–455.
- Hanel, R., B. Conrath, F.M. Flasar, V. Kunde, W. Maguire, J. Pearl, J. Pirraglia, R. Samuelson, D. Cruikshank, D. Gautier, P. Gierasch, L. Horn, and P. Schulte 1986. Infrared observations of the Uranian system. *Science* **233**, 70–74.
- Hofstadter, M.D., G.L. Berge, and D.O. Muhleman 1990. Vertical motions in the Uranian atmosphere: An analysis of radio observations. *Icarus* **84**, 261–267.
- Hofstadter, M.D., and D.O. Muhleman 1987. Latitudinal variations in the atmosphere of Uranus. *Bull. Amer. Astron. Soc.* **19**, 853. [Abstract]
- Hofstadter, M.D., and D.O. Muhleman 1989. Latitudinal variations of ammonia in the atmosphere of Uranus: An analysis of microwave observations. *Icarus* **81**, 396–412.

- Hogbom, J.A. 1974. Aperture synthesis with a non-regular distribution of interferometer baselines. *Astron. Astrophys. Suppl.* **15**, 417–426.
- Ingersoll, A.P. 1976. Pioneer 10 and 11 observations and the dynamics of Jupiter's atmosphere. *Icarus* **29**, 245–253.
- Ingersoll, A.P., and C.C. Porco 1978. Solar heating and internal heat flow on Jupiter. *Icarus* **35**, 27–43.
- Jaffe, W.J., G.L. Berge, T. Owen, and J. Caldwell 1984. Uranus: Microwave images. *Science* **225**, 619–621.
- Kerr, D.E. 1951. *Propagation of Short Radio Waves*. Dover Publications Inc., New York.
- Klein, M.J., and J.A. Turegano 1978. Evidence of an increase in the microwave brightness temperature of Uranus. *Astrophys. J.* **224**, L31–L34.
- Lewis, J.S. 1969. The clouds of Jupiter and the  $\text{NH}_3\text{-H}_2\text{O}$  and  $\text{NH}_3\text{-H}_2\text{S}$  systems. *Icarus* **10**, 365–378.
- Lewis, J.S., and R.G. Prinn 1984. *Planets and their Atmospheres*. Academic Press, Inc., Florida.
- Lindal, G.F., G.E. Wood, G.S. Levy, J.D. Anderson, D.N. Sweetnam, H.B. Hotz, B.J. Buckles, D.P. Holmes, P.E. Doms, V.R. Eshleman, G.L. Tyler, and T.A. Croft 1981. The atmosphere of Jupiter: An analysis of the Voyager radio occultation measurements. *Jour. Geophys. Res.* **86**, 8721–8727.
- Lindal, G.F., D.N. Sweetnam, and V.R. Eshleman 1985. The atmosphere of Saturn: An analysis of the Voyager radio occultation measurements. *Astrophys. J.* **90**, 1136–1146.
- Lindal, G.F., J.R. Lyons, D.N. Sweetnam, V.R. Eshleman, D.P. Hinson, and G.L.

- Tyler 1987. The atmosphere of Uranus: Results of radio occultation measurements with Voyager 2. *Jour. Geophys. Res.* **92**, 14987–15001.
- Lindal, G.F., J.R. Lyons, D.N. Sweetnam, V.R. Eshleman, D.P. Hinson, and G.L. Tyler 1990. The atmosphere of Neptune: Results of radio occultation measurements with Voyager 2. *Bull. Amer. Astron. Soc.* **22**, 1106. [Abstract]
- McKinnon, W.B. 1981. Microwave interferometry and the deep atmosphere of Uranus. *EOS* **62**, 941 (abstract only).
- Mishima, O., D.D. Klug, and E. Whalley 1983. The far-infrared spectrum of ice Ih in the range 8–25  $\text{cm}^{-1}$ : Sound waves and difference bands, with applications to Saturn's rings. *J. Chem. Phys.* **78**, 6399–6404.
- Morris, E.C., and R.W. Parsons 1970. Microwave absorption by gas mixtures at pressures up to several hundred bars. *Australian J. of Phys.* **23**, 335–349.
- Muhleman, D.O., and G.L. Berge 1989. Observations of Mars, Uranus, Neptune, Io, Europa, Ganymede, and Callisto at a wavelength of 2.66 millimeters. *Icarus* **92**, 263–272.
- Orton, G.S., A.T. Tokunaga, and J. Caldwell 1983. Observational constraints on the atmospheres of Uranus and Neptune from new measurements near 10  $\mu\text{m}$ . *Icarus* **56**, 147–164.
- Orton, G.S., M.J. Griffin, P.A.R. Ade, I.G. Nolt, J.V. Radostitz, E.I. Robson, and W.K. Gear 1986. Submillimeter and millimeter observations of Uranus and Neptune. *Icarus* **67**, 289–304.
- Pearl, J.C., B.J. Conrath, R.A. Hanel, and J.A. Pirraglia 1987. Energy balance of Uranus: Preliminary Voyager results. *Bull. Amer. Astron. Soc.* **19**, 852. [Abstract]

- Pearl, J.C., B.J. Conrath, R.A. Hanel, J.A. Pirraglia, and A. Coustenis 1990. The albedo, effective temperature, and energy balance of Uranus, as determined from Voyager IRIS data. *Icarus* **84**, 12–28.
- Perley, R.A., F.R. Schwab, and A.H. Bridle 1986. *Synthesis Imaging*. (Course notes from an NRAO summer school held in Socorro, New Mexico, August 1985.) NRAO/AUI, West Virginia.
- Podolak, M., and R.T. Reynolds 1987. The rotation rate of Uranus, its internal structure, and the process of planetary accretion. *Icarus* **70**, 31–36.
- Podolak, M., R.T. Reynolds, and R. Young 1990. Post Voyager comparisons of the interiors of Uranus and Neptune. *Geophys. Res. Letters* **17**, 1737–1740.
- Pollack, J.B., and P. Bodenheimer 1989. *Origin and Evolution of Planetary and Satellite Atmospheres*, (S.K. Atreya, J.B. Pollack, and M.S. Matthews, Eds.), pp. 564–602. Univ. of Arizona Press, Tucson.
- Pollack, J.B., K. Rages, S.K. Pope, M.G. Tomasko, P.N. Romani, and S.K. Atreya 1987. Nature of the stratospheric haze on Uranus: Evidence for condensed hydrocarbons. *J. Geophys. Res.* **92**, 15037–15065.
- Poynter, R.L. and R.K. Kakar 1975. The microwave frequencies, line parameters, and spectral constants for  $^{14}\text{NH}_3$ . *Astrophys. J. Supplement Series No. 277*, **29**, 87–96.
- Press, W.H., B.P. Flannery, S.A. Teukolsky, and W.T. Vetterling 1986. *Numerical Recipes*. Cambridge University Press, Cambridge.
- Rages, K., and J.B. Pollack 1988. Scattering models of Uranus' atmosphere at low latitudes. In *Uranus*, proceedings of the June 28–July 1 conference hosted by the Jet Propulsion Laboratory in Pasadena, CA, 3.7. [Abstract]

- Smith, B.A., L.A. Soderblom, R. Beebe, D. Bliss, J.M. Boyce, A. Brahic, G.A. Briggs, R.H. Brown, S.A. Collins, A.F. Cook II, S.K. Croft, J.N. Cuzzi, G.E. Danielson, M.E. Davies, T.E. Dowling, D. Godfrey, C.J. Hansen, C. Harris, G.E. Hunt, A.P. Ingersoll, T.V. Johnson, R.J. Krauss, H. Masursky, D. Morrison, T. Owen, J.B. Plescia, J.B. Pollack, C.C. Porco, K. Rages, C. Sagan, E.M. Shoemaker, L.A. Sromovsky, C. Stoker, R.G. Strom, V.E. Suomi, S.P. Synnott, R.J. Terrile, P. Thomas, W.R. Thompson, and J. Veverka 1986. Voyager 2 in the Uranian system: Imaging science results. *Science* **233**, 43–64.
- Spilker, T.R. 1990. Laboratory measurements of microwave absorptivity and refractivity spectra of gas mixtures applicable to giant planet atmospheres. Ph.D. thesis, Stanford University.
- Steffes, P.G., J.M. Jenkins, M.F. Selman, and W.W. Gregory 1986. Laboratory measurements of the microwave opacity of gaseous ammonia (NH<sub>3</sub>) under simulated conditions for Jovian atmospheres. *Bull. Amer. Astron. Soc.* **18**, 787 (abstract only).
- Stone, P.H. 1976. The meteorology of the Jovian atmosphere. In *Jupiter*, (T. Gehrels, Ed.), 586–618. Univ. of Arizona Press, Tucson.
- Thompson, A.R., J.M. Moran, and G.W. Swenson 1986. *Interferometry and Synthesis in Radio Astronomy*. John Wiley & Sons, New York.
- Townes, C.H., and A.L. Schawlow 1975. *Microwave Spectroscopy*. Dover Publications, Inc., New York.
- Trafton, L.M. 1967. Model atmospheres of the major planets. *Astrophys. J.* **147**, 765–781.
- Tyler, G.L., D.N. Sweetnam, J.D. Anderson, J.K. Campbell, V.R. Eshleman, D. P. Hinson, G.S. Levy, G.F. Lindal, E.A. Marouf, and R.A. Simpson 1986. Voy-

- ager 2 radio science observations of the Uranian system: Atmosphere, rings, and satellites. *Science* **233**, 79–84.
- Tyler, G.L., D.N. Sweetnam, J.D. Anderson, S.E. Borutzki, J.K. Campbell, V. R. Eshleman, D.L. Gresh, E.M. Gurrola, D.P. Hinson, N. Kawashima, E.R. Kursinski, G.S. Levy, G.F. Lindal, J.R. Lyons, E.A. Marouf, P.A. Rosen, R.A. Simpson, and G.E. Wood 1989. Voyager radio science observations of Neptune and Triton. *Science* **246**, 1466–1473.
- Van de Hulst, H.C. 1981. *Light Scattering by Small Particles*. Dover Publications Inc., New York.
- Wallace, L. 1980. The structure of the Uranus atmosphere. *Icarus* **43**, 231–259.
- Wallace, J.M. and P.V. Hobbs 1977. *Atmospheric Science*. Academic Press, Inc., Florida.
- Waters, J.W. 1976. Absorption and emission by atmospheric gases. In *Methods of Experimental Physics* Vol. **12**, Part B (M.L. Meeks, Ed.), pp. 142–176. Academic Press, New York.
- Weidenschilling, S.J. and J.S. Lewis 1973. Atmospheric and cloud structures of the Jovian planets. *Icarus* **20**, 465–476.
- Wrixon, G.T. and W.J. Welch 1970. The millimeter wave spectrum of Saturn. *Icarus* **13**, 163–172.
- Wrixon, G.T., W.J. Welch, and D.D. Thornton 1971. The spectrum of Jupiter at millimeter wavelengths. *Astrophys. J.* **169**, 171– 183.

